Second International Symposium on Magnetic Suspension Technology

Edited by
Nelson J. Groom
Langley Research Center • Hampton, Virginia

Colin P. Britcher
Old Dominion University • Norfolk, Virginia

National Aeronautics and Space Administration
Langley Research Center • Hampton, Virginia 23681-0001

May 1994

INTRODUCTION

The 2nd International Symposium on Magnetic Suspension Technology was held at the Westin Hotel in Seattle, Washington on August 11–13, 1993. The symposium was sponsored by the Spacecraft Controls Branch of the Langley Research Center in coordination with the Office of Advanced Concepts and Technology (OACT) at NASA Headquarters. The symposium was chaired by the following people:

Nelson J. Groom, Chairman
NASA
Langley Research Center
Hampton, VA 23681-0001

Dr. Colin P. Britcher, Technical Program Chairman
Dept. of Aerospace Engineering
Old Dominion University
Norfolk, VA 23529-0247

Virginia B. Marks, Administrative Chairman
NASA
Langley Research Center
Hampton, VA 23681-0001

An international steering committee assisted in selecting and reviewing submitted abstracts and in structuring the symposium sessions. The steering committee consisted of the following people:

Dr. Karl Boden
KFA–IGV
PF–1913
W–5170 Julich
GERMANY

Dr. James Downer
SatCon Technology Corporation
161 First Street
Cambridge, MA 02142–1207
USA

Dr. Michael J. Goodyer
Department of Aeronautics and Astronautics
University of Southampton
Southampton, SO9 5NH
ENGLAND

Dr. Robert A. Kilgore
CES Hampton
P.O. Box 4006
Hampton, VA 23664–0006
USA

Dr. Alexander V. Kuzin
Microprocessor Systems, Electronics and Electrical Engineering
Moscow Aviation–Technological Institute
Petrovka, 27
103737, Moscow, K–31
RUSSIA

Dr. Chin E. Lin
Institute of Aeronautics and Astronautics
National Cheng Kung University
Tainan, Taiwan
REPUBLIC OF CHINA

Dr. Hideo Sawada
Aircraft Aerodynamics Division
National Aerospace Laboratory
7–44–1 Jindaiji–higashi–machi
Chofu
Tokyo 182
JAPAN

Dr. Roland Siegwart
Mecos Traxler AG
Gutstrasse 38
CH–8400 Winterthur
SWITZERLAND

Dr. David L. Trumper
Department of Electrical Engineering
Massachusetts Institute of Technology
Cambridge, MA 02139
USA

The goal of the symposium was to examine the state of technology of all areas of magnetic suspension and to review related recent developments in sensors and control approaches, superconducting magnet technology, and design/implementation practices. The symposium included 18 technical sessions in which a total of 44 papers were presented. The technical sessions covered the areas of bearings, bearing modeling, controls, vibration isolation, micromachines, superconductivity, wind tunnel magnetic suspension systems, magnetically levitated trains (MagLev), rotating machinery and energy storage, and applications. A list of attendees is presented in the Appendix.

The first symposium in this series was held at NASA Langley Research Center, Hampton, Virginia in August 1991. The proceedings of this symposium are available as NASA Conference Publication 3152, Parts 1 and 2.

The use of trade names of manufacturers in this report does not constitute an official endorsement of such products or manufacturers, either expressed or implied, by the National Aeronautics and Space Administration.

iv

CONTENTS

PART 1*

SESSION 1—Magnetic Bearings
Chairman: Nelson J. Groom, NASA Langley Research Center

SESSION 2—Applications
Chairman: Willard W. Anderson, NASA Langley Research Center

SESSION 3—Maglev
Chairman: Claude R. Keckler, NASA Langley Research Center

SESSION 4—Superconductivity
Chairman: Nelson J. Groom, NASA Langley Research Center

---

*Part 1 is presented under separate cover.

SESSION 5a—Bearings
Chairman: Karl Boden, KFA-IGV

SESSION 5b—Maglev
Chairman: Michael J. Goodyer, University of Southampton

SESSION 6a—Controls
Chairman: Roland Siegwart, MECOS Traxler

SESSION 6b—MSBS
Chairman: Colin P. Britcher, Old Dominion University

SESSION 7a—Bearing Modeling
Chairman: Hideo Sawada, National Aerospace Laboratory

SESSION 7b—Controls
Chairman: Claude R. Keckler, NASA Langley Research Center

PART 2

SESSION 8—Applications
Chairman: Nelson J. Groom, NASA Langley Research Center

SESSION 9a(i)—Vibration Isolation
Chairman: Douglas B. Price, NASA Langley Research Center

SESSION 9a(ii)—Micromachines
Chairman: Douglas B. Price, NASA Langley Research Center

SESSION 9b—Rotating Machinery and Energy Storage
Chairman: Chin E. Lin, National Cheng Kung University

SESSION 10a—Controls
Chairman: Alexander V. Kuzin, Moscow Aviation Technological Institute

PART 2

Session 8 – Applications

Chairman: Nelson J. Groom
NASA Langley Research Center

INTEGRATION OF MAGNETIC BEARINGS IN
THE DESIGN OF ADVANCED GAS TURBINE ENGINES

A.F. Storace and D. Sood
General Electric Company
Aircraft Engines

J. P. Lyons and M. A. Preston
General Electric Company
Corporate Research and Development

SUMMARY

Active magnetic bearings provide revolutionary advantages for gas turbine engine rotor support. These advantages include tremendously improved vibration and stability characteristics, reduced power loss, improved reliability, fault-tolerance, and greatly extended bearing service life. The marriage of these advantages with innovative structural network design and advanced materials utilization will permit major increases in thrust to weight performance and structural efficiency for future gas turbine engines.

However, obtaining the maximum payoff requires two key ingredients. The first key ingredient is the use of modern magnetic bearing technologies such as innovative digital control techniques, high-density power electronics, high-density magnetic actuators, fault-tolerant system architecture, and electronic (sensorless) position estimation. This paper describes these technologies. The second key ingredient is to go beyond the simple replacement of rolling element bearings with magnetic bearings by incorporating magnetic bearings as an integral part of the overall engine design. This is analogous to the proper approach to designing with composites, whereby the designer tailors the geometry and load carrying function of the structural system or component for the composite instead of simply substituting composites in a design originally intended for metal material. This paper describes methodologies for the design integration of magnetic bearings in gas turbine engines.

INTRODUCTION

The development of active magnetic bearings (AMB) for advanced gas turbine engines is key to expanding present performance envelopes to achieve the goals of the IHPTET (Integrated High Performance Turbine Engine Technology) initiative; namely, doubling propulsion system capability by the turn of the century. The term active magnetic bearings includes the magnetic bearings (actuators), the controller, and the power electronics. The integration of active magnetic bearing rotor suspension and the high specific stiffness and strength primary load path structures which are integral to IHPTET propulsion systems provides a significant further opportunity to increase the structural efficiency, performance, reliability, and maintainability of advanced turbine engines. For example, the pay-offs obtainable by this marriage of advanced structures/materials technologies with the revolutionary advantages of active magnetic bearings are exemplified by the integration of a ceramic fiber-filament reinforced titanium based metal matrix composite (MMC) main engine (fan) shaft with the precise bearing force control provided by magnetic bearing suspension. The main engine shaft operates in a very rigorous, complex loading environment. The loads acting on the main engine shaft include rotordynamic transverse loads, transverse, axial, and torsional loads due to

compressor rotor/low pressure turbine gas pressure loads and compressor flow distortion loads, maneuver loads, and blade-loss loads. Common practice for these shafts has been to use super alloy materials, such as Inconel 718 or Marage 250. The strengths of these materials are satisfactory except their densities are also high which results in relatively low specific stiffness (E/ρ) values. The main engine shaft tends to have significant participation in engine system imbalance response, and supercritical operation is sometimes required. In many cases, complex soft mount bearing support systems incorporating dampers are required. The use of active magnetic bearings and MMC shaft material provides a direct approach for achieving superior dynamic characteristics and high load capability. The high specific stiffness of the MMC shaft material and the larger rotor diameters made possible by the elimination of the DN number (bearing diameter in mm x shaft RPM) restrictions of conventional rolling element bearings results in a dynamically rigid rotor at the high speeds required for advanced gas turbine engines. The result is that vibrational energy is driven into the magnetic bearings where tuning, damping, and active control strategies can be used to suppress the dynamic response for operating conditions extending into the extreme temperatures and speeds required for future advanced gas turbine engines.

The methodologies for the design integration of active magnetic bearings in the engine structural network to achieve a compact, simplified, and structurally efficient engine system are described in this paper. The elements of the advanced fault-tolerant active magnetic bearing system to be described herein include the magnetic bearings (which function as both high-density electromagnetic actuators and displacement transducers - in essence sensorless air gap estimation), the high-speed digital controller, and the high-density power electronics. The control algorithm for the digital controller has the capability to employ a variety of closed and open-loop (feed-forward) control strategies, dependent on the engine operating speeds, and external and internal engine loads. Also discussed are auxiliary bearings which are an additional element in the AMB system. They are needed as a back-up for the magnetic bearings, and to supplement the magnetic bearings for hard maneuvers and extreme loadings, such as blade-loss loads.

ENGINE STRUCTURAL TAILORING FOR ACTIVE MAGNETIC BEARINGS

To meet the exceedingly challenging performance goals of the IHPTET initiative, stringent rotor stage clearance control, engine weight reduction, high cycle temperatures, and higher rotor speeds will be required. The major increases required for the advanced turbine engine concepts in thermal efficiency, thrust/weight for fan engines, and power/weight for turboshaft engines will be obtained by adapting structural geometry for rotors, frames, cases, blades, and discs to take full advantage of advanced material characteristics such as those provided by metal matrix composites (MMC) and ceramic matrix composites (CMC).

Beyond the innovative structural arrangements and utilization of advanced materials, the incorporation of magnetic bearing rotor suspension provides a significant further capability to increase propulsion efficiency. Furthermore, the use of an Integral Starter/Generator (IS/G) mounted directly on the high pressure shaft provides on-board power for the magnetic bearings and engine starting capability[1]. A magnetic bearing engine with an IS/G forms one of the cornerstones of an "All-Electric" or "More-Electric" engine. The IS/G precludes the need for a power take-off (tower) shaft and an external gearbox to drive engine accessories (external generator, starter, pumps, actuators) such as shown in Figure 1 for present day engines. The magnetic bearing - IS/G combination provides for the virtual elimination of engine self-generated rotor whirling, elimination of the lube system required for rolling element bearings (refer to Figure 2), elimination of rotor dampers, engine structural simplification, engine weight reduction, potential for unlimited bearing service life, elimination of secondary engine power extraction, reduced vulnerability, and significantly improved reliability and maintainability.

436

POWER TAKE-OFF FOR AIRCRAFT DRIVEN COMPO-NENTS

ENGINE ACCESSORY GEARBOX AND POWER TAKE-OFF (TOWER) SHAFT

FAN MOMENT CAPABILITY PROVIDED BY REACTION AT TWO MAINSHAFT FORWARD (NO. 1 AND NO. 2) BEARINGS

RELATIVELY SMALL DIAMETER OF MAINSHAFT DUE TO CORE ROTOR BEARING DN NUMBER AND DISC BORE DIAMETER LIMITS

NO. 1
NO. 2
NO. 3
NO. 4
NO. 5
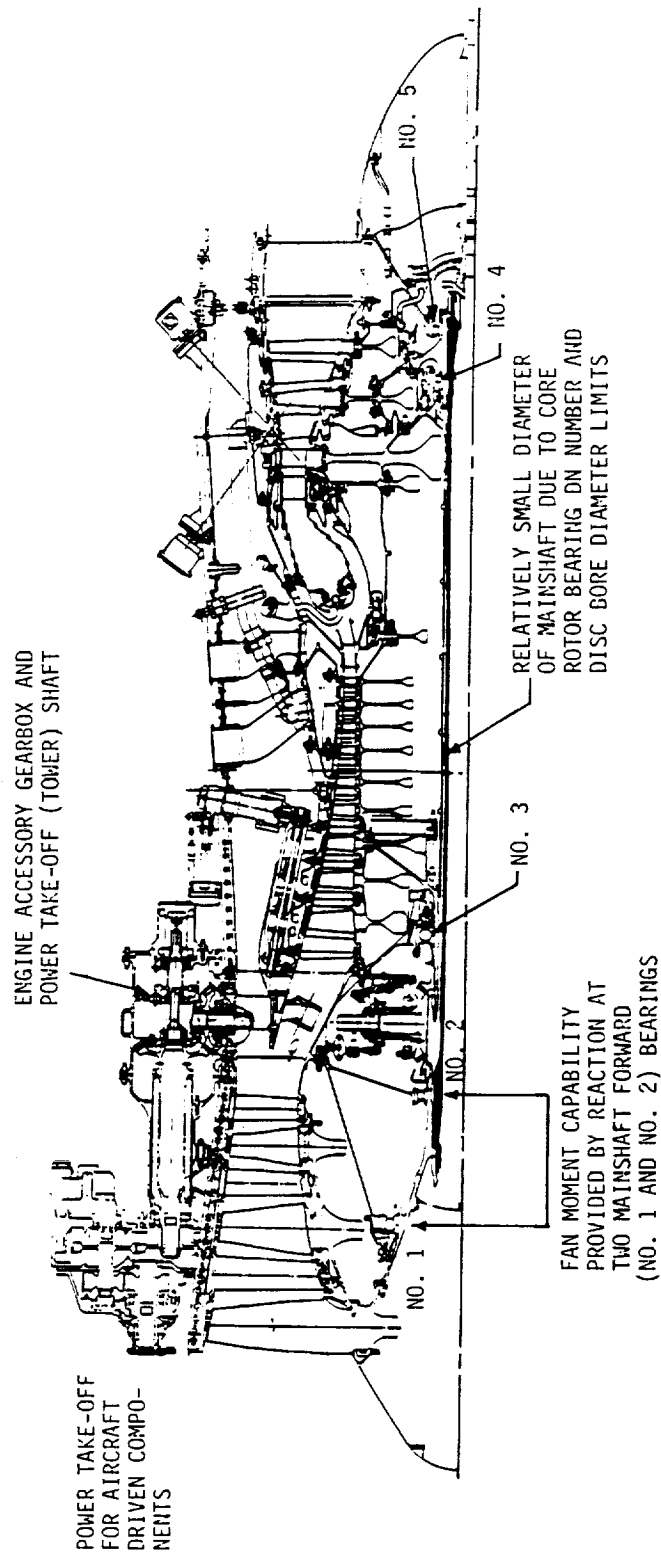
FIGURE 1
PRESENT DAY FIVE BEARING TURBOFAN ENGINE
STRUCTURAL AND ACCESSORY GEAR BOX ARRANGEMENT
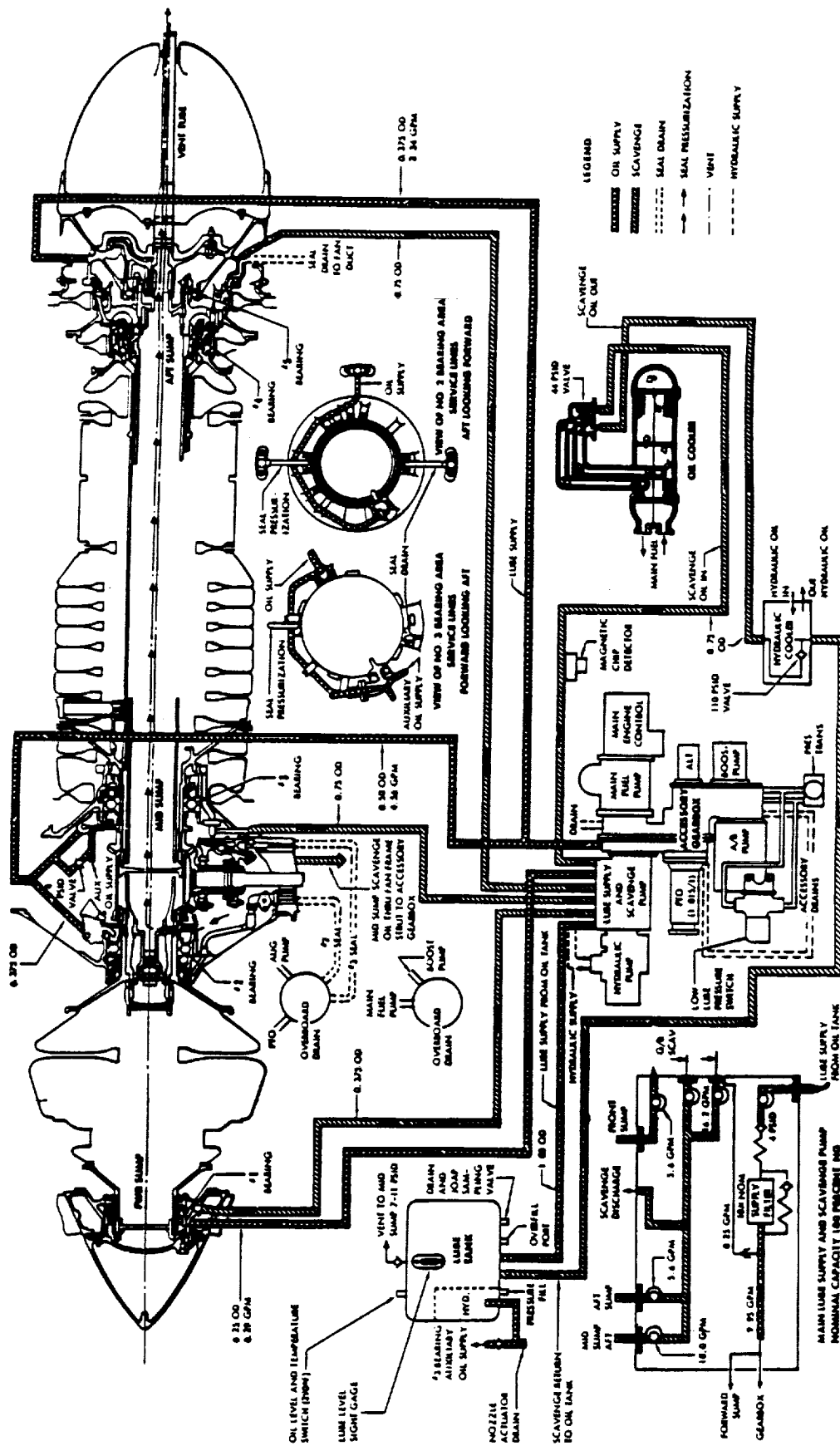
FIGURE 2
PRESENT DAY ENGINE LUBRICATION SYSTEM SCHEMATIC

The synergism of magnetic bearings and improved component designs incorporating advanced materials permits the development of turbine engines with a fewer number of bearings while also achieving significant improvement in rotordynamics characteristics and greatly reduced sensitivity of rotor stage clearance closures due to maneuver loads. Consider the main engine or fan shaft. This shaft spans across the core engine and in conventional engines has a large length-to-diameter ratio. In order to avoid critical speed problems and unacceptable maneuver load deflections at the fan and low pressure turbine for fan engines, redundant mounting is used. Figure 1 shows a large, present day five bearing military engine which uses three rolling element bearings (Nos. 1, 2, and 5) to support the main shaft. Couple support across the No. 1 and No. 2 bearings reacts the large overturning moment generated by the fan during in-flight gyro maneuver conditions and provides the stiffness required to avoid fan nodding modes in the operating speed range. This couple support is needed to control fan tip deflection as very little moment carrying capability is provided by the main shaft aft of the two forward bearings due to its low bending stiffness. This low bending stiffness is caused by the relatively small outer diameter of the main shaft required to meet core rotor bearing DN number (approximately 1.5 million) and disk bore diameter limits. The bore diameters of the core rotor disks of present day engines are minimized to maintain the stresses in the monolithic material disks within allowable limits at the maximum engine speeds. However, when magnetic bearings are used, DN numbers approaching or exceeding 3.5 million (based on maintaining magnetic bearing rotor lamination stresses within allowable limits) are achievable. In addition, significantly increased allowable disk stress levels and the attendant larger disk bore diameters can be achieved through the use of circumferential fiber reinforced composite material, such as Titanium based MMC for the compressor disks, and ceramic matrix composite for the turbine disk.

Three Bearing Support - Super
Alloy Main Shaft

Two Bearing Support - Stiff
Increased Diameter MMC
Main Shaft
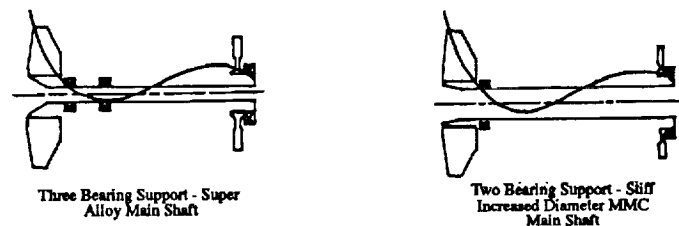
Figure 3. Main Engine Gyroscopic Loading Deflections

The need for three bearing support of the main engine shaft to prevent unacceptable fan pitching under gyro maneuver and dynamic loads is eliminated through the use of magnetic bearings and a high stiffness main shaft. Fabricating the main shaft from Ti 6AL-2Sn-4Zr-2Mo matrix material reinforced with continuous ceramic (silicon carbide) fibers allows the obtainment of high shaft stiffness. Note that the metal matrix composite (MMC) material is not stiffer than super alloy materials presently used in turbine engine shafts. However, it has a lower density allowing larger main shaft diameters to be used to obtain high stiffness without a weight penalty. The increase in high pressure rotor bore diameters required to obtain sufficient main shaft stiffness to permit two bearing support (at each end of the shaft with the two forward-couple bearings replaced by a single bearing) requires core rotor bearing DN numbers in the range of 3.5 million - well within the capability of magnetic bearings. The equivalence between three bearing support and an increased stiffness main shaft supported by two bearings is shown in Figure 3. In addition to controlling fan pitching due to gyro maneuver loads and avoiding fan nodding modes in the operating speed range, the high specific stiffness (E/e) MMC material reduces the participation of the main shaft mid-region in engine system criticals with the result that main shaft unbalance response sensitivity is further decreased.

Running the reinforcing fibers parallel to the axis of the main shaft results in the greatest improvement of shaft bending stiffness. However, in order to provide the required torsional strength, angle-ply fiber orientations are used. The MMC lamina are wrapped so that the fibers form a helix which advances along the shaft length. This scheme still provides a significant payoff in increased absolute and specific stiffness in the axial direction. References[2,3] discuss the benefits in gas turbine engine structural efficiency and performance achievable through the use of metal matrix composites with continuous fiber reinforcement in component structures. Table 1 shows a stiffness comparison of Ti 6-2-4-2/SiC angle-plied MMC material and selected super alloys at elevated temperature. Note the increased specific stiffness in the axial direction obtainable with angle-plied Ti 6-2-4-2/SiC MMC material.

	TI 6-2-4-2/SIC Angle Plied MMC	INCO 718	RENE'95	MARAGE 250
Density (lb/in^3)	0.145	0.296	0.297	0.289
1000°F Modulus (MSI)	25	25	27	21
1000°F E/ρ (in)	$172*10^{-6}$	$84*10^{-6}$	$91*10^{-6}$	$73*10^{-6}$

Table 1. Stiffness/Weight Comparison of Titanium-Based MMC to Selected Superalloys

In addition to a stiff main shaft, the higher DN numbers made possible by magnetic bearings also permit a stiff high pressure or core rotor. This results in dynamically rigid rotors with the result that vibration energy is driven into the magnetic bearings. This permits a number of different control strategies to be effectively used to suppress rotor vibration over the complete operating spectrum. These control strategies will be discussed later in this paper.

It should be noted that auxiliary or back-up bearings are an integral part of the magnetic bearing design. These bearings are designed to operate at approximately half the clearance of the magnetic bearings and thus prevent damage to the magnetic bearings at touchdown. In addition to providing support during shipment, storage, and for all other non-operational time, the auxiliary bearings share momentary overloads due to shock and blade-loss, and provide support following magnetic bearing failure. There are two likely candidates for the auxiliary bearings. The first auxiliary bearing candidate is a hydrostatic gas bearing integrated with the magnetic bearing structure and configured to act in parallel continuously or be activated on demand. This gas bearing would be supplemented by a self lubricated sleeve bearing for shock- and extreme-load conditions as well as at low engine speeds (below idle). The second auxiliary bearing candidate is a dry-lubricated, high-temperature, rolling-element bearing designed to operate for short periods at above 3.0 million DN at temperatures above 800° F. To dissipate the heat generated by the dry-lubricated bearing, cooling air will be supplied by engine bleed. Lubrication can be provided by a dry powder delivered to the bearing from an emergency canister activated when a loss of rotor control is sensed by the magnetic bearing controller. The following dry bearing configurations are candidates for auxiliary bearings: a hybrid with rolling elements and tungsten alloy races, a hybrid with rolling elements and intermetallic races, and an all fiber-reinforced-ceramic bearing.
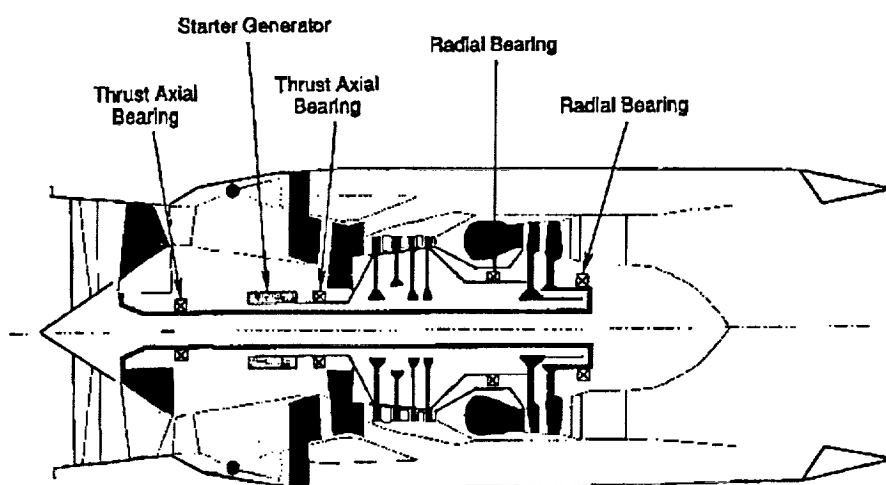
Figure 4. Advanced Four Bearing Turbofan Engine with
Magnetic Bearings and Integral Starter/Generator

440

Figure 4 shows a simplified engine structural network made possible by full magnetic bearing integration and incorporation of an integral starter/generator on the high pressure spool. These technologies permit a four bearing configuration, and the elimination of the lube system, power take-off shaft, and the external gearbox. In addition to significantly improved reliability and maintainability, the weight savings are substantial, amounting to more than 200 lbs for a large military engine.

CONTROL ALGORITHMS

A digital controller will be used to implement control algorithms for rotor stabilization and vibration reduction. It will be noted that a digital controller permits the easy change of control algorithms. Hence, a wide range of control options are easy to implement for the magnetic bearing suspension control system. The control strategies fall into two categories: Closed and Open Loop Control. The former is incorporated into the feedback loop and can impact stability of the active magnetic bearing system. The latter is a feed-forward method whereby external control forces are superimposed on the feedback control forces to reduce vibration. This method separates the rotor suspension and vibration control problems, and thus permits the feedback control to be designed solely to provide maximum stability.

Two approaches that can be used to implement closed loop control are adaptive stiffness/damping control, and the tracking notch filter method. The former method reduces vibration by critical speed tuning and vibration energy dissipation. This is accomplished by varying bearing stiffness and damping to eliminate resonances or to heavily suppress response at rotor critical speeds. This method can provide robust performance when the shaft/bearing system is subjected to external disturbances. For the latter closed loop method, a tracking notch filter is placed in the feedback loop to permit accommodation of synchronous disturbances. This causes the magnetic bearing to have greatly reduced stiffness and damping at the running speed, thus desensitizing the rotor to imbalance because it tends to spin about its inertial axis.

The open-loop control can be implemented as either an active vibration control scheme, or as a bearing synchronous force cancellation scheme for selected frequencies. Typically, for the former approach, vibration displacements are canceled at the magnetic bearing plane or at some other location, such as on the engine casing. This is a disturbance rejection method and is accomplished by the injection of open-loop forces which can be calculated using influence coefficients. In the latter open-loop approach, the force actuator commands can be adjusted so as to eliminate the synchronous component of these forces. This disturbance accommodation approach can be characterized as an open-loop notch filter as the bearings exert no active synchronous forces, which results in isolation of the rotor at the running frequency.

Effective control of the magnetic bearing/rotor system will require the implementation of a combination of the control elements discussed above. For example, active vibration control accomplished through the injection of open-loop forces can be used for low speed operation (rotor start-up to idle speed) to cancel rotor synchronous vibration displacements at the magnetic bearing planes. In this scheme, the engine is modeled *on line* through the generation of dynamic influence coefficients which are used to construct reduced dynamic stiffness matrices used in the calculation of vibration canceling forces. One method to obtain the influence coefficients involves processing trial force signals injected at the magnetic bearings and the resulting response signals at discrete rotor speed points during exploratory accels/decels. This method is adaptive in that the amplitudes and phases of the corrective forces are dependent on the engine speed, vibratory characteristics, and imbalance levels, and the influence coefficients are updated to reflect changes in the engine system frequency response characteristics. The influence coefficients and measured response are then used to calculate corrective forces which are used in an open loop mode to cancel the synchronous response due to rotor imbalance. Since the synchronous response is highly correlated, it may be altered without feedback. Thus, the system stability is not affected by the open loop control. This active vibration control method would not be used for high speed operation because the injected forces needed to reduce displacement levels at the magnetic bearing sensors can actually increase the transmittal forces at the magnetic bearings in this speed regime.

441

For operation above idle speed, the closed or open-loop notch filter method can be used to suppress synchronous vibration. This method is not suitable for low speed operation in the vicinity of the rigid body criticals (resulting from bearing stiffness suppression) because the synchronous imbalance response is basically uncontrolled in this speed regime.

ELECTROMAGNETIC ACTUATORS

Figure 5 shows a fault-tolerant radial magnetic bearing. The bearing uses 3 radial control axes which are made up of 12 electromagnetic stator poles organized into 6 force-producing pole-pairs with 60° radial spacing. Two pole-pairs at 180° radial separation combine to create a single control axis.
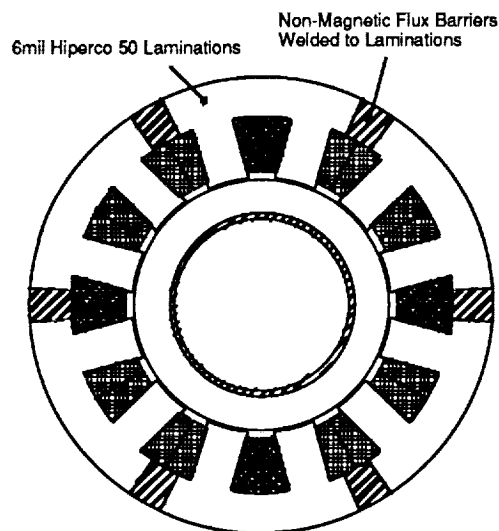
Figure 5 - Fault-Tolerant Radial Magnetic Bearing
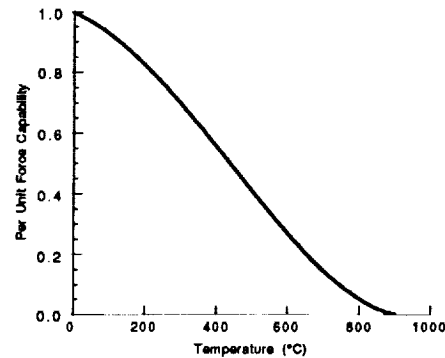
Figure 6 - Effect of Temperature on Cobalt-Iron Force-Production Capability

The stator core is segmented with non-magnetic sections in order to minimize the magnetic coupling between adjacent pole-pairs. The magnetic isolation provided by the stator segmentation will allow non-faulted force-actuation pole-pairs to continue functioning in the proximity of faulted magnetic poles. Since any 2 of the 3 (or more) control axes are sufficient to maintain rotor suspension, the third control axis in this magnetic structure provides inherent redundancy and given appropriate control measures, continued bearing operation in the presence of a variety of faults (e.g. faulted magnetic poles, power electronic shorts, phase power loss, etc.) is possible. Greater inherent redundancy/fault tolerance can be readily achieved by adding more than 3 axes of control.

This magnetic structure for the stator can be constructed using a stack of composite laminations as has been done for electric machine rotors[4,5] or by bonding solid non-magnetic segments to a stack of laminations as has also been done for electric machine rotors[4,5]. The bearing laminations are made from a Cobalt-Iron alloy which has superior magnetic, thermal degradation and mechanical properties, but is slightly more lossy than alternative materials. A maximum operating temperature is chosen as a compromise between bearing size and cooling requirements. Bleed air would be used to limit the temperatures. Figure 6 shows the effect of temperature on per unit force production capability of Cobalt-Iron laminations.

The magnetic material used for rotors has to withstand the centrifugal force induced stresses at maximum rotor speed and maximum temperature. Cobalt-Iron in its normal anneal at 1550°F (840°C) has a 0.2% yield of 44 ksi up to 300°F (150°C). At temperatures of 500°F (260°C) this reduces to less than 40 ksi. A second material option is the 1350°F (740°C) anneal version of the same Cobalt-Iron. This material has a 0.2% yield of better than 80 ksi at 140°C and remains much stronger at higher temperatures (75 ksi at 500°F). The price paid for the higher strength is 5 to 10% reduction in maximum force production capability and higher rotor eddy current losses.

The stator windings must withstand temperatures significantly higher than the magnetic material since heat transfer from the windings to the stator is generally poor. A silicon-mica based insulation system, Thermidur, as demonstrated by Siemens, Germany, for 10,000 hrs life at 752°F with occasional excursions to 932°F is preferred.

ELECTRONIC (SENSORLESS) POSITION ESTIMATION

The rotor position sensors used with magnetic bearings are a major cost and reliability handicap. It is possible to use the magnetic bearing actuators themselves as magnetic position sensors thereby eliminating the need for external position sensors. This can be done using one of two methods, inductance or flux-current, which are based on the magnetic model shown in Figure 7.

The inductance measurement measures time rate of change of current to estimate inductance which can be functionally related to rotor-stator airgap. There are two problems with this approach. First the rate of change of current is dependent on airgap velocity as well as rate of change of current and this causes large errors in the airgap estimate for high-speed bearings. Second, when the soft magnetic materials in the bearing begin to saturate, the relationship between inductance and airgap becomes multi-valued; that is there are many possible airgaps associated with a given inductance. The actuator current can be used to reduce this to two choices, but some knowledge of position history is required to choose the correct airgap.

ϕ_s - Stator Flux
$R_s(\phi_s)$ - Stator Reluctance, Saturable
f_1 - Leakage Flux
R_1 - Leakage Reluctance
R_g - Airgap Reluctance
ϕ_r - Rotor Flux
$R_r(\phi_r)$ - Rotor Reluctance, Saturable
Ni - Ampere-Turns per Coil
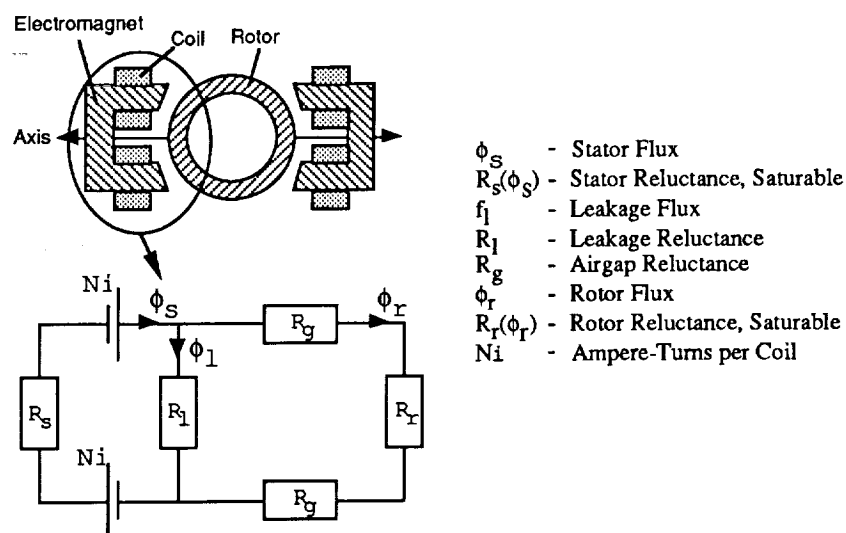
Figure 7 - Magnetic Model of Fault-Tolerant Bearing

The flux-current method uses the relationship $\phi_s = \int \frac{v - ir}{N} dt$ to determine the flux in an excited winding. Then, given the actuator current and a suitable magnetic model of the actuator, a unique rotor-stator airgap can be determined. This method works regardless of airgap velocity or magnetic saturation. The primary difficulty here is in maintaining an accurate flux estimate where the excitation waveform is not cyclic and the required integrator cannot be reset periodically. This method has been used successfully with switched reluctance motors[6,7].

FAULT-TOLERANT ENGINE ELECTRICAL SYSTEM

Figure 8 illustrates a conceptual electric system for an advanced aircraft engine. This is a fault-tolerant system relying on 3 independent 270 vdc buses for distribution amongst a variety of loads, including active magnetic bearing (AMB) controls and power electronics.
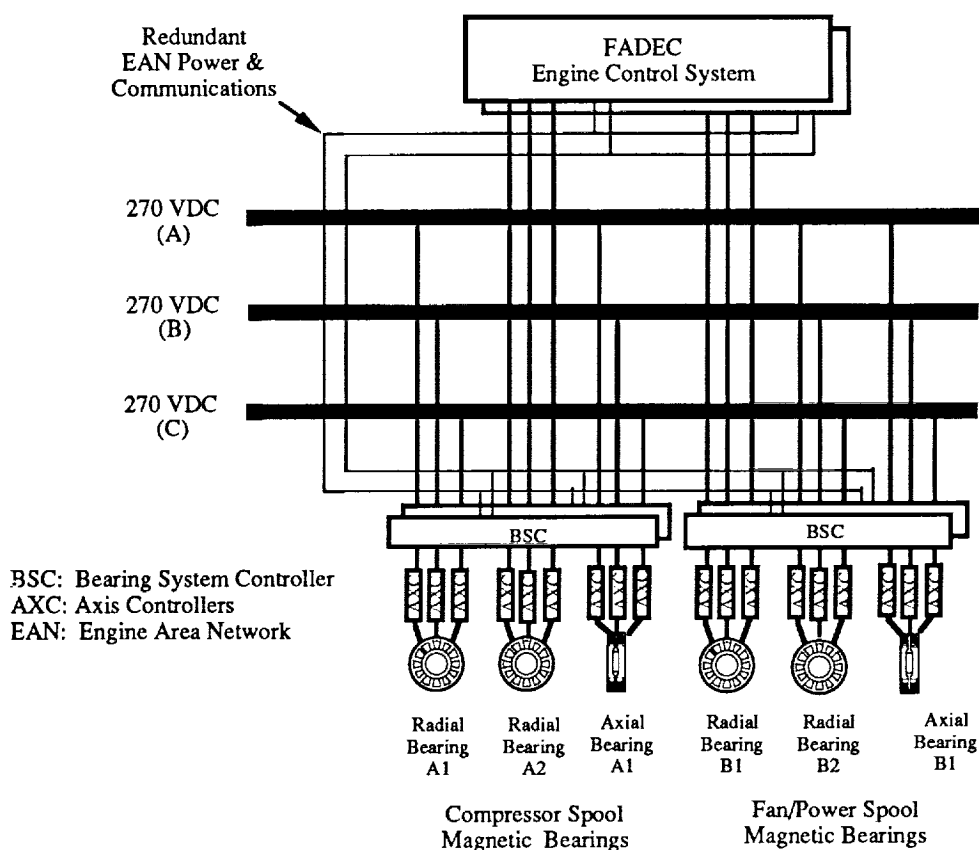
Figure 8. More Electric Engine Electrical System

The 3 distribution buses would appear to represent a conventional triple modular redundancy with 200% overcapacity, but this is not the case. The electric distribution system would be designed for 50% over-capacity, i.e., each bus designed for 50% of the needed system capacity, thereby requiring 2 of the 3 buses at any time in order to avoid system failure.

The radial active magnetic bearings are configured with 3 magnetically independent control axes per bearing placed at 60 degrees radial separation. These 3 control axes cooperate to control the radial rotor position such that

control can be maintained with only 2 of the control axes functioning. Each of the 3 bearing control axes are powered from a different dc bus; therefore the radial bearings require 2 active dc distribution buses in order to maintain rotor position control. The total available force vector is angle dependent, but is a minimum of 0.866 times the force capacity of a single control axis.

The axial active magnetic bearings are configured in a similar fashion with 3 magnetically independent control axes, each control axis with 50% force capability - thus 2 of the 3 available control axes are required for rated thrust loading. Each of the axial control axes are also fed from different dc electrical distribution buses.

MAGNETIC BEARING CONTROLS

The magnetic bearing controls consist of 2 hierarchical levels: a supervisory level - Bearing System Controller (BSC), and an actuation level - Axis Controller (AXC). The supervisor controllers are configured in a duplex fault tolerant configuration, with one supervisor in active control and the second in an active standby mode. Each Bearing System Controller is configured to control one engine spool (8 control axes).

The actuation controllers are essentially smart, self-protecting, power amplifiers capable of exciting a single independent AMB axis (2 electromagnetic windings, + and -). A radial bearing will thus require 3 AXC's. Each actuation controller is capable of accepting commands from and delivering feedback information to multiple supervisors, thereby enabling redundancy at the supervisor level.
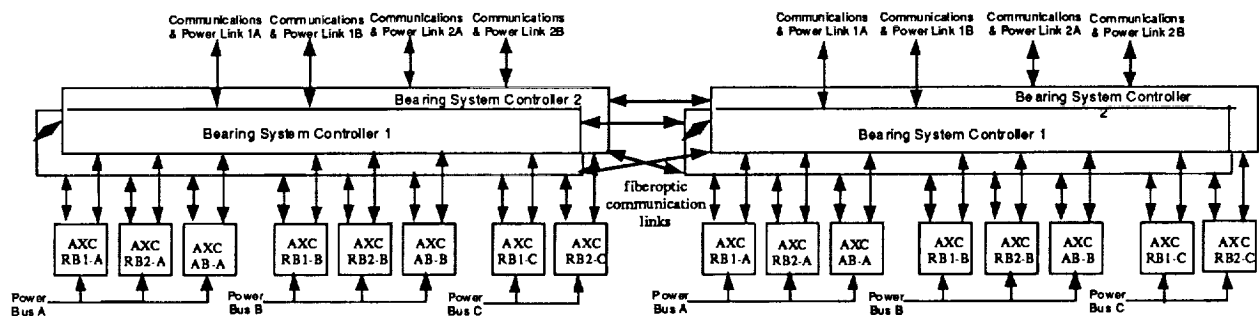
Figure 9. Twin Spool Active Magnetic Bearing Control System with Duplex Supervisor

The duplex supervisory controllers are essentially an extension of the dual-redundant engine controller (FADEC) acting as intelligent high-bandwidth actuators. The supervisor controllers are powered from the FADEC control power and communicate with the FADEC via a multi-drop Engine Area Network (EAN). Two redundant EAN communication/control power channels are provided. An actuation controller is powered, along with the power electronic switches it controls, directly from an individual dc electrical distribution bus. Communication between the supervisory and actuation levels is accomplished in a manner to maintain electrical isolation e.g. fiberoptic communication links.

Figure 9 illustrates the active magnetic bearing controller architecture for a twin spool engine. Each spool has a duplex supervisory Bearing System Controller which is responsible for coordinated control of the rotor position, vibration, and imbalance - this coupled control will execute at a 6.7 kHz task execution rate and transmit new force commands to the axis controllers. The Axis Controllers are responsible for force control & linearization, gap

445

position & velocity inference, fault detection & isolation - the axis controller will execute at a 20 kHz task execution rate which results in power electronic switching at an equivalent frequency.

Each axis controller is capable of accepting 2 command streams from each of the duplex Bearing System Controllers via high-bandwidth half-duplex serial communication channels. The controlling supervisor will transmit a current state information packet, once per control iteration, to the active standby BSC both as a heartbeat indicator and to enable a smooth transition to the backup supervisor if required. The supervisory controllers for each engine spool are capable of communicating once per control iteration with each other to transmit required dynamic coupling information. The BSC peer-peer communications are high-bandwidth full duplex serial communications links. The BSC's are also required to communicate with the FADEC over slower half-duplex communication links.

AMB SYSTEM MODELING AND SIMULATION

Figure 11 illustrates a SimPEl simulation of the AMB control system. SimPEl (Simulator for Power Electronics) is an object-oriented dynamic simulator developed by GE CR&D. SimPEl uses explicit numerical integration procedures to predict the responses of dynamic systems. Each of the physical elements of an active magnetic bearing system have been included, including the three 270 vdc buses (amb-bus in Fig. 11), axis controller power electronic converters (axc-pe), radial & axial bearing magnetic actuators (rb and ab), rotor dynamics (rotor), axial & radial catcher bearings (rcb and acb), bearing mechanical support structures (stator), and the AMB control system itself (amb_control). The rotor model includes rigid body rotor dynamics which are currently being extended to include flexible-rotor modeling. The magnetic bearings are modeled using the model shown in Figure 7. Figure 10 illustrates simulated radial bearing force waveforms produced by SimPEl.

AMB Controller Force

10 gm-in Rotor Imbalance @ 12,500 rpm
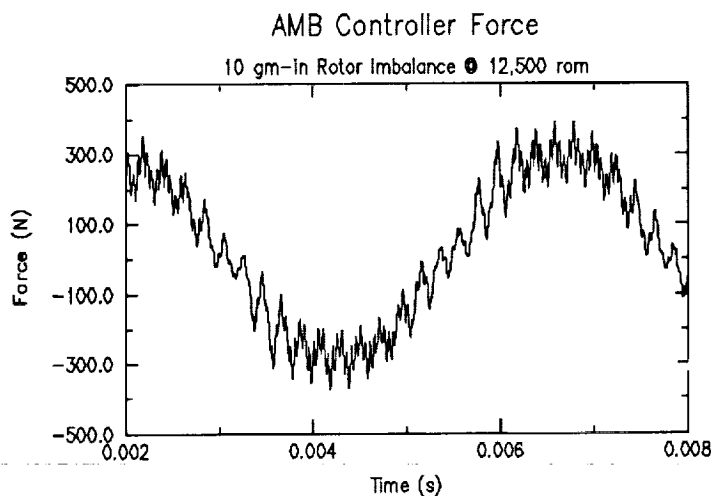
Figure 10. Force Waveforms with 20 kHz Ripple
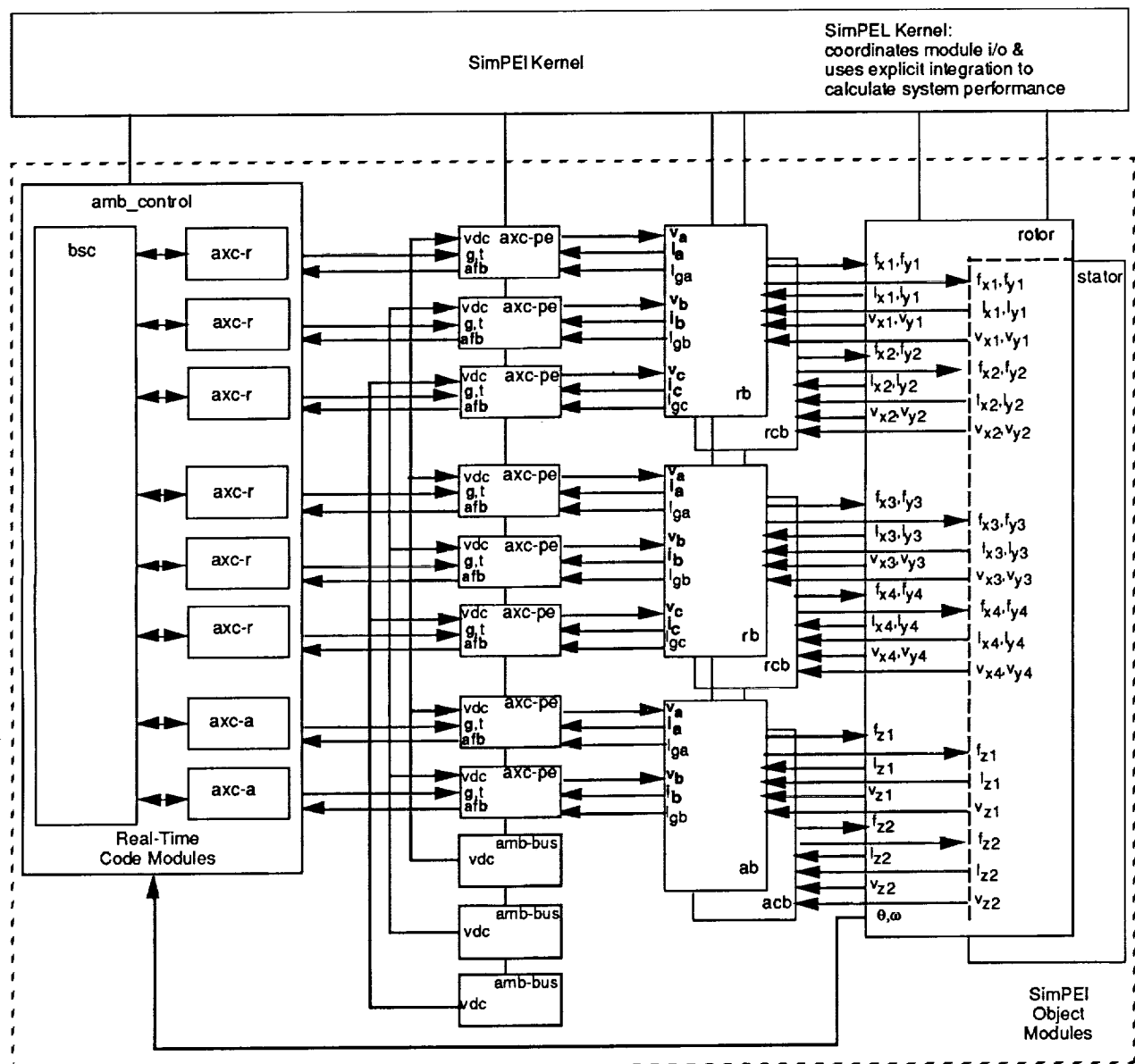
Figure 11. SimPEl Active Magnetic Bearing System Simulation

The SimPEl amb_control module contains the target source codes for the BSC and AXC digital signal processor modules. These source codes enable simulated rotor suspension along with axis availability dependent force and gap transformations to and from orthogonal yz control axes and coupled abc control axes. The SimPEl simulation as configured allows extensive debugging of the control source codes under simulated conditions, prior to the availability of the target hardware.

447

The test rig shown in Figure 12 has been developed by General Electric for validation testing of advanced magnetic bearings and digital controls/power electronics systems. This effort will encompass programs for the use of magnetic bearings for marine and aeroengine main shaft support and applications for stationary power plant turbomachinery and generator rotor support. The conventional proximity sensors depicted in Figure 12 will be used initially for rotor displacement calibration measurements. Later, the sensorless air gap estimation technique based on utilizing the magnetic bearings as both force actuators and displacement transducers will be used.
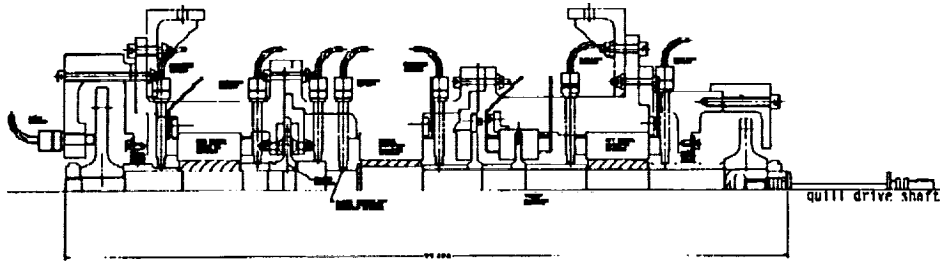
Figure 12. GE Single Spool Magnetic Bearing Test Rig

The test rig utilizes two radial magnetic bearings located fore and aft, an excitation radial magnetic bearing located at approximately mid-span, a thrust magnetic bearing, and a thrust excitation magnetic bearing. The forward direction is to the left. Radial auxiliary bearings are mounted out-board of the radial magnetic bearings. The radial auxiliary bearings are turbine engine class bearings, and the radial clearance between the shaft OD and the bearing inner ring ID is equal to 10 mils. This precludes the possibility of damage to the radial magnetic bearings for overloads or rotor drop as the radial clearance of the magnetic bearings is equal to 20 mils. An axial auxiliary or bumper bearing is utilized to prevent damage to the thrust magnetic bearing.

Overhung disks located fore and aft simulate a fan and turbine and provide balance planes for mechanical balancing. An additional balance plane is available at the disk of the thrust excitation magnetic bearing. The rig is driven by a 20 HP electric motor through a quill drive shaft located at the aft end of the rotor.

General Electric will be developing a generic two shaft magnetic bearing test rig for use in dual rotor magnetic bearing engine studies. This will be accomplished by developing a shaft/case module and coupling case to permit expansion of the single shaft rig shown in Figure 12 into a two-shaft magnetic bearing test rig. The two shaft rig will provide experience and proven methodologies for use in the design of future twin spool magnetic bearing engines.

Figure 13 shows initial layouts for the two shaft magnetic bearing test rig. The lower configuration has a tuning spring (shown as an outer case over the right shaft/case module) which may be necessary to achieve dynamic coupling between the two shafts representative of two spool engine dynamics.

DRIVE SHAFT   SPOOL 2 MODULE   SPOOL 1 MODULE   DRIVE SHAFT
FOR SPOOL 2   FOR SPOOL 1
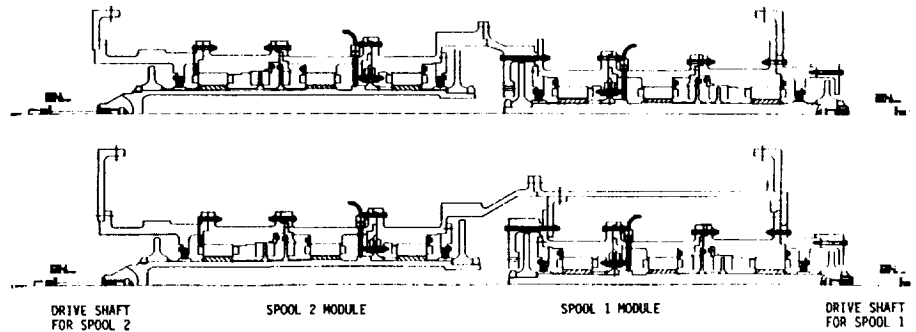
Figure 13. GE Twin Spool Magnetic Bearing Test Rig Configurations

ACKNOWLEDGMENT

REFERENCES

1. Richter E., Anderson R. E., Severt C., *The Integral Starter/Generator Development Progress*, SAE Paper 920967, April 1992.
2. Storace, A. *Turbine Engine Structural Efficiency Determination*, AIAA 89-2571, July 1989.
3. Signorelli, R.A., *Metal Matrix Composites for Aircraft Engines*, NASA Technical Memorandum 83379, April 1983.
4. *Composite Rotor Lamination for Use In Reluctance, Homopolar and Permanent Magnet Machines*, U.S. Patent No. 4,916,346, Inventor: G.B. Kliman, assigned to GE, Dec. 28, 1987.
5. *Method of Fabricating Composite Rotor Laminations for Use In Reluctance, Homopolar and Permanent Magnet Machines*, U.S. Patent No. 4,918,831, Inventor: G.B. Kliman, assigned to GE, Oct. 20, 1989.
6. Lyons, J.P., MacMinn, S.R., and Preston, M.A., *Flux/Current Methods For SRM Rotor Position Estimation*, Proceedings of the 1991 IEEE Industry Applications Society Annual Meeting, Sept. 28-Oct. 4, 1991, Dearborn, MI, pp. 482-487.
7. Preston, M.A. and Lyons, J.P., *A Switched Reluctance Motor Model with Mutual Coupling and Multi-Phase Excitation*, IEEE Transactions on Magnetics, Vol. 27 No. 6, Nov. 1991, pp. 5423-5425.

SUPERCONDUCTING REBALANCE ACCELERATION AND RATE SENSOR

R. Torti, M. Gerver, V. Gondhalekar, B. Maxwell
SatCon Technology Corporation
12 Emily Street
Cambridge, MA 02139

SUMMARY

The goal of this program is development of a high precision multisensor based on a high Tc superconducting proof mass. Design of a prototype is currently underway.

Key technical issues appear resolvable. High temperature superconductors have complicated, hysteretic flux dynamics but the forces on them can be linearly controlled for small displacements. Current data suggests that the forces on the superconductors decay over a short time frame and then stabilize, though very long term data is not available. The hysteretic force characteristics are substantial for large scale excursions, but do not appear to be an issue for the very small displacements required in this device. Sufficient forces can be exerted for non-contact suspension of a centimeter sized proof mass in a vacuum sealed, nitrogen jacket cryostat. High frequency capacitive sensing using stripline technology will yield adequate position resolution for 0.1 µg measurements at 100 Hz. Overall, a reasonable cost, but very high accuracy system is feasible with this technology. A summary of system parameters is given below.

Multisensor Performance	0.1 µg acceleration resolution
	10^{-5} rad/sec^2 angular resolution
Pointing Mount Sensor Noise	1.6×10^{-5} A/hr drift
	6×10^{-10} °/hr drift

INTRODUCTION

There is a need for improved acceleration and angular rate sensors for inertial guidance, vibration testing, and spacecraft pointing mounts. Current high precision rate gyros and gyroscopic accelerometers use spinning balls or wheels to increase their sensitivity. The complete systems with motors, sensors, and delicate balance are therefore very complicated and expensive.

SatCon has undertaken as a Phase II SBIR from NASA Langley Research Center (Contract NAS1-19938) the development of a combined rate and acceleration sensor ("multisensor") using high temperature superconductors and high resolution capacitive sensors that provide more accurate information, and are also less complex than current systems. These sensors may be operated as stand alone sensors or combined with a satellite mount for high accuracy pointing and tracking. We have focused on the feasibility of using a high temperature superconductor as the

proof mass and identifying the best sensor technology. Similar high accuracy sensors have been built using low temperature niobium superconductors, notably the superconducting gravimeter[1] and the NASA Grav-B gyro[2]. These systems, however, require expensive helium cooling, and do not provide angular and linear rates like the multi-sensor proposed here.

APPROACH

The concept behind the superconducting multisensor is very similar to a proof mass accelerometer. Proof mass accelerometers either measure the displacement of a spring restrained mass, and estimate the acceleration from knowledge of position and the spring constant or use feedback to maintain a constant position and use knowledge of actuator dynamics to estimate acceleration. Typically, high precision instruments use the rebalance scheme to minimize non-linearities in the spring restraint system, sensors, and actuators. The limited proof mass motion inherent in a rebalance system also allows more accurate position measurements to be made and improves performance. A suspended proof mass device, while more complex than spring restraint systems, has the further advantage of active control of the different stiffness and damping characteristics at different frequencies. This allows better vibration isolation from external disturbances.

A conceptual drawing of the sensor is shown in Figure 1. It consists of a cubical high temperature superconducting proof mass whose position is sensed and controlled by a set of co-located high frequency capacitive sensors and high T_c superconducting control coils fixed to the cryostat inner wall. The control coils are actuated based on sensor signals by an electronic control system to maintain a constant cube position. Knowledge of the mass dynamics of the cube and the actuator control signals allows three accelerations and three angular rates to be estimated. Though six sensors and actuators are sufficient to control the six degrees of freedom of the cube, twelve sets are shown to allow for averaging and redundancy. The cube, sensors, and control coils are contained in an evacuated cryostat with a cryogenically cooled jacket. The sensors and actuators are fixed to the cryostat and the cube is freely suspended. For use in ground based systems, a separate gravity lift coil would be placed in the outer cryogenic. The sensor and control electronics would be external to the cryogen and pass signals through hermetically sealed leads. The entire system excluding electronics is roughly softball-sized, about 8 cm in diameter.

The device has several features that should give it high accuracy. First, the high frequency capacitive sensors offer position sensitivities of 10^{-3} angstroms/$\sqrt{Hz}$. Second, the proof mass, sensors and coils are cooled to 77 degrees Kelvin. This reduces the thermal noise in the system. Third, the use of a superconducting proof mass and actuator generates very little heat in the system, reducing thermal gradients which would degrade precision. Overall, the device could have stand alone resolution of 0.1 μg acceleration and 10^{-5} rad/sec^2 angular acceleration and would drift 75 angstroms and 5×10^{-5} degrees in one hour due to sensor noise. These numbers are based on a bandwidth of 100 Hz, the use of capacitive position sensors with noise of 1.5×10^{-3}Å/$\sqrt{Hz}$ and a cube of diameter 2 cm. The drift is assumed to be a random walk, with time step $(10^{-2}/2\pi)$ seconds, and spatial step equal to the sensor noise at 100 Hz. Any systematic (non random) drift would be in addition to drift from sensor noise.

452

A selection of materials and their properties is shown in Table 1[3]. The YBaCuO compounds combine acceptable transition temperature with repeatable, well known, fabrication processes, and non-toxicity. The current proof mass design is based upon the YBa_2CuO_x compound. It is readily available, and the processed proof mass cube can be made to order by vendors.
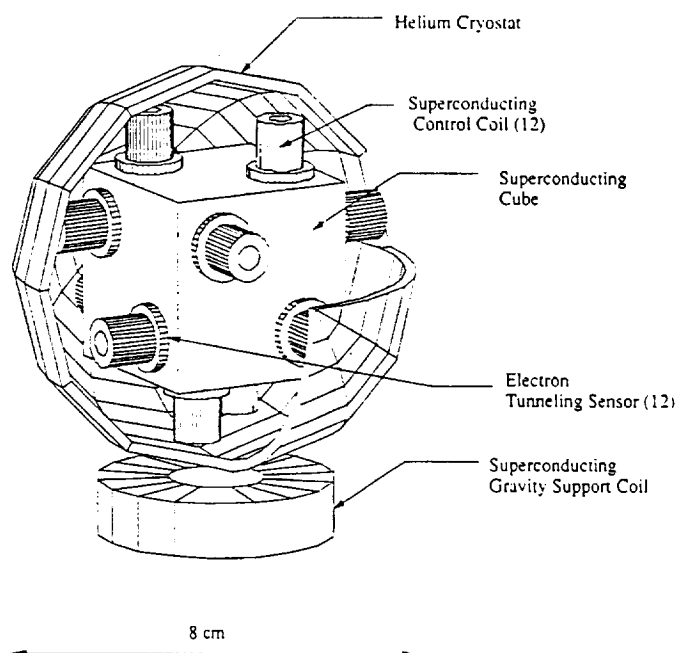
Figure 1. Superconducting Multisensor Concept

Table 1.

Material System	$T_c(K)$	Coherence Length (Å)	Known Synthesis Properties
Isotropic			
$(BA,K)BiO_3$	20-30	43	Difficult (Hygroscopic)
$YBa_2Cu_3O_x$	60-90	31	Most well Known
Tl/A/Cu/O	90-120	16-30	Toxic, Not Well Known
$(Nd,Ce)_2CuO_{4+x}$	22-30	70	Not Well Known
Bi-Sr-Pb-Ca-Cu-O	88-110	30-40	Relatively Well Known
Bi-Sr-Sb-Ca-Cu-O	90-132	---	Unknown
Most Anisotropic			

For practical applications of high temperature superconductors, the area of greatest research is the phenomenology of forces on high T_c materials. The global force characteristics of these materials are very complicated and depend on temperature, field, chemical composition, and fabrication. The repulsive force mechanism arises from supercurrents that arise in the bulk superconductor in response to external magnetic fields. Since these currents are persistent and act to counter externally imposed fields, a persistent repulsive force is generated.

Macroscopically, the force is described by an integral of the Lorentz force between the supercurrents and externally applied field over the volume of the superconductor:

$$F = \iiint J_c \times B_r \, dV \qquad \text{Eq. 1}$$

Analytical and/or finite element solutions to this equation can be used to estimate the repulsive forces. Rao[4] presents experimental verification of finite element analyses of the repulsive forces between a magnet and HT_c superconductor.

An analytical approximation was made for the geometry of interest, as shown in Figure 2.

superconductor
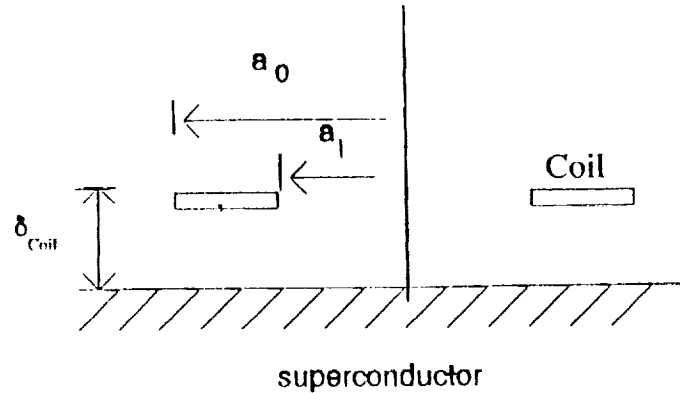
Figure 2. Coil Geometry

In the gap, if $\delta_{coil} \ll a_0 - a_i$, the magnetization H is approximately:

$$H = \frac{I}{a_0 - a_i} \qquad \text{Eq. 2}$$

$$B = \frac{I\mu_0}{(a_0 - a_g)} \qquad \text{Eq. 3}$$

$$\text{Field energy} = \int dV\ B \cdot H = \frac{I^2 \mu_0\ \delta_{coil}}{2(a_0 - a_i)}\ \pi(a_0 + a_i) \qquad \text{Eq. 4}$$

$$F = \frac{\pi}{2}I^2\mu_0\ \frac{(a_0 + a_i)}{(a_0 - a_i)} \qquad \text{Eq. 5}$$

The force can be calculated from the differential of the field energy $\int dV\ B \bullet H$, as above. The net force can be made linear in I by running a bias current, with opposing coils in series, as usual in magnetic bearings.

An issue of concern is in the effect of flux pinning on the magnet forces. High temperature superconductors have the capacity to trap (or "pin") flux in their interiors if it is present when the material makes the transition to the superconducting state. This phenomena allows a permanent magnet to stably suspend below an HT_c sample and is also responsible for the range of stable suspension points, with little spring restraint between them.

This behavior is not desired for an instrument such as this, where a consistent force behavior is needed for accurate performance. Fortunately, work at Argonne National Laboratory[5], and at the Institute of Chemical Physics Academy of Sciences of the USSR[6] shows that this behavior disappears if alternating fields exist in the sample. This opens up the possibility of using a small field dither or control forces generated in response to environmental vibration to avoid these effects. Also, the proof mass motion under rebalance control will be so small that any hysteretic effects will be effectively linearized.

SENSORS

The key aspect of the superconducting multi-sensor is high resolution position sensors. Sensors derived from two technical developments were considered: electron tunneling and near microwave frequency driven capacitive sensors.

Electron Tunneling Sensors

Recent developments in the application of electron tunneling phenomena to instrumentation capable of producing sub-angstrom topographical maps of the surfaces have opened up many exciting new possibilities in imaging and sensing.

However, while electron tunneling sensors possess extremely high position sensitivities independent of sensor size and without complicated electronics, they have several disadvantages in this application. They are subject to mechanical shock and are too sensitive to surface topography.

Since the tip must protrude beyond the mechanical guard surface, an external shock which overwhelms the electronic stiffness of the control system may force the superconducting proof mass into a tip with possible tip and surface damage and an apparent acceleration renormalization.

Furthermore, since the tip is extremely sensitive to separation and does little spatial averaging, lateral motion of the proof mass will result in a trace of atomic-sized surface features as in the scanning microscope. The device would then be mapping the proof mass surface features instead of measuring accelerations and rates.

Capacitive Sensors

Capacitive sensors are widely used to sense displacement. They are mechanically simple, robust, and can be used to make fairly accurate position measurements. Because they sense the capacitance of a finite area, they can be designed insensitive to surface topology.

Operation utilizes displacement currents across gaps between capacitively coupled surfaces. Typically, a constant current sine wave is imposed on a flat sensor plate set near the target. The voltage and current are related by:

$$I = V \omega C$$

where C is the capacitance of the sensor to the target. This capacitance has the form:

$$C = \varepsilon \, A/d$$

where ε is the permittivity of the space between them, A is the sensor area, and d the separation. Since C is inversely proportional to gap, for a constant current, voltage is directly proportional to gap:

$$V = I \, d/(\varepsilon \, A \, \omega)$$

Practical drive circuits utilize an oscillator which drives a constant current into the measured capacitance. To reduce the effects of stray capacitance, the signal is co-axially guarded between the electronics and the sensor head. A feedback loop forces the guard voltage to be the same as the drive voltage, thus eliminating the effect of stray capacitances. The guard voltage is then proportional to the gap distance, and is demodulated and filtered to produce a linear output signal.

Commercially available sensors come in various sizes and ranges, with larger sensors being used for longer ranges (so the capacitances stay roughly the same). The typical dynamic range of 1000 gives a commercial sensor with 0.066" diameter a range of 0.001" and about 25 nm resolution which is not in the same league as electron tunneling sensors.

In a conventional electromagnetic sensor, circuit shot noise may be expected to dominate at frequencies above 1 kHz. We can estimate resolution limitations from shot noise in a capacitive sensor. The current is:

$$I = V \, \omega C = V \, \omega \, \varepsilon \, A/d$$

where d is the plate separation, ω is oscillator drive frequency, and A is the plate area.

If limited by shot noise, the position sensitivity limit is:

$$\delta d = d \sqrt{(2e/I)}.$$

δd can be reduced, however, by increasing the drive frequency. In standard guarded sensor circuits, this is not done because the guard loop must respond at a much higher frequency, several megahertz typically. Increasing the oscillator frequency has its limits because it is difficult to increase the guard frequency with standard electronics packaging. The stripline surface mount circuit developed by RCA for a capacitive video disc reader operates at 915 MHz. It uses high speed bi-polar semiconductors and placement of the circuits very near the sensor plate (within a few centimeters). Moreover, guarding is not required since the capacitance is compensated so that the device operates in a limited region on the slope of the tuning curve.

This technology has been demonstrated in a high precision seismometer at JPL[7]. The position sensitivity of the sensor is about 0.0015 A/√Hz; not quite as good as tunneling tips but in a package that is much more robust and reliable than electron tunneling sensors and is compatible with the acceleration resolution anticipated with the superconducting multisensor.

In order to evaluate the suitability of the proposed high frequency electronics as for sensing, we have acquired a commercial RCA video and are modifying essential components into suitable test electronics.

A re-construction of the resonator circuit is shown in Figure 3. The resonator section is driven from the oscillator shown at the lower left side. Variations in capacitance result in movement along the slope of the tuning curve and are detected through D2 and buffered by Q1 to produce the detector output. Additionally, this signal is coupled into an AFC circuit which in turn maintains the operating point within desired limits.
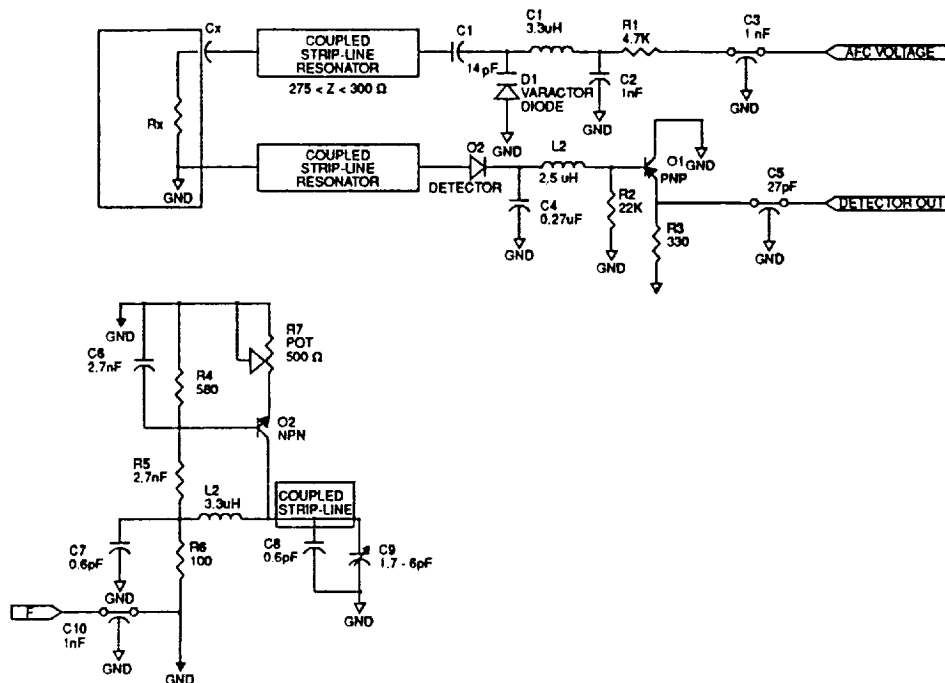
Figure 3. Re-construction of Resonator for RCA VideoDisc Player.

SYSTEM CONFIGURATION AND SIZING

This section explains the rationale behind the system configuration and sizing. As discussed earlier, the underlying goal was to design a high performance combined acceleration and angular rate sensor that is less complex and expensive than current inertial instruments. To this end, high temperature superconducting materials were selected instead of low temperature materials because liquid nitrogen cooling is much simpler and cheaper. Though the high temperature materials have less well understood and more complex flux dynamics, these effects are effectively eliminated by a control loop. The position of the suspended body is maintained so closely that the hysteretic features cannot be seen.

Proof Mass Shape

Since the instrument was conceived as a six degree of freedom device, it follows that the proof mass must have six degrees of freedom. This further implies a completely suspended and controlled proof mass. Acceleration sensitivity comes from sensing translations of the proof mass center and rotation sensitivity from sensing rotations about the center. The simplest practical shape that allows this is the cube. By sensing the distance between strategically placed sensors and the proof mass, it is possible to determine the translations and rotations with six sensors.

Sizing Issues

Initial sizing estimates were driven by observations of similar instruments. Superconducting gravimeters are sensitive two axis accelerometers that use a 1 inch niobium sphere suspended in superfluid liquid helium with superconducting control coils, capacitive position sensors, and rebalance control. The NASA Grav-B gyro, meant to be the most accurate gyro ever, with less than 10^{-10} degrees/hr drift rate uses a similar sized quartz sphere coated with niobium, suspended with capacitive sensors, and controlled by electrostatic actuators.

The sizing of these instruments and the superconducting multisensor is driven by several factors: resolution, cooling, suspension, and cost among others. Fundamental sensitivity is usually increased with increased mass and size. For a given resolution sensor, longer moment arms or greater proof mass imply smaller angular rate changes or result in larger control coil rebalance currents. Other issues such as mechanical rigidity and thermal drift and thermal gradients have generally limited this trend since larger systems are more likely to have undesirable structural resonances or thermal gradients.

In this superconducting sensor, there were additional factors involved in determining overall system size: superconductor fabrication considerations, suspension control, and cooling.

Fabrication

Structural integrity of the brittle high T_c materials precludes fabrication of cubical shapes much greater than a 2 cm face.

Control

From a control aspect, suspension of the proof mass in a vacuum avoids coupling to and damping by a gaseous medium and corruption of sensor signals. Vacuum operation also minimizes the exposure of the surfaces to humidity and gaseous corrosives.

Cooling

For operation at 77° K in a vacuum, the cooldown time becomes an issue. This places a constraint on proof mass size since heat content goes with volume while radiative cooling goes with area. The cooling from combined radiational and conduction loss can be expressed by:

$$\dot{Q} = \frac{dT}{dt}C_v m = (T_i - T_o)R4\pi K + \sigma \epsilon A(T_i^4 + T_o^4) \qquad \text{Eq. 6}$$

Here A_i is the surface area of the proof mass, σ the Stefan-Boltzmann constant, ϵ the emissivity, m the proof mass, T_i the interior temperature, T_e the external temperature, a and b the temperature dependent coefficients of a specific heat, K the thermal conductivity of the gaseous medium, $C_v = a + b \cdot T$, and R the effective radial separation to the chamber walls. For this analysis, it is assumed that the emissivity, ϵ, is the same for the proof mass and the surrounding inner wall of the nitrogen jacket.

Cooldown time can be calculated by solving for dt and integrating over the temperature range. Results are displayed in Figure 4.

The following values were used:
m = 51g
ϵ = 0.96 (approx. black body, typical for roughened metals)
a = 30 J/kg - °K
b = 1.8 J/kg - °K^2
K = 0.04 to 0.12 watts/(sec•m•°C)
R = 0.02 m

A cube 2 cm on a face requires cooling in a vacuum and requires a barely acceptable 12 hours to drop from room temperature to about 80° K. However, the simple expedient of back-filling the chamber with a dry gas to aid in heat transfer, then proceeding with evacuation once the proof mass is at temperature, drastically reduces cooldown time.

Actuator Coils

The heat analysis also gives another important result. Because there is no convective heat transfer, and no conduction from the suspended mass, only a limited amount of heat can be generated in the cryostat and maintain temperature below transition. In this case, with the dimensions as above, approximately 4 mW can be removed by radiation.
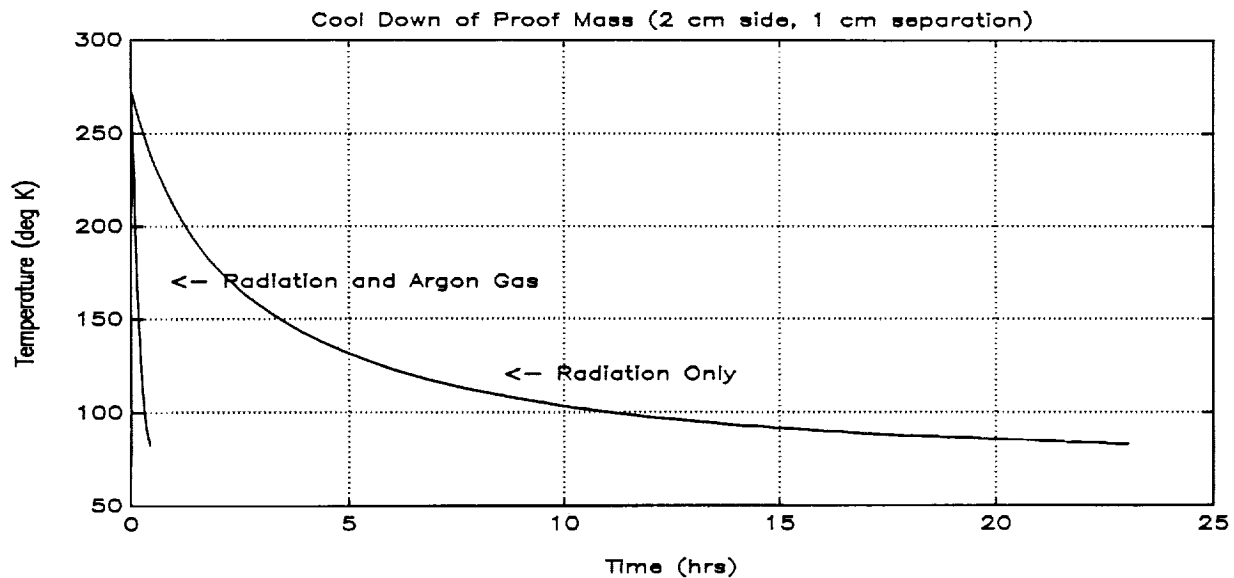
Figure 4. Proof Mass Cooldown.

This limited power dissipation puts serious constraints on the system. Copper control coils could only produce 0.1 g of the control force within this limitation if all heat is removed radiatively. Use of superconducting control coils obviates this with about the same volume as copper coils. We can obtain an acceleration of 0.8 g using two coils on a side, each with a current of 180 amp-turns, 1 cm outer diameter, and a square cross sectional of 2 mm a side. This fits easily within the available space and with the proof mass size.

Gravity Suspension

Operation in a ground based system requires a static force to offset gravity. This can be provided either with coils or permanent magnets.

High strength permanent magnets are clearly capable of suspending the proof mass with the obvious advantage of operating without power. However, the magnet material is long term unstable to a few percent and so a change in magnet field would change the vertical equilibrium position of the proof mass, which would be interpreted as a static acceleration.

Additionally, because of the flux pinning effects, HT_c materials can have different force characteristics depending on their magnetization state when the superconductor passes through its transition temperature. As shown by Chu[8], the force between an HT_c superconductor and a magnet is different for the field cooled, and the zero field cooled cases, with the zero field cooled case having more force.

These problems can be overcome, however, with the use of a coil to provide the static lifting force. A larger sized superconducting coil can be placed in the liquid nitrogen jacket and driven with a current control loop to generate the required support field, but with much better long term stability. This also allows the proof mass to be zero field cooled for better performance.

460

Mechanical Structure and Integration

The current mechanical structure of the system will be unlike the concept illustrated earlier. The cryostat will be a three chamber cylindrical shaped structure made of stainless steel with an insulating nitrogen jacket, cryostat, and inner chamber. The top cap will be removable and contain the entire active apparatus: proof mass, sensor electrode supports, support positioning, coils and include provision for electrical feedthrus and vacuum pumping. Speed sensor and control electronics will be placed external to the outer cryostat and operate at room temperature with RF
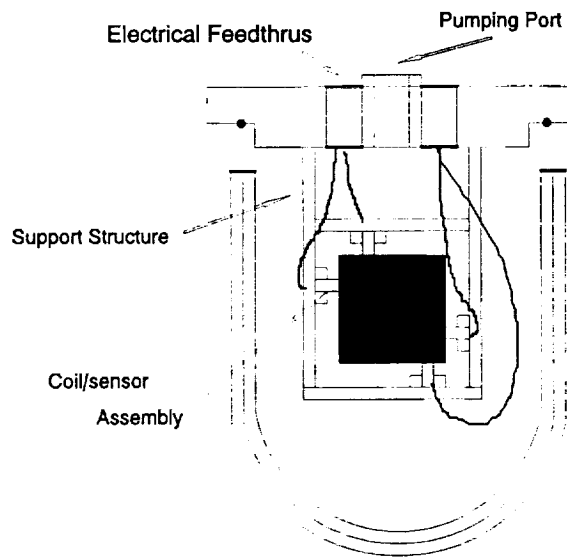
Figure 5   Current Mechanical Structure Including Cryostat, Proof Mass, Sensor Electrodes, Coils, and Feedthrus.

feedthrus in the cap. The cryostat design will be done in conjunction with the vendor.

CONTROL SYSTEM ANALYSIS AND DESIGN

The operation of the Superconducting MultiSensor is based on measurement of force and moments required to restore the proof mass, i.e., the superconducting cube, to a center zero orientation. A force/moment rebalance controller with a displacement feedback is the basis for achieving this aim. The principle is best illustrated with a single degree of freedom force rebalance system as shown in Figure 6. The block diagram in the figure shows a position feedback loop around a proof mass. F_{ext} is the external force acting on the proof mass. The force rebalance loop utilizes the position feedback signal to cancel out the external force F_{ext} with a force F_c thus forcing back the proof mass to a center zero position. The transfer function F_c/F_{ext} with reference to Figure 6 is

461

$$F_c/F_{ext} = C(s)*P(s)*H(s)/(1 + C(s)*P(s)*H(s)) \qquad \text{Eq. 7}$$

where s is the Laplace operator.

The force error $F_e = F_{ext} - F_c$ is a measure of the difference between the external force and the control force. The transfer function for the error F_e is:

$$F_e = 1/(1 + C(s)*P(s)*H(s)) \qquad \text{Eq. 8}$$
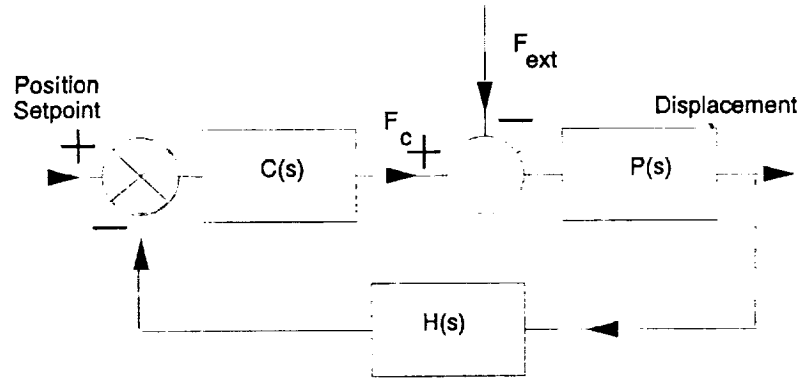
Figure 6 Single Degree Of Freedom Force Rebalance

Ideally, the steady state error F_e should be zero to give an accurate measure of the external force given that the control force F_c is known.

With normal proof mass based accelerometers, the proof mass "m" is supported on a cantilever with a finite stiffness coefficient "k" and a small damping coefficient "c". Hence the transfer function P(s) relating applied force F to displacement D is

$$P(s) = D/F = 1/(m*s^2 + c*s + k) \qquad \text{Eq. 9}$$

The source of stiffness or damping action on the S/C Multi sensor proof mass can potentially arise due to a flux pinning effect within the superconducting material and viscous damping introduced by the gases surrounding the proof mass. However, if the control forces are small; that is, if the control currents and the corresponding magnetic flux excursions experienced by the superconducting material are small, then the flux pinning will be minimal. Moreover the superconducting multisensor is housed in an evacuated dewar thus eliminating viscous damping. Under these conditions both the coefficients "k" and "c" will be zero. Eq. 8 becomes:

$$F_e = m*s^2/(m*s^2 + C(s)) \qquad \text{Eq. 10}$$

This will assure a zero steady state error. The transfer function is:

$$F_c/F_{ext} = C(s)/(m*s^2 + C(s)) \qquad \text{Eq. 11}$$

462

which gives the frequency response of the measurement. The form of the compensator C(s) will determine this frequency response.

The multisensor has six degrees of freedom: namely x,y,z translation and θ_x, θ_y, and θ_z rotations as shown in Figure 7. The actuator coils and capacitive sensors are collocated. There can be one or two sensors and actuators reacting against each face of the cube shaped proof mass (six or twelve total). Each actuator coil and sensor pair is located on a diagonal of the face as shown in Figure 7.
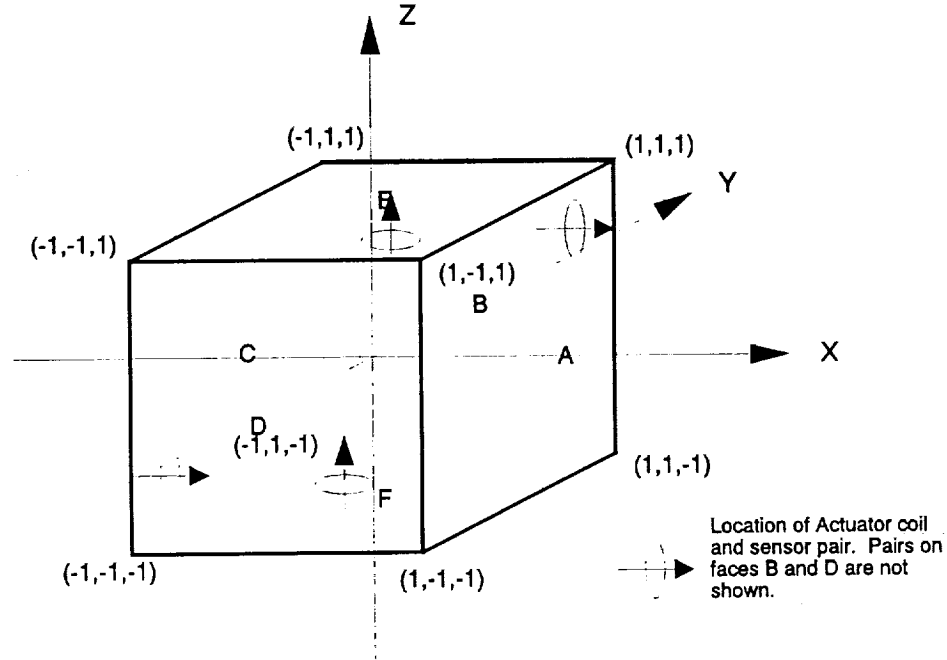
Figure 7 Sensor And Actuator Location Nomenclature

By virtue of the location of the actuator coil/sensor pair, each pair can generate a force along one translational axis and a moment around two rotational axes. If the forces generated by the actuator coils are defined by a vector

$$F_{act} = [F_a, F_b, F_c, F_d, F_e, F_f]^{-1}$$

then a transformation can be found which relates F_{act} the forces and moments

$$FM = [F_x, F_y, F_z, M_x, M_y, M_z]^{-1}$$

where the forces are defined along the translational axis and the moments are defined around these axes; i.e.,

$$FM = [T]^*F_{act}$$

As the sensors are collocated with the actuator coils, the displacements measurement "d" at each sensor can be transformed to translations and rotations using the same matrix [T], i.e.,

$$[X, Y, Z, \theta_x, \theta_y, \theta_z]^{-1} = [T][d_a, d_b, d_c, d_d, d_e, d_f]^{-1}$$

The coefficients k_{n1}, k_{n0}, k_{d1} and k_{d0} of the compensation C(s) can now be tailored to meet the frequency response requirements of the sensor system. The numerator and denominator roots or the zeros and poles of the compensation C(s) were designed to be at 503 rad/sec and 3745 rad/sec respectively. The frequency response with this compensation scheme has an overshoot of 4db at 107 Hz with a 3db point attenuation at about 200 Hz. An improved performance can be achieved using a more complex controller.

REFERENCES

1. M. Browne, "Scientists Clock The Ticking Of The Earth's Core", New York Times, Page C1, March 31, 1992.

2. "Testing Einstein With Orbiting Gyroscopes", Stanford University Publication Services, NASA Astrophysics Division, 1990.

3. L. Rochemont et al, "Recent Progress Towards Developing a High Field, High-Tc Superconducting Magnet for Magnetic Suspension and Balance Systems", International Symposium on Magnetic Suspension Technology, August 19-23, 1991.

4. D. Rao, "Effect of Flux Penetration on the Load Bearing Capacity of Superconducting Bearings", International Symposium on Magnetic Suspension Technology, Langley Research Center, Hampton, VA August 19-23, 1992.

5. J. Hull, and M. Mulcahy, "Phenomenology of Forces Acting Between Magnets and Superconductors", pre-print.

6. A. Terentiev, and A. Kuznetsov, "Levitation of $YBa_2Cu_3O_7$ Superconductor In A Variable Magnetic Field". International Symposium on Magnetic Suspension Technology, Langley VA, August 19-23, 1992.

7. T. Van Zandt, T. Kenny, W. Kaiser, "Novel Position Sensor Technologies for Micro Accelerometers", Jet Propulsion Laboratory, Pasadena, CA

8. Chu, et al, "Hybrid Superconducting Magnetic Bearing For High Speed Drives", International Symposium on Magnetic Suspension Technology, Langley Research Center, Hampton VA, August 19-23, 1991.

Session 9a (i) – Vibration Isolation

Chairman: Douglas B. Price
NASA Langley Research Center

ELECTROMECHANICAL SIMULATION AND TEST OF ROTATING SYSTEMS WITH MAGNETIC BEARING OR PIEZOELECTRIC ACTUATOR ACTIVE VIBRATION CONTROL

S_3-37

$//911$

$P. /2$

Alan B. Palazzolo, Punan Tang, Chaesil Kim, Daniel Manchala and Tim Barrett
Department of Mechanical Engineering, Texas A&M University
College Station, TX

Albert F. Kascak*, Gerald Brown, Gerald Montague** and Eliseo DiRusso
NASA Lewis
Cleveland, OH
* U.S. Army at Lewis, ** Sverdrup at Lewis

Steve Klusman
GMC Allison Gas Turbine
Indianapolis, IN

Reng Rong Lin
A.C. Compressor
Appleton, WI

ABSTRACT

This paper contains a summary of the experience of the authors in the field of electromechanical modeling for rotating machinery - active vibration control. Piezoelectric and magnetic bearing actuator based control are discussed.

INTRODUCTION

The stability analysis of conventionally supported rotating machinery has been treated extensively for many years. More recently attention has been focused on the stability analysis of magnetically supported flexible rotor or rotor-bearing installations with active vibration control systems. Assembling the model for this analysis has four basic steps:

(a)   Form the passive mass, stiffness, damping model from the shaft and disc geometry and
        from the flow, fluid and geometric properties of bearings and seals;
(b)   Obtain transfer function representation of all frequency dependent components in the
        feedback loop of the control system. This typically includes sensors, power amplifiers,
        digital signal processors and actuators;
(c)   Assembly (coupling) of the frequency dependent component representations in (b) with the passive rotor-
        bearing-seal system model in (a);
(d)   Solution of the characteristic equation of the closed loop system for the eigenvalues and
        inspection of the eigenvalues to investigate stability.

In a previous paper [1], the authors demonstrated how step (b) could be accomplished by curve fitting the component's frequency response to that of a 2nd order low pass electrical filter. This approach provided a 2nd order linear differential equation representation of the component which could be very easily coupled to the rotor system model to accomplish task (c). Task (d) was then performed utilizing the QR algorithm to extract the eigenvalues from the finite element formulated closed loop model.

Maslen and Bielk [2] presented an approach for coupling a frequency dependent, feedback loop component with a generically defined transfer function, to a standard finite element rotor system model. This method avoids the problems encountered in transfer matrix based approaches to solving the closed loop stability problem, namely non-collocated sensor-actuators and frequency dependent feedback components.

Ramesh and Kirk [3] presented a comparison between their F.E. approach to electromechanical system (ES) modeling and a transfer matrix based approach. Their results show good agreement between the methods; however, no analytical treatment of their F.E. approach was provided. Ku and Chen [4] present a F.E. based method for stability analysis of ES models and demonstrate it on our industrial pump model. The approach appears very accurate but it may be somewhat inefficient in that the eigenvalue problem must be solved repeatedly while making guesses at the natural frequencies.

This manuscript provides a review of the author's experience in electromechanical system modeling for this application. Theory and test results are given, along with a chronologically based description of the evaluation of the current modeling's methodology.

DISCUSSION

The test and theoretical results for piezoelectric actuator active vibration control are given in reference [5]. The test rig employed in that study is shown in Figure 1. The theoretical results in that paper assume ideal actuators, amplifiers and controllers which do not exhibit phase lag or amplitude roll off. Typical predicted unbalance response curves for various derivative feedback gains are shown in Figure 2. The governing equation for this system only represents pure proportional feedback gain (constant gain, zero phase lag) and pure derivative feedback gain (linear dependence of gain on frequency, 90° phase lead).

This simulation approach was improved in reference [1] where the actuator and amplifier's frequency response functions were represented by 2nd order low pass filters. Figures 3 and 4 show the measured and curve fit frequency response functions of a piezoelectric actuator. The curved fit representation represents 2nd

order differential equations which are assembled with the mechanical model to form a closed loop electrome-chanical model. Figures 5 and 6 show the shape of the measured and predicted unstable mode shapes for the same test rig as shown in Figure 1. Note that the frequency of that instability is approximately 2100-2400 Hz. The closed loop model was employed to investigate the effects of a 4th order low pass filter on stability of the unstable mode yielding the plots of Real (eigenvalue) versus feedback gain and cutoff frequency in Figure 7.

The authors [6] improved on this approach by employing a general order transfer function-state variable representation of any component in the feedback path. The approach is similar to [2]; however, a systematic method is provided for obtaining the transfer function from test data. A theory-test correlation is presented in this paper employing the test rig shown in Figures 8 and 9. This test rig was previously described in reference [7]. Figure 10 shows the measured and curve-fit 8th order transfer function through the summed proportional and derivative feedback paths of the digital controller. State space representations of this controller and the power amplifier were assembled along with a finite element model of the rotor (Figure 9) to predict the stability bounds of the coupled electromechanical system. Figure 11 shows a comparison between the pre-dicted and measured stability boundaries in the proportional-derivative feedback gain space. Simulation results are shown for various values of a parameter that characterizes the back emf induced by vibrations of the shaft, as explained in reference [6].

Actuators and sensors are always mounted on a support structure with some flexibility and inertia of its own. Reference [7] describes a simulation study for closed loop stability including effects of actuator and sensor mount flexibility. The rotor model was the same one as employed in references [1] and [5], and is depicted in Figure 12. The casing was simulated with 9 node, isoparametric thick shell elements and the actuators and sensors were attached to the flexible casing. Figures 13 and 14 are typical of results shown in reference [7]. Note how one of the three unstable modes shown in Figure 13 for the case of sensor mounted to casing does not appear if the sensor mount is assumed to be rigid as shown in Figure 14.

Figure 15 depicts a current research test being conducted by the authors for predicting stability bounds for a gas turbine engine simulator. This installation employs a PID based digital controller, pulse width modulated power amplifier and a high temperature magnetic bearing. Figure 16 shows the measured and curve fit transfer function through the summed proportional and derivative paths of the controller. The measured and predicted stability bounds will be determined and published in the near future.

SUMMARY

This manuscript summarizes the authors' efforts in the area of active vibration control related—electromechanical system modeling. Initial efforts employed ideal feedback component characterizations that were free of rolloff and phase lag. The later research of the authors utilized more realistic models based on transfer functions through the feedback components. The future work in this area will concentrate on additional test verifications of the method.

ACKNOWLEDGMENTS

REFERENCES

1. Lin, Reng Rong and Palazzolo, A.B., "Electromechanical Simulation and Testing of Actively Controlled Rotordynamic Systems with Piezoelectric Actuators," *Trans. ASME Journal of Gas Turbines and Power*, Vol. 115, April, 1993, pp. 324-335.

2. Maslen, E.H. and Bielk,J.R., "Implementing Magnetic Bearing in Discrete Flexible Structure Models," submitted to *Trans. ASME Journal of Dynamics and Controls*, 1991.

3. Ramesh, K. and Kirk, R.G., "Subharmonic Resonance Stability Prediction for Turbomachinery with Active Magnetic Bearings," *Proceedings of the Third International Symposium on Magnetic Bearings*, Alexandria, Virginia, July, pp. 113-122.

4. Ku, C.-P.R. and Chen, H.M., "An Efficient Method for Stability Analysis for Active Magnetic Bearing System," *Proceedings of the Third International Symposium on Magnetic Bearings*, Alexandria, Virginia, July, pp. 133-142.

5. Palazzolo, A.B., et. al, "Test and Theory for Piezoelectric Actuator - Active Vibration Control of Rotating Machinery," *ASME Journal of Vibrations and Acoustics*, April, Vol. 113, 1991, pp. 167-175.

6. Tang, P., Palazzolo, A.B., Brown, G., DiRusso, E. and Kascak, A., *International Gas Turbine Conference ASME*, 5/24-5/27, 1993, paper no. 93-GT-382.

7. Barrett, T., Palazzolo, A.B. and Kascak, A.F., *International Gas Turbine Conference ASME*, 5/24-5/27, 1993, paper no. 93-GT-293
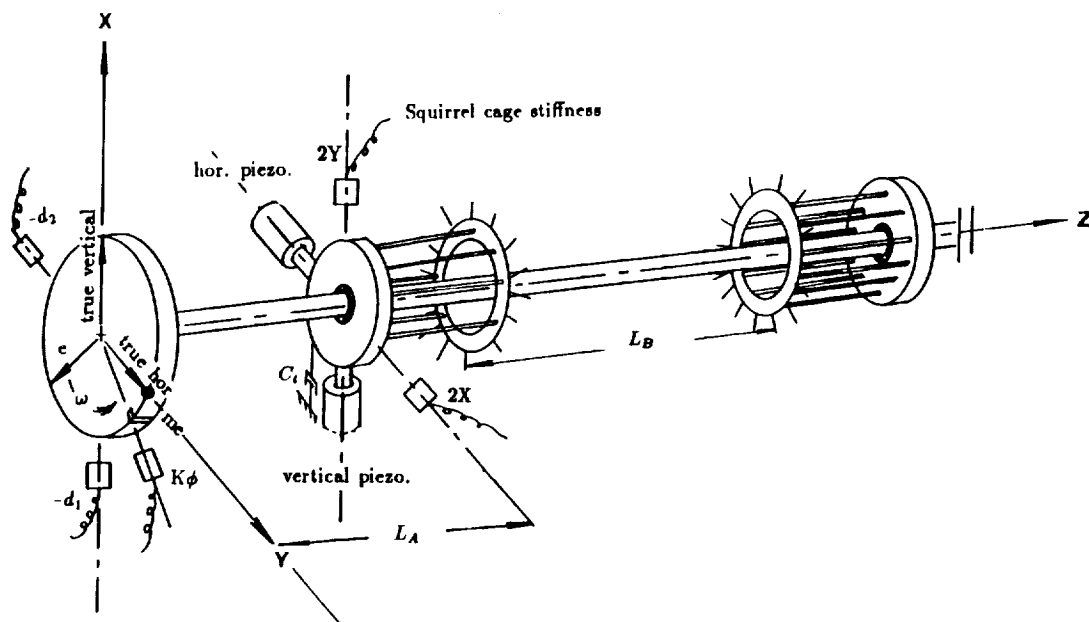
Figure 1. Diagram of test rig with Piezoelectric pushers.
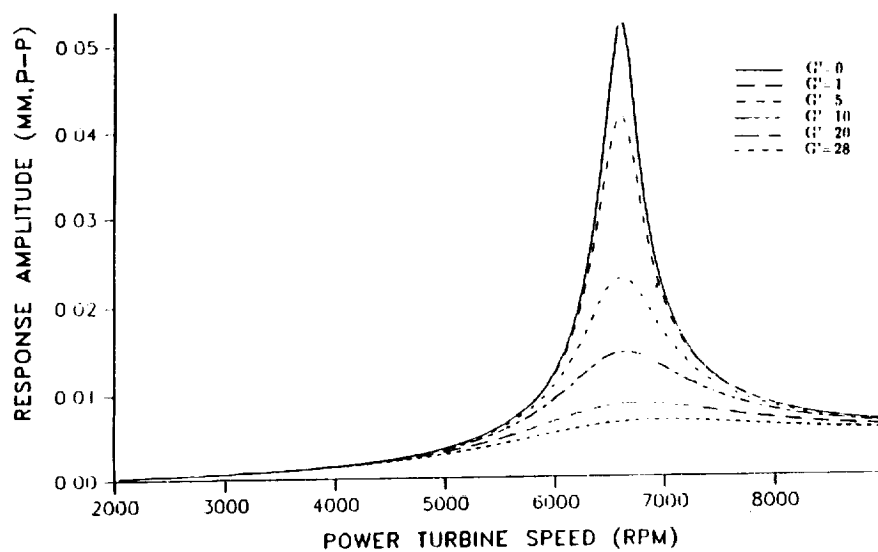
Figure 2. Simulation unbalance response at probe 2X or 2Y
vs. feedback gain coefficients in ADFT.
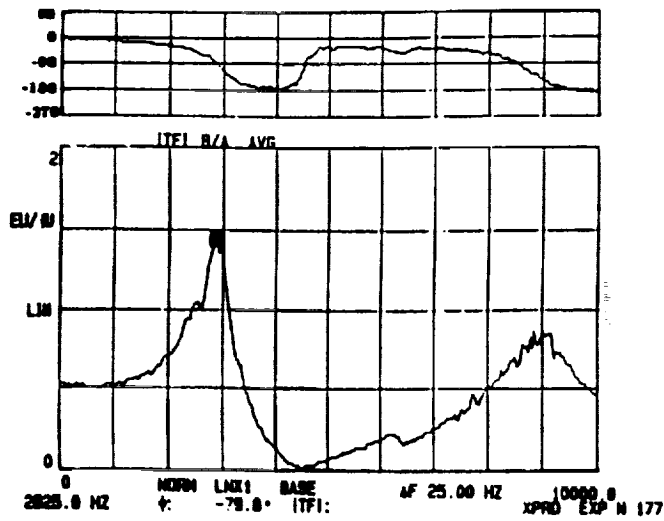
Figure 3. Transfer function plot of a typical pusher.
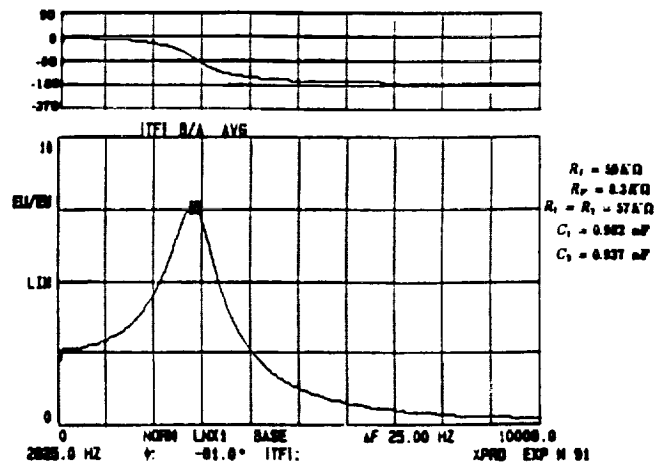
Figure 4. Transfer function plot of realized electrical circuit of pusher A.

472
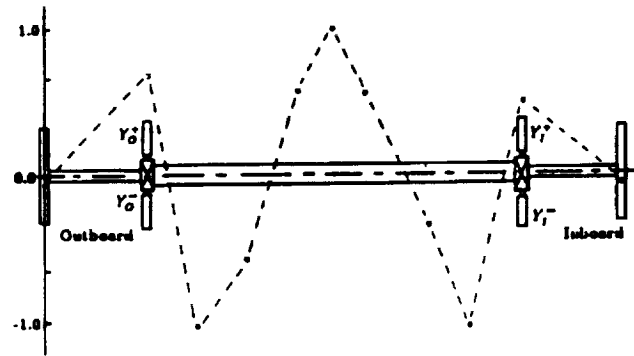
Figure 5. Measured mode shape of unstable mode at a frequency of 2100 Hz.
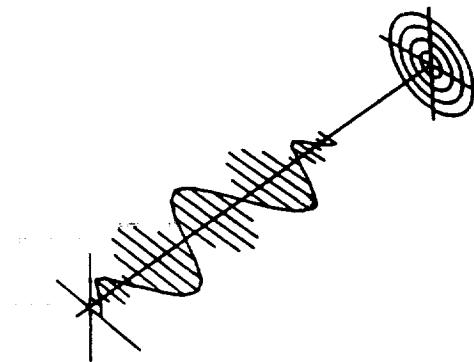
Figure 6. Predicted mode shape of unstable mode at 2400 Hz.
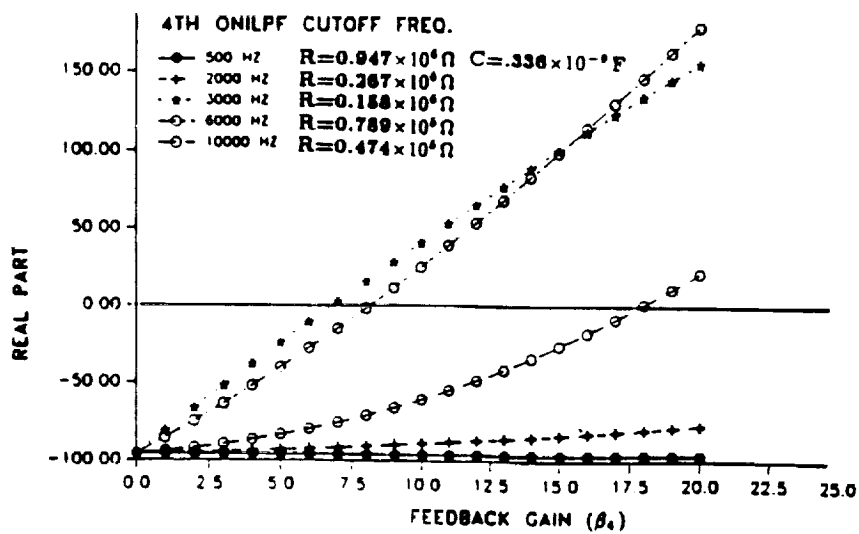
Figure 7. Effects of cutoff frequency of 4NILPF on the system instability onset gain.
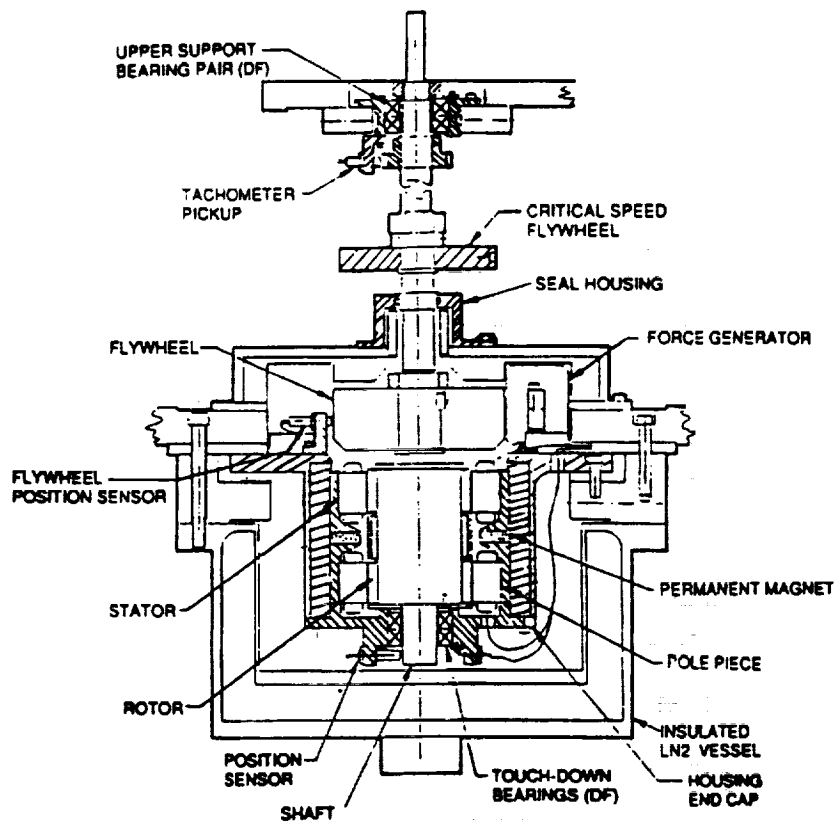
Figure 8. Cryogenic Magnetic Bearing Test Facility Design.
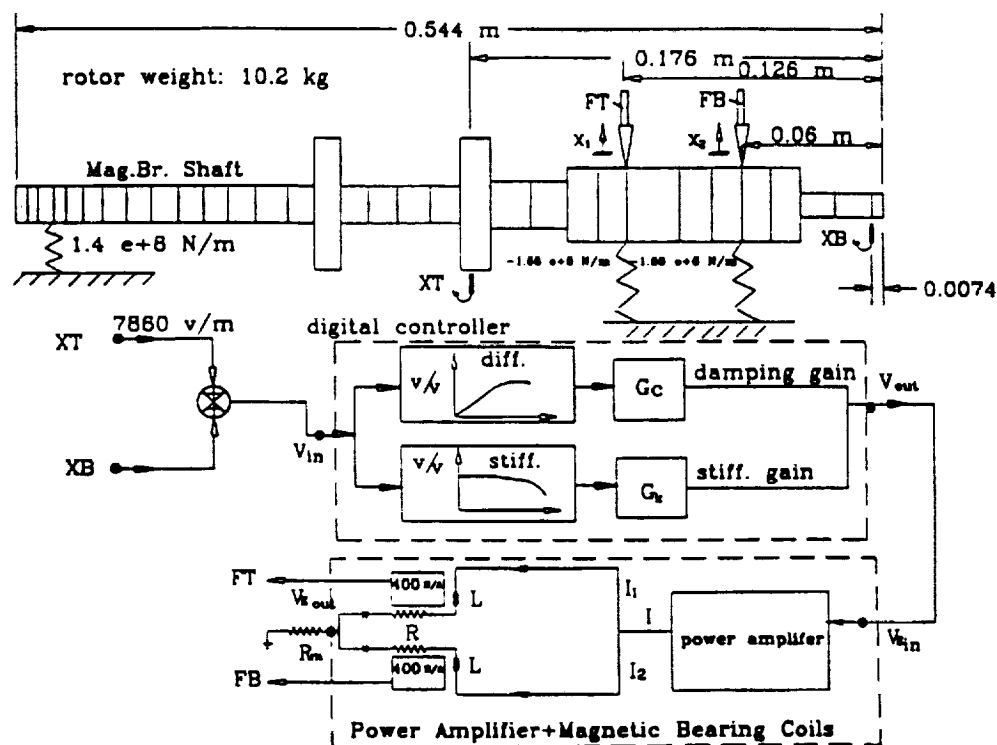
Figure 9. Block Diagram of rotor controller and magnetic bearing.
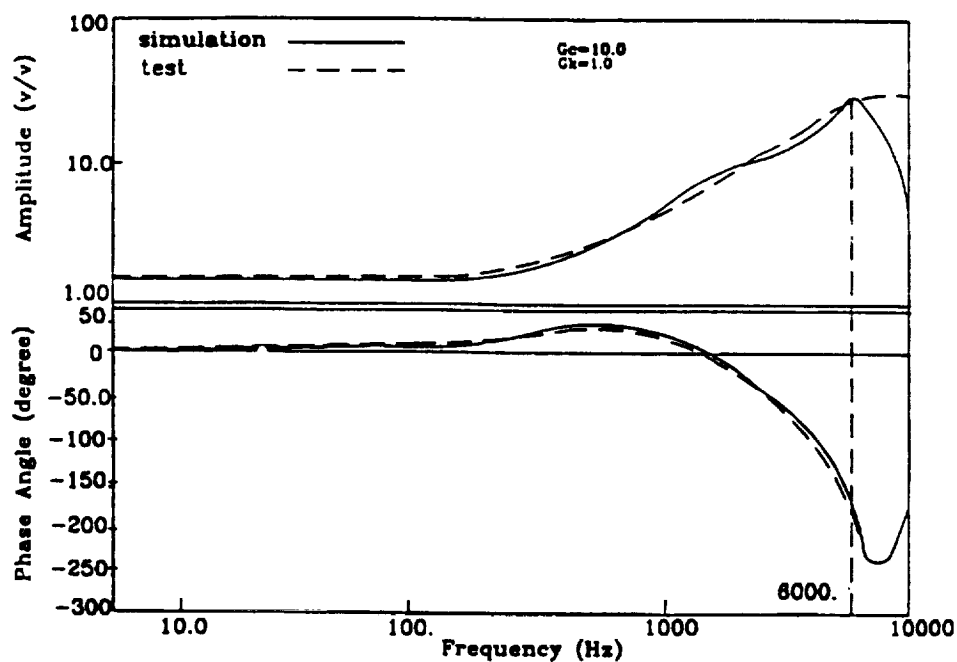
Figure 10. Measured and Curve Fit frequency response function for DSP.
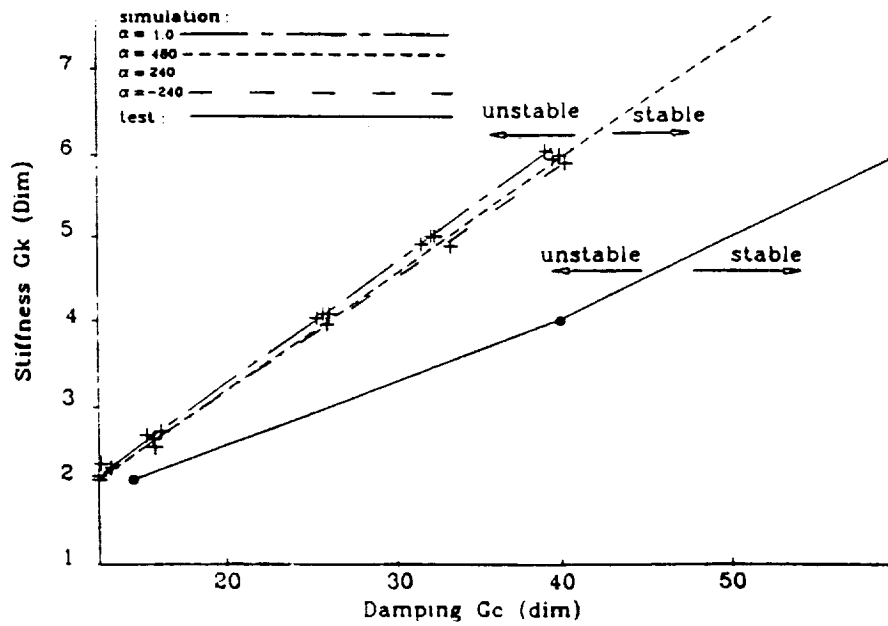
Figure 11. Comparison of measured and predicted natural frequencies
on the instability threshold.
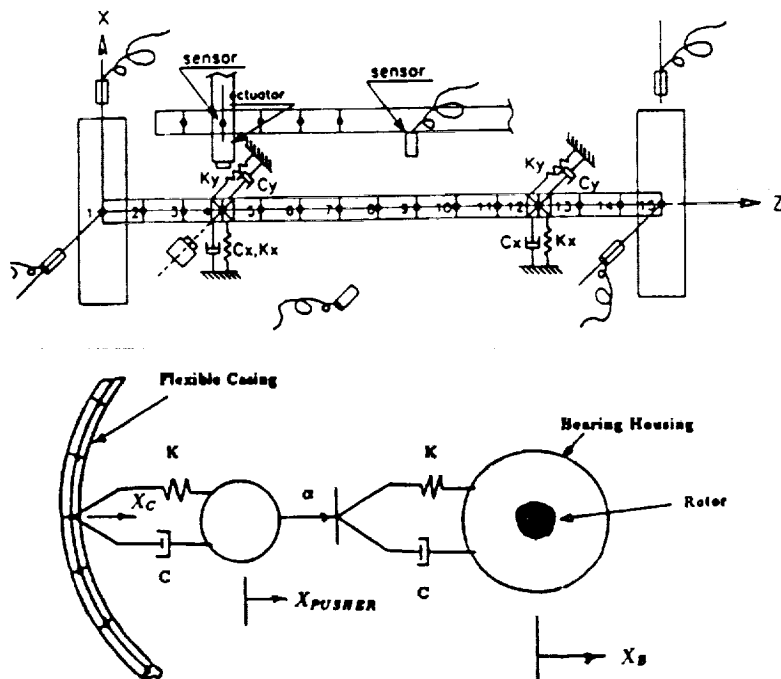
Figure 12. Fourteen mass rotor model and actuator connection.
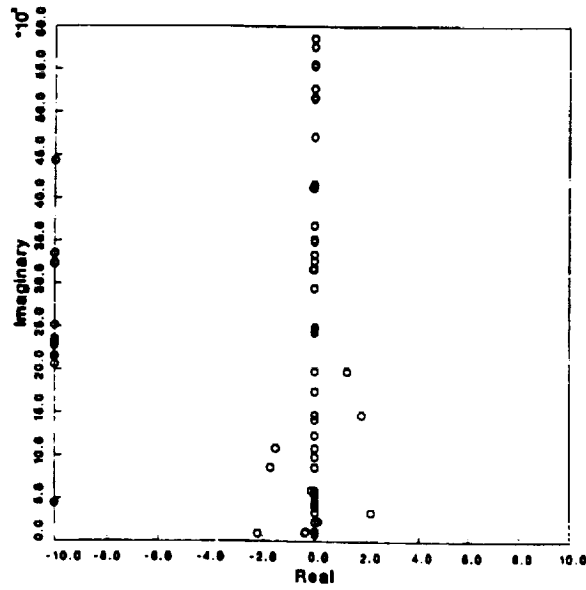
Figure 13. 1/16" casing wall thickness eigenvalue stability graph.
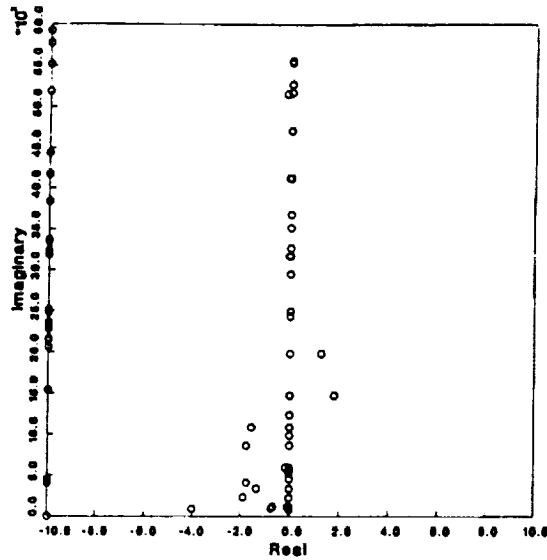
Figure 14. Uncoupled sensor - (1/16" casing).
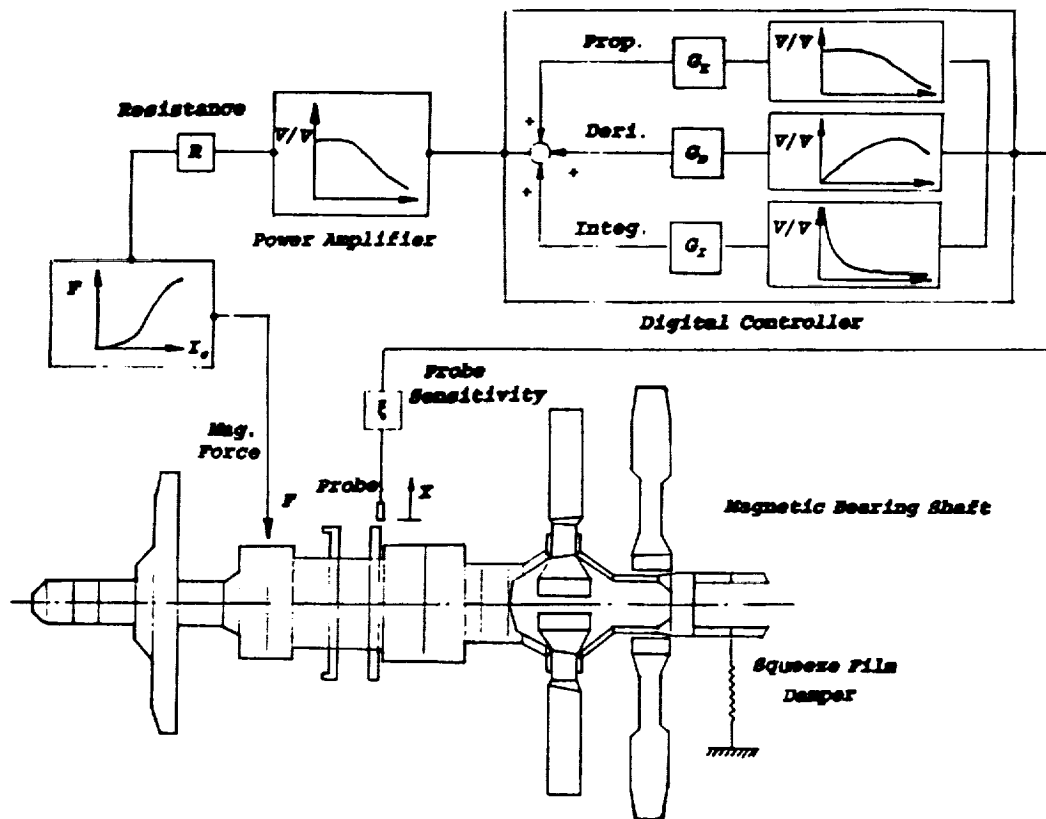
Figure 15. Block diagram of industrial magnetic bearing rotor.
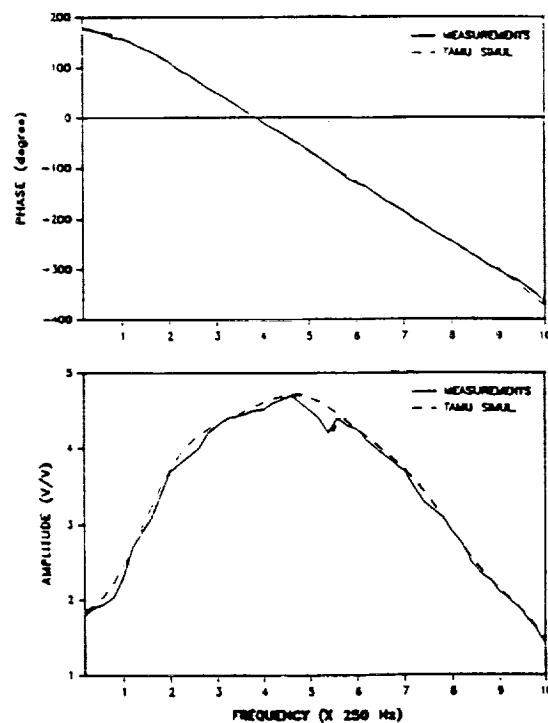
Figure 16. Comparison of TAMU simulation and Measurement (p:-10 and D:-50).

ELECTROMAGNETICALLY LEVITATED VIBRATION ISOLATION SYSTEM FOR THE MANUFACTURING PROCESS OF SILICON MONOCRYSTALS

Yoichi Kanemitsu , Katsuhide Watanabe
Ebara Research Co., Ltd., 2-1, Honfujisawa 4-chome, Fujisawa City, 251, Japan

Kenichi Yano, Takayuki Mizuno
Kajima Technical Research Institute, 19-1, Tobitakyu 2-chome, Chofu-shi, Tokyo, Japan

SUMMARY

This paper introduces a study on an Electromagnetically Levitated Vibration Isolation System (ELVIS) for isolation control of large-scale vibration.

This system features no mechanical contact between the isolation table and the installation floor, using a total of four electromagnetic actuators which generate magnetic levitation force in the vertical and horizontal directions. The configuration of the magnet for the vertical direction is designed to prevent any generation of restoring vibratory force in the horizontal direction.

The isolation system is set so that vibration control effects due to small earthquakes can be regulated to below 5(gal) versus horizontal vibration levels of the installation floor of up to 25(gal), and those in the horizontal relative displacement of up to 30 (mm) between the floor and levitated isolation table.

In particular, studies on the relative displacement between the installation floor and the levitated isolation table have been made for vibration control in the horizontal direction. In case of small-scale earthquakes (Taft wave scaled: max. 25 gal), the present system has been confirmed to achieve a vibration isolation to a level below 5 gal. The vibration transmission ratio of below 1/10 has been achieved versus continuous micro-vibration (approx. one gal) in the horizontal direction on the installation floor.

Keywords:
Vibration isolation system, Magnetic levitation, Electromagnetic actuator, Transmissibility, Vibration control, Relative feedback control, Large-scale vibration, Micro-vibration

INTRODUCTION

Recent progress in semiconductor device technology is resulting in more high precision semiconductor manufacturing and semiconductor inspection equipment. The requirements of such equipment include high precision, high performance, and high reliability.

One vital factor for satisfying these requirements is the establishment of an effective measure against vibratory effect. The use of vibration isolation systems is one such measure and such systems must feature overall prevention of vibratory effects, thus allowing uninterrupted semiconductor manufacturing processes. This means that they must prevent various vibratory effects, from those caused by small-scale earthquakes to micro-vibration effects coming from air conditioning systems, even those caused by a person moving around.

There is currently a lot of research and development being carried out on new vibration control techniques [2][3]. In particular, vibration in the horizontal direction causes ill effects on semiconductor manufacturing equipment in the majority of the cases.

Attempting to isolate vibration in the horizontal direction by using conventional air springs and coil springs necessitates a drop in the supportive stiffness of the equipment in order to decrease the natural frequency of the isolation system. Mounting equipment that has height may result in rocking movement.

Moreover, conventional vibration isolation mechanisms carry a problem in that they are incapable of isolating different kinds of vibration, i.e. from low-frequency large-amplitude vibrations to micro-vibration.

The present research is focused on a vibration isolation system which had none of the above problems. The isolation table on which the system is installed featured a non-contact support , i.e. the isolation table is levitated using electromagnets. This enables a complete isolation of the isolation table, in the horizontal direction, with the installation floor, thus preventing any transmission of horizontal direction vibration from the installation floor to the isolation system.

In particular, the ratio between the supportive stiffness in the horizontal direction and that in the vertical direction is made high as a measure against rocking movement.

The prototype electromagnetically levitated vibration isolating system (ELVIS) was capable of isolating any earthquake induced vibration from the installation floor of up to maximum input acceleration of 25 gal (seismic intensity of approximately 3 on the Japanese scale), including low frequency components, in the horizontal direction, and controlling such vibration to be decreased to below 1/5 of the intensity.

The following discusses the design factors of the ELVIS electromagnetic actuators and control system, and also introduces results of simulation tests and evaluation tests, the latter for which a large hydraulic shaker has been used.

NOMENCLATURE

m	Mass
$I_\alpha, I_\beta, I_\gamma$	Moment of inertia around inertia principal axis
g	Gravitational acceleration
F_x, F_y, F_z	Total controlling force of the actuators
F_{ix}, F_{iy}, F_{iz}	Controlling force of each actuator $i (i = 1 \cdots 4)$
$M_\alpha, M_\beta, M_\gamma$	Total moment of the actuators
x, y, z	Isolation table displacement
α, β, γ	Isolation table rotational displacement
u, v, w	Floor displacement
ξ, η, ζ	Floor rotational displacement
K	Constant determined by the number of turns in the coil, magnetic permeability and cross-sectional area of magnetic pole
i_p, i_n	magnetizing current of both facing magnets
h_o	Gap at equilibrium(at center of clearance)

TEST APPARATUS

Electromagnetically Levitated Vibration Isolation System

Figure 1 shows a schematic diagram of the ELVIS whose main components include the isolation table, for mounting equipment which need to be free from vibratory effects, the electromagnetic actuators, and the controller.

The electromagnetic actuators have built into them electromagnets and displacement sensors for controlling the levitation in the horizontal and vertical directions. The electromagnetic actuators are secured to the nodes of the first flexible mode of the isolation table to make the system unobservable and uncontrollable versus the first flexible mode of the table.

The isolation table is levitated without contact by the vertical control electromagnets built into the electromagnetic actuators.

As for horizontal control, the restoring force generated between the actuators in horizontal direction and the isolation table levitated by electromagnets is minimized so that there would be almost no stiffness in the horizontal direction.

The vertical direction levitating system has been made highly rigid to withstand any occurrence of rocking motion caused when mounting a piece of equipment with a height on the isolation table.

Figure 2 shows the components of the control system. They consist of vertical and horizontal control systems, and feature an analog type controller. Relative displacement in the vertical direction, between the installation floor and the isolation table, is detected
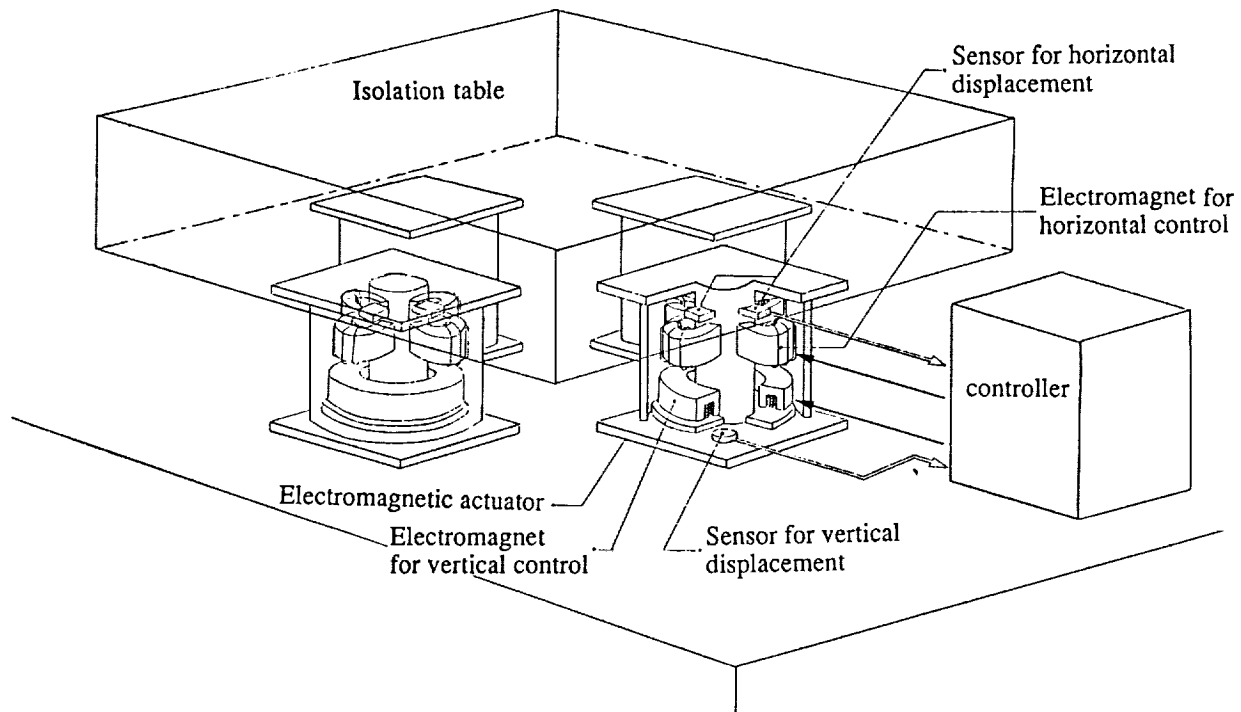
Figure 1. a schematic diagram of the ELVIS
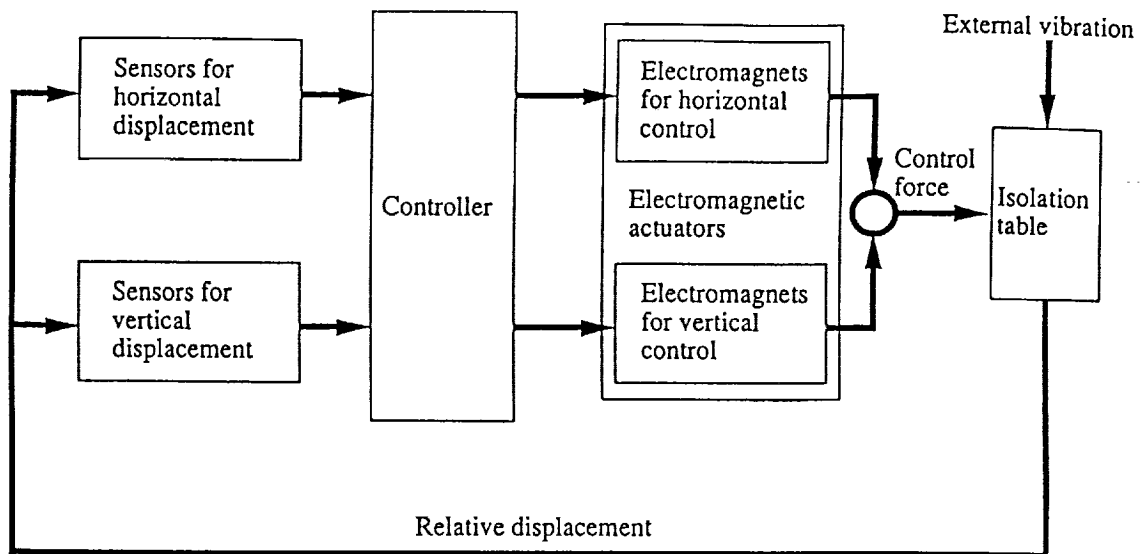
Figure 2. the components of the control system

by proximity sensors and a negative feedback of the relative displacement is used for the levitation.

Any vibratory effect caused by an earthquake in the horizontal direction is also isolated by controlling the relevant displacement to be within the allowable limit.

The specifications of the ELVIS are shown in table 1.

Table 1. the specifications of the ELVIS

Isolation performance in the horizontal direction		Earthquake	Micro-vibration
Vibration on the installation floor	Acceleration	Max. 25 gal	Max. 1 gal
	Displacement*	Max. 30 mm	————
Transmissibility		< 1 / 5	< 1 / 10

*Relative displacement between the floor and the isolation table

Electromagnetic Actuators

The electromagnetic actuators have built-in DC electromagnets, for controlling the levitation and the motion in the vertical directions and regulating the motion in the horizontal direction , and sensors, for detecting relative displacement between the installation floor and isolation table as shown in Figure 1.

The features of each component will be discussed in the following.

(a) Features of electromagnets

The ELVIS uses a magnetic levitation technique by which non-contact support of an object becomes possible.

Equipment that needs to be free from vibratory effect can be mounted on an isolation table which is completely isolated from the installation floor in the horizontal direction. For this, an actuator capable of keeping the stiffness ratio between the horizontal and vertical directions at $1 : 10^3 \sim 10^4$ has been developed.

A conventional vibration isolation system using air spring or rubber spring has relatively larger stiffness ratio than the isolation system using the magnetic levitation.

The actuators are designed so that the stiffness in the horizontal direction can be kept smaller than that in the vertical direction, allowing the input vibration amplitude of up to ±30 mm in the horizontal direction.

Figure 3 (a) shows the attractive electromagnetic force (analytical and measured) of a vertical direction controlling electromagnet versus the magnetizing current, while Figure 3(b) shows the measured restoring force of the vertical electromagnet versus displacement in the horizontal direction from a neutral point. The abscissa represents the displacement in horizontal direction between center positions of the levitation magnet pole and the levitated disk.

The attractive force shown in Figure 3 (a) is of a case where the magnetizing current is increased under a condition of constant gap (which is equal with the control gap during levitation). The abscissae represents the nondimensional magnetizing current, necessary for non-contact support of the levitated body and normalized by the magnetizing current for lavitating the isolation table , and the ordinate represents the nondimensional attractive force which is generated by the magnetizing current and is normalized by a gravity froce of the lavitated table (design values: 5kN).

Figure 3 (a) shows that the electromagnet is capable of generating a magnetic force that is approximately three times the desired value for the levitation until magnetic saturation is reached.
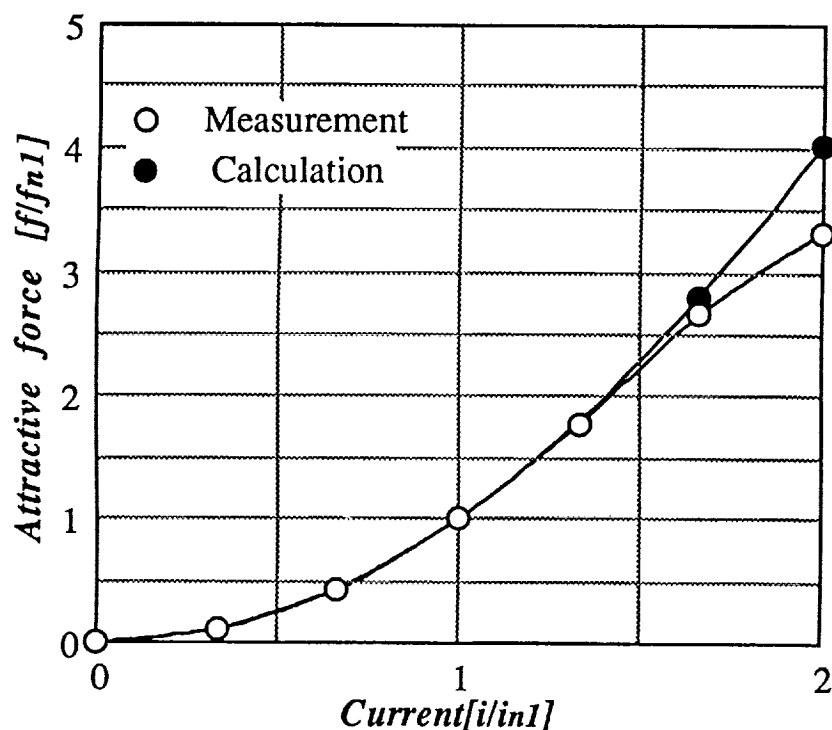
Figure 3 (a) attractive force of electromagnet for vertical control

In contrast, Figure 3(b) shows that the restoring force in the horizontal direction, generated by magnetic flux leakage of the vertical direction controlling electromagnet, is shown to be four notches below the attractive force. The inclination of this force is the passive spring constant taking effect in the horizontal direction, indicating that there is almost no horizontal force generated by the vertical control electromagnet .

The horizontal electromagnets have been designed to face each other as single-bodied electromagnets, capable of generating an attractive force within the gap of ±30 mm, and controlling vibration in horizontal direction.

FEM have been employed to calculate the attractive force between the magnet and the attracted yoke precisely.
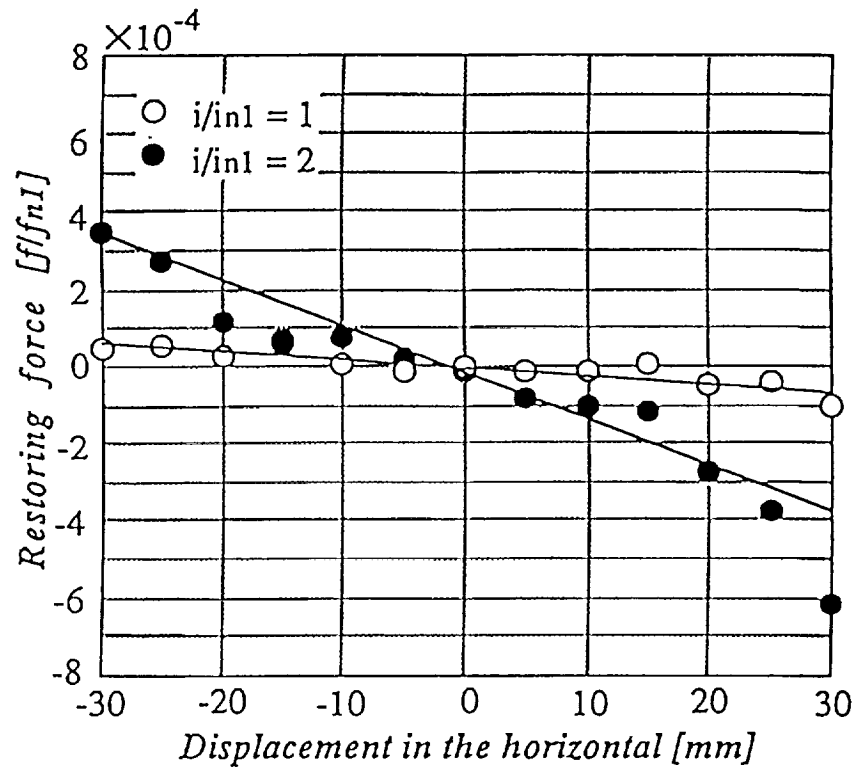
(b) restoring force of electromagnet in horizontal direction

Figure 3. attractive and restoring force of electromagnet
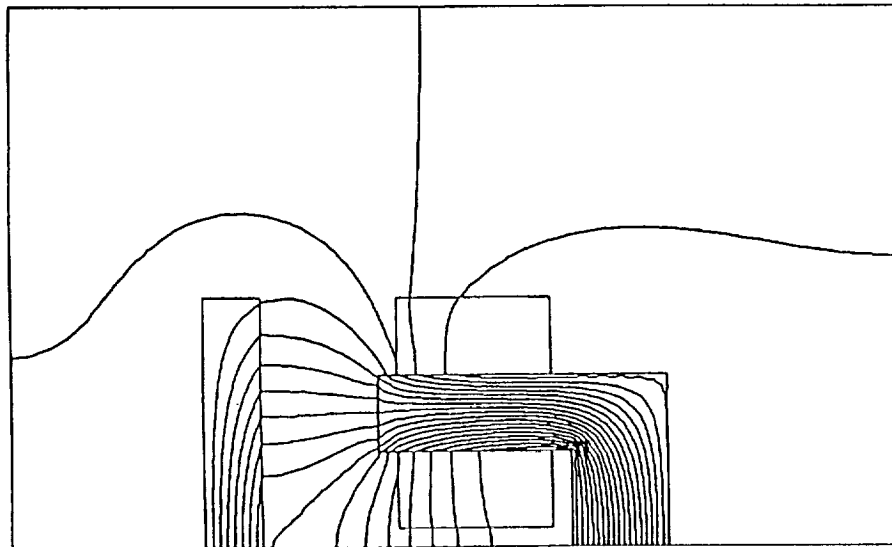
Figure 4. an example of FEM analysis results on the magnetic field of the horizontal control electromagnet with a gap of 30 mm

Figure 4 shows an example of FEM analysis results on the magnetic field of the horizontal control electromagnet with a gap of 30 mm. We can see from the figure that here is a lot of magnetic flux leakage due to the great gap between them.

Figure 5 shows calculated and measured results of the nondimensional attractive force with a gap of 30 mm. The calculated results correspond with the measured results.

(b) Features of large-scale displacement sensors

Prototypes of large-scale displacement induction type sensors, which use the bottom surface of the levitated disk for vertical control, have been developed. These sensors are used for detecting the large horizontal relative displacement between the installation floor and the isolation table, thus enabling control of horizontal vibration.

Figure 6 shows the characteristics of these sensors for horizontal displacement. The specified linearity (error below 6.0%) and specified sensitivity (5.0V/30 mm) have been achieved within the measurement range which is the design specification of ±30 mm.
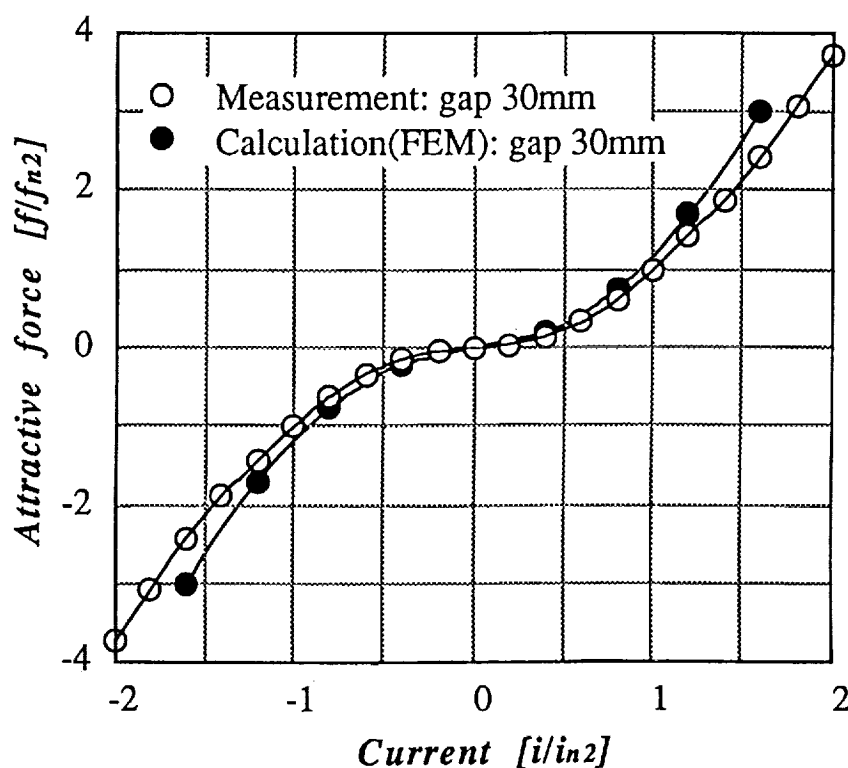
Figure 5. calculated and measured results of the nondimensional attractive force with a gap of 30 mm
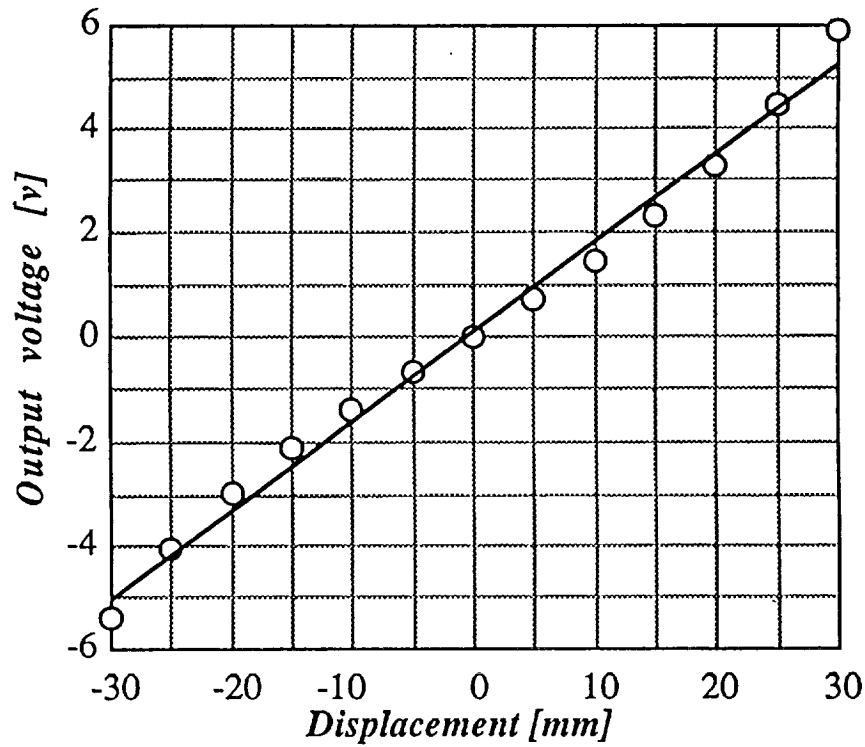
Figure 6. the characteristic of sensor for horizontal displacement

CONTROL SYSTEM

Model of the isolation system

Figure 7 shows a model of the **ELVIS** wherein the isolation table is supported by four electromagnetic actuators. Each actuator's supportive direction is aligned with the coordinate axes and it is assumed that the actuator's points of application are on the x - y surfaces and the coordinates of axes are matched with principal axes of inertia and products of inertial are removed.

The equations of motion of the isolation system, indicated below in (1) $\cdots$ (6), are written with each freedom of movement expressed independently and any cross-coupled effects are removed.

They represent rigid vibration modes of the table whereby flexible vibration modes of the isolation table are neglected.

$$m\ddot{x} = F_x = (F_{1x} + F_{2x} + F_{3x} + F_{4x}) \tag{1}$$

$$m\ddot{y} = F_y = (F_{1y} + F_{2y} + F_{3y} + F_{4y}) \qquad (2)$$

$$m\ddot{z} = F_z = (F_{1z} + F_{2z} + F_{3z} + F_{4z}) \qquad (3)$$

$$I_\alpha\ddot{\alpha} = M_\alpha = l(F_{3z} - F_{1z}) \qquad (4)$$

$$I_\beta\ddot{\beta} = M_\beta = l(F_{2z} - F_{4z}) \qquad (5)$$

$$I_\gamma\ddot{\gamma} = M_\gamma = l(F_{1x} - F_{2y} - F_{3x} + F_{4y}) \qquad (6)$$

From the above equations, the isolation system is expressed in 3-D with six degrees of freedom.

However, we decided to design and assess the system with the target of isolating vibration in the horizontal direction (x and y directions) under a 2-D condition.

As mentioned before, non-contact support of the isolation table makes it possible to remove almost all stiffness in the horizontal direction. It is therefore possible to regulate the acceleration of the isolation table without any transmission of vibration coming from the installation floor.

However, the relative displacement between the installation floor and the isolation table
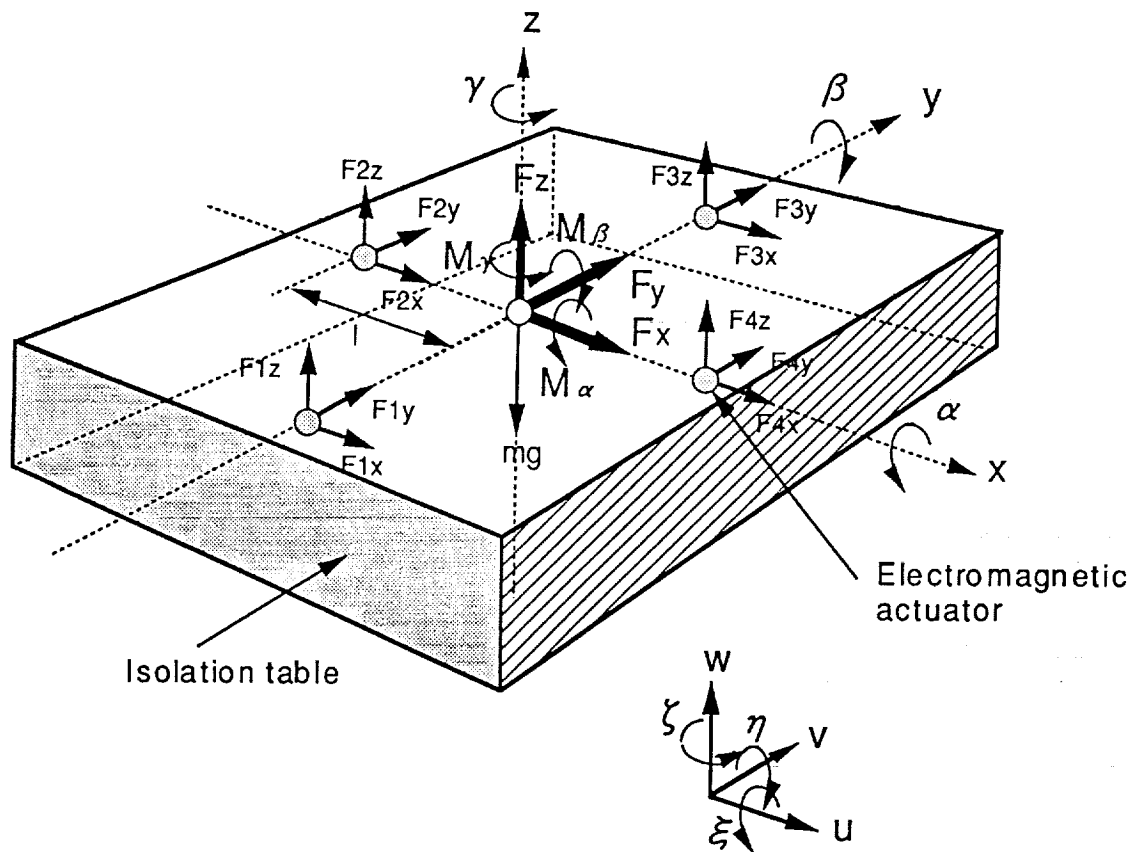
Figure 7. model of the **ELVIS** wherein the isolation table is supported by four electromagnetic actuators

becomes greater and there is a risk of contact between the electromagnets and members of attracted yokes, i.e. depending on the intensity of vibration (displacement amount) at the installation floor.

Furthermore, if there is unevenness on the surface of the installation floor, the isolation table may shift to the lower side as there is no stiffness. For these reasons, it becomes necessary to augment appropriate stiffness and damping in the horizontal direction.

A horizontal isolation system, featuring the use of relative displacement feedback, has been designed to cope with the situation. The horizontal isolation system (translation motion) will be focused hereon.

Model of the electromagnets

The attractive force of the horizontal control electromagnets carries a non-linear characteristic as clearly defined in Figure 5. The following equation (7) can be used for calculating this attractive force.

$$ f = K(\frac{i}{h})^2 = K(\frac{i_p}{h_0 - x + u})^2 - (\frac{i_n}{h_0 + x - u})^2 \tag{7} $$

Normally, the linear relationship between the electric current and attractive force is plotted after passing a bias magnetizing current into the electromagnet. However, it was difficult to do this due to the big gap (30 mm $\sim$ 60 mm).

Applying the bias current also results in an imbalance stiffness (negative stiffness), necessitating an increased feedback amount for stabilization. In such case, the stiffness becomes increased but the isolation performance deteriorates.

In our case, output signals from a phase compensation circuit flow into the amplifier via a square root circuit for enabling a simplified assimilation whereby a linear relation is made consisting of amplifier input signals and the attractive force.

Amplifier input signals and the output current are proportional. Accordingly, the following equation can be used to express the magnetic attractive force versus the ouput signals from the phase compensation circuit(input signals of the root circuit).

$$ f = K_c v_c \tag{8} $$

where v_c is the ouput signals from the phase compensation circuit.

Results of actual measurement indicated that Kc = 0.5. However, the value of Kc changes with fluctuations in the gap.

Horizontal Controller

The following discusses the design of the isolation system for horizontal control by negative feedback of the relative displacement. The equations of motion for the translation motion are as indicated in the following:

$$m\ddot{x} = \sum_{i=1}^{4} F_{ix} \tag{9}$$

$$m\ddot{y} = \sum_{i=1}^{4} F_{iy} \tag{10}$$

where

$$F = F_{ix} = F_{jy}(i = 1 \cdots 4, j = 1 \cdots 4)$$

and Laplace transforming equations (8) and (9), we get

$$ms^2 X(s) = 4F(s) = 4K_c v_c(s) \tag{11}$$

Considering x_r as the relative displacement between displacement u of the installation floor and displacement x of the isolation table, and feeding back this relative displacement value together with the relative velocity by controller $G(s)$ indicated in equation (11), equation (11) is transformed into equation (12). The transfer function of the vibration transmissibility of this isolation system becomes as indicated in equation (14) via equation (13).

$$G(s) = -(K_0 + K_1 s) \tag{12}$$

$$ms^2 X(s) = 4K_c G(s) X_r(s) = -4K_c (K_0 + K_1 s)(X(s) - U(s)) \tag{13}$$

$$\frac{X(s)}{U(s)} = \frac{4K_c K_{1s} + 4K_c K_0}{ms^2 + 4K_c K_{1s} + 4K_c K_0} \tag{14}$$

Parameters K_0 and K_1 of controller $G(s)$ are set to be as the isolation system's natural frequency of 0.3 Hz with the damping ratio of 0.2. The value of K_c used is that at the location of equilibrium (gap of 30 mm).

Figure 8 shows the transmissibility of the isolation system, wherein measured and calculated transfer functions in both the horizontal and vertical directions are shown for comparison.

We can see from the figure that the bandwidth of the isolation system in vertical direction is up to 35Hz and the natural frequency in horizontal direction is 0.3Hz.

NUMERICAL SIMULATIONS

Numerical simulations have been carried out to confirm whether the designed feedback system is capable of obtaining an isolation performance which satisfied the specifications.

Taft waves, including low frequency components of below 1 Hz, and micro-vibration (White Noise $\leq$ 1.0 gal) are input into the mathematical model of the isolation system.

Although Taft waves are typical seismic waves for assessing antiseismic performance, they constitute high vibration waveforms. For this reason, they had to be scaled down to below Max. 25 gal, the design specification. Figure 9 shows results of numerical simulation on isolation performance versus seismic and micro-vibration. Figure 9(a) shows input acceleration waveform of Taft's wave to the installation floor in horizontal direction. Figure 9(b) shows absolute acceleration waveform on the levitation table in horizontal direction.

Figure 8. measured and calculated transfer functions of the isolation system in both the horizontal and vertical directions

Figure 9(c) shows relative displacement waveform between the installation floor and the levitation table in horizontal direction. Figure 9(d) shows absolute acceleration waveform of micro-vibration to the installation floor in horizontal direction , whose maximum amplitude is up to 1.0 gal. Figure 9(e) shows absolute acceleration waveform 6f micro-vibration on the table in horizontal direction.

It is acknowledged from the simulation results of simulations that for the seismic vibration, isolation is achieved to below 1/5, while for micro-vibration, to below 1/100.

(a) input acceleration waveform of Taft's wave to the installation floor in horizontal direction

(b) absolute acceleration waveform on the levitation table in horizontal direction
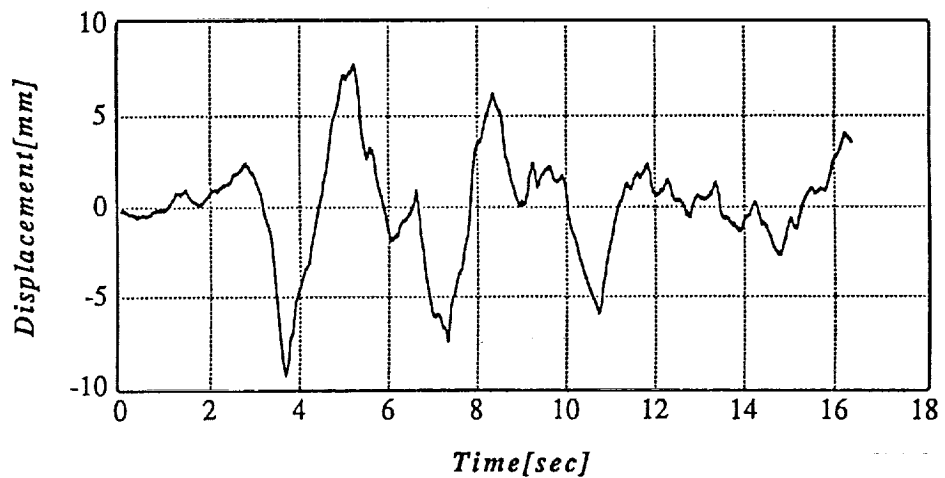
(c) relative displacement waveform between the installation floor and the levitation table in horizontal direction

Figure 9. results of numerical simulation on isolation performance versus seismic and micro-vibration 5mm
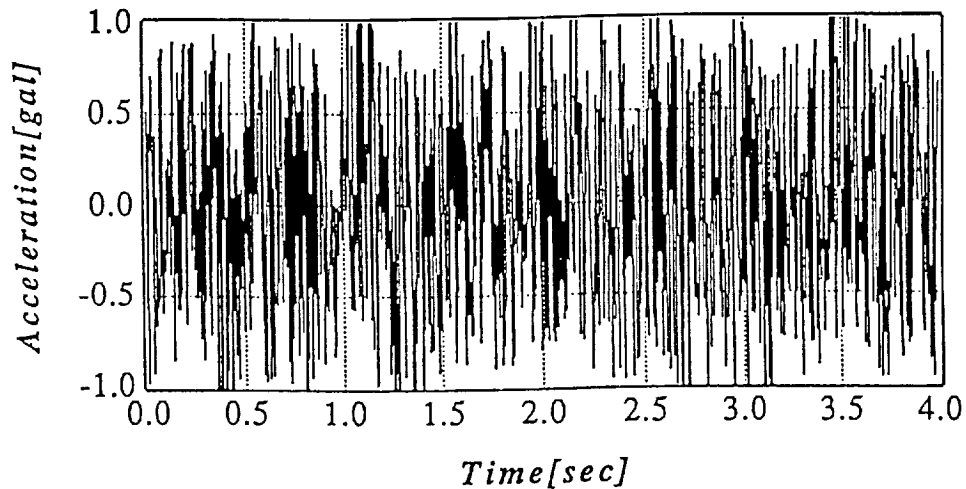
(d) absolute acceleration waveform of micro-vibration to the installation floor in horizontal direction whose maximum amplitude is up to 1.0 gal
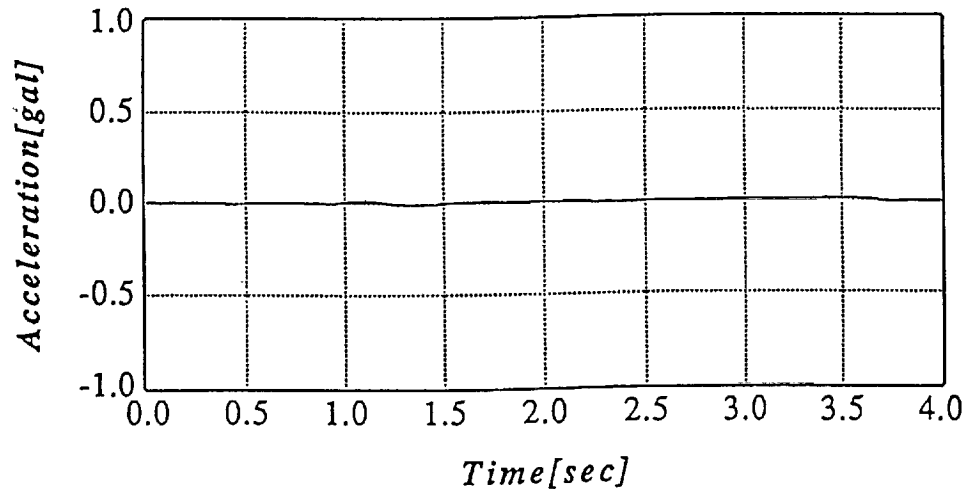
(e) shows absolute acceleration waveform of micro-vibration on the table in horizontal direction

Figure 9. results of numerical simulation on isolation performance versus seismic and micro-vibration

SHAKER TESTS

The ELVIS is mounted on a shaking table and vibration tests have been carried out by the input of seismic waves. Figure 10 shows a general view of the ELVIS mounted on the shaking table, while Figure 11 shows results of the isolation tests by shaker. Figure 11(a) shows input acceleration waveform of Taft's wave to the installation floor in horizontal direction. Figure 11(b) shows absolute acceleration waveform on the levitation table in

horizontal direction. Figure 11(c) shows relative displacement waveform between the installation floor and the levitation table in horizontal direction. Figure 11(d) shows absolute acceleration waveform of micro-vibration to the installation floor in horizontal direction, whose maximum amplitude is up to 1.0 gal. Figure 11(e) shows absolute acceleration waveform of micro-vibration on the table in horizontal direction.

The shaker test using Taft waves (Max. 25 gal) indicated that an isolation to below 1/5 has been achieved, matching the result of the relevant simulation result. As for the isolation of micro-vibrations, isolation has been achieved to below 1/10. This is nowhere near the same by the simulation result (below 1/100), a drop in isolation performance probably due to sensor noise.

The transmissibility for the horizontal direction is identical to those measured in the numerical simulations as seen in figure 8.

The characteristics for the vertical direction indicate a natural frequency of 35 Hz and a damping ratio of 0.5.

Shaker tests have been also carried out whereby shifts of 45 degrees from the X- and Y-axes are made, the results of which are identical to the former shaker tests. It is thus confirmed that the isolation system has no effect on the transmissibility in the horizontal direction, by excitation direction , indicating that there is not any problem as for the direction of input vibration.
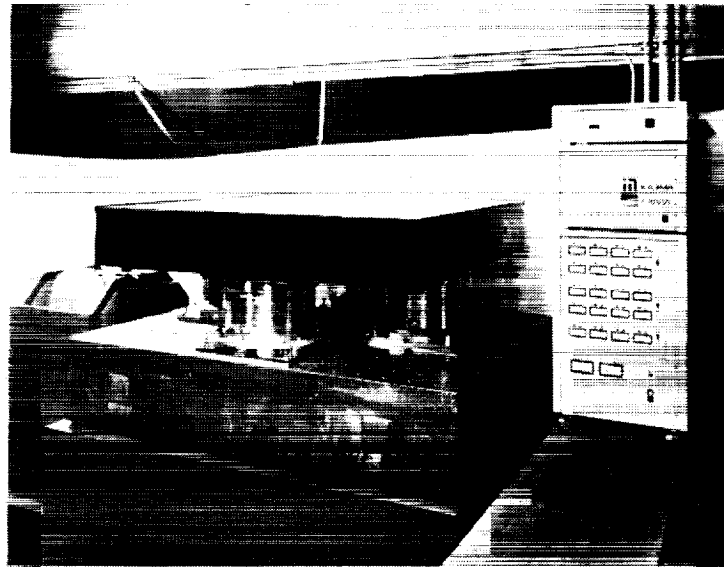
Figure 10. general view of the **ELVIS** mounted on the shaking table
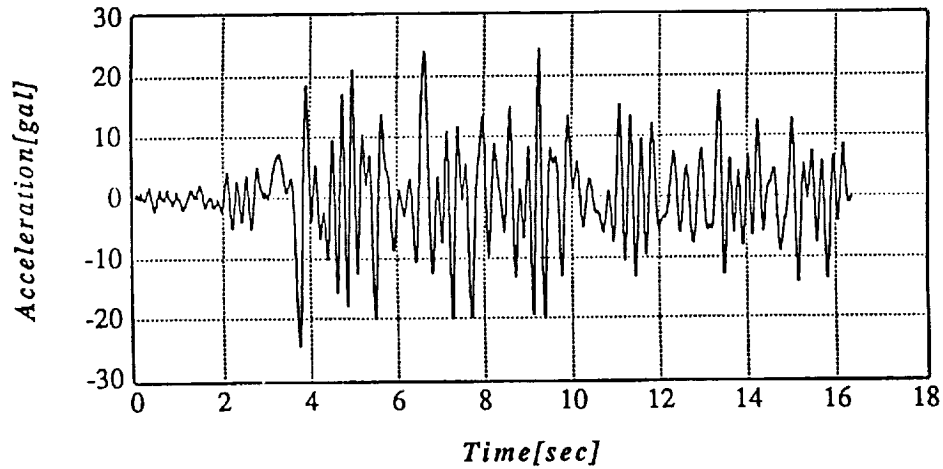
(a) input acceleration waveform of Taft's wave to the installation floor in horizontal direction

(b) absolute acceleration waveform on the levitation table in horizontal direction

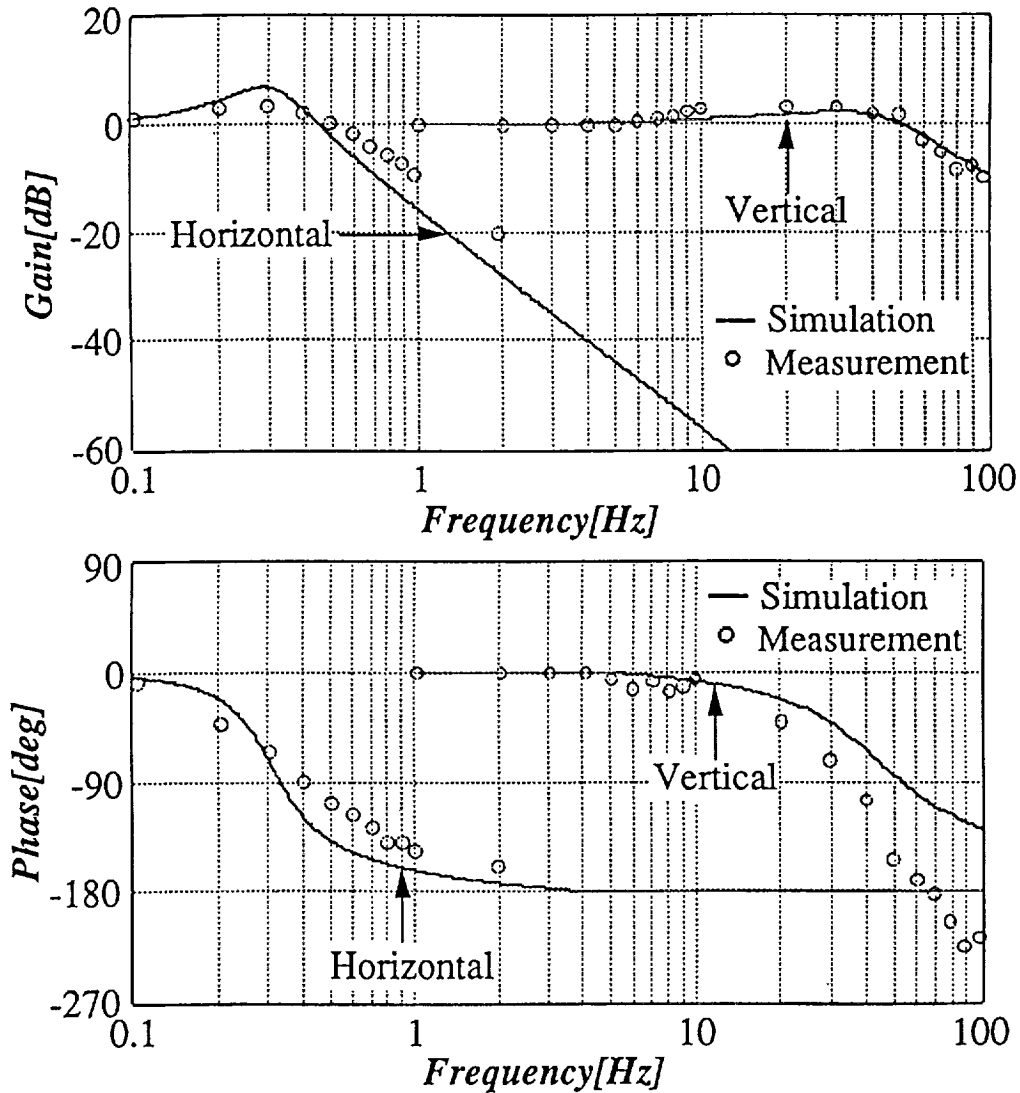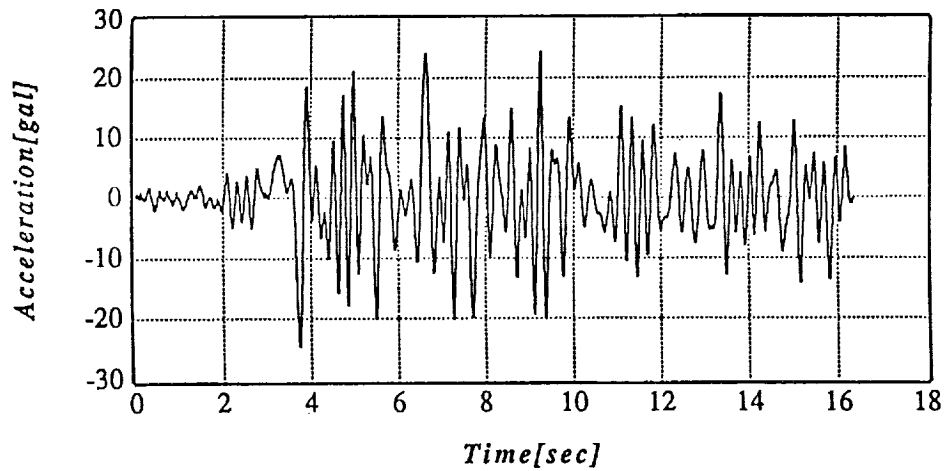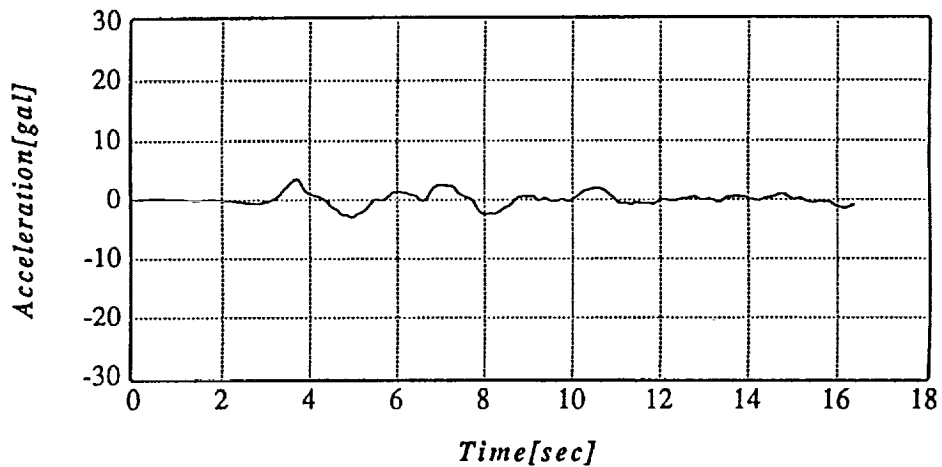(c) relative displacement waveform between the installation floor and the levitation table in horizontal direction

Figure 11. results of the isolation tests by shaker

495
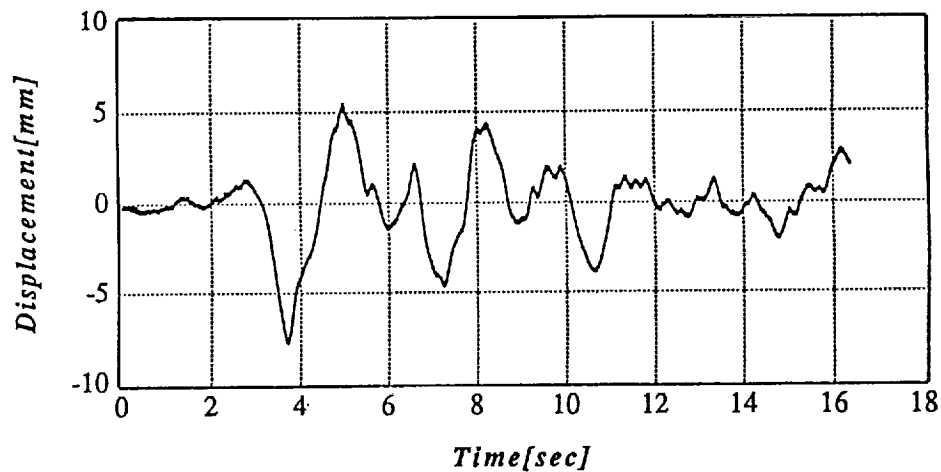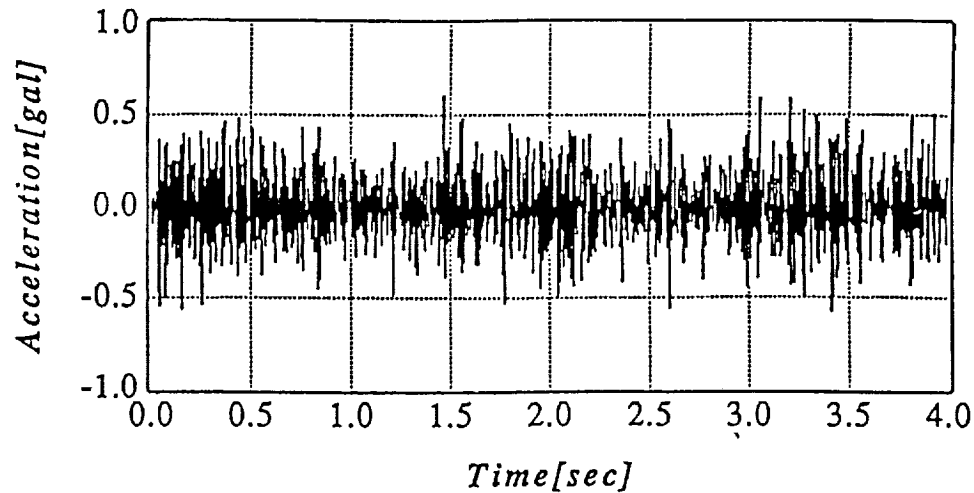
(d) absolute acceleration waveform of micro-vibration to the installation floor in horizontal direction ,whose maximum amplitude is up to 1.0 gal
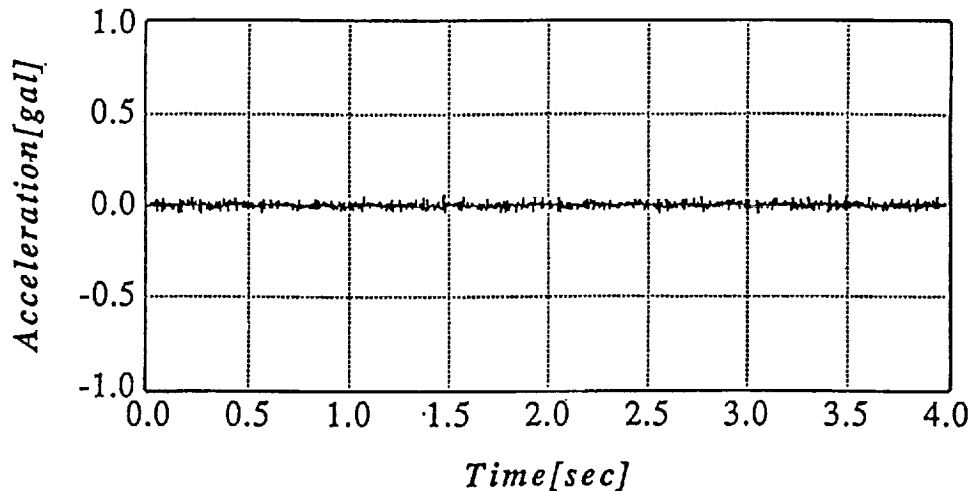
(e) absolute acceleration waveform of micro-vibration on the table in horizontal direction

Figure 11. results of the isolation tests by shaker

CONCLUSIONS

The two-dimensional horizontal direction prototype of electromagnetically levitated vibration isolation system, featuring a magnetic levitation technique for vibration isolation, has been tested to confirm its vibration isolation performance. The following are conclusions obtained from the results.

1. It is confirmed that magnetically levitating the isolation table for mounting equipment that need to be free from vibratory effects results in omitting stiffness in the horizontal direction and isolating vibration that is otherwise transmitted from the installation floor.

2. It is confirmed through shaker tests that an isolation to below 5 gal is achieved using Taft waves of maximum amplitude 25 gal, including components which are below 1 Hz (transmissibility is below 1/5) . As for the isolation of micro-vibrations of approximately 1 gal, isolation is achieved to below 0.1 gal (transmission ratio is below 1/10).

3. The degree of stiffness for the horizontal and vertical directions can be set independently. A horizontal direction two-dimensional isolation system, featuring no occurrence of rocking, can be established by controlling the stiffness for the vertical direction to be approximately 10,000-fold of that for the horizontal direction.

REFERENCES

(1) TokiTa, Morimura: Vibration Control Handbook(Fuji Technosystem)
(2) Takahashi et al: A Study on Active Vibration Control System using a Linear Motor, J. of Struct. Const. Eng. Architectural Institute of Japan , No. 412, June 1990
(3) Fujita: Research on Earthquake Resistant Structures , Takashi Fujita Laboratory Report, No. 2 , Institute of Industrial Science , University of Tokyo

Session 9a (ii) – Micromachines

Chairman: Douglas B. Price
NASA Langley Research Center

PLANAR ROTATIONAL MAGNETIC MICROMOTORS WITH INTEGRATED SHAFT ENCODER AND MAGNETIC ROTOR LEVITATION

$S_5 - 33$

$//9/3$

$P- //$

H. Guckel, T.R. Christenson, K.J. Skrobis, J. Klein
Wisconsin Center for Applied Microelectronics
Department of Electrical and Computer Engineering
University of Wisconsin
Madison, WI 53706

M. Karnowsky
Sandia National Laboratories
Albuquerque, NM 87185

ABSTRACT

Deep x-ray lithography and electroplating may be combined to form a fabrication tool for micromechanical devices with large structural heights, to 500 μm, and extreme edge acuities, less than 0.1 μm run-out per 100 μm of height. This process concept which originated in Germany as LIGA[1] may be further extended by adding surface micromachining[2]. This extension permits the fabrication of precision metal and plastic parts which may be assembled into three-dimensional micromechanical components and systems.

The processing tool may be used to fabricate devices from ferromagnetic material such as nickel and nickel-iron alloys. These materials when properly heat treated exhibit acceptable magnetic behavior for current to flux conversion and marginal behavior for permanent magnet applications.

The tool and materials have been tested via planar, magnetic, rotational micromotor fabrication. Three phase reluctance machines of the 6:4 configuration with 280 μm diameter rotors have been tested and analyzed[3,4]. Stable rotational speeds to 34,000 rpm with output torques above 10 x 10^{-9} N-m have been obtained. The behavior is monitored with integrated shaft encoders which are photodiodes which measure the rotor response. Magnetic levitation of the rotor via reluctance forces has been achieved and has reduced frictional torque losses to less than 1% of the available torque.

The results indicate that high speed limits of these actuators are related to torque ripple. Hysteresis motors with magnetic bearings are under consideration and will produce high speed rotational machines with excellent sensor application potential.

INTRODUCTION

In 1959 J.W. Beams reported on experiments in which he levitated a ferromagnetic sphere in a magnetic suspension in a hard vacuum environment[5]. The sphere with a diameter of a few hundred micrometers was rotated via magnetic induction to speeds above 50,000,000 rpm which eventually led to plastic deformation of the ferromagnetic material. The reported run-up and coast-down times were several days. Beams's experiment fundamentally contributed to gyro and ultra centrifuge progress. It is possible to argue that Beams's work also affects modern micromotor development in the sense that (a) his rotor diameter is of the same size as micromotor rotors and (b) that performance of micromotors which approaches Beams's results would have major implications on application possibilities for micromachines.

The challenges to micromotor fabrication and design in the present context are many. All micromotors will have small torque outputs. This is simply a consequence of available energy density and working volume. Since maximum energy densities for magnetics and electrostatics are fixed and the working volume is small the low torque output statement is justified. The argument can be taken one step further: micromachines with a small chip area profit from construction techniques which utilize the structural height of the device for volume and therefore torque increases.

With small output torques motor losses must be minimized. In the present context this implies a non-contact bearing and, of course, hard vacuum operation. Since true electrostatic and magnetic bearings are open circuit unstable appropriate sensors and feedback mechanisms become part of the motor design.

The third point involves the motor type. Micromotors have a small moment of inertia. This is good and bad. If the torque versus rotational angle behavior of the machine has large ripple the machine will become a stepping motor which will cause major problems with maximum speeds because the rotational speed will become angle dependent and pole

overshoot will lead to synchronization problems[6]. A constant torque versus rotational angle behavior avoids this issue and simplifies motor control schemes significantly.

The driving mechanism for the anticipated machine can be electrostatic or magnetic. Maximum energy densities are slightly larger for magnetics. Processing convenience favors electrostatics because the structures are less three dimensional than magnetic devices because of the enveloping coil requirement for current to flux conversion. The motor control aspect for rotational speed to 1×10^6 rps and possibly many pole configurations · require microelectronics with fairly high clock rates. Integrated circuits for high speed current switching, and magnetics are available. High speed, high voltage control circuitry is much more limited. System perspectives do therefore favor magnetics for the immediate future. The torque ripple issue which is a severe problem for nearly all electrostatic machines tilts the implementation towards magnetics.

MAGNETIC MOTOR FABRICATION AND DESIGN

In the previous section the goals for a high speed motor program have been discussed. The stated requirements are of course very ambitious and are subdivided into a preliminary phase with the goals of (1) providing a planar magnetic motor (2) demonstrating a one-dimensional magnetic bearing and (3) incorporating rotor position sensors.

The technology of choice is a combination of integrated circuit processing, deep x-ray lithography and metal plating and surface micromachining. The motor design is that of a three phase machine: six poles, with a salient rotor with symmetry about the x and y axis. Levitation is provided by fabricating the rotor at a structural height which is less than the stator height and therefore produces an upward force due to the stator field. The rotor support shaft is fluted to reduce frictional losses and to produce centering via currents during atmospheric operation. Rotor position sensing is achieved by a shaft encoder which is formed from diffused photodiodes which are located in the substrate. Figure (1) illustrates the general concepts.
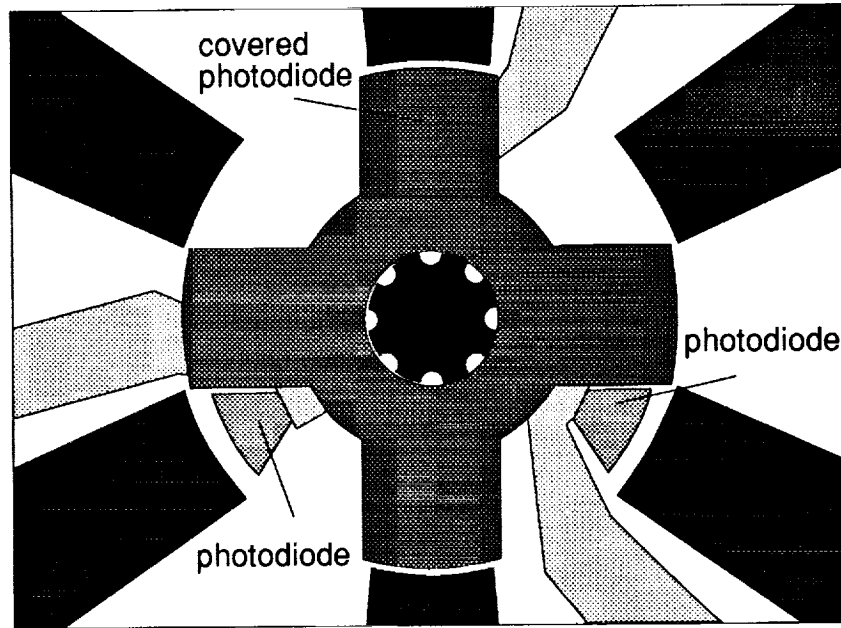
Figure 1. Stator, rotor, fluted shaft and photodiode layout.

The processing sequence starts with a 3" silicon substrate which is oxidized and patterned with the photodiode diffusion mask via standard IC-processing. The passivated substrate is next covered with a nickel layer which is patterned with the lower sections of the coil windings which will eventually surround the magnetic material. These coils will have to be insulated which implies a dielectric cover which in the present case is formed by a layer of chemical vapor deposited oxide. Both of these processes, nickel and oxide deposition, are more or less standard integrated circuit processing procedures; the same comment applies to the removal of the oxide over the nickel in the area in which the vertical sections of the coil are to be attached.

The procedures become unusual in the next sequence which deals with surface micromachining. A sacrificial layer of soft polyimide is applied and patterned in those areas of the wafer in which for instance free magnetic structures such as the rotor are to be produced. After this process the entire wafer is covered with a sputtered plating base: 150Å of titanium followed by 150Å of nickel. These procedures are again nearly routine IC-fabrication procedures.

Unusual processing which is related to the high structural height requirement starts at this point. The wafer is covered with a casted film of x-ray sensitive photoresist. The thickness of this layer is typically 300 micrometer which is of course very unusual for
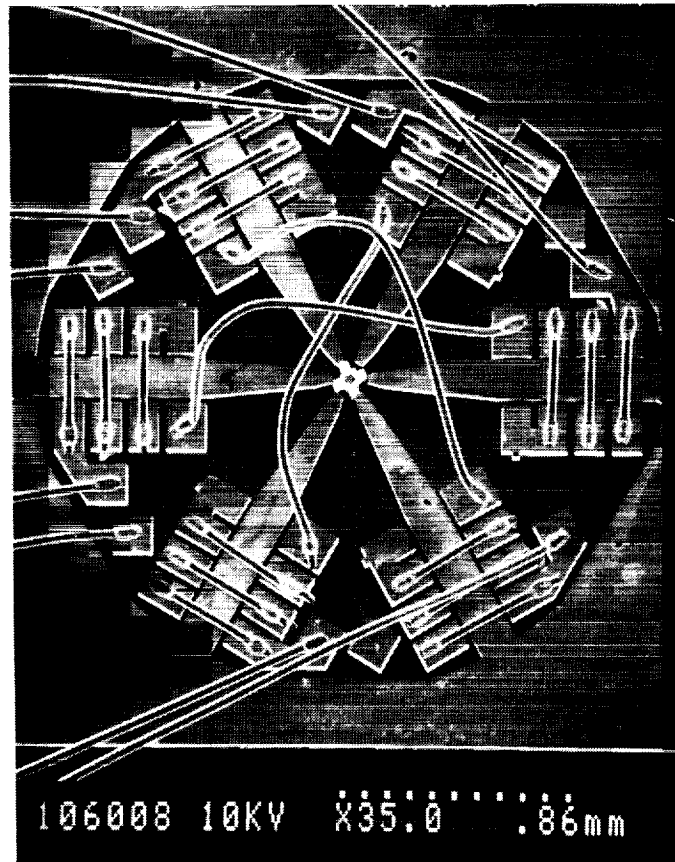
Figure 2. SEM photograph of completed integrated planar magnetic micromotor. The configuration is that of a 6 pole stator and 4 pole rotor stepping motor with six turns per pole pair.

photoresist thicknesses which are typically near 1 micrometer. The x-ray photoresist is exposed by using synchrotron radiation with wavelengths between 2 to 3 Å, through an x-ray mask which is aligned to the working substrate. Because synchrotron radiation is collimated very well and x-ray absorption cannot produce standing waves, developing of the exposed pattern produces a photoresist mold with nearly perfect definition and, in particular, pattern run-out of less than 0.1 μm per 100 μm of structural height. The developed mold recesses are next filled with electroplated metal: in the present case nickel or permalloy 80% Ni, 20% Fe. The x-ray photoresist is removed, any unwanted plating base is etched off and the sacrificial layer is chemically dissolved. The substrate now consists of fully attached parts such as the stator with partially finished coils and the center hub and of course free parts such as the rotor. The coils are completed by wire bonding with 30 μm diameter wire. The rotor is assembled to the shaft in a micromanipulator and the device as shown in Fig. 2 is ready for testing.

505

The actual design of a planar micromotor insists on closed magnetic circuits which are in the plane of the substrate. The total reluctance in this geometry involves not only the two air gaps between rotor and stator but also the reluctance of the rotor and the flux return path. Since the return path reluctance is parasitic on motor performance it must be minimized to obtain maximum gap flux. This minimization involves the magnetic properties of the material: a high permeability is desirable and the geometry: short path lengths with large cross-sections are favored. In this sense, the chip area which a motor for given torque output uses becomes very much a function of magnetic material properties.

The processing tool as discussed here can produce shaft to rotor clearances which are submicron. The reason for this is found in the fact that assembly implies shaft to rotor clearances which are obtained by subtracting two optically defined dimensions. These two individual dimensions cannot be submicron. However, their differences can. This observation together with the low flank run-out allows the fabrication of motor air gaps with demonstrated dimensions of less than 0.25 μm. This is advantageous from two perspectives: reduced friction due to precision bushings and large potential magnetic gap pressures. These large magnetic flux densities can, however, only be achieved if the return path reluctance is small in comparison to the gap reluctance. This condition has not been achieved with pure annealed nickel ferromagnetics. However, recent improvements in magnetic materials as shown in Figure 3 allow designs with magnetic flux densities in the gap of better than 3000 gauss.
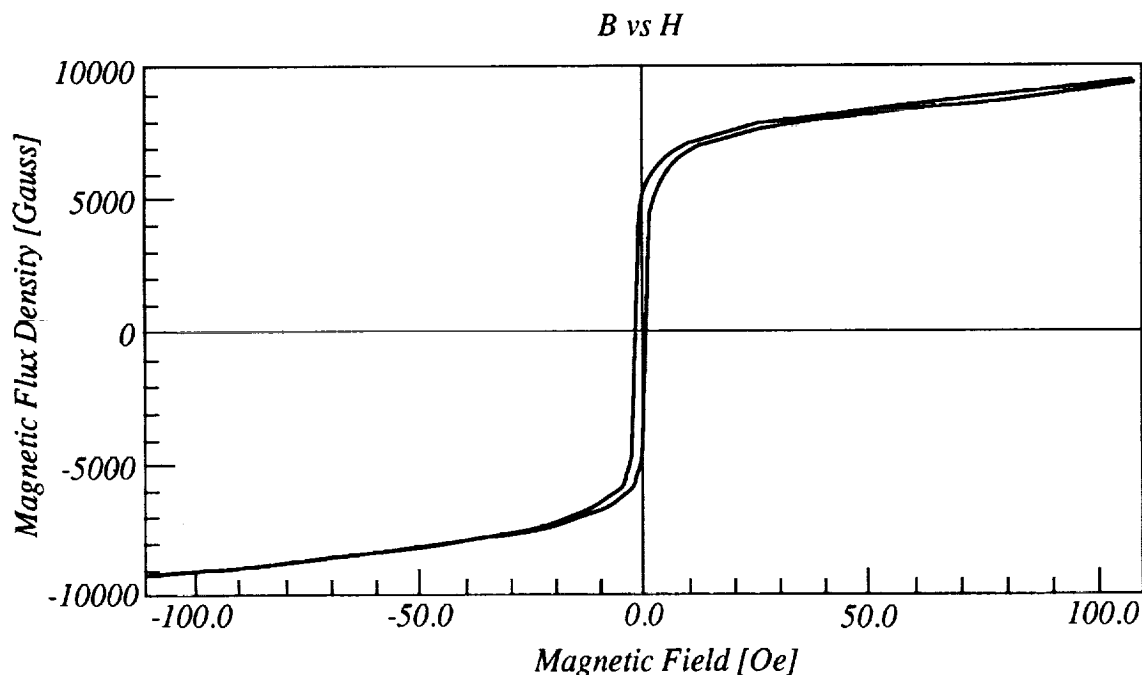
Figure 3. Magnetic behavior of as deposited 78Ni-22Fe permalloy.

In the current motor designs rotor thickness is less than stator thickness. This implies that the rotor will levitate in the stator field. The amount of levitation depends on the gap flux and the weight of the rotor. Self-centering can be achieved if the motor shaft is fluted and if the device is operated in modest pressure ambients. Theoretical analysis of the detailed rotor behavior requires at the very least a three-dimensional magnetic field analysis which can also estimate the motor torque output. This has been achieved by using Flux 3D[7]. The anticipated results are shown in Fig. 4.

$$Torque/mmf^2 \; [nNm] \; vs \; theta$$
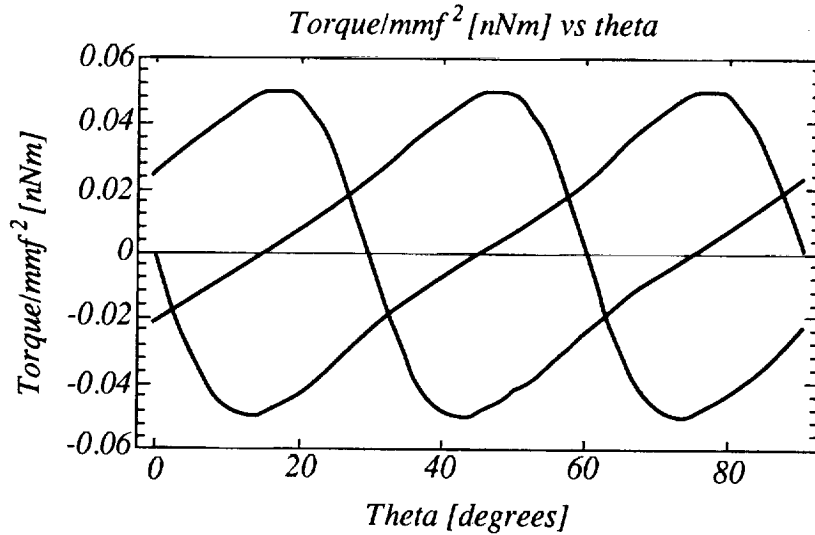
Figure 4. Simulated normalized torque curves for 90° of motor rotation. Stator-rotor alignment occurs at 0° and every 30° thereafter. These curves assume a square wave excitation. The current excitation waveform shape will modulate these torque curve shapes further. These curves apply to a motor which has a 285 μm diameter rotor, 80 μm in thickness centered about a stator of 160 μm thickness.

Software which can handle fluid mechanics and magnetics or mechanical deformation due to magnetic forces is not available. It would aid design tremendously.

TEST RESULTS

In order to test experimental structures the motors are packaged into flat packs as shown in Figure 5.
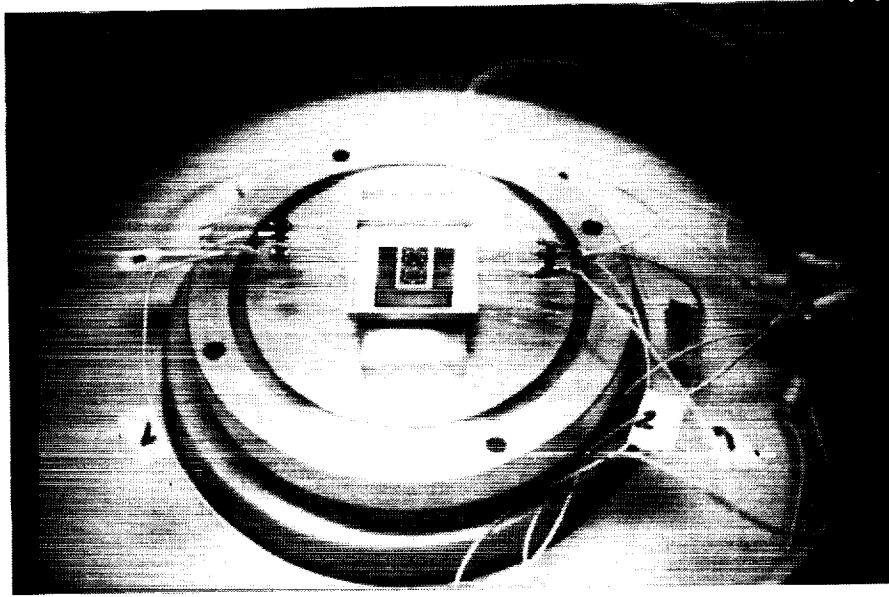
Figure 5. Packaged micromotor shown in vacuum system.

Motor behavior is studied via visual examination which typically involves video tapes. Much more detailed data is obtained from the photodiode shaft encoder. Both data sets result in the conclusion that this type of reluctance motor functions as a stepping motor with significant pole overshoot. This overshoot causes a loss of synchronization for open loop operation and therefore a maximum open loop rotational speed. The estimated failure frequency is given by

$$f_N = \frac{1}{2\pi} \left(\frac{T'}{J_R} \right)^{\frac{1}{2}} \tag{1}$$

Where T is the slope of the torque curve near rotor alignment and J_R the rotor polar moment of inertia[8,9]. Typical values for a 280 µm rotor which is 80 µm thick and is suspended in a 160 µm tall stator are $J_R = 1.7. \times 10^{-16}$ kg - m^2 if the shaft diameter is 72 µm with a torque slope of ... The predicted maximum rotational speed becomes 44,000 rpm. Experimental data resulted in a maximum speed of 33,000 rpm. A word of caution is in order: these speeds refer to open loop operation with non-overlapping square wave excitation on the three phases. For these test conditions which were performed in room air ambients frictional losses are roughly 0.5% of available torque. A comparison of room

ambient to vacuum operation did not change the upper speed significantly and produced no significant modification in the pole overshoot behavior. The frictional loss appears to come from shaft friction which is low because of shaft geometry and the inherently low radial forces for this type of machine. A new design with improved magnetic material and smaller rotor radius has been constructed. It is anticipated that rotational speeds above 100,000 rpm will be achieved.

Rotor levitation during these tests is roughly 45 µm. Substrate friction is therefore absent. Long term testing at maximum speed did not affect motor performance. Shaft wear via electron microscope examination was not detectable.

CONCLUSIONS

Planar reluctance motor design, construction and testing have been accomplished in the presence of a one-dimensional magnetic bearing and integrated shaft encoder. Experimental and theoretical performance are in rough agreement.

The use of micromotors for very high speed operation hinges on two issues: torque ripple and friction. Torque ripple is inherent to reluctance motors which are expected to peak out between 100,000 and 200,000 rpm. This class of motors will therefore not achieve very high speed directly but could do this by step-up gear boxes and closed loop control. Other motor types, for instance hysteresis motors, have inherently less torque ripple and are currently under investigation[10].

Frictional losses must be reduced significantly for high speed devices. This can be accomplished by two methods: a true magnetic bearing for which the position sensors have already been demonstrated or a form of non-contact bearing which is unique to micromechanics. Both approaches are under active investigation.

The available torque output from micromotors, currently 20×10^{-9} Newton - meter, can be improved significantly. If this torque is available with minimized ripple and non-contact bearings, micromotors will approach Beams's experimental results. Ramp speeds which in Beams's case involved several days to reach maximum speed will be comparable and acceptable even if modest angular momentum storage devices are to be driven by this type of machine.

ACKNOWLEDGMENTS

REFERENCES

[1] E.W. Becker, W. Ehrfeld, P. Hagmann, A.Maner, D. Münchmeyer, "Fabrication of Microstructures with High Aspect Ratios and Great Structural Heights by Synchrotron Radiation Lithography, Galvanoformung, and Plastic Moulding (LIGA Process), " *Microelectronic Engineering*, 4, 1986, pp. 35-56.

[2] H. Guckel, T. Christenson, and K. Skrobis, "Metal Micromechanisms via Deep X-Ray Lithography, Electroplating, and Assembly," Proceedings of Actuator '92, Bremen, Germany, June 1992, pp. 9-12.

[3] H. Guckel, T.R. Christenson, K.J. Skrobis, T.S. Jung, J. Klein, K.V. Hartojo, and I. Widjaja, "A First Functional Current Excited Planar Rotational Magnetic Micromotor," Proceedings of IEEE Micro Electro Mechanical Systems (MEMS '93), Fort Lauderdale, FL, USA, Feb. 1993, pp. 7-11.

[4] H. Guckel, T.R. Christenson, K.J. Skrobis, J. Klein, and M. Karnowsky, "Design and Testing of Planar Magnetic Micromotors Fabricated by Deep X-Ray Lithography and Electroplating," in Digest of Technical Papers, 7th International Conference on Solid-State Sensors and Actuators-Transducers '93, Yokohama, Japan, 7-10 June 1993, pp. 76-79.

[5] J.W. Beams, "High-Speed Rotation," Physics Today, July 1959, pp. 20-27.

[6] C.K. Taft, R.G. Ganthier, T.J. Harned, *Stepping Motor System Design and Analysis*, University of New Hampshire, 1985.

[7]   Magsoft Corporation, FLUX3D, Troy, New York.

[8]   Y.C. Tai and R.S. Muller, "IC-Processed Electrostatic Synchronous Micromotors," Sensors and Actuators, 20, 1989, pp. 49-55.

[9]   J. Cemus and V. Hamata, *Transient Stability Analysis of Synchronous Motors*, New York: Elsevier, 1990.

[10] B.R. Teare, Jr., "Theory of Hysteresis - Motor Torque," AIEE Transactions, Vol.59, 1940, pp. 907-912.

ELECTROSTATICALLY SUSPENDED AND SENSED MICRO-MECHANICAL RATE GYROSCOPE

$S_6 - 35$

$1/9/4$

$P - 13$

R. Torti, M. Gerver, V. Gondhalekar, S. Bart, B. Maxwell

SatCon Technology Corporation
12 Emily Street
Cambridge, MA 02139

SUMMARY

The goal of this work is development of fully electrostatically suspended and rebalancing angular rate sensing micro-gyroscope fabricated according to standard VLSI techniques. Fabrication of test structures is proceeding. Off chip electronics for the electrostatic sensing and driving circuits has been tested. The prototype device will be assembled in a hybrid construction including the FET input stages of the sensors.

INTRODUCTION

SatCon Technology is currently in the design and fabrication phase of a proof of principle, fully electrostatically suspended and rebalancing angular rate sensing micro-gyroscope. The structure will be fabricated according to current VLSI micromachining methods. Performance targets include angular rate sensitivity of 0.01°/s at 100 Hz for 8.3 kHz (revolutions/s) spin rate. The program is supported under contract by NASA-Langley Research Center (# NAS1-19590) as a Phase II SBIR.

To date, a set of test microstructures designed in-house has been fabricated by a VLSI supplier, prototype capacitive sensing electronics and rotor drive electronics have been tested, and the design and analysis of structures suitable for a prototype gyro is underway.

APPROACH

Micro-electronic fabrication technologies have recently been applied to produce novel micro-mechanical devices such as motors, pressure sensors, and linear actuators. Their small size, integration compatibility with electronic circuits, and potential low cost invite research. The micro-mechanical gyroscope, proposed for this research effort, is a device that would have application to aerospace, commercial, and military systems. The final instrument goal is shown in Figure 1 and would consist of entirely integrated electronics and RF signal transmitter and lithium battery for a long-life, wireless accelerometer and rate sensor.

The prototype goal for this work, however, is more modest. As shown in Figure 2, the
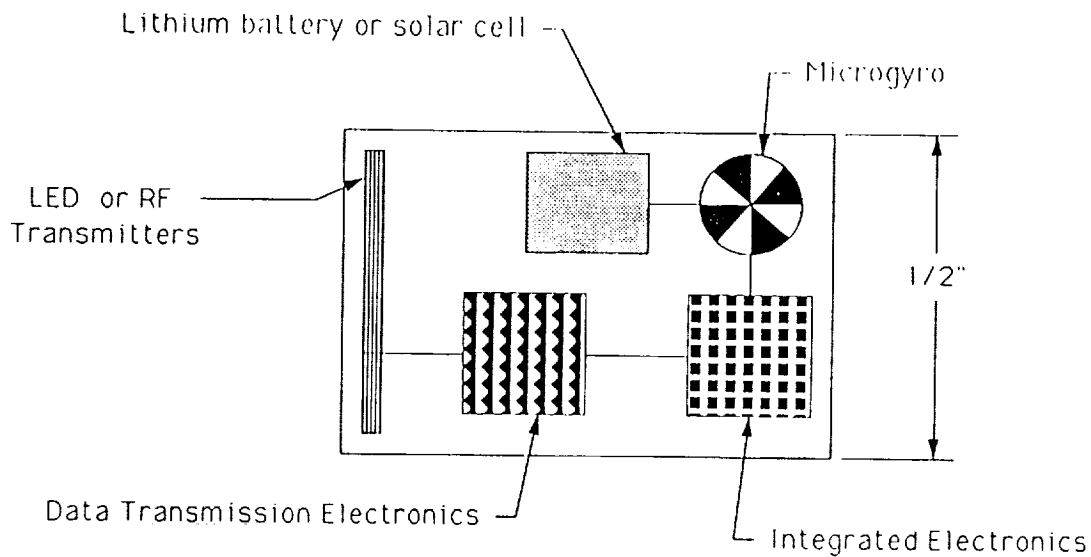
Figure 1. Integrated Microgyro Concept.

mechanical gyro structure would consist of a VLSI fabricated multi-layer polysilicon. The essential geometry is a circular disc rotating at 8 kHz and driven, suspended, rebalanced, and sensed completely electrostatically. This structure or set of structures will be at the center of and connected to a hybrid structure which includes the FET front ends of the capacitive sensor set. Drive electronics and the sensor filters and demodulators will be off chip.
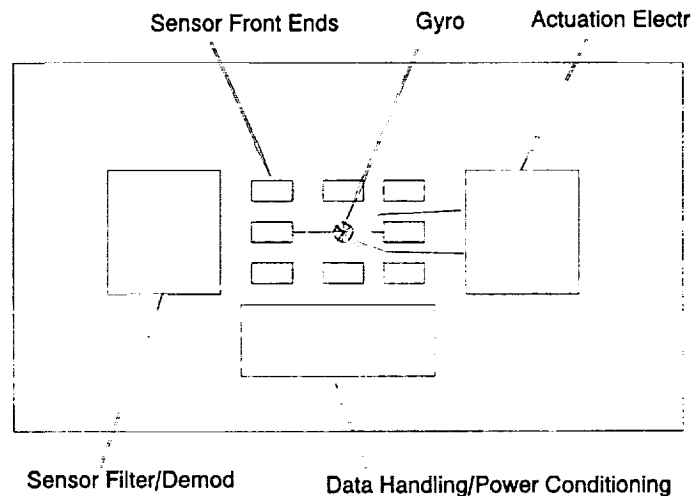
Figure 2. Configuration of Prototype Micro-Gyro.

A "rebalanced" gyroscope has a control system designed to hold the gyro in a constant position while it is subject to external forces. Since the controlled mass (the gyro rotor in this case) is held to a nearly constant position, the linearity of the sensors and actuators is improved, and the overall dynamics are simplified. A block diagram of the gyro system is shown in Figure 3.

514
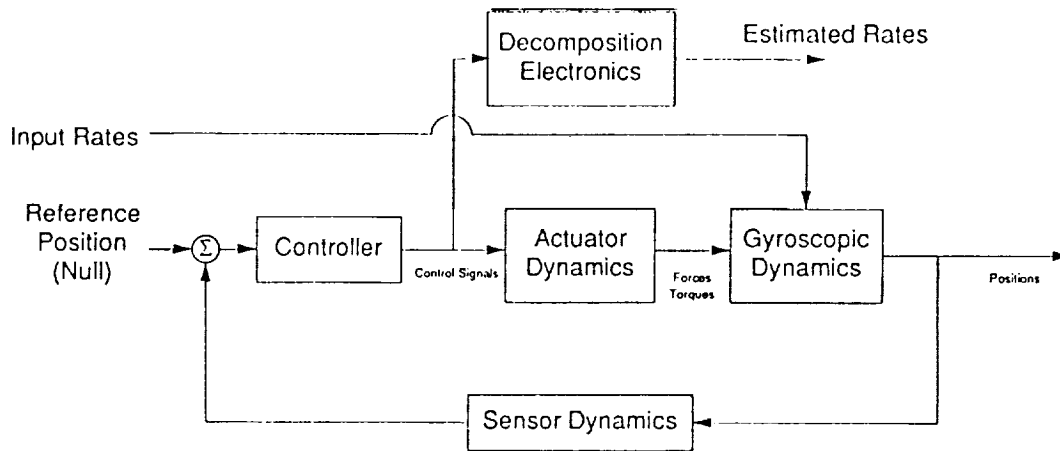
Figure 3. Microgyro Block Diagram.

Angular rotations of the gyro support frame cause torques to be applied to the rotor. The mechanical dynamics of the rotor transform these forces and torques into rotor displacements. Sensors determine these displacements in relation to the reference position and the resulting error signal is sent to a control system. The control system sends the appropriate signals to the actuators, returning the gyro to a null position. Knowledge of the actuator dynamics allows the input rates to be estimated from the actuator control signals.

The device consists of three types of electroquasistatic components - the motor drive, position sensors, and the non-rotary actuators for rebalance and suspension. As with suspended macroscopic gyros, the rotor is spun by a motor to produce angular momentum, suspended and controlled by force and torque actuators, and sensed by various position sensors.

Position control must be effected in both axial and radial directions requiring four sets of actuators, two for the upper and lower axial suspension and two for upper and lower radial rebalance actuator/sensors - and the motor driver actuator. These may be combined so that electrodes are shared. Each active conductive layer of the rotor is composed of structural polysilicon and separated from the other conductive layers by an insulating silicon nitride layer.

Capacitive sensing is used throughout with all sensor electrodes placed below the rotor away from actuating electrodes. The sensors are driven at 100 kHz by SatCon designed electronics.

SPECIFICATIONS AND CONFIGURATION

In order to reduce the complexity of the VLSI and utilize well developing processing techniques, we have reduced the rotor structure geometry to a two layer polysilicon construction sandwiching a thin insulating layer. A total of three polysilicon and three nitride layers are required above the electrodes placed over the substrate. This will reduce the complexity of the control system requirements as well as allow sensing at higher signal to noise ratios.

This design is shown conceptually in Figures 4, 5 and 6. All sensing electrodes will be placed below the rotor over the substrate either as an ion implanted pattern or a "polysilicon #0" layer over nitride. Sensors will detect capacitance between a pair of active electrodes and the disc underside of the rotor. The outer rings (Figure 4) will sense radial deflections in two directions while the inner rings will detect tilting. The upper rotor electrodes will be articulated. Radial forces will provide combined drive torque and radial actuation, while the overhanging axial electrodes will couple with the large area electrodes to provide tilt correction. A variety of geometries will be included on the die.

Cutaway View of Fully Suspended Geometry
Showing Stator Electrode Pattern on Substrate

Axial Sense Electrode

PS#3
PS#2
PS#1

Tilt Sensing Electrodes

Radial Positioning Sense Electrodes
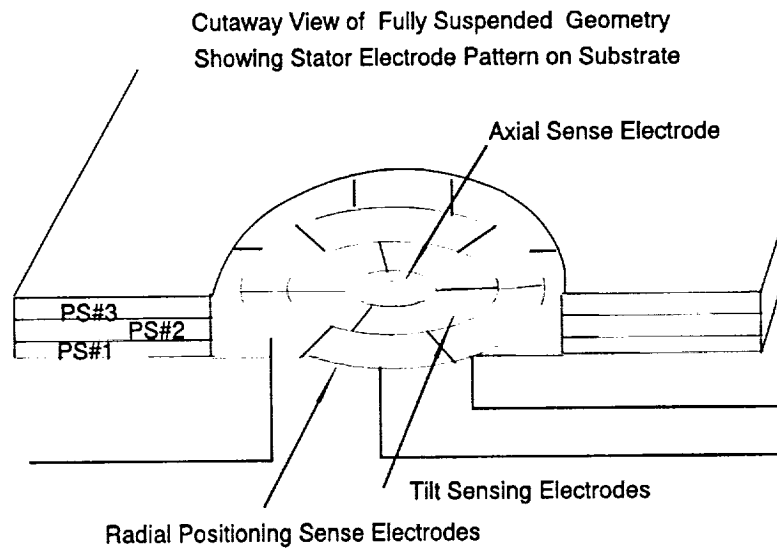
Figure 4. Full Suspended Geometry Showing Sensing Electrodes.

Cutaway View Showing Rotor
and Overhanging Tilt Actuators

Fully Suspended Rotor With Polysilicon Pattern
for Axial and Radial Actuation
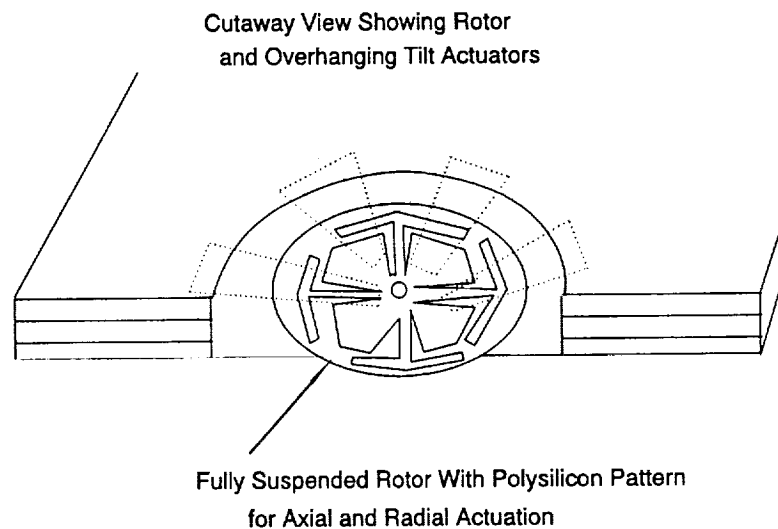
Figure 5. Fully Suspended Geometry Showing Rotor Electrodes.

Upper Axial Actuator   Insulating Layers

Upper Radial Actuator/sensor

Motor Actuator

Lower Radial Actuator/sensor

Implanted/Diffused Lower Electrodes
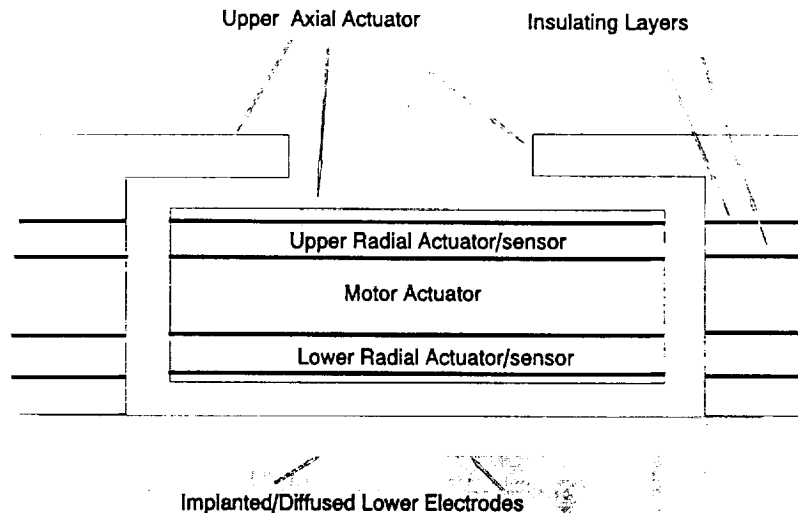
Figure 6. Cross Section Fully Suspended Geometry.

Sizing

The target rotor diameter, 200 μ, was chosen as the largest size that could be fabricated without significant warpage due to residual stress buildup during fabrication. The rotation rate is constrained by stress limits in the rotor and electronics limits in the motor driver circuitry. A rate of 500,000 rpm (8.3 kHz) was chosen as a reasonable extension of current motor rates (about 20,000 rpm). This is well below the ultimate spin rate (about 10,000,000 rpm) determined by material strength limits.

The fabrication of this design requires a total of three layers on the rotor. The top structure which contains the topology for both the upper actuators and the radial and drive actuators should be at least 1-2 μm thick for reasonable actuation forces. The insulating nitride layer can be much thinner than this, say 0.2 μm. The lowest layer (polysilicon) used for sensing interacts axially with substrate pattern and therefore can be as thin as can be stably fabricated.

The axial gap between substrate and rotor is nominally 2 μ. This represents a tradeoff between gap capacitance and rotor unstable frequency but is also influenced by VLSI fabrication considerations. A smaller gap would make sensor measurements more accurate at the cost of raising the unstable frequency and complicating the control problem. The 2 μ gap gives a 300 Hz unstable frequency.

SENSORS

The position sensor mechanism is the electrostatic detection of capacitance. The electrode pattern in the substrate provides enough electrodes to discern radial position and angle, tilt off

rotation axis and overall axial position. Capacitive position sensing is commonly used in macroscopic devices, and has also been successfully applied to other micromechanical devices. The basic concept is to drive a constant current across an air gap (whose capacitance varies inversely with gap distance) and read the resulting voltage which is linearly proportional to the gap. High frequency modulation and demodulation allow good noise immunity. Though the capacitance of the microgyro axial gap will be very small (about 10^{-14} farads), the placement of FETs via a hybrid construction on the silicon substrate as preamplifiers in conjunction with guard wires to the sensing electrodes will allow the dynamic range required to meet the resolution requirements.

ELECTRONICS

Sensor Electronics

The capacitance of the position sensor varies inversely with the distance from the sensor to the target with detectable variations of the order of 10^{-17} F. Any stray capacitance on the sensor leads will affect the linearity of the measurement unless the leads are appropriately guarded. The ability to detect position accurately is also hampered by any load placed on the sensor capacitance by the measurement electronics.

Electrostatic Sensor/Actuator Circuitry

Referring to Figure 7 we see that U12 is VCO/Function Generator IC with triangle, square, and sine wave outputs. R34 and R35 determine the charge-up and charge-down currents into C35. The charge-to and charge-from voltage levels are set by internal references in the ICL8038. This gives a charge/discharge time τ from $E = I\tau/C$ which sets the frequency for a triangle wave. This triangle wave is the input to a diode break point sine wave function generator. Trim Pots R31, R34, and 37 are adjusted to minimize sine wave distortion.

Q1 is a programmable zener diode, which is set up for -5 v. The -5 v. is one end of a 10-turn Pot (R2) and ground is the other. The wiper of the Pot is buffered by U1, and summed with the sine wave from U12 into U2. The Q1, U1, R2 circuit's output is the electrostatic levitation voltage for the rotating disc. Summation output from U2 is the input to U3, which drives one side of a 5 MΩ resistor and one input of a differential amplifier U5.

The other side of the 5 MΩ resistor is connected to the active electrode of the "Cap Gauge" and the input of a low input capacitance unity gain amplifier. Q2, Q3, Q4, Q5, Q6, U4, and U6 are used to implement the low input capacitance unity gain amplifier. Q2A and Q2B are the input differential source followers. Their source impedances are two 200 micro-amp current sources Q4, Q5 and Q6. The source follower's source voltage follows changes in gate voltage (input) by the relationship $g_mR_l/(1+g_mR_l)$. The greater the product g_mR_l, the more closely the source follows the gate. R_l in this case is a current source with an output impedance greater than 2 MΩ and the g_m of the FETs is greater than 1000 μmhos, so the source should follow the gate to better than 1 part in a thousand, which means the effective gate-to-source input capacitance is reduced, first order, by a factor of 1000.

518

Figure 7. Schematic of Capacitive Sensing/Electrostatic Actuation Electronics.
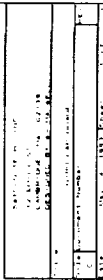
The sources of Q3 are connected to the drains of Q2, and its gates are connected to the sources of Q2. G_{os} of C2 is less than 2 μmhos, so R_l for source followers Q3 is greater than 500 kΩ which means the drains of C2 will follow the gates of C2 to one part in 500, thus reducing input gate to drain capacitance. With careful layout and guarding a total input capacitance of 50 fF is achievable.

Q2's sources are connected to the inputs of U4, whose output is connected to the input of U6, a high output current buffer. The output of U6 is fed back to the gate of Q2B (amplifier inverting input) to implement unity gain for low capacitance amplifier. U6's output drives the active plate guard, and is fed back to the inverting input of U3, so that the summation output from U3 maintains the summation at the cap gauge active plate. Also, U6's output is connected to the remaining input of differential amp U5. The current that flows through the capacitor which is defined by the active plate area and the distance to the current return plate flows through the 5 MΩ resistor to generate a voltage across the 5 MΩ resistor. This voltage is indirectly measured by differential amp U5. It is proportional to the defined capacitor, and inversely proportional to the distance between the active area plate and the return plate.

The output of U5 is connected to the U7 input of a second-order bandpass filter centered at U12's sine wave frequency. A full wave rectifier (U8, U9, and associated components) rectifies the output of the Band-Pass filter. The rectified signal is then subjected to a 4-pole low-pass filter (U10, U11, and associated components). The output of the 4-pole filter is a DC signal with less than 0.1% carrier ripple.

Motor Drive Electronics

The gyro wheel-motor is a three-phase bipolar variable-capacitance motor. Since this motor type is synchronous, i.e., produces torque only when the rotation frequency and excitation frequency are the same, it requires a variable-frequency drive source. In addition, the push-pull excitation required for each of the three bipolar phases will require six high-voltage output stages. The motor is driven with balanced bipolar voltages so that the rotor will remain near zero potential so that the axial actuators will not require a large DC bias.

Motor start-up will require that the excitation frequency start at the sub-Hertz level and ramp up to the full-speed value of 25 kHz. This is accomplished with a ramp generator and voltage-to-frequency (V/F) converter. The bipolar three-phase generator takes the single-phase output of the V/F converter and produces three square-waves with 120 degrees phase difference and their complementary signal for driving the output stages. In addition, the circuit generates the signal pair which develops the bipolar waveforms. The output circuit contains six high-voltage drivers, one for each bipolar phase, and can deliver up to 120V.

CONTROL DESIGN

One of the goals of the controller is to keep the orientation of the rotor fixed, in the null position, relative to the orientation of the "stator" frame of the gyroscope. In addition, the

C-2

controller must provide accurate measurement of the torque that is required to maintain the rotor in the null relative orientation. As usual, the simplest controller that can meet the performance objectives is desired in order to minimize hardware complexity. In particular, a fixed-gain, linear controller is desired that can be easily implemented in analog electronics. This will force some performance and stability robustness tradeoffs, in particular because the plant dynamics are a strong function of the operating speed and are open-loop unstable. Because of the open-loop unstable nature of the plant -- an inverted pendulum at low speeds -- closed-loop control is required from zero speed to the full operational speed. The challenge, then, is to find a fixed gain controller that will provide adequate performance at all speeds.

Modeling

Three sources of torque will be considered in this model, the gravity torque, the motor radial torque, and the actively controlled torque produced by the electrostatic actuators. The motor produces a stabilizing or restoring radial torque. For small angles, this can be linearized to give a stabilizing radial torsional spring. The torsional spring constant for motor under operating voltages is expected to be $\approx$ -1 x 10^{-13} Nm/rad.

The electrostatic actuators are voltage biased to provide a linear relation between input voltage and torque. The linearized model of these actuators includes, in addition to the voltage induced torque, an "unstable" spring torque that is proportional to the relative orientation of the rotor to the "stator" frame. The unstable torsional spring caused by the actuator (with an associated unstable frequency of 300 Hz) is seen to dominate the stable torsional spring caused by the motor (with an associated stable frequency of 71 Hz).

Open-Loop Dynamics

The variation of the plant dynamics from zero speed to operational speed of 500,000 rpm (8,333 Khz) is dramatic. At zero speed, the plant is a two-degree-of-freedom unstable pendulum. The two by two plant transfer function matrix relating control voltage inputs to rotor orientation output becomes diagonal in this case, with no cross-coupling between the x-direction tilt dynamics and the y-direction tilt dynamics. At zero speed, therefore, the plant can be treated as two identical single-input, single-output (SISO) systems. At frequencies below 300 Hz, the dynamics of this parallel or diagonal transfer function are seen to be dominated by the unstable torsional spring produced by the combination actuator and motor torsional effects. The unstable spring produces the flat low frequency magnitude response between input voltage (torque) and output orientation (angle) with the 180 degrees of phase indicating an unstable spring. At frequencies above the 300 Hz unstable frequency, the transfer function falls off with a slope of minus two, caused by the double integration of torque to angle, and scaled by the voltage to torque constant and the radial moment of inertia of the rotor.

At full speed (500,000 rpm or 8,333 Hz) the plant dynamics are dominated by gyroscopic effects. Because of the x-y symmetry, the two diagonal or parallel transfer functions (x voltage to x orientation and y voltage to y orientation) are the same. Similarly, the two off-diagonal or cross-coupling transfer functions (x voltage to y orientation and y voltage to x orientation) are also the

same. The plant is completely characterized by two transfer functions, the parallel (diagonal) and cross (off-diagonal) transfer functions.

Controller Design

The design approach to develop a fixed-gain controller for this speed varying plant was to first examine how optimal, full-state feedback controllers change with changing plant speed. This full-state feedback controller is then implemented as an output feedback controller using lead-lag compensators to provide estimates of the velocity states.

The first step in this design approach was to develop full-state feedback controllers for various operational speeds. These full-state feedback controllers were designed using the linear-quadratic-regulator (LQR) approach. This controller is the "optimal" initial condition regulator, which closely matches the regulator type performance goals of the controller for the micro-gyroscope.

Both the zero-speed, and full-speed state feedback compensators suffer from performance problems when used over the full speed range. The zero-speed state-feedback compensator exhibits slow decay time and low-bandwidth at full-speed. The full-speed state-feedback compensator becomes unstable at low speeds. By using a combination of these compensators, however, a tradeoff can be effected between high-speed performance and low-speed stability. This procedure involved iteratively trying linear combinations of the zero-speed compensator. The design parameters are the ratio of zero-speed to full-speed feedback gains, and the compensator bandwidths controlled by the cost-on-control-weighing parameters. These parameters were iterated to yield a state-feedback compensator with a minimum of 1000 Hz bandwidth and the largest minimum decay time over the whole speed range. In addition, the ratio between zero-speed and full-speed bandwidth was keep under a factor of 10.

The resulting "best" compensator uses less parallel-proportional gain than the zero-speed design and less cross-proportional gain than the full-speed design. The resulting closed-loop root-locus versus rotational speed is shown in Figure 8 along with the zero-speed case. The "best" compensator has improved damping and decay time compared to the zero-speed case.

Sensor Testbed

A set of structures compatible with the first multi-user run[1] at MCNC was designed around a single nitride, two layer polysilicon process. Masks for key structures and a view of the results are shown in Figures 9 and 10. The rotor geometries will allow testing of the accuracy and response of capacitive sensing circuitry and the effectiveness of guarding and the response to actuation voltages. Additionally, they will serve to acquaint us with the techniques of driving, manipulating, and evaluating micromechanical structures.

522
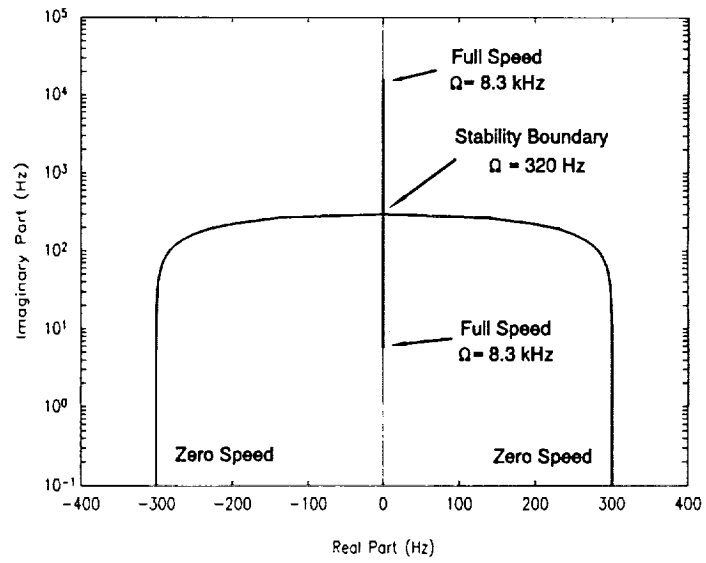
Figure 8. Root-locus of Plant Eigenvalues versus Rotational Speed.
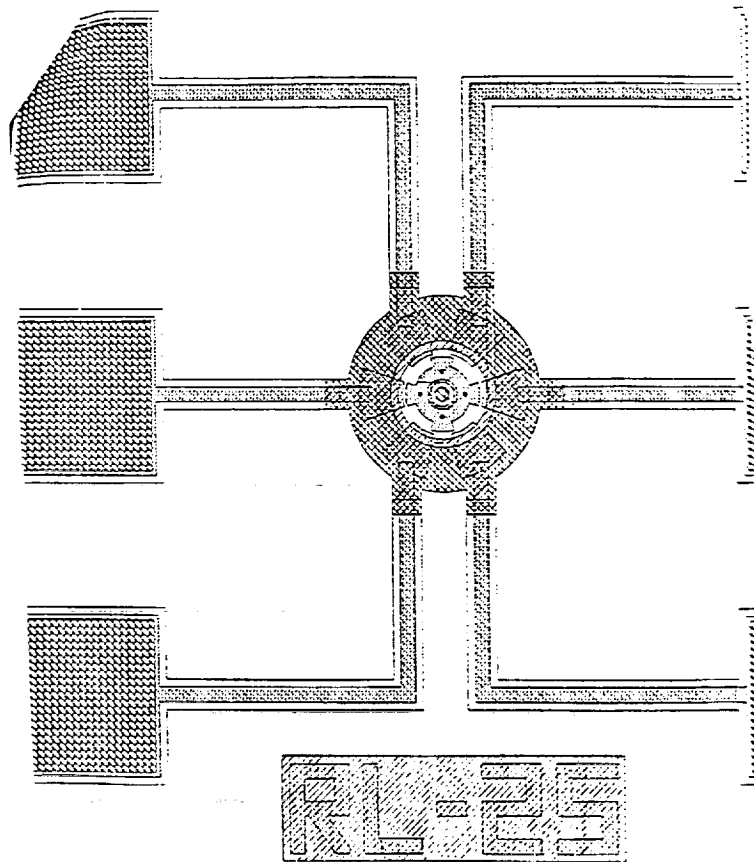
Figure 9. Composite Mask of Bushed Motor.
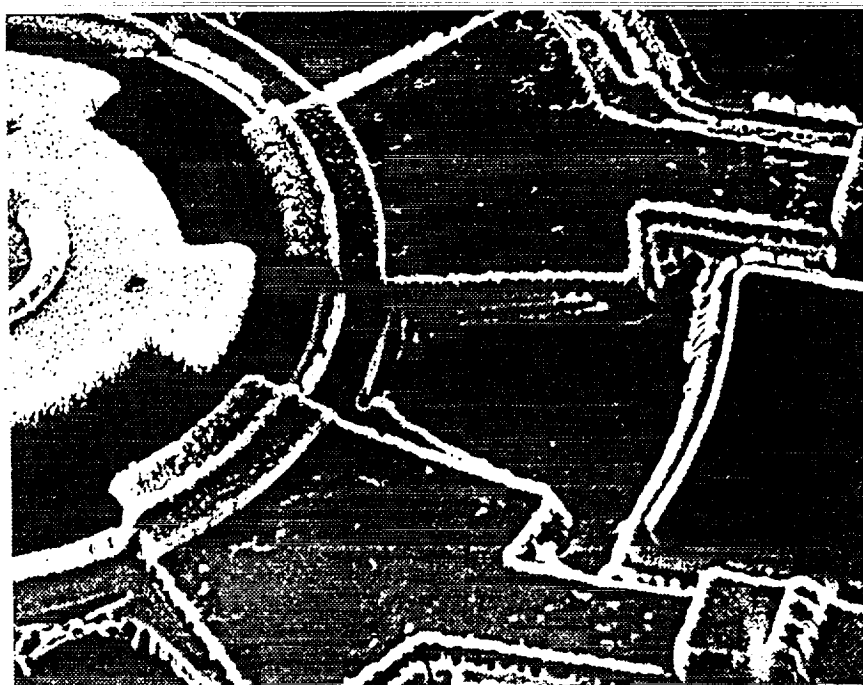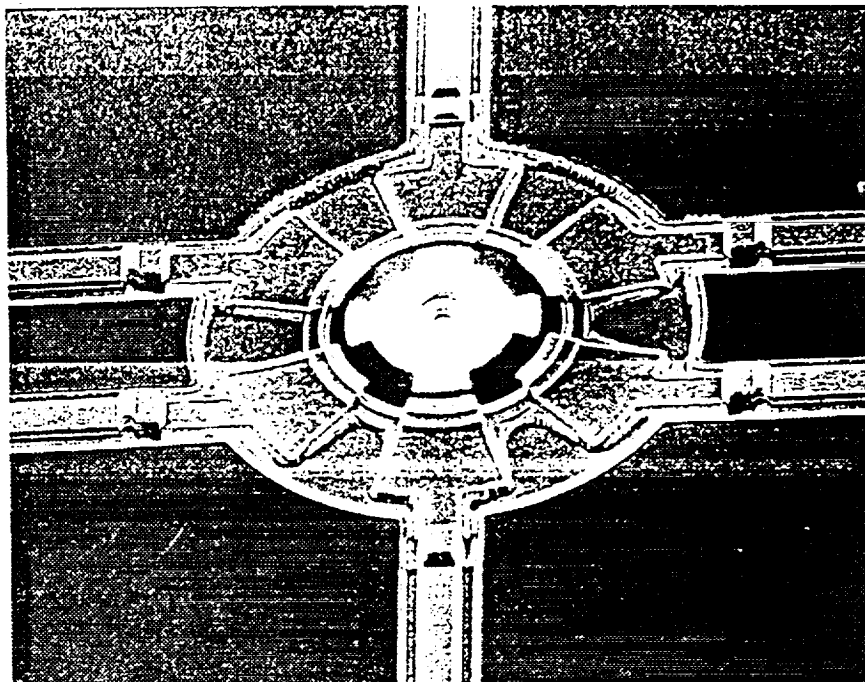
Figure 10. SEM of VLSI Fabricated Motor.

Performance Specifications

A summary of system parameters is given in the table.

Table 1. Microgyro Performance Specifications

Spin Angular Speed	8.3 kHz (500 kRPM)
Spin Moment of Inertia	1.5×10^{-18} kgm-m^2
Precession Moment of Inertia	8×10^{-19} kgm-m^2
Minimum Angular Rate	0.01°/s
Thermal Sensor Noise	$< 0.4 \times 10^{-3}$ v
Angular Sensitivity	$< 0.008°$
Thermally Limited Rebalance Rate	100 Hz
Sensor Electrode Capacitance	$\sim 3 \times 10^{-14}$ F
Sensor Operating Current (0.5 V)	$\sim 0.4 \times 10^{-9}$ A
Nominal Drive Actuator Potential	5 v
Drive Torque Per Pole	10^{-11} N-m
Viscously Induced Torque	$< 10^{-11}$ N-m
Spindle Friction Torque	0.2×10^{-12} N-m
Rotor Radius	100 μm
Radial Gap	2.0 μm
Vertical Gap	2.0 μm
Rotor Thickness	2.0 μm
# Stator Poles	6
# Rotor Poles	4
Nominal Gap Voltage	0.5 v

1. DARPA sponsored at Microfabrication Center, Research Triangle Park, NC. Dies were delivered in April.

Session 9b – Rotating Machinery and Energy Storage

Chairman: Chin E. Lin
National Cheng Kung University

CONCEPTS OF FLYWHEELS FOR ENERGY STORAGE USING
AUTOSTABLE HIGH-T$_c$ SUPERCONDUCTING MAGNETIC BEARINGS

H. J. Bornemann, R. Zabka, P. Boegler, C. Urban and H. Rietschel
Kernforschungszentrum Karlsruhe GmbH
Institut für Nukleare Festkörperphysik
P.O. Box 3640, D-76021 Karlsruhe, Germany

SUMMARY

A flywheel for energy storage using autostable high-T$_c$ superconducting magnetic bearings has been built. The rotating disk has a total weight of 2.8 kg. The maximum speed is 9240 rpm. A process that allows accelerated, reliable and reproducible production of melt-textured superconducting material used for the bearings has been developed. In order to define optimum configurations for radial and axial bearings, interaction forces in three dimensions and vertical and horizontal stiffness have been measured between superconductors and permanent magnets in different geometries and various shapes. Static as well as dynamic measurements have been performed. Results are being reported and compared to theoretical models.

INTRODUCTION

In times of rapidly increasing energy consumption, facing an impending shortage of natural resources for energy production, the need has arisen for highly efficient, regenerative energy storage systems. Energy can be stored in the form of chemical (e.g. batteries), thermal (e.g. latent heat), electromagnetic and mechanical energy. Applications of mechanical energy storage devices include compressed gas facilities, pumped hydroelectric storage and flywheels. A flywheel stores energy in the form of kinetic (rotational) energy. Whereas each energy storage system has its inherent advantages and disadvantages compared to the others, it is the overall system performance and simplicity of flywheels that make them especially useful for a variety of applications.

With the introduction of magnetic bearings which allow frictionless, non-contact support of a rotating body, the efficiency of flywheels for energy storage for which reduced friction is of crucial importance could be increased consid-

erably. The bearings have been developed over the last years for applications that are exceptionally critical concerning friction and/or wear. In the field of power systems, such applications include, in addition to flywheels, all cold machines for which wear is a considerable problem such as generators, motors and cold compressors.

However, these configurations which involve permanent magnets and coils are intrinsically unstable due to Earnshaw's theorem [1-3]. Therefore, at least one component has to be adjusted continuously. In order to function, these active magnetic bearings require elaborate control systems. The reduction of the complexity and cost of such control systems as well as the increase in reliability of these bearings are still points of major concern in the field.

On the other hand, such drawbacks can be avoided with completely passive autostable magnetic bearings involving superconducting materials combined with permanent magnets. The high-temperature superconductor $YBa_2Cu_3O_7$ (YBCO) looks especially promising because it requires cooling by liquid nitrogen (T=77 K) only. In contrast, conventional superconductors have to be cooled by liquid helium which adds considerable cost and complexity to practical applications.

In small magnetic fields, superconductors can prevent magnetic field penetration absolutely, which is known as the Meissner effect [4]. In this situation a magnet can levitate above a superconductor and vice versa. However, the interaction is relatively weak which limits the range of possible applications. Much stronger levitation forces can be obtained in high magnetic fields, when the superconductor exhibits pinning.

With increasing magnetic field strength H, the field starts to enter the superconductor in the form of magnetic flux bundles. The field where the transition takes place is called the lower critical field H_{c1}. For superconducting YBCO $H_{c1} \approx 100$ Oe at 77 K. Type II superconductors, also called hard superconductors, have the ability to pin those flux lines. Inside the superconductors the flux bundles are shielded by ring currents flowing throughout the volume and the gradient of the magnetic induction B is proportional to the critical current density J_c. The superconductor is in the critical state or Shubnikov phase. It is because of the pinning effect that melt-textured YBCO exhibits considerable levitation forces in high magnetic fields. The dc magnetization M is irreversible over an extended magnetic field range, resulting in a magnetic hysteresis loop. According to Bean's law [5], for a given value of the magnetic field H, the difference in magnetization, M_+-M_-, is proportional to the

critical current density J_c and to the size of the shielding current loop d

$$M_+-M_- \sim J_c \cdot d \qquad (1)$$

Here, M_+ and M_- are magnetization values obtained for the ascending and descending branch of the hysteresis loop, respectively, d is the diameter of the current loop. In one dimension, the levitation force F can be written as

$$F \sim M \cdot V \cdot grad(H) \qquad (2)$$

where V is the volume of the superconductor and grad(H) is the field gradient produced by a magnet. Together with eqn. (1) it follows that large levitation forces are obtained in high magnetic field gradients for superconducting materials that exhibit large values of both the critical current density J_c as well as the size of the shielding current loop d.

In superconducting YBCO J_c is localized in individual grains. Therefore large levitation forces require samples with large grains (large d) which exhibit strong pinning forces (large J_c). Murakami et al. developed the so called MPMG (Melt Powder Melt Growth) process [6] which allows fabrication of well-textured, large grain YBCO samples with large J_c values and strong pinning forces. The material exhibits considerable levitation forces as demonstrated by levitating a person on a disk with 200 Nd-Fe-B magnets embedded (total weight, person+disk was 1100 N) above 200 melt processed YBCO superconducting pellets [7].

We have investigated concepts of flywheels for energy storage using autostable high-temperature superconducting magnetic bearings. Static as well as dynamic interaction forces between melt-textured superconducting materials and permanent magnets have been measured. Results are being reported and compared to theoretical models.

EXPERIMENTS

Samples were prepared using commercially available YBCO powder [8]. The process used is similar to the melt process (Melt-Texture Growth, MTG process) originally devised by Jin et al. [9] and further developed by Salama et al. [10] and by Hojaji et al. [11]. We made the following modifications: Instead of adding Y_2BaCuO_5 to the starting material, we added finely ground Y_2O_3 powder. The first step of the MPMG process - heating to 1400 °C with a subsequent quench - was omitted. In addition to Y_2O_3, Ag_2O was added to avoid the formation of cracks. A detailed descrip-

tion of the process will be published elsewhere. Compared to MPMG, our process is shorter and simpler and therefore it can easily be scaled up to industrial production which requires a direct, reproducible process for sample production on a routine basis.

Pellets were mainly produced in two standard sizes: Small size (ϕ 14 mm, mass $\approx$ 14 g) for control samples to optimize the melt-texture process and large size (ϕ 38 mm, mass $\approx$ 100 g) for levitation force measurements and for applications such as in prototype bearings.

Samples were characterized with respect to macrostructure (e.g. grain size, twin structure, precipitates), microstructure (e.g. grain boundaries, inclusions, defects), critical currents and pinning properties. Characterization in terms of macrostructure was carried out with a polarization microscope. Phase purity was checked on a routine basis by X-ray diffraction. The microstructure was analysed using a high resolution TEM with attached EDX/EELS equipment. Critical shielding currents were determined by dc-SQUID magnetization measurements. Detailed results will be published elsewhere.

In order to optimize the melt-texture process, samples were analysed in terms of their flux trapping capabilities and pinning potential. Pellets of the small standard size (ϕ 14 mm) were cooled in the field of a $Nd_2Fe_{14}B$ magnet (ϕ 25 mm, magnetic field $H = 5$ kOe at the surface, axial polarization). Then the magnet was removed and the remnant magnetic flux was measured as a function of location across the pellets. The magnetic field sensor (Hall probe) had an active area of 0.2 mm^2. The maximum value of the trapped flux was used as criterion of sample quality. For small standard size pellets the grain size is approximately equal to the sample size. Therefore there is a direct correlation between the maximum value of the trapped flux and levitation force (see eqn. (2)). Although the data have local character only, they were found to be quite useful for evaluation of the sample quality and thus provided important input for optimization of the melt-texture process (e.g. temperature profile, amount of Ag_2O and Y_2O_3) with respect to large levitation forces. Fig. 1 shows the maximum trapped flux as a function of both Ag_2O and Y_2O_3 content for a series of small standard size samples. For this series the optimum is reached for 12.5 wt% Ag_2O and 25 at% Y_2O_3 or 17.5 wt% Ag_2O and 20 at% Y_2O_3.

The pinning potential was deduced from magnetic relaxation measurements in a dc-SQUID on representative pieces of pellets. At $T = 77$ K, the magnetic field was first ramped to $H = 10$ kOe and then to $H = 0$. Then, the remnant magnetic moment ($\approx$ trapped

532

flux) of the specimen was recorded as a function of time over several hours. These experiments also provide information about the total flux trapped by the specimen and the time rate of change of trapped flux. The latter is of special importance with respect to possible applications of these materials such as in superconducting magnetic bearings or in superconducting permanent magnets. For the bearing, the levitation force is proportional to the magnetization (or trapped flux) of the superconducting material (see eqn.(2)). Flux motion will be associated with dissipation resulting in damping which is unwanted in long term applications such as in a flywheel energy storage device. The total remnant flux ϕ in the specimen was found to change logarithmically over a time interval of 14 hours, i.e.

$$\Delta\phi \approx \ln(t/t_o) \tag{3}$$

here t_o is typically taken as the time from stabilization of the magnetic field at $H = 0$ to the first reading of the SQUID (usually 10 - 20 sec). Assuming that the flux continues to decay according to eqn (3) for times > 14 hours it follows that even after 5 years the specimen retained almost 80 % of the flux originally trapped at $t = t_o$. For practical applications this means that the superconducting material - adequate cooling provided - can be operated for years without 'recharging'.

Three dimensional interaction forces and vertical and horizontal stiffness have been measured between superconductors and permanent magnets in different geometries and various shapes as a function of relative position. Strain gauges were used for the three geometric axes. Resolution was 10 mN. The permanent magnets were mounted at the end of a tripod and mechanically connected to the force sensors via a gimbal suspension. The superconducting pellets were fixed in a liquid nitrogen dewar and mounted on a x-y-z microslide.

It was found that interaction forces depend upon: (I) distance between magnet and superconductor, (II) field and field gradient produced by the magnet, (III) sample size, (IV) sample quality (grain size, pinning forces), and (V) magnet size. Only magnets which can be approximated by a point dipole were used (the ideal magnetic dipole is a sphere) to ensure that the measured data are compatible to theoretical model calculations. Fig. 2 shows the log-log representation of the levitation force F_z as a function of vertical distance r_z between superconductor and magnet for different sized Nd-Fe-B magnets. Magnet data are summarized in table 1. The superconductor was a large standard size YBCO pellet (ϕ 30 mm).

Three distinct regions can be distinguished in fig. 2. For large distances between magnet and superconductor the correlation between $\log_{10}(F_z)$ and $\log_{10}(r_z)$ is linear with a slope of

approximately -4, i. e. $F_z \sim 1/r_z^4$. The distance r_{zo} where the data deviate from the straight line decreases with decreasing magnet size. We find $r_{zo} \approx 20$ mm for magnet A, $r_{zo} \approx 32$ mm for magnet B and $r_{zo} \approx 50$ mm for magnet C. The positions r_{zo} are approximately equal to the points where the vertical component H_z of the field of magnets A, B and C, respectively, has dropped to H_{c1} (see table 1). With decreasing r_z, F_z increases considerably. Close to the superconductor the dependence of $\log(F_z)$ upon $\log(r_z)$ is linear again with a slope of about -2, i.e. $F_z \sim 1/r_z^4$.

For small magnetic fields ($H < H_{c1} \approx 100$ Oe at 77 K) the interior of the superconducting pellet is completely shielded. By using the image method, the vertical force F_z [N], acting on a magnetic dipole m [A·m^2] levitated at a distance r_z [m] above an infinite superconducting plane in the Meissner state can be calculated as follows [12]

$$F_z(r_z) = k \cdot m^2/r_z^4 \qquad (4)$$

where k is a constant, $k = 3.75 \times 10^{-8}$ VsA^{-1}m^{-1}. The dashed line in fig. 2 represents a least-squares fit to the experimental data produced by magnet A for $r_z > 20$ mm. In this region the field of the magnet is < 100 Oe. From the fit it was found that $F_z(r_z)$ varies as $1/r_z^{4.4}$, in good agreement with the theoretical prediction given in eqn. (4). The magnetic dipole moment m of the magnet was found to be 0.1 Am^2, compared to a calculated value of 0.08 Am^2 using data specified in table 1. The main reasons for the deviation of the experimental data from theory are not surprising, because (i) the magnet is not a perfect dipole and (ii) the superconductor does not represent an infinite plane.

For smaller r_z, $H > H_{c1}$ and the field starts to penetrate the superconductor. A gradual transition to the critical state takes place. The dash-dotted line in fig. 2 is a least-squares fit to the experimental data obtained for magnet C for $r_z < 5$ mm. We find $F_z \sim 1/r^{1.8}$. Hellman et al.[13] have proposed a model for calculating the vertical force on a magnetic dipole levitated above a superconductor in the critical state. Assuming that flux bundles pass straight through the superconductor, the levitation force is found to scale as $1/r_z^2$ in good agreement with our experimental data.

For a given distance, the levitation force is maximum when the size of the magnet is comparable to the size of the superconducting pellet. On the other hand, when the magnet is much larger compared to the superconducting pellet, the levitation force apparently saturates within the range typical for gaps in magnetic bearings (e < 5 mm). This is shown in the insert of fig. 2. Here the superconductor was a small standard size pellet, ϕ 14 mm).

534

Differences in sample quality, evidenced by levitation force measurements, are shown in fig. 3. Magnet C was used for the measurements. All samples are ϕ 30 mm x 18 mm. In the Meissner phase, all samples are alike. Both levitation force F_z and vertical stiffness K_z, given by $\delta F_z/\delta r_z$, depend upon the magnet only. K_z is typically in the range of several mN/cm. With the transition to the critical state, the difference in sample performance with respect to levitation force and vertical stiffness reflects different pinning capabilities. The sample with the highest levitation force also exhibits the strongest vertical stiffness, $K_z \approx 10$ N/cm for $r_z < 3$ mm.

FLYWHEEL ENERGY STORAGE SYSTEM

An engineering model of a flywheel system with an autostable superconducting magnetic thrust bearing has been built and tested. The system comprises the following components: (1) aluminum flywheel disk, (2) superconducting magnetic thrust bearing consisting of a Nd-Fe-B magnet (integrated into the flywheel disk) and 6 melt-textured YBCO pellets on a sample mounting plate, (3) driving unit including drive shaft with couplings, motor/generator and frequency converter, (4) liquid nitrogen cryostat and (5) mounting structure. The components of the superconducting magnetic bearing are shown in fig. 4. The maximum levitation force was 65 N at zero gap. Vertical stiffness at 1 mm gap was 440 N/cm, lateral stiffness was 130 N/cm. Specifications are summarized in table 2.

Test runs were made with the superconducting magnetic bearing placed in a liquid nitrogen cryostat at ambient pressure. The magnet had a special coating to avoid material deterioration due to moisture collecting on the surface during prolonged experiments. The flywheel disk was driven by a 3 phase asynchronous, 380 V motor/generator connected to a frequency converter. Maximum power was 1.5 kW. A schematic of the flywheel system is shown in fig. 5. During high speed runs the unit was placed in a concrete enclosure measuring 1 x 0.8 x 0.8 m. The maximum speed attained was 9240 rpm. The energy capacity at this speed was calculated to be 1.8 Wh. A summary of technical data is given in table 3.

Obviously this set-up was not optimized for energy efficiency. We encountered quite substantial losses resulting from aerodynamic drag, especially during high speed runs and at lower speeds during extended runs when icing of the flywheel disk had occurred. Nevertheless, this preliminary experiment demonstrated the technology of autostable superconducting magnetic bearings and their application in a flywheel for energy storage. The next step will be to integrate the flywheel system into a vacuum

housing where much higher speeds should be possible. Metal parts in the path of the rotating magnetic field will be avoided to reduce losses from eddy currents due to deviations of the field from perfect rotational symmetry. The superconductors will be placed in a closed liquid nitrogen cryostat made from fiberglass. The same driving unit will be used. The projected speed is 24 000 rpm.

SUMMARY

In summary we have shown that large, good quality, monolithic pieces of superconducting YBCO can be produced on a routine basis using a melt-texture growth process. The material exhibited substantial levitation forces and good long term stability. A passive, superconducting magnetic bearing was built and integrated into a flywheel system. The bearing, though only a thrust bearing by design, provided both vertical as well as lateral stiffness. A 2.8 kg flywheel disk was rotated safely at speeds up to 9240 rpm at ambient pressure. The maximum energy capacity was 1.8 Wh. It can be expected that further refinement of this technology will allow operation of superconducting flywheels in the kWh range. Possible applications range from uninterruptable power supplies for computers to momentum/reaction wheels for spacecrafts.

ACKNOWLEDGEMENTS

REFERENCES

1. S. Earnshaw, *Trans. Cambridge Philos. Soc. 7*, 1882, pp. 97-112.
2. L. Tonks, *Elect. Engineering. 59*, 1940, pp.118-119
3. W. Braunbeck, *Zeitschrift für Physik 112*, 1939, pp. 764-769.
4. W. Meissner and R. Ochsenfeld, *Naturwissenschaften* 21, 1933, pp. 787-788.
5. C. P. Bean, *Phys. Rev. Lett. 8*, 1962, pp. 250-253.
6. M. Murakami, T. Oyama, H. Fujimoto, T. Taguchi, S. Goto, Y. Shiohara, N. Kosizuka, and S. Tanaka, *Jpn. J. Appl. Phys. 29*, 1990, pp. L1991-L1994.
7. M. Murakami, ed.: *Melt Processed High-Temperature Superconductors*, World Scientific, 1992, pp. 9-10
8. Hoechst AG, YBaCO 123 powder grade 2.
9. S. Jin, T. H. Tiefel, R. C. Sherwood, R. B. van Dover, G. W. Kammlott and R. A. Fastnacht, *Phys. Rev. B 37*, 1988, pp. 7850-7858.
10. K. Salama, V. Selvamanickam, L. Gao and K. Sun, *Appl. Phys. Lett. 54*, 1989, pp. 2352-2354.
11. H. Hojaji. K. A. Michael, A. Barkatt, A. N. Thorpe, F. W. Mathew, I. G. Talmy, D. A. Haught and S. Alterescu, *J. Mater. Res. 4*, 1989, pp. 28-36.
12. Z. J. Yang, T. H. Johansen, H. Bratsberg, A. Bhatnagar, *Physica C* 197, 1992, pp. 136-146.
13. F. Hellman, E. M. Gyorgy, D. W. Johnson, Jr., H. M. O'Bryan, and R. C. Sherwood, *J. Appl. Phys. 63*, 1988, pp. 447-450.

Table 1: Specifications of the Nd-Fe-B Magnets
(Direction of Magnetization: Axial)

Magnet		A	B	C
Diameter	mm	7	14	25
Height	mm	6	14	21
Mass	g	2.5	19.6	77.4
Max. Field	kOe	4.2	4.5	5.0
Distance where $H_z < H_{c1}$	mm	18	32	48

Table 2: Superconducting Magnetic Bearing -- Specifications

Magnet:	neodymium-iron-boron with coating dimensions: ϕ 90 x ϕ 60 x 15 mm weight: 397 g polarization: axial maximum field: 4 kOe
Superconductors:	6 pellets of melt-textured YBCO dimensions: ϕ 30 x 18 mm (pellet) weight: 100 g (pellet)

Operating temperature:	77 K (liquid nitrogen)
Maximum levitation force:	65 N
Stiffness at 1mm gap:	
Vertical	440 N/cm
Lateral	130 N/cm

538

Table 3: Flywheel -- System Data

Flywheel disk:	$AlMg_3$, ϕ 200 x 30 mm, 2.43 kg + integrated Nd-Fe-B magnet total mass: 2.8 kg allowable tensile stress: 210 N/mm^2 moment of inertia: 0.014 $kg \cdot m^2$
Motor/Generator:	3-phase asynchronous, 380 V, 50 Hz, watercooled dimensions: ϕ 176 x 275 mm maximum torque: 1.2 Nm
Maximum speed: Projected speed: Energy capacity: Maximum power:	9240 rpm 24 000 rpm (in vacuum) 1.8 Wh at maximum speed 12.3 Wh at projected speed 1.5 kW
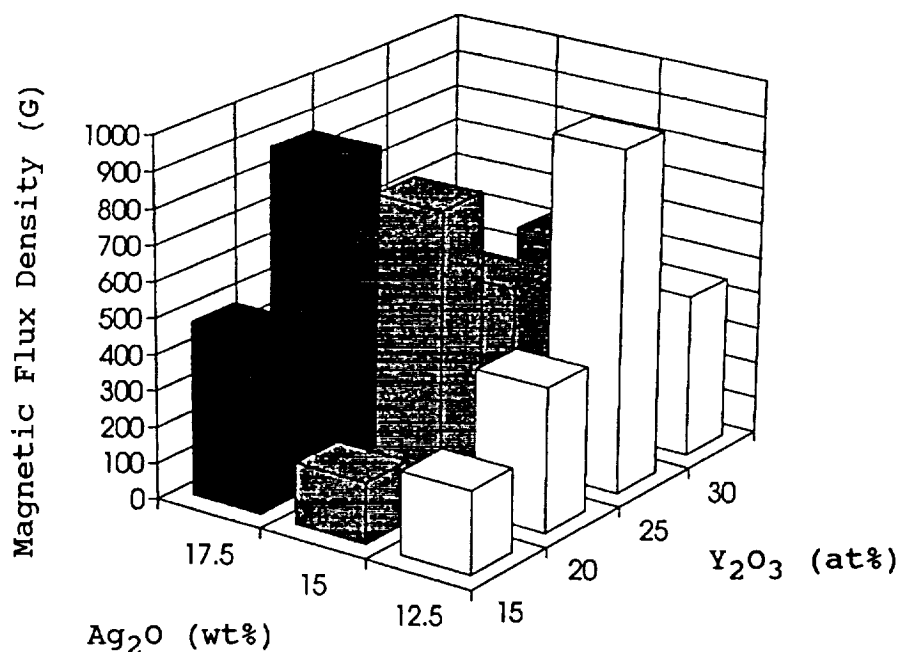
Figure 1: Maximum trapped flux as a function of Ag_2O and
Y_2O_3 content for a series of small standard size
pellets (ϕ 14 mm).
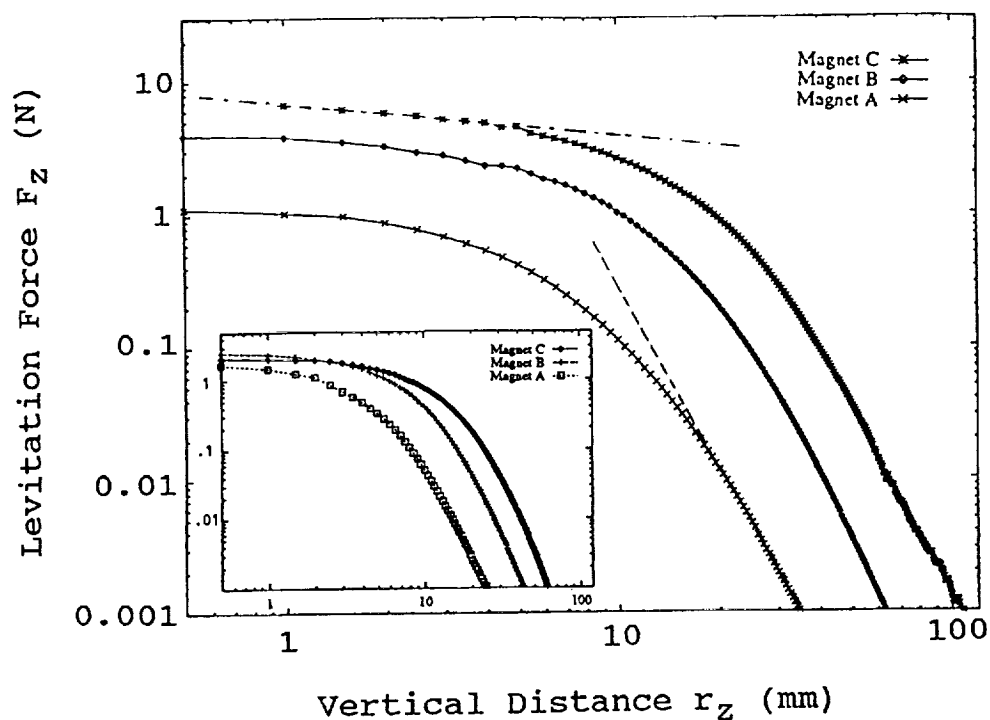
Figure 2: Levitation force as a function of vertical distance for different sized magnets. The superconductor was a large standard size pellet (ϕ 30 mm), composition 20 at% Y_2O_3, 15 at% Ag_2O. For the insert: Small standard size (ϕ 14 mm), composition was 20 at% Y_2O_3, 17.5 at% Ag_2O.
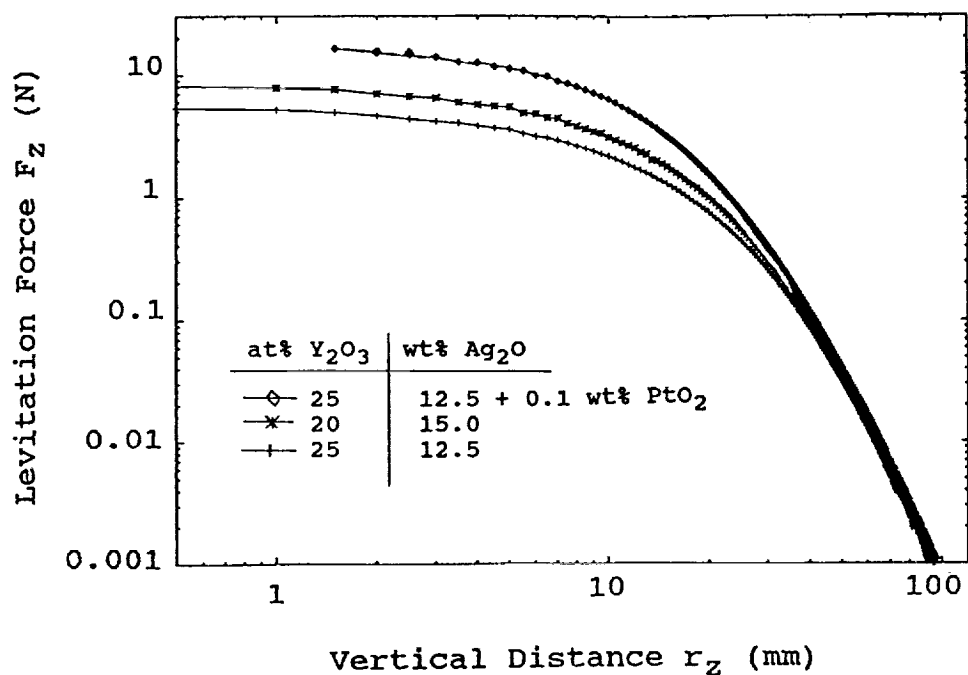
Figure 3: Correlation between levitation force and sample composition.
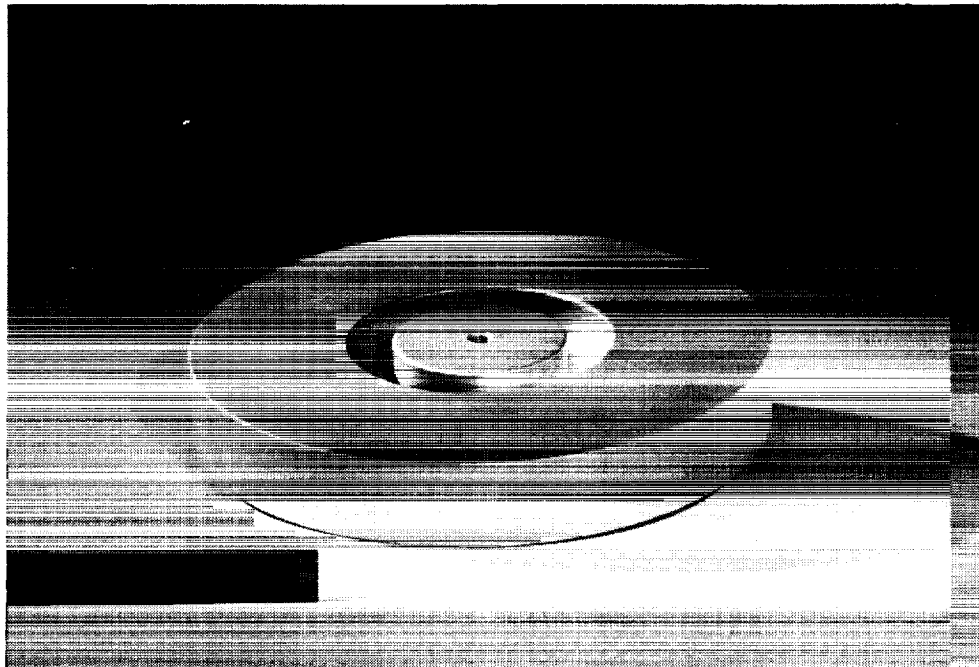
Figure 4: Components of the superconducting magnetic
bearing. Top: Superconducting YBCO pellets
(ϕ 30 x 18 mm) integrated into the sample mounting
plate and Nd-Fe-B magnet. Bottom: Aluminum
flywheel disk.
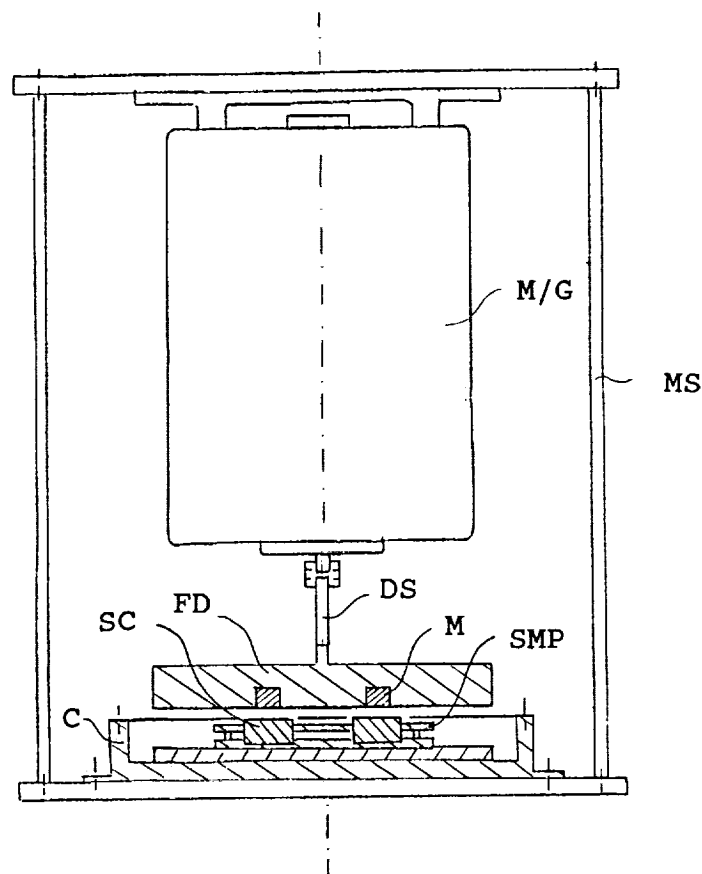
Figure 5: Schematic of the flywheel system.
C: cryostat, SC: YBCO pellet, FD: flywheel disk
DS: driveshaft with couplings, M: magnet,
SMP: sample mounting plate, M/G: motor/generator
MS: mounting structure

MANUFACTURING AND TESTING OF A MAGNETICALLY SUSPENDED COMPOSITE FLYWHEEL ENERGY STORAGE SYSTEM

Stephen Wells
FARE Inc.
College Park, MD

Da-Chen Pang
Dr. James A. Kirk
University of Maryland
College Park, MD

ABSTRACT

This paper presents the work performed to develop a multiring composite material flywheel and improvements of a magnetically suspended energy storage system. The flywheel is constructed of filament wound graphite/epoxy and is interference assembled for better stress distribution to obtain higher speeds. The stationary stack in the center of the disk supports the flywheel with two magnetic bearings and provides power transfer to the flywheel with a motor/generator. The system operates under a 10^{-4} torr environment and has been demonstrated to 20,000 rpm with a total stored energy of 15.9 Wh. When this flywheel cycles between its design speeds (45,000 to 90,000 rpm), it will deliver 242 Wh and have a usable specific energy density of 42.6 Wh/kg.

INTRODUCTION

The flywheel energy storage system has higher specific energy density (SED), larger power output, and longer cycle life than typical battery systems for spacecraft applications [1]. The flywheel and test apparatus shown in figure 1, which was manufactured and tested, consist of the following components:

- A multi-ring interference assembled flywheel fabricated from graphite-epoxy, including two magnetic bearing return rings and motor/generator magnets.
- Two active "pancake" magnetic bearings which together form the top and bottom portions of a test apparatus (stack).
- A motor/generator mounted between the two magnetic bearings. This provides power transfer into and out of the test apparatus.
- A vacuum enclosure supporting the top and bottom of the "stack" and completely surrounding the flywheel.
- Display/control panel offering control and data acquisition of the system.

COMPOSITE FLYWHEEL

The construction of the composite flywheel cylinders by filament winding consists of four major steps. The first step is design, which includes the selection of materials, geometry of the part, and orientation of the fiber. Step two includes selection and control of conditions which are to be maintained during the manufacturing process. The third step is the machining and assembly of the flywheel. The final step involves testing the materials to determine if their strength matches theoretical values.

Flywheel Design

The flywheel energy storage system is designed to cycle between 37.5% to 75% of its maximum strength with speeds of 45,000 rpm to 90,000 rpm. This will deliver 242 watt hours and have a usable energy density of 42.6 Wh/kg.

The flywheel inside diameter and height were designed to fit within an existing test apparatus [2] and consists of two composite rings and an inner metal ring. The metal ring consists of aluminum rings for balancing, nickel iron rings for magnetic suspension, a ring containing the motor/generator magnets, and aluminum spacers. The nominal diameters of the two composite rings are 4.68 inches (118.87 mm) inside diameter and 5.6 inches (142.24 mm) outside diameter for the first ring and 6.61 inches (167.89 mm) outside diameter for the second ring. FLYANS code was used to determine optimal composite ring dimensions to produce favorable stresses [3,4,5] and a 0.006 inch (0.1524 mm) interference fit was selected for the composite rings.

From micrographic tests of a preliminary composite flywheel, abnormal end effects on the microstructure were found. The effect is due to the filament winder carriage changing directions, thus the composite rings were made 0.25 inches (6.35 mm) longer on each end. The height of the first composite ring was 9.5 inches (241.3 mm) long and the second composite ring was made 0.002 inches (0.0508 mm) longer so that the top surfaces of the rings would not be flush when pressed together. The final height of the flywheel once the ends were cut off is 9 inches (228.6 mm).

Flywheel Manufacture

Two composite rings were filament wound using a Toho G40-800 carbon graphite fiber and a Shell Epon 826 epoxy resin. The rings were filament wound onto steel winding mandrels using a two-axis filament winding machine as shown in figure 2. The winding angle, α, is the angle between the axis and the fiber shown in figure 3. For the flywheel, fibers are oriented as close as possible to the tangential direction, i.e., a winding angle of 90° (for practical purposes the fiber angle is 87°). This ensures that for one revolution of the mandrel the carriage should advance one fiber bandwidth. Reversal at the end of carriage travel needs to be accurately controlled to avoid excessive build-up at the flanges of the mandrel. A precision lead screw is used to control the carriage movement. The fiber is pulled through a tensioner into the matrix bath. Wet winding epoxy resins are sufficiently low molecular weights that they are fluids at room temperature. To assist in wetting the fiber during the winding process, a 250 Watt heat lamp with temperature control was used to heat the resin. This increases resin temperature, dropping the viscosity of the resin.

Heating the resin reduces the viscosity from 100 poise to 6-7 poise, or a 93% reduction of viscosity. A disadvantage of heating the resin is that the resin bath pot life is reduced from eight hours to three hours.

Due to voids observed in digital imaging samples of filament wound parts, it was decided to integrate a vacuum bagging technique into the flywheel manufacturing process. Vacuum bagging uses air pressure to apply force around the part which consolidates the fibers, removes excess resin by trapping it in layers of bleeder cloth, and removes volatiles which produce voids.

Once the part is vacuum bagged, the mandrel is placed onto a cradle which has been fitted with bearings to allow for rotation during the curing process. The mandrel rotates to prevent collection of resin at one point and sagging of the fiber. The part is cured at 175°F for one hour to allow resin to flow, and then cured at 350°F for two hours to cure the epoxy.

Flywheel Machining and Assembly

To produce the interference fit, a 0.4 degree taper was machined on the outside surface of the inner filament wound ring creating a 73% engagement between the first and second rings. The two rings were lubricated with epoxy and then pressed together with 30,000 pounds of force. Once the rings were pressed together, 1/4 inch of material was removed from the top and bottom to give the final flywheel height of nine inches. The inside and outside diameters of the pressed composite rings were machined to designed size dimensions using standard carbide cutting tools. The aluminum balancing rings, aluminum spacers, motor return ring, and magnetic bearing rings were press fit into the flywheel with a LN1 press fit (0.0005 inch or 0.0127 mm) using a lathe end dead center. Alternating dark and light markings were painted for motor commutation and rpm sensors to complete the flywheel.

Testing of Materials

To verify the composite material properties, acid digestion, micrograph, and digital imaging tests were performed to determine void content and volume fraction, and NOL tension tests were conducted for tensile strength and composite stiffness in the fiber direction. Fiber modulus and tensile strength was 20% and 25% below theoretical. Machining generates broken fibers and cracks and the less than perfect geometry of the NOL ring specimen was suspected to contribute to these errors. Volume fraction was measured to be 62% fiber which is comparable to high performance composite materials. Void content was measured at 7% using a digital imaging technique with a non-vacuum bagged part, thus the decision to vacuum bag all future composite parts to decrease the void content.

TESTING APPARATUS

The test apparatus performs the task of containing and spinning the composite flywheel to high speeds. The test apparatus consists of two magnetic bearings for suspension of the flywheel, an electrical system to provide control and monitoring of the system, a

motor/generator to provide the means for the input and output of energy to the flywheel, and a vacuum chamber capable of 10^{-5} torr to simulate a zero atmosphere environment. A block diagram of the electrical paths of the test apparatus is shown in figure 4.

Magnetic Bearing

The magnetic bearings allow rotation of the flywheel without contacting any surfaces. Our system consists of two magnetic bearings for stability of the system. The bearing consists of a combination of permanent magnets (PMs) which provide passive support through permanent magnets in the axial direction and electromagnets (EMs) which provide active positioning control in the radial direction. The bearing is divided into four quadrants to decouple the flux produced by adjacent quadrants. The flux paths are separated into two independent axes, east-west and north-south, and each axis has its own independent control system. If the flywheel is not centered, the permanent magnets will create a destabilizing force to pull it farther off center. The control system responds to the displacement by sending a current through the EM, which results in additional corrective flux which adds to the bias flux to produce a net restoring force.

A block diagram of the magnetic bearing system is shown in Figure 5. There are four major components in the system: the magnetic bearing actuator, rotor dynamics, displacement sensors, and control system. Voltage feedback from the control system goes into magnetic bearing actuators. The actuator consists of the power amplifier, power supply, and electromagnetic coils which provide additional flux in the air gap to generate stabilized force. The power amplifier is a voltage-to-current bridge circuit design which can drive large inductive load with twice the output power. The actuator force F_c, combined with the disturbance force F_d, affect the rotor dynamics. The rotor dynamics models the mechanical system and the destabilizing force from the permanent magnet flux distribution in the radial direction. The eddy current transducers measure the displacement of the flywheel with sensor error η. Then the sensor output is fed back into the control system. The control system has a proportional and derivative compensation circuit to optimize system performance. The reference voltage input in the forward loop is used to center the flywheel. The error signal, subtracting the feedback signal from reference voltage signal, passes an adjustable gain and a low pass filter before going into the actuator. The adjustable gain is used to stabilize the system and change the magnetic bearing stiffness.

Motor/Generator

The motor/generator, located between the two magnetic bearings, converts the stored mechanical energy into electrical energy. The motor/generator is a permanent magnet, electronically commutated, ironless armature DC brushless design. The motor/generator was designed by Niemeyer [6] and was implemented by Lashley [7,8]. Motor commutation is provided by position sensors and switching transistors, which is based on the sensor measurement of the rotor position, i.e., the angular location of the magnet poles relative to the armature windings. The transistors switch the armature current to maintain a unidirectional torque. The position sensors are optical emitter-detector pairs, chosen for their small size. Speed control is provided by pulse width modulation (PWM) through an Automation Inc. LC4C motor controller [9].

Display/Control Panel

The display systems which are integrated into the energy storage system are as follows:

- Displacement
- Power amplifier voltage and current output
- Power supply voltage and current
- Percentage of PWM waveform of motor
- Vacuum of system
- Temperature of motor and magnetic bearings

The control capabilities of the system are:

- Magnetic bearing controller with adjustable stiffness and damping
- Flywheel position
- Motor speed
- Motor controller voltage

Vacuum System

To avoid windage losses during flywheel rotation, the flywheel energy storage system is placed inside a vacuum chamber as shown in figure 6. The vacuum chamber is a two piece design consisting of a vacuum chamber on an aluminum base plate sealed by a rubber gasket. Vacuum is pumped down in a two stage process. A roughing pump provides vacuum to 10^{-3} torr and a diffusion pump provides vacuum down to 10^{-5} torr. High vacuum electrical feed-throughs are used to provide power to the motor, sensor signal paths, and magnetic bearing coil power through the vacuum chamber.

TESTING AND PERFORMANCE ENHANCEMENT

Before higher speeds could be obtained by the system, several issues had to be addressed. The number of turns of the magnetic bearing actuator coil, power amplifier voltage, motor commutation, motor/controller inductance matching, system ultimate vacuum, system vibration response, system balancing, and magnetic materials limited the speed of the flywheel.

Voltage Saturation

The system had magnetic suspension failure at 6,000 rpm due to voltage saturation of the power amplifiers. To decrease the voltage demand of the EM coils, the number of turns in the actuators was decreased. Also, the power amplifiers which drive the EM coils were changed from APEX PA01 to APEX PA61 which have higher voltage and current capacities [10]. The power supply voltage was increased from 24 volts to 48 volts to

accommodate for the new power amplifiers. The power amplifiers used a voltage-current bridge design which generates twice the power of the previous design. These changes eliminated the voltage saturation issues currently, but if voltage saturation occurs again at higher speeds, it would be necessary to redesign the system using switch amplifiers.

Motor/Generator

The motor/controller combination used in our system is limited by their impedance mismatch. The Automation LC4C motor controller has a minimum inductance load of 150 μH and a suggested inductance of 1 mH [9] and the motor has an inductance value of 54 μH. The low inductance of the motor causes a high current slew rate and current saturation of the motor controller then limiting the motor speed. Methods to correct for this mismatch were to decrease the controller input voltage and add dummy inductors into the motor windings.

Motor commutation was originally provided using OPTEK OPB701 optical sensors. These sensors use a photodarlington output, which gives a higher gain but a lower response time of 1 ms [11]. Due to the slow response time, the system could not reach speeds above 15,000 rpm and thus the optical sensors were replaced by OPTEK OPB700 phototransistor sensors with a schmitt trigger. These sensors provide a response time of 0.1 ms and is enhanced by a schmitt trigger for square wave output. A comparison of the output of the two sensors and motor current is shown in figures 7 and 8.

Vacuum System

To avoid windage losses during flywheel rotation, the flywheel energy storage system is placed inside a vacuum chamber. Since windage loss is proportional to the gas density, the system can achieve high speed under vacuum [12]. Spin-down testing for our flywheel energy storage system under air and 10^{-4} torr was conducted as shown in figure 9.

Vibration Analysis

Dynamic analysis performed on our system showed a significant undamped resonance at 5400 rpm. Since the structure itself is very stiff, modes below approximately 300 Hz are due to mounting stiffness of the structure. The effective mounting stiffness was reduced by the use of rubber pads under the feet of the stack and of the vacuum chamber. A repeat modal test showed that the mode disappeared and all of the rigid-body modes of the structure were much lower. It is also theoretically possible to increase the stiffness and push the modes up the frequency scale, but this is more difficult in practice.

Balancing

For the high speed of rotation, the mass balancing of the flywheel becomes very important. In-situ balancing methods had originally been adopted for our flywheel system from Bruel & Kjaer data [13]. Initial experiments gave poor results due to the larger than

anticipated third harmonic content of the measured vibration signal. Attempts were made to commercially balance the flywheel. Since the flywheel does not have a shaft, which is required by balancing machines, a precision ground shaft and precisely machined collars were used to set up the center for balancing. Even though the flywheel/shaft/collar assembly was balanced as accurately as possible, the vibration increased when the flywheel spin tested. It was concluded that it is not possible to recreate the magnetic bearing center using mechanical fixtures for balancing, and all balancing must be done in-situ. A final attempt at balancing was made, using trial and error procedures, by observing the X-Y orbit of the flywheel and adding or subtracting small weights to make this orbit smaller, which produced desirable results.

For a composite flywheel, balancing is a difficult issue because it is undesirable to drill holes within the composite part. To circumvent this problem, a thin aluminum ring is pressed into the composite and set screw holes were drilled every 30 degrees. Weight is changed by adding or removing set screws from the aluminum ring. For the composite wheel, it was found that only a few grams of added weight were necessary to achieve the proper balance for the flywheel.

Third Harmonic Noise

A large third harmonic component was measured in the displacement signal causing a diamond shaped X-Y orbit as shown in Figure 10 as compared to a displacement signal without the third harmonic shown in Figure 11. This third harmonic noise is undesirable because it requires more control voltage and current and the system is more difficult to balance. From testing different batches of return rings, it was found that the third harmonic noise was caused by magnetic material saturation. The magnetic bearing return rings are made of Carpenter High Permeability 49% nickel iron material which has a magnetic saturation value of 1.2 Tesla [14]. Most magnetic properties quoted for this material are for thin laminations. Solid materials utilized in our system may present non-uniform properties after heat treatment processing. The preliminary magnetization test suggested that the solid material has the same magnetic saturation value but much lower permeability and higher core losses.

DISCUSSION AND CONCLUSIONS

The manufacturing process and testing for a composite flywheel has been sucessfully conducted. The magnetically suspended composite flywheel energy storage system has been developed and reached the speed of 20,000 rpm. In the process to achieve higher speed, the problems of voltage saturation, vibration, motor commutation, and balancing have been solved. Additional R&D is necessary before commercialization of the final prototype. A new motor and motor controller design is necessary to reach higher speeds, and further magnetic modeling and testing of the magnetic bearings should be performed to eliminate the third harmonic noise.

ACKNOWLEDGMENT

Chris Lashley and Bob Linkins from the University of Maryland, and John Chandler from Automotion Inc. for their technical support.

REFERENCES

1. Kirk, J.A., Anand, D.K., Satellite Power Using a Magnetically Suspended Flywheel Stack, Journal of Power Sources, Vol. 22, pp. 301-311, 1988.
2. Magnetically Suspended Flywheels for Inertial Energy Storage, Final Report, NAS5-30091, 1991.
3. Ries, Douglas M., Manufacturing Analysis for a Composite Flywheel, M.S.Thesis, University of Maryland, 1990.
4. Kirk, J.A., Ries D.M., Manufacturing Analysis of Composite Mulit-Ring Flywheel, Aerospace Engineering, October 1992, pp. 14-18.
5. Kirk, J.A., Anand, D.K., Overview of a Flywheel Stack Energy Storage System, Proceedings of the 23rd Intersociety Energy Conversion Engineering Conference, July 31 to August 5th, Denver, Colorado, 1988.
6. Niemeyer, W.L., Design of a High-Efficiency Motor/Generator for Flywheel Energy Storage, M.S. Thesis, University of Maryland, 1988.
7. Lashley, Christopher, Development of a High-Efficiency Motor/Generator for Flywheel Energy Storage, M.S. Thesis, University of Maryland, 1991.
8. Lashley, C., Anand, D., Zmood, R. B., Development of a High-Efficiency Motor/Generator for Flywheel Energy Storage System, 26th Intersociety Energy Conversion Engineering Conference, 1991.
9. Automation, Inc., Model LC-4 Users Manual, Ann Arbor, Michigan, 1988
10. Apex Microtechnology Corporation, APEX Hybrid & IC Handbook, Tucson, Arizona, 1991.
11. Optek Technology, Inc., OPTEK Optical Sensors Handbook, Carrollton, TX, 1993.
12. Dugger, G.L. et al, Heat-Engine/Mechanical-Energy-Storage Hybrid Propulsion Systems for Vehicles, John Hopkins University Applied Physics Laboratory, 1972.
13. Broch, J.T., Mechanical Vibration and Shock Measurements, Bruel and Kjaer Measuring Systems Inc., Naerum, Denmark, 1973.
14. Carpenter Technology, Soft Magnetic Alloys, Carpenter Technology Brochure, 1991.
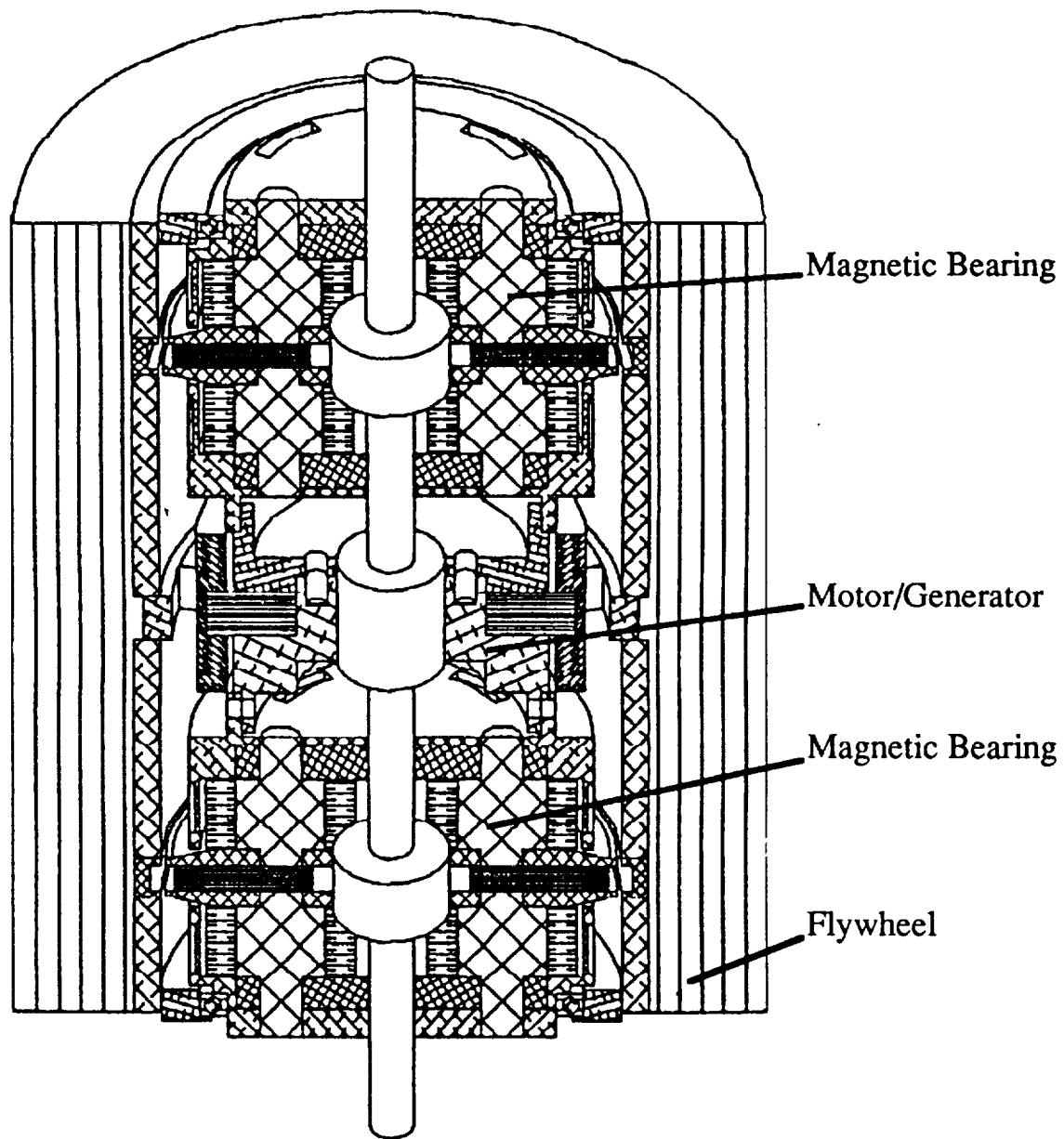
Figure 1. Magnetic Bearing System

Magnetic Bearing

Motor/Generator

Magnetic Bearing

Flywheel
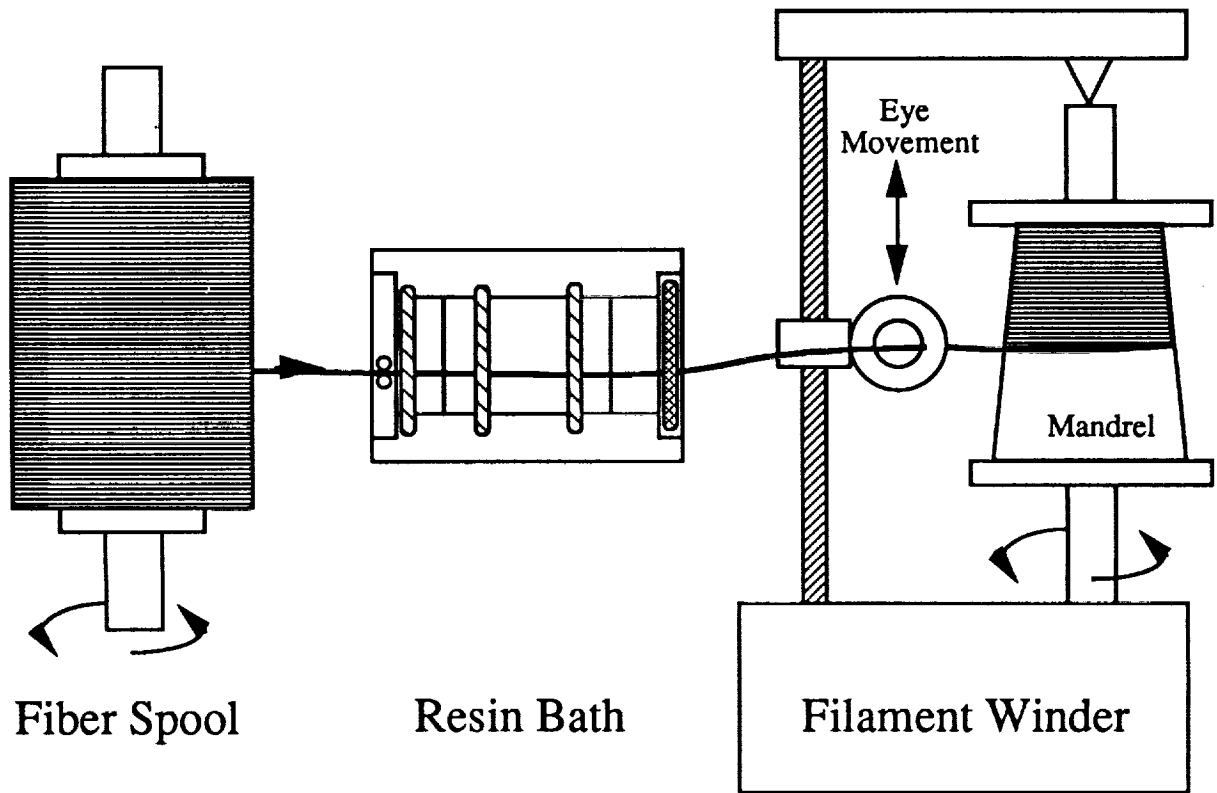
Figure 2. Two-Axis Filament Winding Process
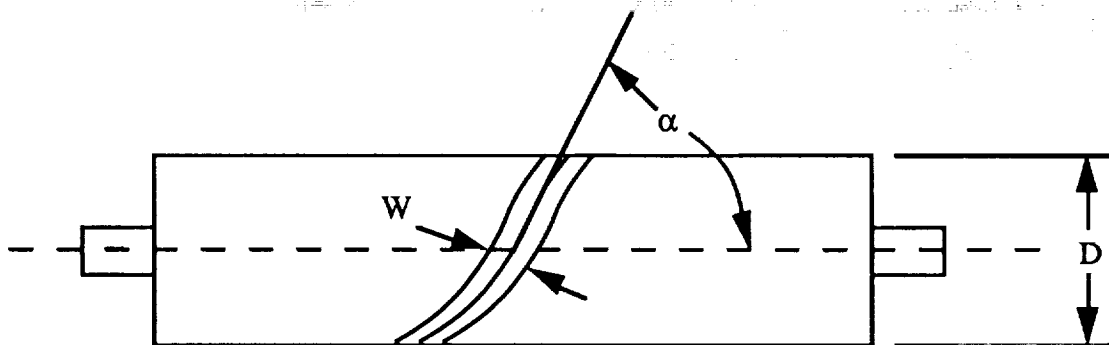
Figure 3. Wind angle
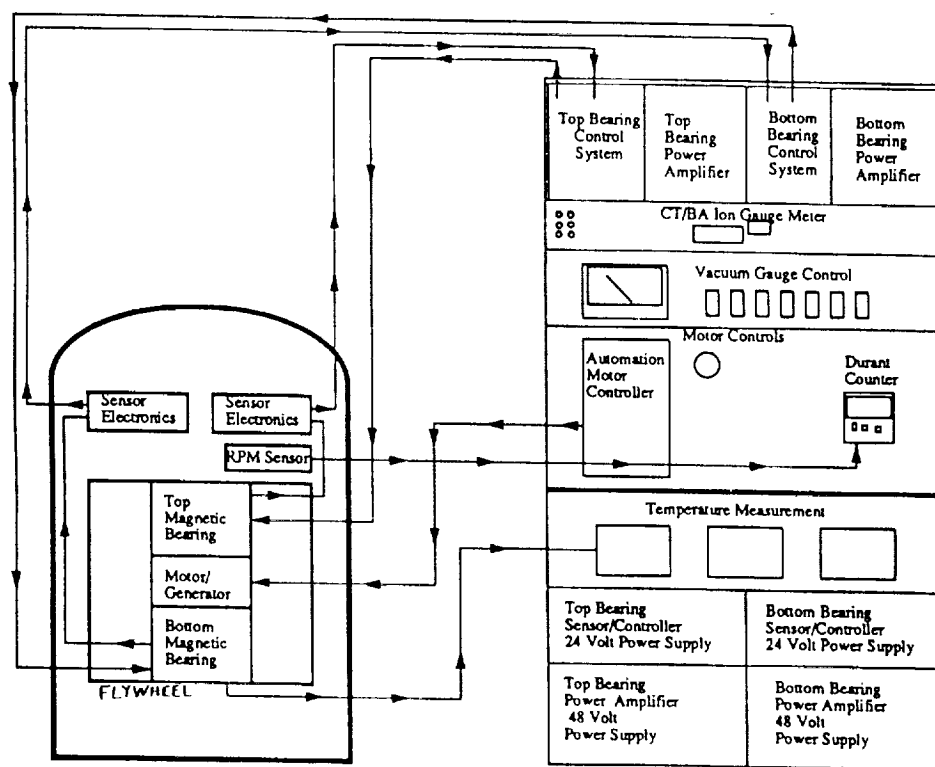
Figure 4. Magnetic Bearing Electronic Setup
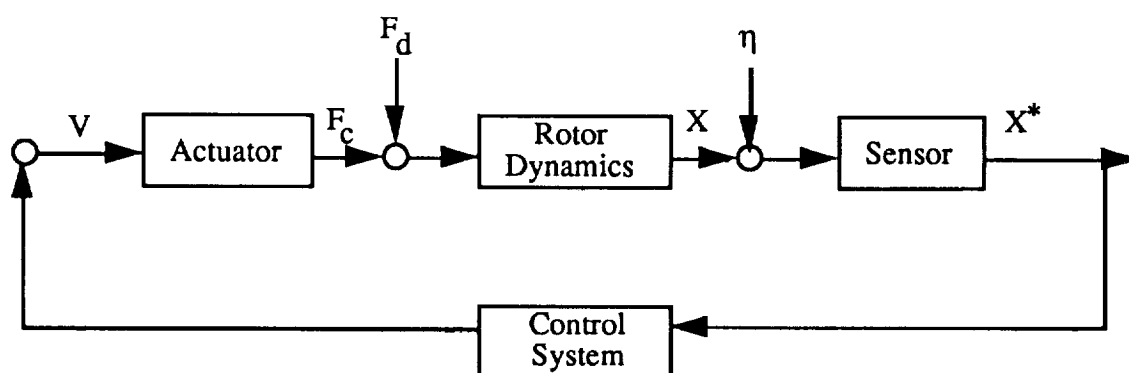
Figure 5. System Block Diagram
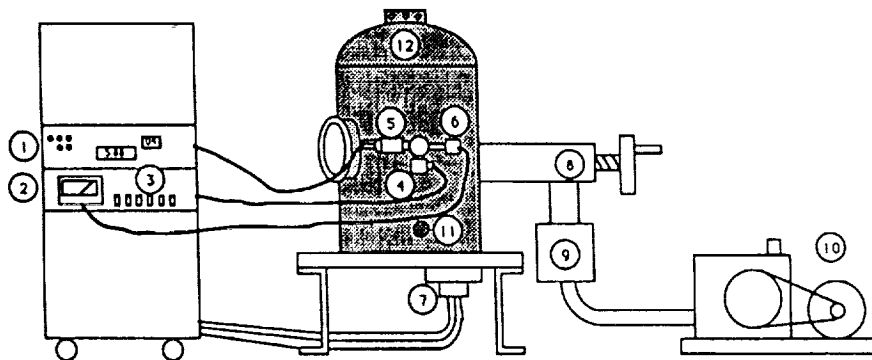
1　CT/BA Ionization Gauge Control for 10^{-5} Torr system
2　Hastings Vacuum Gauge Control for 10^{-3} Torr system
3　Vacuum control switches
4　Emergency vent valve
5　Ionization Gauge
6　Hastings Vacuum Gauge
7　Vacuum feedthroughs (Electrical wires through vacuum chamber)
8　Vacuum chamber valve
9　Diffusion pump for 10^{-5} Torr system
10　DuoSeal Model 1402 Vacuum Pump for 10^{-3} Torr system
11　Available port for cold trap (to remove water vapor)
12　Vacuum chamber

Figure 6. Vacuum Chamber Setup
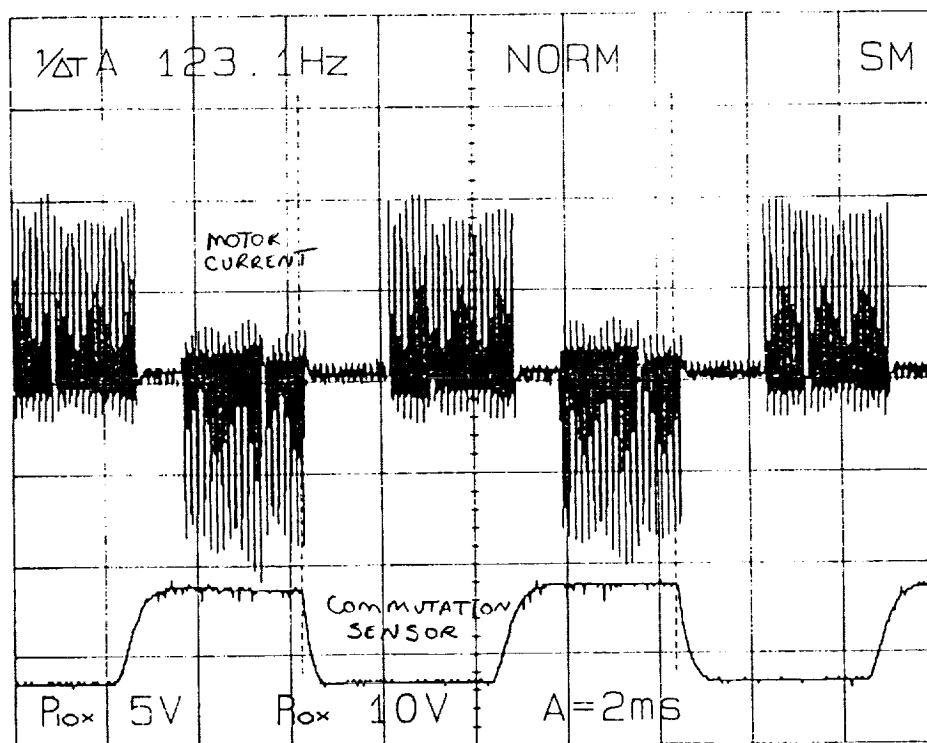
Figure 7. Photodarlington Optical Sensor Output
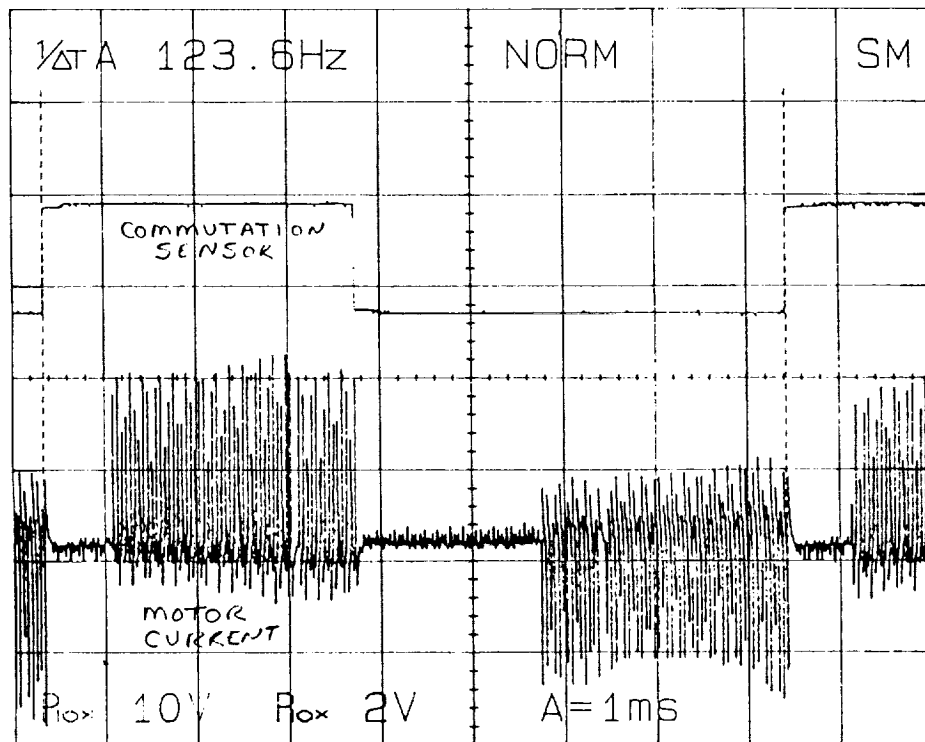
Figure 8. Phototransistor Optical Sensor Output

Spin Down Test of Flywheel Energy Storage System
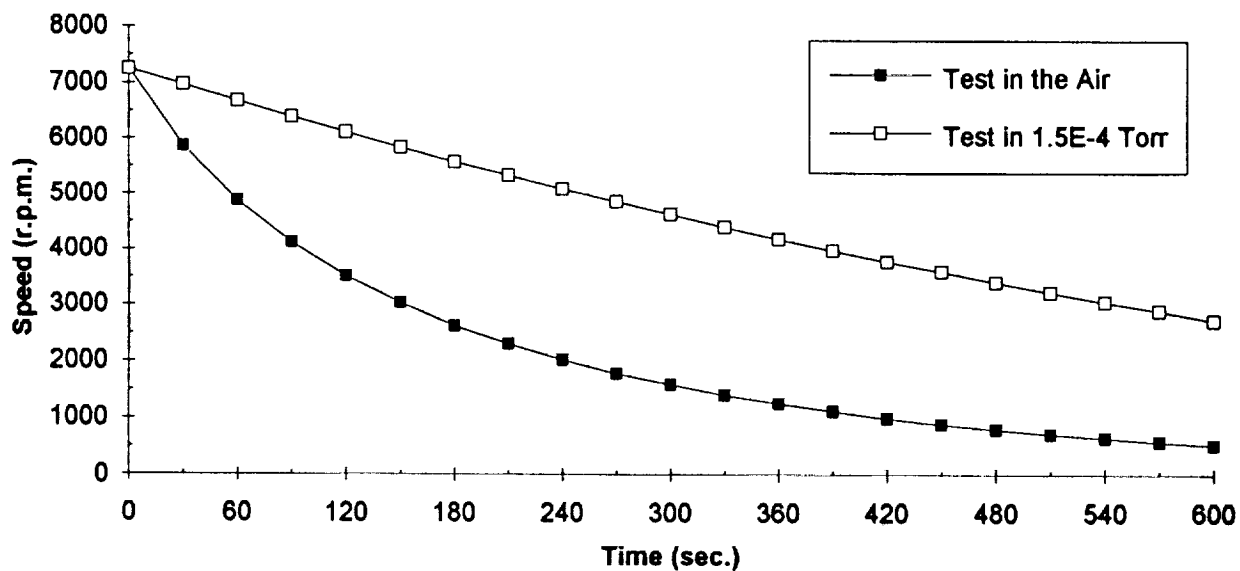
Figure 9. Spin-down Tests of the Energy Storage System in Air and in Vacuum
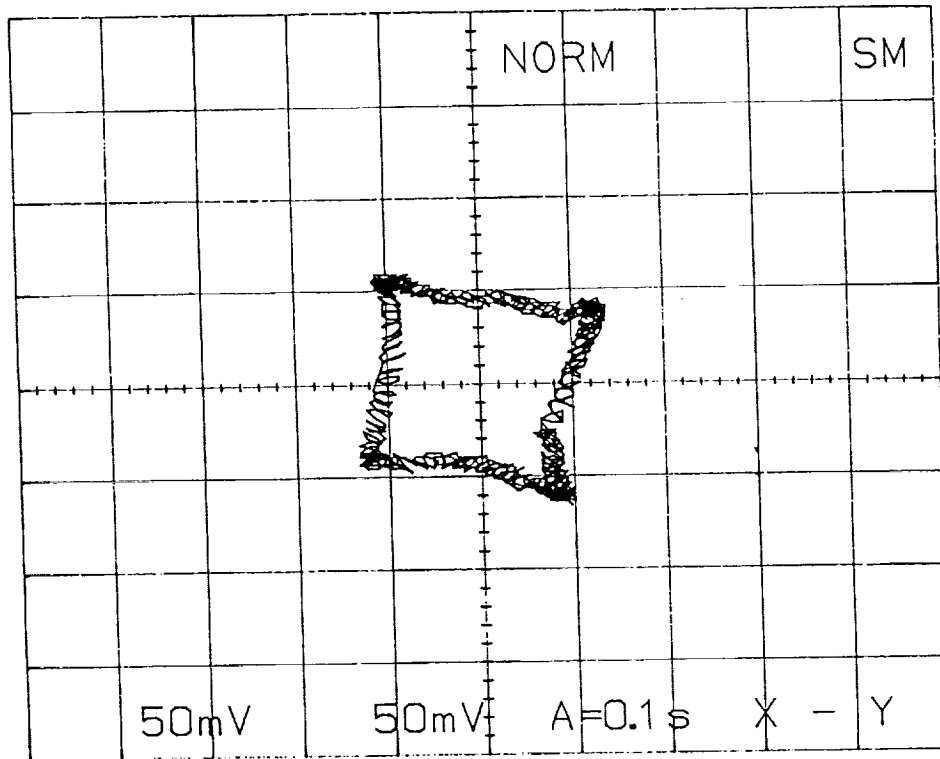
Figure 10. X-Y Orbit with Third Harmonic Present
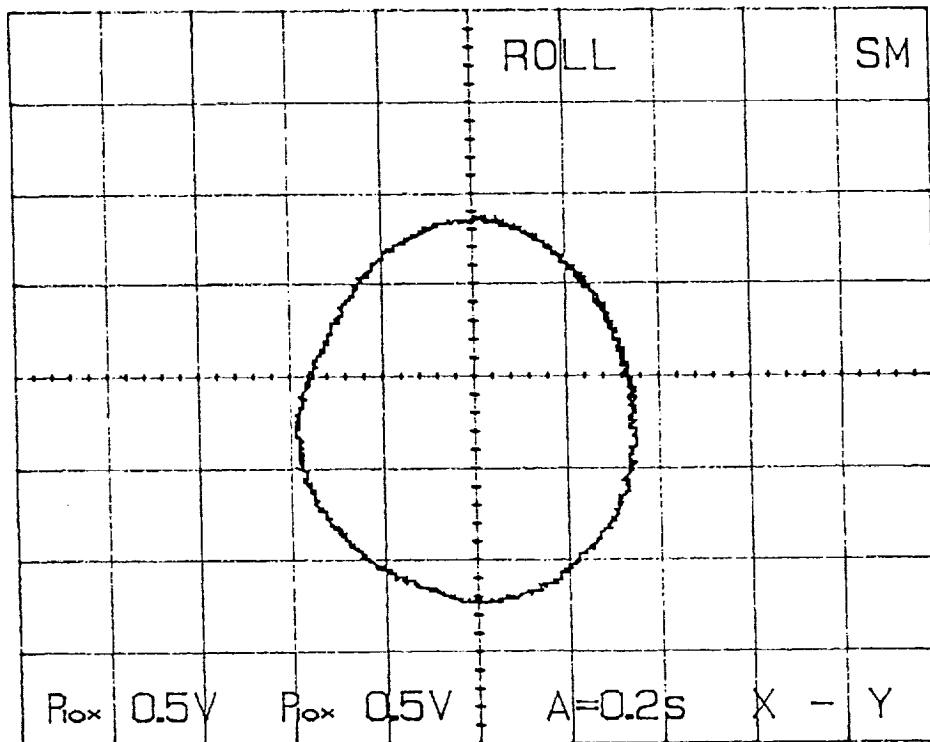
Figure 11. Normal X-Y Orbit

ROTOR DYNAMIC BEHAVIOUR OF A HIGH-SPEED OIL-FREE MOTOR COMPRESSOR WITH A RIGID COUPLING SUPPORTED ON FOUR RADIAL MAGNETIC BEARINGS

J. Schmied
Sulzer Escher Wyss
Zurich, Switzerland

J.C. Pradetto
Sulzer Escher Wyss
Zurich, Switzerland

SUMMARY

The combination of a high-speed motor, dry gas seals and magnetic bearings realized in this unit facilitates the elimination of oil. The motor is coupled with a quill shaft to the compressor. This yields higher natural frequencies of the rotor than with the use of a diaphragm coupling and helps to maintain a sufficient margin of the maximum speed to the frequency of the second compressor bending mode. However, the controller of each bearing then has to take the combined modes of both machines into account. The requirements for the controller to ensure stability and sufficient damping of all critical speeds are described and compared with the implemented controller. The calculated closed loop behaviour was confirmed experimently , except the stability of some higher modes due to slight frequency deviations of the rotor model to the actual rotor. The influence of a mechanical damper as a device to provide additional damping to high modes is demonstrated theoretically. After all, it was not necessary to install the damper, since all modes could be stabilized by the controller.

INTRODUCTION

The task of the motor compressor unit is to fill a cavern with natural gas for storage purposes. A compressor without any oil is desirable for this application, since the smallest quantities of oil in the gas cause considerable additional maintenance costs for the pipes. The elimination of any oil could be realized by the combination of a high-speed motor (no gear necessary), dry gas seals replacing oil seals and magnetic bearings substituting oil bearings. Figure 1 shows a cross section of the compressor and Figure 2 the whole unit. The motor is located in a seperate housing. Its shaft is connected to the compressor shaft with a quill shaft.

The suction pressure of the compressor is 50 bar and the maximum discharge pressure is 150 bar. The maximum output of the motor is 2MW and the operating speed ranges from 14000 rpm to 20000 rpm.

The discharge pressure of the compressor at the drive end is sealed against atmospheric pressure with a triple dry gas seal. The helium cooling gas of the motor at the drive end is also sealed with a dry gas seal. The thrust bearing and the radial bearing on the non drive end side are surrounded by the natural gas working fluid, but at a lower pressure than suction pressure in order to reduce windage losses. This requires another seal between the first compressor stage and the thrust bearing.

Due to the high efficiency requirements, the compressor does not have a balance piston with its relevant high leakage losses. The thrust is balanced by a digital valve controlling the flow into a chamber at the non drive end of the compressor as a function of the flux of the magnetic thrust bearing, which is proportional to the thrust force. The resulting pressure in the balance chamber is also sealed with a dry gas seal.

The main object of the paper is to describe the predicted and measured rotordynamic behaviour of this unit and its influence on the design of the digital controller, with special regard to the aspects of the quill shaft coupling. In comparison with a diaphragm coupling, this type of coupling offers several advantages:

- Less weight (yields higher natural frequencies),
- additional stiffness (yields higher natural frequencies),
- high reliability (the possibility of diaphragm cracks is eliminated),
- requirement of only one bearing to take the thrust.

The main reason for the choice of the quill shaft is the higher natural frequencies of the rotor yielding a greater margin of the maximum speed to the second bending mode frequency of the compressor. However, because of this type of coupling the alignment of the compressor had to be handled very carefully, since it changes the bearing loads, and the controller of each bearing had to account for the combined modes of both rotors (compressor and motor).

DESCRIPTION OF THE ROTOR AND ITS DYNAMIC BEHAVIOUR

The basic data of the two shafts connected with a quill shaft are as follows:

Weight of the motor shaft:	240 kg.
Weight of the compressor shaft:	100 kg.
Length of the motor shaft:	app. 1.1 m.
Length of the compressor shaft:	app. 1.2m
Frequency of the first bending mode (motor alone in free condition):	440 Hz.
Frequency of the first bending mode (compressor alone in free condition):	220 Hz.

The connecting quill shaft has a length of 285mm and a diameter of 30mm.

Figure 3 shows the modes of the connected shafts at standstill and supported on soft springs. The vertical lines indicate the sensor (outer lines) and actuator positions (inner lines). It can be seen that each mode shape exhibits dominating deflections in one of the two rotors; hence they can be classified almost as the modes of the single rotors. However, every mode also has slight deflections in the other rotor.

Table 1 shows the observability (sensor not in a node) and commandability (actuator not in a node) of each mode. All modes below the maximum speed (up to the fifth) should be readily observable and commandable in order to enable the bearings to provide sufficient damping. Higher modes need not be well damped, but they must not be excited by the bearings. Good observability and commandability of these modes are not necessary, and in some cases not desirable either.

Figure 4 shows the natural frequencies of the modes at standstill and at full speed. It shows how the frequencies are shifted by the gyroscopic effect.The frequencies of the modes above the fourth are not shifted by more than 5%. The magnetic bearing controllers must be insensitive to these shifts.

REQUIRED AND REALIZED BEARING TRANSFER FUNCTION

The transfer function of the magnetic bearing (= relation between input (=sensor displacement signal) and output (= bearing force)) is mainly determined by the controller. Hence designing the transfer function means tuning the controller.

Figures 5,6 and 7 show the realized transfer functions (amplitude and phase) for the motor and compressor bearings. They also include an approximation for the amplifier and actuator. The motor bearing function has the order 12 in the z domain, those of the two compressor bearings 13. The relationship between amplitude and phase of the transfer function and stiffness and damping of the bearing is given by the following formulae.

$$A = \sqrt{(d\omega)^2 + k^2} \tag{1}$$

$$\phi = \arctan(d\omega/k) \tag{2}$$

or

$$k = A \cos \phi \tag{3}$$

$$d = A \sin \phi / \omega \tag{4}$$

An analysis of the compressor rotor was carried out with two similar bearings having a spring and damper characteristic in order to get an idea in the design phase of the necessary bearing damping for a sufficient damping ratio of all modes below the maximum speed. The noncollocation of sensor and actuator is taken into account as described in /1/ and /2/. The analysis was carried out for the compressor only, because its bending mode is in the operating speed range.

Figures 8 and 9 show the eigenvalues (damping ratio and frequency) of the first three compressor modes for two bearing stiffnesses (10^7N/m and $2 \cdot 10^7$N/m) and various bearing damping coefficients. The stiffness should not be lower than 10^7N/m in order to enable the bearing to withstand aerodynamic excitations. On the other hand, it should not be much higher because the bearing damping then becomes less efficient. A damping ratio of 10% is normally the minimum requirement for safe operation in the critical speed, although much higher damping ratios are possible.

Table 2 shows a comparison of the realized and necessary characteristics needed to damp the compressor bending mode according to the minimum requirement of 10%. It is not fulfilled on the drive

end side, whereas it is surpassed on the non drive side. An analysis of the eigenvalues of the closed loop system will show whether the combination can fulfil the requirement.

The modes above the maximum speed, which must not be excited by the bearings, are the reason that the realized bearing damping is to be of a magnitude equal to the minimum requirement and not much higher. For positive bearing damping, an excitation can happen if the mode shape has a node between sensor and actuator. It can also happen if the bearing damping becomes negative due to phase losses in the actuator and amplifier or due to phase losses caused by the sampling of the digital controller. In order to prevent an excitation a bad observability or commandability of the mode and a low amplitude of the transfer function are helpful. A low amplitude in the high frequency region limits the bearing damping at the bending mode frequency. For the well observable and commandable high modes, the transfer function should provide some damping. This means it should have a phase between either 0° and 90°, or between -180° and -270°. This yields positive damping according to equation (4). The latter case yields a negative stiffness according to equation (3), but is not destabilizing for high modes. The compressor DE bearing can observe and command all modes up to 1500 Hz, most of them well (see table 1). The tuning of this bearing was particularly difficult therefore. An analysis of the eigenvalues will show if all modes are stable in the higher frequency region.

THE CLOSED LOOP BEHAVIOUR

Analysis

All analog parts are transformed to the z domain, duly considering the zero order hold, for the analysis of the closed loop behaviour. The analog parts are the rotor (its finite element model), the sensor and the actuator. These three parts are in series mode at each bearing. The closed loop system with the digital controller can then be built in the z domain. All these operations are carried out with the programme MATLAB. The modeling of the rotor and the plotting of eigenvectors are carried out with the finite element programme MADYN /3/. Figure 10 provides an overview for the procedure of the closed loop calculations.

Results

Figure 11 shows the modes (real and imaginary part, which are the shapes at two instances $\omega t=90^o$ apart) of the closed loop system up to 1500 Hz at standstill. The demonstrated modes are only modes with major deflections in the rotor. They correspond to the modes of the rotor supported on soft springs. Due to the controller coordinates, additional modes arise which are not shown here. They are well damped, have relative small rotor deflections and normally are of no practical importance.

Table 3 shows the calculated damping ratios as well as a comparison of the calculated frequencies with measured frequencies. The coincidence of measured and calculated frequencies is not poor up to the seventh mode (second compressor bending mode). There are considerable deviations above this mode.

Two of the modes above the maximum speed (20000 rpm = 33 Hz) are unstable: The eighth and eleventh mode. This is due to the inaccurate frequencies of these modes. Due to the deviation of the calculated frequency, the eighth mode is in a region, where the transfer function of the DE bearing of the compressor has a phase angle of about -150° yielding a negative damping. In reality, the frequency is in a region, where the phase is about -200° yielding a positive damping. The other bearings have only very little or no influence on the stability of this mode. In case of the eleventh mode, the calculated frequency is in a region where the motor bearing transfer function has a phase angle of about -40°, hence a negative damping, whereas in reality the frequency is in a region with positive damping (positive phase angle of about 45°). The compressor bearings have little or no influence on this mode.

The damping ratios for all modes are sufficently high within the speed range. The first bending mode of the compressor has the lowest damping ratio of these modes. It is 11.8%, which is still above 10%. An unbalance response calculation helps to assess whether this is sufficient to run on the critical speed of this mode.

Figure 12 shows the calculated response of all bearing forces to two parallel unbalances of 60 gmm at the compressor shaft ends. This corresponds to G2.5. The magnetic bearing capacity for dynamic loads is about 600 N. It is reached at the NDE compressor bearing at the critical speed of the bending mode with a balance quality of G1.8, whereas the achieved balance quality is G0.65. An unbalance at the shaft ends is very unfavourable (because it is a very sensitive location) and unlikely to occur in reality. Assuming an unbalance in the middle of the compressor yields even more margin. The permissible unbalance then is more than twice as high. This proved to be sufficient during the extensive test programme of the machine.

EFFECT OF A MECHANICAL DAMPER

Figure 13 shows a sketch of a mechanical damper, which can be mounted on the non drive end side of the compressor. Its purpose is to provide additional damping to the higher modes above the maximum speed. It was prepared as a way out in case the tuning of the magnetic bearing proved unsuccessful. It was not necessary to be installed after all. However, its effect was studied theoretically. For this purpose, the damper was modeled as a concentrated mass (without moments of inertia) attached to the rotor with a spring and damper. The data are as follows:

Mass:	$m = 1.5$ kg
Stiffness:	$k = 2.1 \cdot 10^7$ N/m $\Rightarrow f_k = (\sqrt{k/m})/(2\pi) = 600$ Hz
Damping ratio (damper alone):	$D = 25\%, 50\%$

Since they were not exactly known two values were assumed for the damping ratio.

Figure 14 shows the effect of the damper on the frequencies and damping ratios of all modes up to 1500 Hz. The high compressor modes 5 to 8 and 10 are affected more than the motor modes 9 and 11. The damping effect on the compressor modes above the damper mode is considerable. The frequencies above the damper mode are increased for a damper damping ratio of 25% , whereas they are slightly decreased as all the others for the 50% case.

CONCLUSIONS

A transfer function of the magnetic bearings was designed which is able to fulfil all necessary requirements: It provides sufficient damping to all modes below maximum speed, especially to the compressor bending mode, which is in the operating speed range and is able to ensure the stability of all modes above maximum speed. This was achieved in spite of a rigid coupling with the consequence, that each bearing has to consider the modes of both rotors. The main advantage of the coupling is a higher margin of the maximum speed to the frequency of the second compressor bending mode. It was not necessary to mount a mechanical damper, which could provide additional damping to the higher modes, as was shown theoretically .

ACKNOWLEDGEMENTS

REFERENCES

1. Schmied, J.: Experience with Magnetic Bearings Supporting a Pipeline Compressor. Proceedings of the 2nd International Symposium on Magnetic Bearing, July 12-14, 1990, Tokyo, Japan.

2. Schmied, J., Pradetto, J.C.: Selbsterregte Schwingungen bei magnetgelagerten Rotoren. VDI Berichte Nr. 957, 1992.

3. Klement, H.D.: MADYN - Ein Programmsystem für die Maschinenberechnung. Unix/mail 5 (1987).

Table 1. Observability and Commandability of Natural Modes

mode	motor NDE	motor DE	comp. DE	comp. NDE
1, motor parallel	O yes / C yes	O yes / C yes	O weak / C weak	O no / C no
2, comp. parallel	O yes / C yes	O yes / C yes	O yes / C yes	O yes / C yes
3, motor tilting	O yes / C yes	O yes / C yes	O yes / C yes	O yes / C yes
4, comp. tilting	O yes / C yes	O yes / C yes	O yes / C yes	O yes / C yes
5, 1.bend. comp.	O weak / C weak	O weak / C weak	O yes / C yes	O yes / C yes
6, 2.bend. comp.	O weak / C weak	O weak / C weak	O yes / C yes	O yes / C yes
7, 2.bend. comp.*	O weak / C weak	O weak / C weak	O yes / C yes	O yes / C no
8, 3.bend. comp.	O weak/ C weak	O weak / C no	O yes / C yes	O no / C yes
9, 1.bend. motor	O yes / C yes	C yes / O yes	O yes / C yes	O no / C yes
10, 3.bend.comp.+	O yes / C yes	O yes / C yes	O yes / C yes	O yes / C yes
11, 2.bend.motor	O yes / C yes	O yes / C no	O weak / C weak	O weak / C weak

* Quill shaft has one more node compared to 6.
+ Quill shaft has one more node compared to 8.
O = Observability
C = Commandability

Table 2. Necessary and Realized Compressor Bearing Characteristics at the Bending Mode Frequency.

	according to figure 5	according to figure 6	DE bearing	NDE bearing
k [N/m]	10^7	$2 \ 10^7$	$1.66 \ 10^7$	$2.3 \ 10^7$
d [Ns/m]	8000	8000	$2.44 \ 10^3$	$1.4 \ 10^4$
A [N/m]	$1.55 \ 10^7$	$2.4 \ 10^7$	$1.7 \ 10^7$	$3.2 \ 10^7$
ϕ [degree]	50	33	12.5	42

Table 3. Frequencies and Damping Ratios of the Closed Loop System

mode	$f_{calculated}$ [Hz]	$D_{calculated}$ [%]	$f_{measured}$ [Hz]	$|\Delta f/f_{measured}|$
1, motor parallel	45.5	31.3	45	0.0 %
2, comp.parallel	68.1	23.2	68	0.0 %
3, motor tilting	102.1	27.5	102	0.0 %
4, comp. tilting	124.7	34.1	125	0.2 %
5, 1.bend. comp.	243.2	11.6	240	1.3 %
6, 2.bend.comp.	389.5	1.9	405	3.8 %
7, 2.bend.comp.*	514.8	0.1	540	4.7 %
8, 3.bend.comp.	754.7	-1.8(unstable)	840	10.1 %
9, 1.bend.motor	1038.7	0.5		
10, 3.bend.comp.+	1158.4	0.2	1180	1.8 %
11, 2.bend.motor	1470.9	-1.0(unstable)	1350	9.0 %

* Quill shaft has one more node compared to 6.
+ Quill shaft has one more node compared to 8.

1 Auxiliary bearings
2 Radial magnetic bearings
3 Axial magnetic bearing
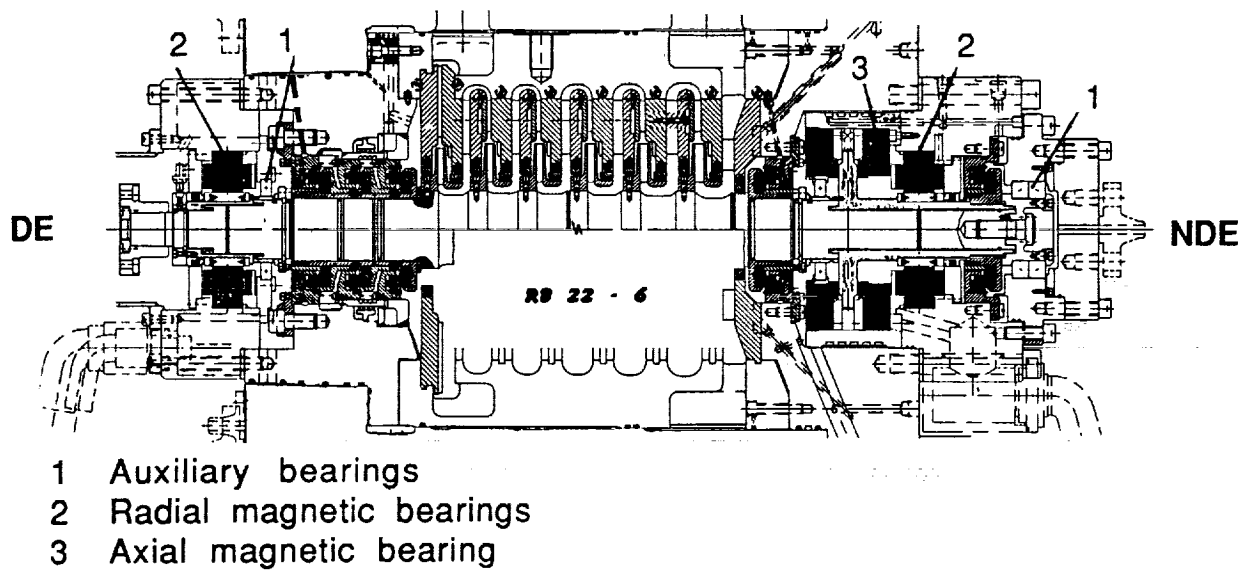
Figure 1. Cross section of the compressor.
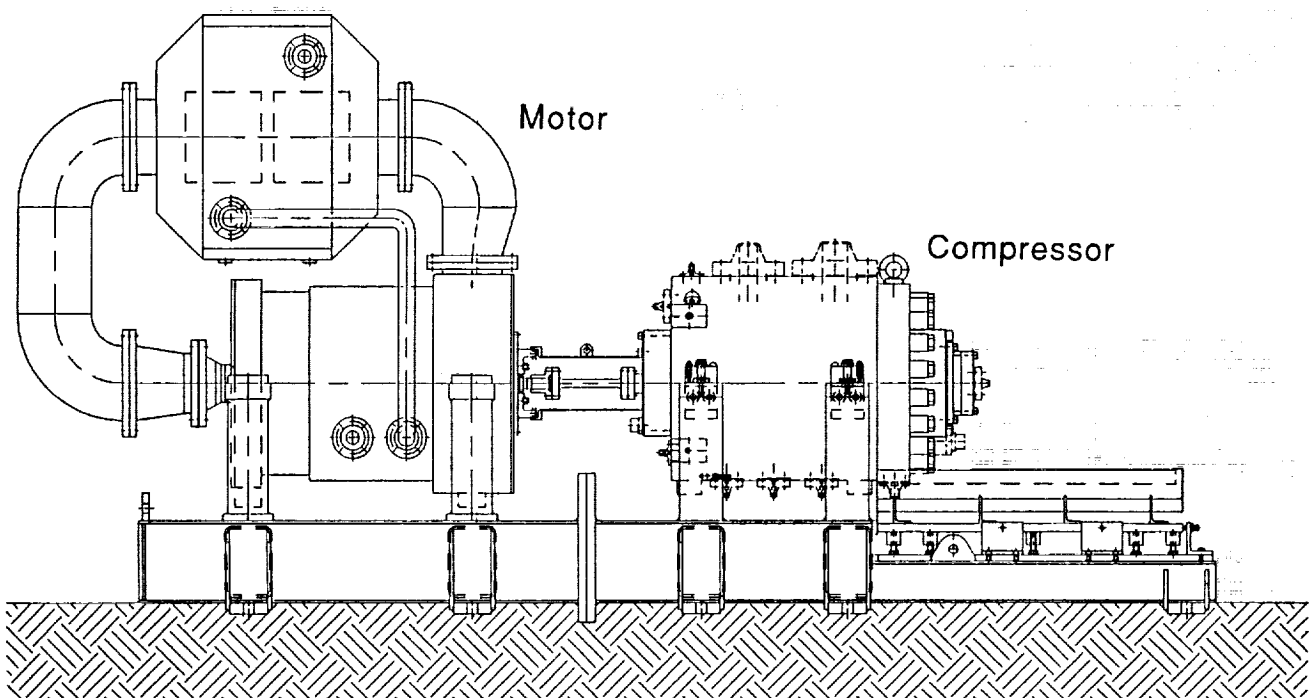
Figure 2. Arrangement of the motor compressor unit.
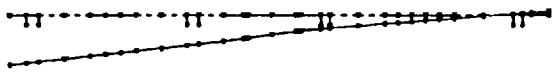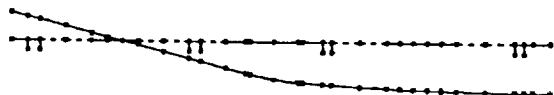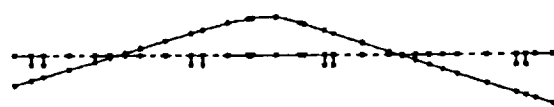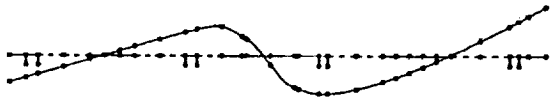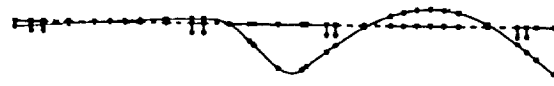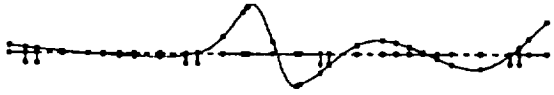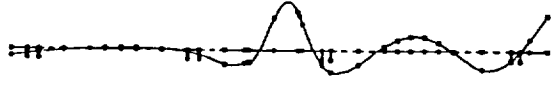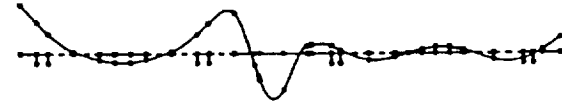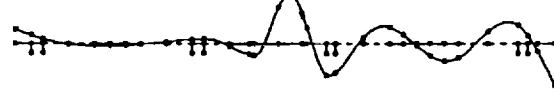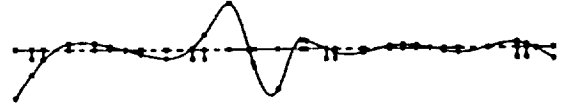
Mode Shape	Number, Frequency
	1, 15.0Hz
	2, 22.4Hz
	3, 29.2Hz
	4, 76.4Hz
	5, 220.9Hz
	6, 378.9Hz
	7, 515.4Hz
	8, 787.1Hz
	9, 994.9Hz
	10, 1162.5Hz
	11, 1463.0Hz

Figure 3. Modes of the coupled shaft supported on soft springs ($k=10^6 N/m$).
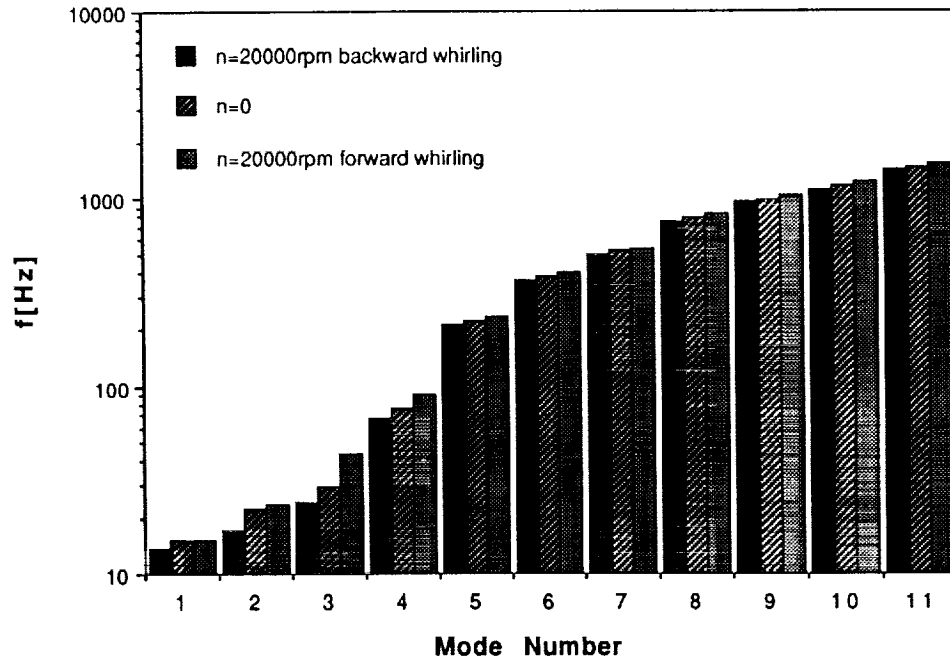
Figure 4. Natural frequencies of the shaft at standstill and full speed.
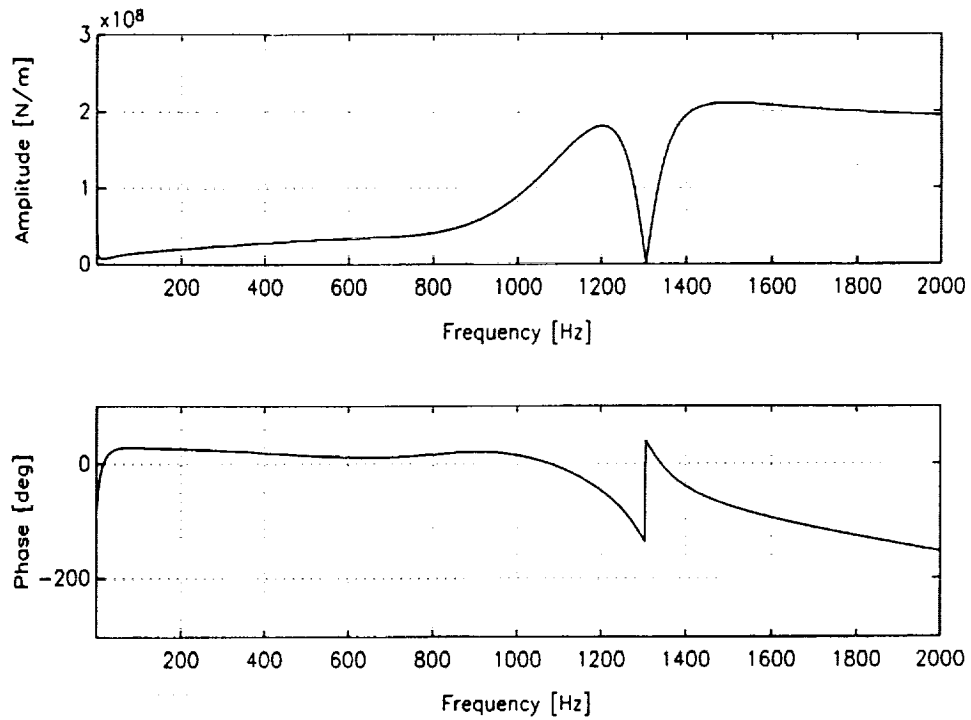
Figure 5. Transfer function of the motor magnetic bearings.
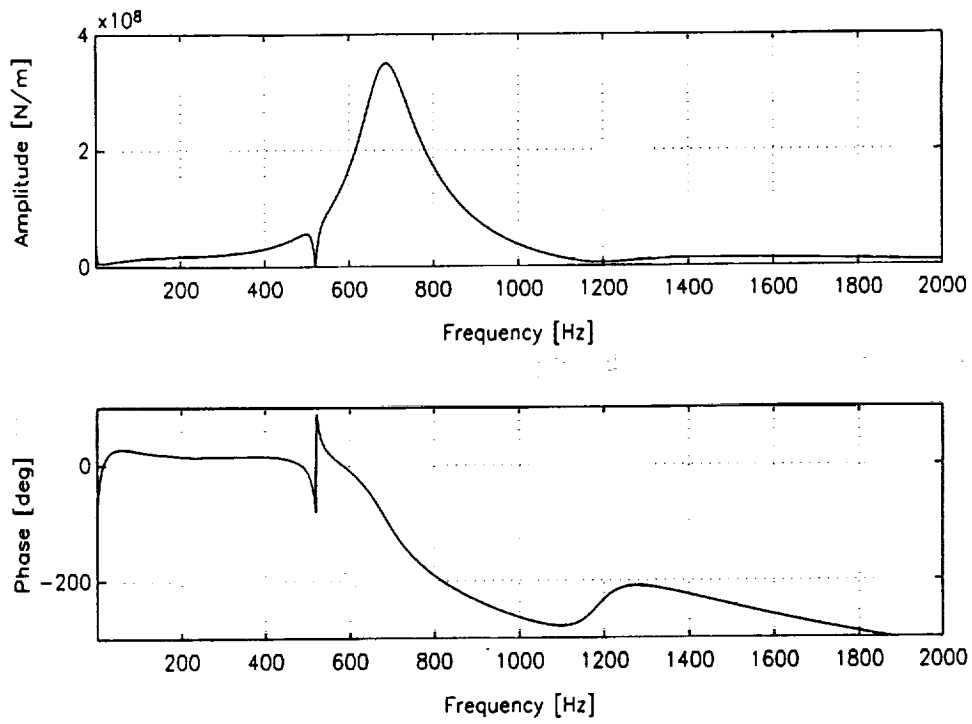
Figure 6. Transfer function of the DE compressor magnetic bearing.
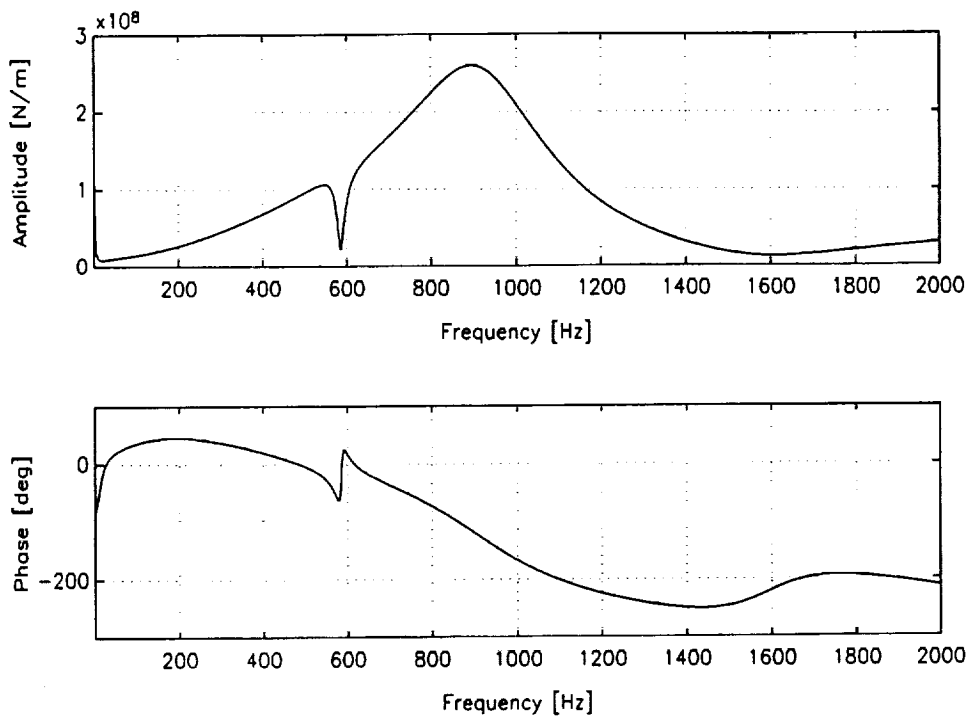
Figure 7. Transfer function of the NDE compressor magnetic bearing.
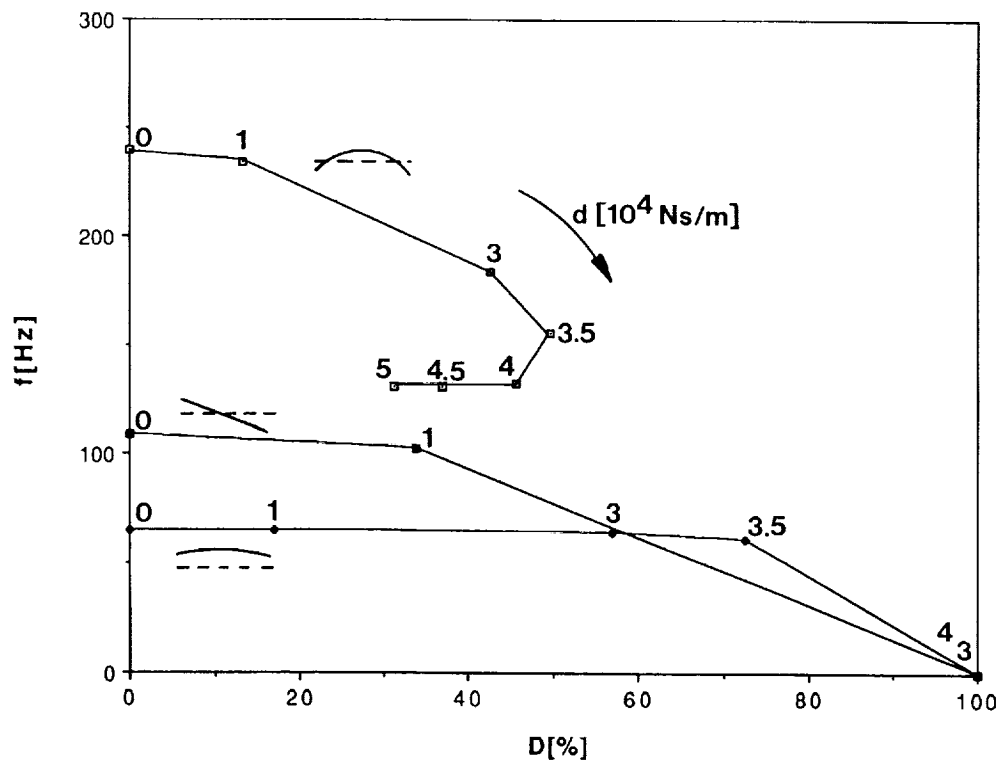
Figure 8. Eigenvalues of the compressor rotor as a function of the bearing damping for a bearing stiffness of 10^7N/m.
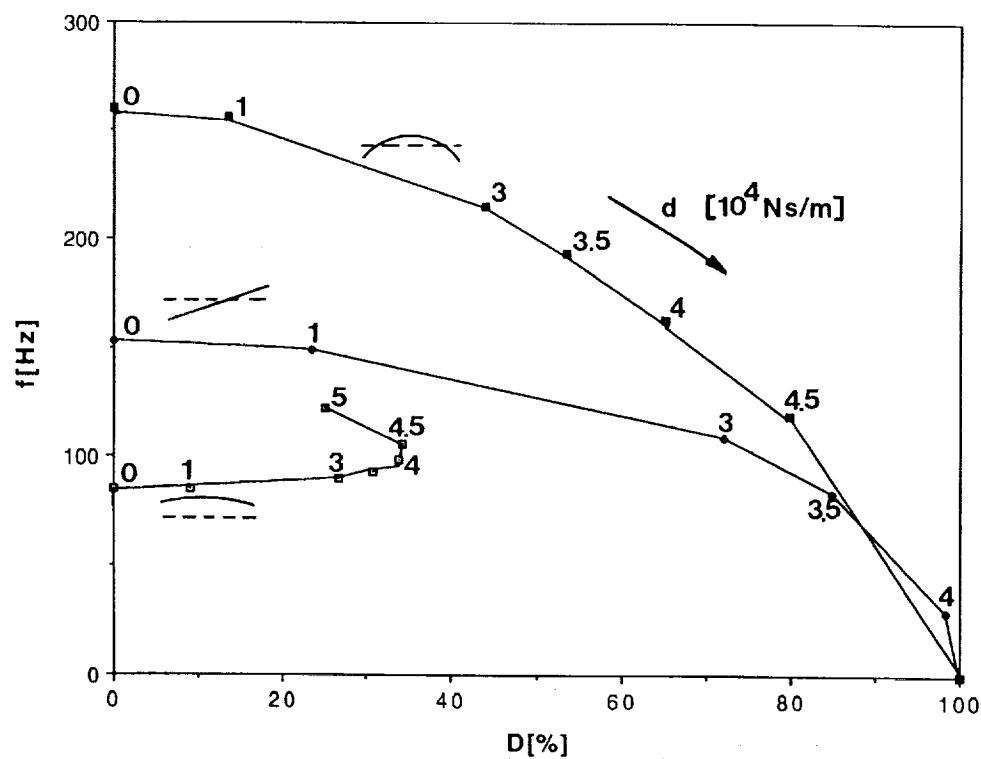
Figure 9. Eigenvalues of the compressor rotor as a function of the bearing damping for a bearing stiffness of 2.0 10^7N/m.
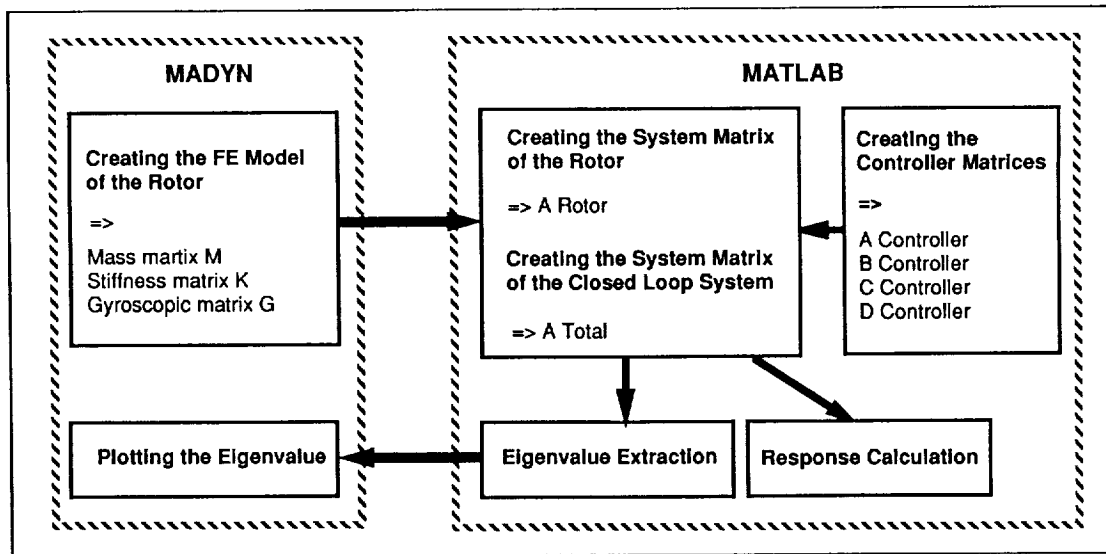
Figure 10. Procedure for closed loop calculations.
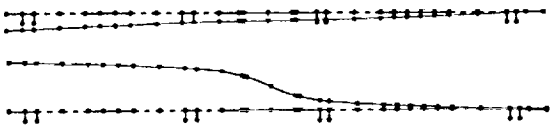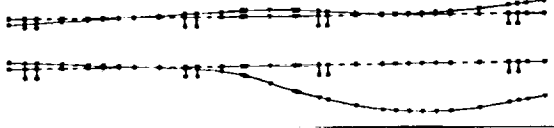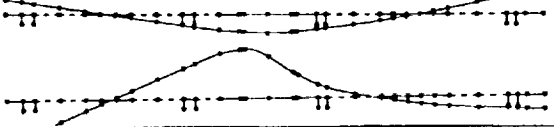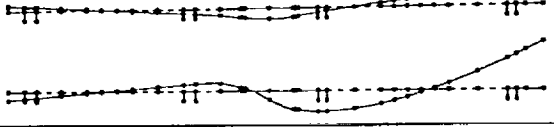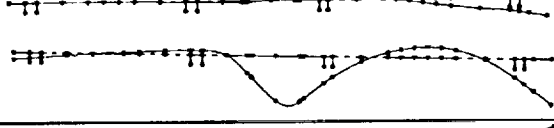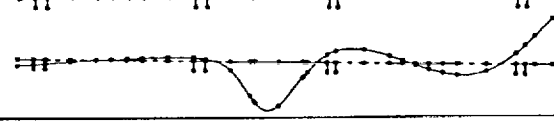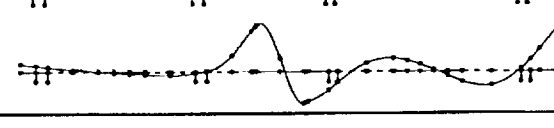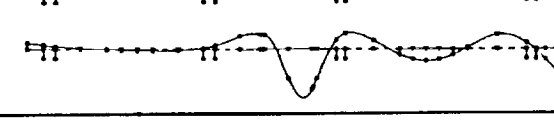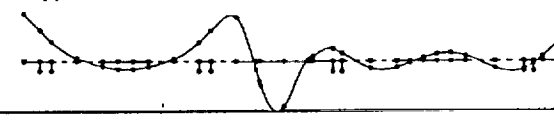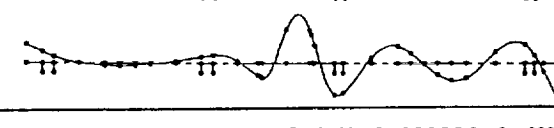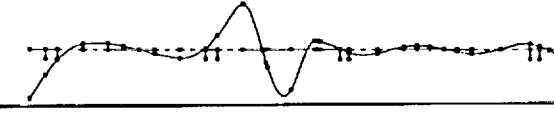
Mode Shape	Number, Freq., Damp.Ratio
Im Re	1, 45.5Hz, 31.3%
Im Re	2, 68.1Hz, 23.2%
Im Re	3, 102.1Hz, 27.5%
Im Re	4, 124.7Hz, 34.1%
Im Re	5, 243.2Hz, 11.6%
Im Re	6, 389.5Hz, 1.9%
Im Re	7, 514.8Hz, 0.1%
Im Re	8, 754.7Hz, -1.8%
Im Re	9, 1038.7Hz, 0.5%
Im Re	10, 1158.4Hz, 0.2%
Im Re	11, 1470.9Hz, -1.0%

Figure 11. Rotor modes of the closed loop system.
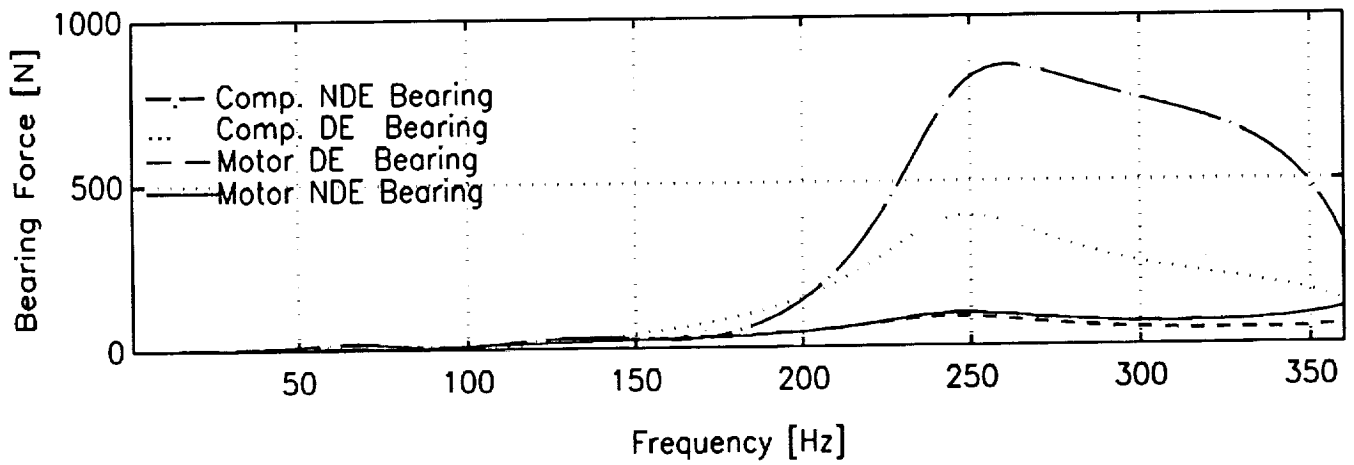
Figure 12. Bearing responses to a parallel unbalance (G2.5) in the compressor.
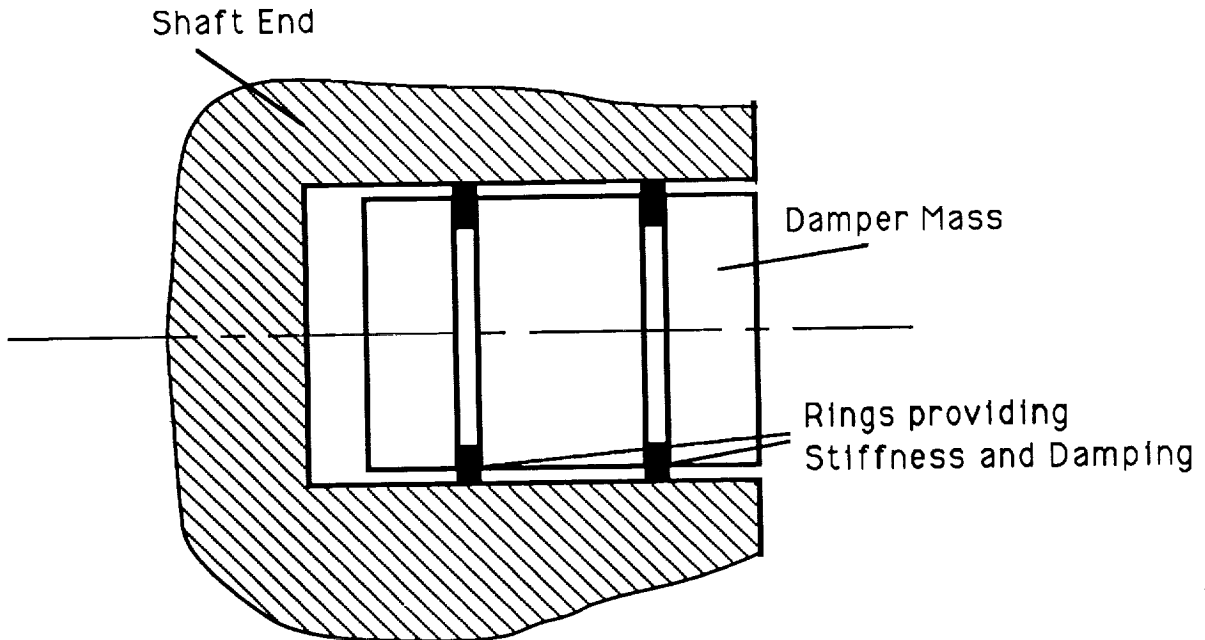
Figure 13. Sketch of the mechanical damper.
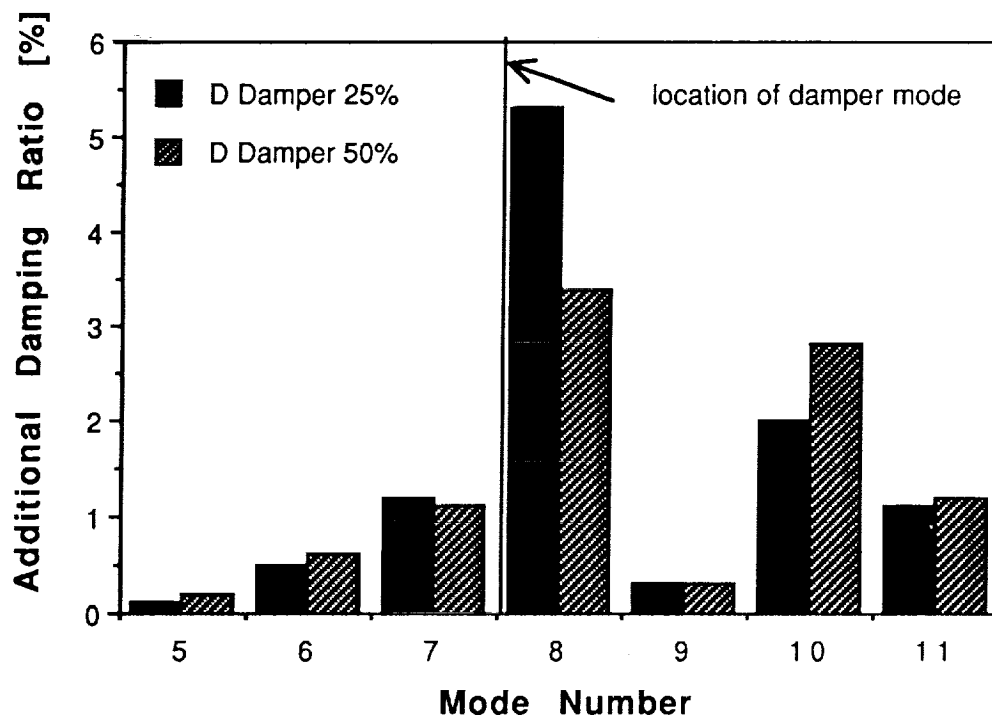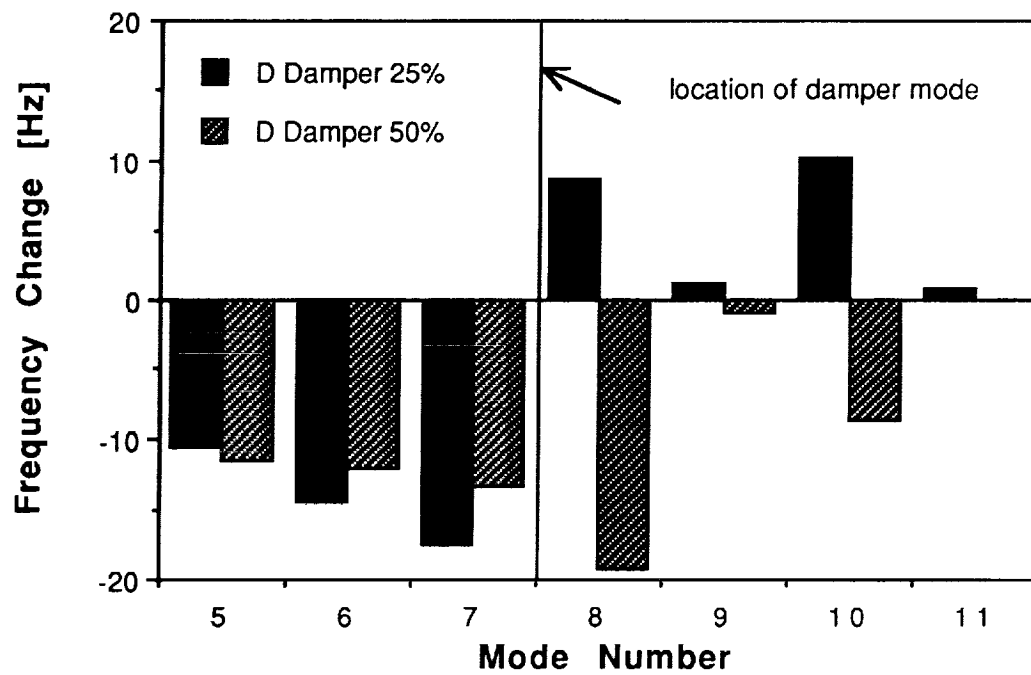
Figure 14. Effect of a mechanical damper on the rotor modes.

Session 10a – Controls

Chairman: Alexander V. Kuzin
Moscow Aviation Technological Institute

NONLINEAR FEEDBACK MODEL ATTITUDE CONTROL USING CCD
IN MAGNETIC SUSPENSION SYSTEM

CHIN E. LIN   ANN-SAN HOU

INSTITUTE OF AERONAUTICS AND ASTRONAUTICS

CHENG KUNG UNIVERSITY
TAINAN, TAIWAN, CHINA

$S/0 - 37$

$//9/8$

$P- 8$

ABSTRACT

A model attitude control system for a magnetic suspension system using CCD camera is studied in this paper. In a recent work, a position and attitude sensing method was proposed using CCD [1]. From this result, model position and attitude in a magnetic suspension system can be detected by generating digital outputs. Based on this achievement, a control system design using nonlinear feedback technique for magnetic suspended model attitude control is proposed.

THE PROPOSED METHOD

In the CCD sensing system, positions of specified points on the model are detected, x_1 and x_2. The pitch angle, θ, and its $\sec(\theta)$ are calculated by hardware circuit. Assuming that two magnetic coils are used in such a system to levitate and control the magnetic suspended model in the test area, the control circuit then generates voltage outputs for magnet coils to induce appropriate currents. A studied magnetic suspension system as shown in Fig. 1 includes two controlled magnets with a longitudinal model. The proposed system block diagram is shown in Fig. 2.

Referring to the magnetic suspended model in Fig. 1, the energy equations of the model are described as:

the kinetic energy:

$$T = (\frac{m}{2}) [(\dot{X_1} + \dot{X_2})/2]^2 + (\frac{1}{24}m\,l^2)\,\dot{\theta}^2 \quad (1)$$

the potential energy:

$$V = -[(X_1 + X_2)/2]\,m\,g \quad (2)$$

where x_1 and x_2 are positions of the specified points on the model, θ is the pitch angle of the model, m is the model mass on the center of gravity, l is the effective distance between two specified points on the model, and g is the gravitational acceleration, with a constraint equation of:

$$\sin(\theta) = (X_2 - X_1) / l \qquad (3)$$

From the Lagrange equation, we have:

$$\frac{d}{dt}(\partial L / \partial \dot{X}_1) - (\partial L / \partial X_1) = -F_1 + \lambda$$

to get:

$$(\frac{m}{4})(\ddot{X}_1 + \ddot{X}_2) - mg/2 = -F_1 + \lambda \qquad (4)$$

for variable x_1; then

$$\frac{d}{dt}(\partial L / \partial \dot{X}_2) - (\partial L / \partial X_2) = -F_2 - \lambda$$

to get:

$$(\frac{m}{4})(\ddot{X}_1 + \ddot{X}_2) - mg/2 = -F_2 - \lambda \qquad (5)$$

for variable x_2; and

$$\frac{d}{dt}(\partial L / \partial \dot{\theta}) - (\partial L / \partial \theta) = l\,\cos(\theta)\,\lambda$$

to get:

$$(m\,l^2 / 12)\,\ddot{\theta} = l\,\cos(\theta)\,\lambda \qquad (6)$$

for variable θ, where F_1 and F_2 represent the magnetic forces to the model, λ and $l\,cos(\theta)\lambda$ represent the constraint forces.

Subtracting Eq. 4 from Eq. 5,

$$\lambda = (F_1 - F_2) / 2$$

and substituting into Eq. 6, we get:

$$(m\,l^2 / 12)\,\ddot{\theta} + [\,(F_2 - F_1)/2\,]\,l\,\cos(\theta) = 0 \qquad (7)$$

Summing Eq. 4 and Eq. 5, we get:

576

$$m (\ddot{X_1} + \ddot{X_2}) / 2 - m g = -(F_1 + F_2) \qquad (8)$$

Using the nonlinear feedback technology, let the relations of applied magnetic forces and feedback signals be:

$$F_2 - F_1 = (-k_0 + k_1\theta + k_2\dot{\theta}) \sec(\theta) \qquad (9)$$

$$F_2 + F_1 = C_0 - C_1(X_1 + X_2) - C_2 (\dot{X_1} + \dot{X_2}) \qquad (10)$$

where k_i's and C_i's are system constants.
Substitute Eq. 9 into Eq. 7 to get:

$$(m \, l^2 / 12) \ddot{\theta} + (l / 2) (-k_0 + k_1\theta + k_2\dot{\theta}) = 0 \qquad (11)$$

and Eq. 10 into Eq. 8 to get:

$$(m / 2) (\ddot{X_1} + \ddot{X_2}) + C_1 (X_1 + X_2) + C_2 (\dot{X_1} + \dot{X_2}) = mg + C_0 \qquad (12)$$

From Eq. 11 and Eq. 12, the external forces F_1, F_2, pitch angle θ and model position at its center of gravity $(x_1 + x_2)/2$ can be steadily controlled to a stable condition.
Summing Eq. 9 and Eq. 10, we get:

$$F_1 = [(-k_0 + k_1\theta + k_2\dot{\theta}) \sec(\theta) + C_0 - C_1(X_1 + X_2) - C_2(\dot{X_1} + \dot{X_2})]/2 \qquad (13)$$

$$F_2 = [-(-k_0 + k_1\theta + k_2\dot{\theta}) \sec(\theta) + C_0 - C_1(X_1 + X_2) - C_2(\dot{X_1} + \dot{X_2})]/2 \qquad (14)$$

From a known magnetic force model of the relationship between magnetic force and coil current in quadratic forms,

$$F_1 = (M_1 + C(i_1)i_1^2) / P(x_1, y_1) \qquad (15)$$

$$F_2 = (M_2 + C(i_2)i_2^2) / P(x_2, y_2) \qquad (16)$$

where M_1 and M_2 are magnetic dipoles. $P(x, y)$'s are polynomial functions of x and y. $C(i)$ is constant dependent on control current i .
The magnetic coil currents can be obtained as:

$$i_1 = [F_1 P(x_1, y_1) - M_1]^{1/2} \qquad (17)$$

$$i_2 = [F_2 P(x_2, y_2) - M_2]^{1/2} \qquad (18)$$

The control parameters of magnetic coil current can be calculated and controlled.

In this paper, the control system which feedbacks position signals from CCD camera and then generates appropriate output currents to the magnetic suspension system is designed and implemented using hardware circuits. System description and experimental results are demonstrated in a two coil magnetic suspension system.

SYSTEM IMPLEMENTATION

For the implementation of the proposed method, the block diagram shown in Figure 2 is designed and fabricated into hardware circuits. In the design process, the output data of the position and attitude are generated as shown in Figure 3. The input data of Figure 3 are generated from the proposed CCD measurement system [1]. The detailed block diagram of the real time control system for position and attitude control of the suspended model through CCD is designed as shown in Figure 4. Before applying the control method to the proposed system as shown in Figure 1, system model and parameters should be obtained. The system parameter measurement is carried out via magnetic field and force measurement from different locations within the control range of the two-pole levitation system. Assume that x denotes the vertical suspending distance from the pole, and y denotes the horizontal shift distance between two poles. The parameter measurement process sets the locations of y at 0 mm, 8 mm, and 16 mm for magnetic coil currents of 1.0 A to 5.0 A with 0.5 A each step. The magnetic force in g is measured and plotted on to figures similar to Figure 5. By a curve fitting process, the constant C with respect to coil current i is measured to get Figure 6. Via the described procedures, the polynomial function $P(x,y)$ as defined previously can be fitted into a figure as shown in Figure 7 with respect to different values of y. The data of $P(x,y)$ is used to substitute into Eqs. 15 and 16 to calculate the required magnetic force from each electromagnet pole. In the implementation, the applied power supply voltage V_{c1} and V_{c2} should be determined. From circuit designs, the relationship of voltage to current is fixed: $V_{c1} = i_1/2$, and $V_{c2} = i_2/2$, respectively. In the control concept, a ROM-mapping method is used. The basic idea of ROM-mapping is to memorize all possible positions and attitude control data into the read-only memory (ROM). The corresponding control data of power voltage will be searched from the ROM, and sent out as control commands.

PRELIMINARY RESULTS

In this study, the magnetic suspended model control is accomplished by CCD cameras. From the position and attitude sensing [1], two CCD's are proposed for six degrees of freedom measurements, such as Zc, Xc, and θ_{pitch} for CCD#1, and Yc,θ_{roll} , θ_{yaw} for CCD#2. The control approach can also follow the previous results. Some control results will be demonstrated in the conference. More details will be prepared on a revised version of the paper, and will be published in the conference proceedings. In this paper, the control system which feedbacks position signals from CCD camera and then generates appropriate output currents to the magnetic suspension system is designed and implemented using hardware circuits. System description and experimental results are demonstrated in a two coil magnetic suspension system.

ACKNOWLEDGEMENT

REFERENCES

[1] C. E. Lin, A. S. Hou, "A Real Time Position and Attitude Sensing Using CCD in Magnetic Suspension System Application", IEEE Instrumentation and Measurement Technology Conference, May 18-20, 1993, Irvine, California, USA.

[2] C. E. Lin, H. L. Jou, "Force Model Identification for Magnetic Suspension System via Magnetic Field Measurement", IEEE Transaction on Instrumentation and Measurement, June 1993, accepted.
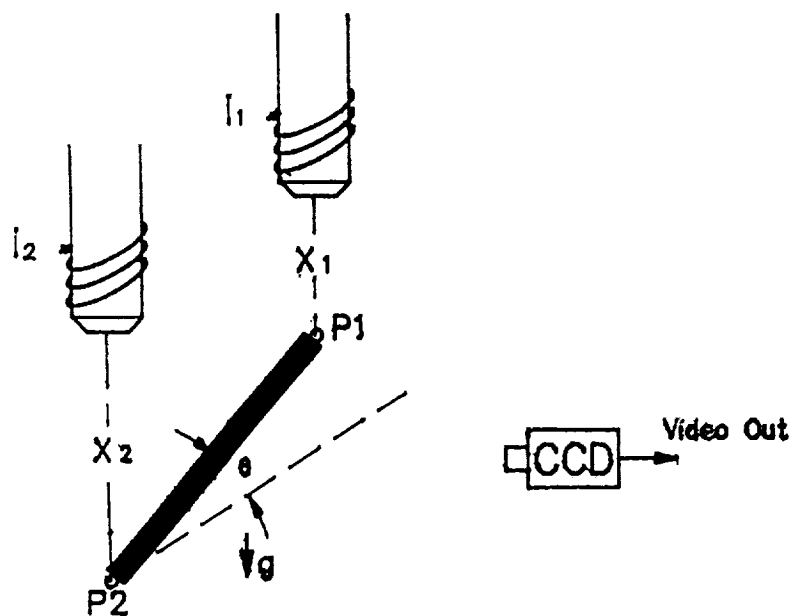
Fig. 1. The proposed experimental system using two electromagnet poles.
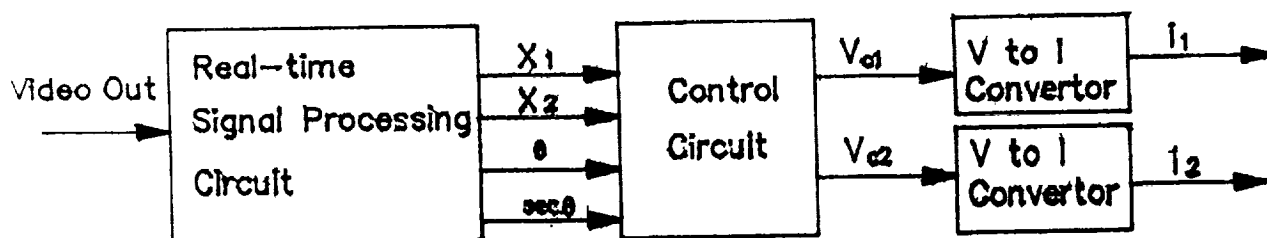
Fig. 2. The block diagram of real time position and attitude control from CCD measurement.
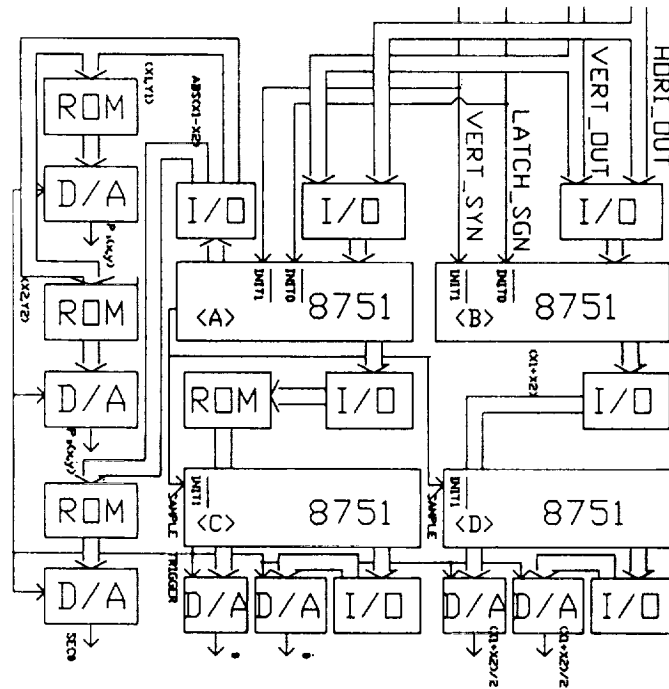
Fig. 3. The designed circuit in block diagrams to generate $\theta, \sec\theta$ and $(X_1 + X_2/2)$.
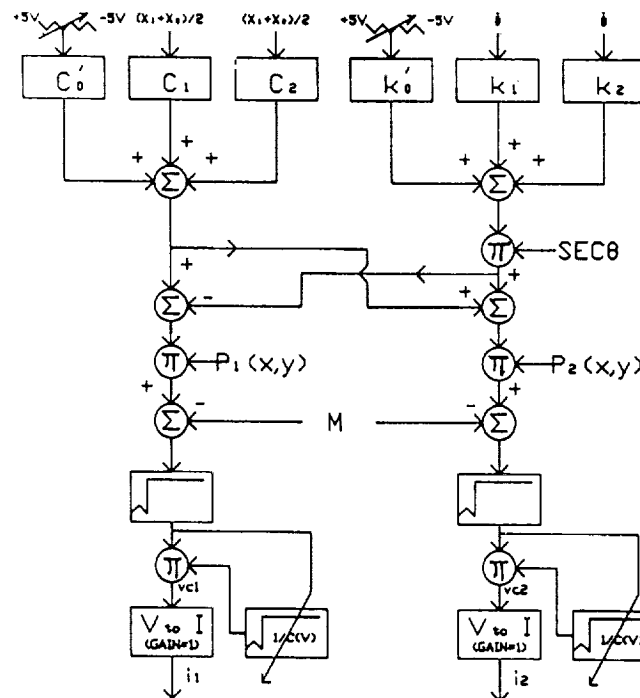
Fig. 4. The designed circuit in block diagrams to implement control algorithm .
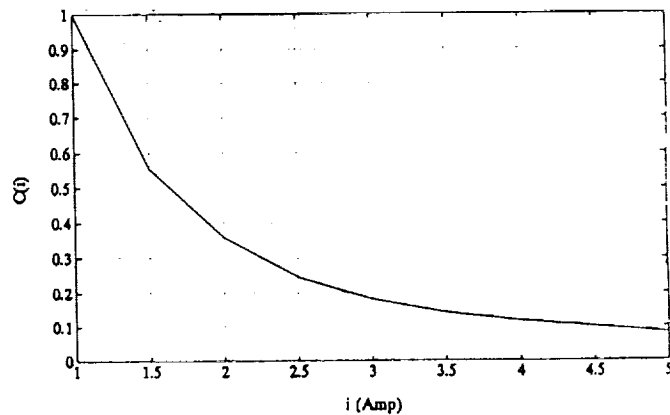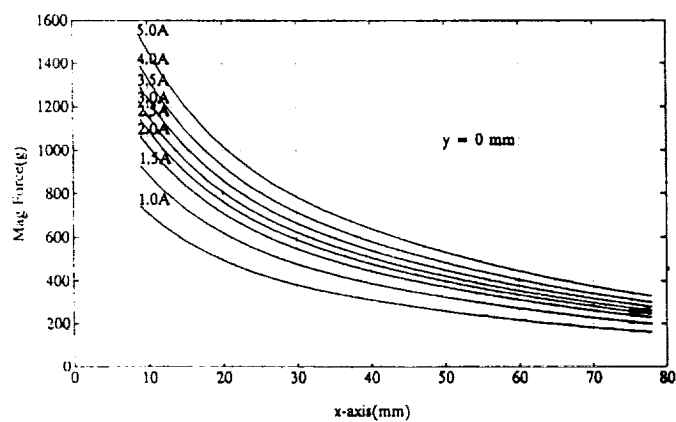
Fig. 6. Curve fitting result of constant C.
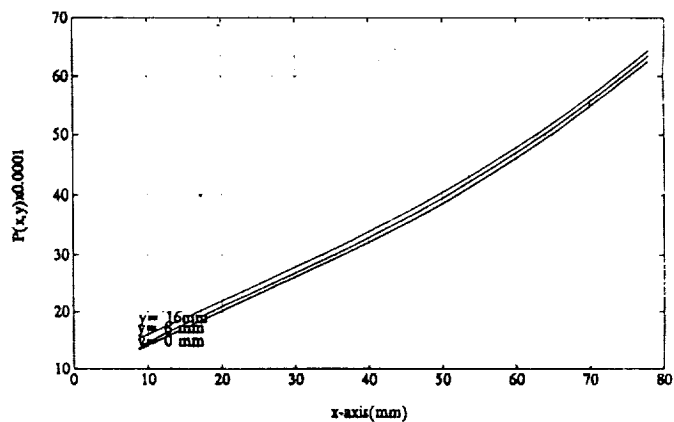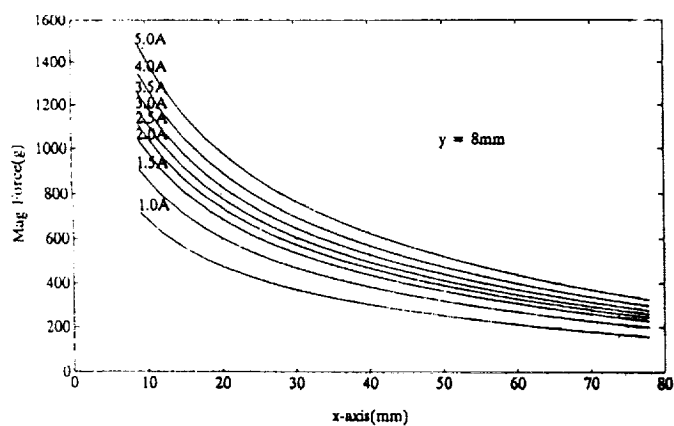
Fig. 7. The polynomial of P(x,y) obtained from results of Fig. 5.
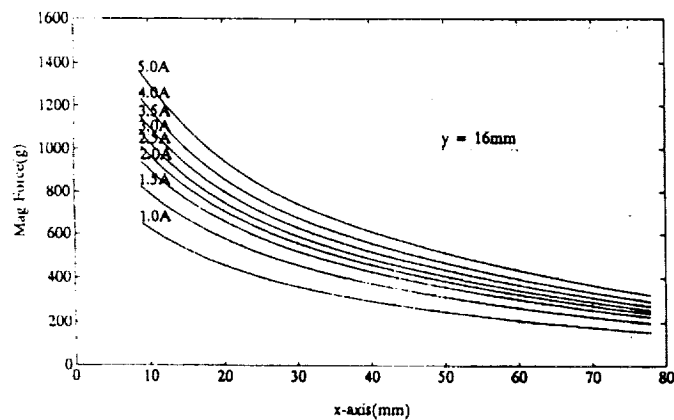
Fig. 5. Magnetic force measurement with respect to different coil currents.

ROBUST TRACKING CONTROL OF A MAGNETICALLY SUSPENDED RIGID BODY

Kyong B. Lim* and David E. Cox[†]
NASA Langley Research Center
Hampton, Virginia

$S_{11} - 37$

11919

$P. 21$

SUMMARY

This study is an application of H_∞ and μ-synthesis for designing robust tracking controllers for the Large Angle Magnetic Suspension Test Facility (LAMSTF). The modeling, design, analysis, simulation and testing of a control law that guarantees tracking performance under external disturbances and model uncertainties is investigated. The type of uncertainties considered and the tracking performance metric used is discussed. This study demonstrates the tradeoff between tracking performance at low frequencies and robustness at high frequencies. Two sets of controllers were designed and tested. The first set emphasized performance over robustness while the second set traded off performance for robustness. Comparisons of simulation and test results are also included. Current simulation and experimental results indicate that reasonably good robust tracking performance can be attained for this system using a multivariable robust control approach.

1 Introduction

The Large Angle Magnetic Suspension Test Facility (LAMSTF) has been assembled by NASA Langley Research Center for inhouse research in magnetic suspension technology. Reference [1] and the references therein give a detailed description of the facility and discuss in detail the open-loop dynamic properties of the magnetic suspension system. This system represents a scaled model of a planned Large-Gap Magnetic Suspension System (LGMSS). Robust tracking control for the LAMSTF consists of controlling the attitude and position of the suspended rigid body in the presence of external disturbances and model uncertainties. The motion of the suspended rigid body is in general nonlinear and hence the linear, time-invariant perturbed motion about an equilibrium state is considered in this study.

The underlying assumption in this study is that sufficiently accurate nominal and uncertainty models can be obtained from first principles combined with laboratory experiments. Indeed, currently there is a great deal of interest in the robust control community involving system identification for robust control. This motivates designing controllers that are robust to modeled uncertainties. We note that although empirical models could be synthesized through extensive testing in the laboratory or even in space, there are always physical limitations on the accuracy of the empirical model. The novelty in this paper consists in defining robust tracking performance, modeling of uncertainties, and evaluating simulation and experimental results.

The work reported herein parallels references [2]-[6]. The study reported in [2]-[6] considers vibration attenuation and fine-pointing control for a stable large flexible laboratory structure. In stark contrast to the above passively stable flexible structure, the LAMSTF system considered is a highly unstable rigid body. Furthermore, the nature of the uncertainties in the two systems differ; the uncertainty in the system in [2]-[6] is mostly due to inaccurate knowledge of damping, frequency and modeshapes of the structural modes and truncated higher frequency structural modes while for LAMSTF, the uncertainty is mostly due to errors

---

*Research Engineer, Spacecraft Controls Branch, Guidance and Control Division.
[†]Research Engineer, Spacecraft Controls Branch, Guidance and Control Division.

in the linearization about the equilibrium state, an inaccurate knowledge of the spatial distribution of the magnetic field, errors in the sensor system hardware, and errors at the plant input due to induced eddy currents.

2   LAMSTF Model

The system shown in Fig.1 is the LAMSTF system located at NASA Langley Research Center. This system basically consists of five electromagnets which actively suspend a small cylindrical permanent magnet. The cylinder is a rigid body and has six independent degrees of freedom, namely, three displacements and three rotations.

g - Acceleration due to Gravity
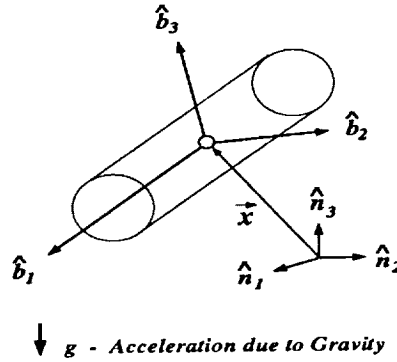
Figure 1: LAMSTF Configuration

2.1   Nonlinear Model

Let the unit vectors, $\hat{b}_i$ and $\hat{n}_i$, denote the i-th components of body and inertial coordinates which are initially assumed to be colinear. Define the following variables: the angular velocity of cylinder with respect to inertial frame $\vec{\omega} = \sum_{i=1}^{3} \omega_i \hat{b}_i$, disturbance torque about centroid $\vec{\Gamma} = \sum_{i=1}^{3} \Gamma_i \hat{b}_i$, centroid velocity $\vec{v} = \sum_{i=1}^{3} v_i \hat{n}_i$, position of centroid relative to origin of inertial frame $\vec{x} = \sum_{i=1}^{3} x_i \hat{n}_i$, and disturbance force acting on cylinder excluding magnetic forces as $\vec{F}_{ex} = \sum_{i=1}^{3} F_i \hat{n}_i$. Let $(\beta_0, \beta_1, \beta_2, \beta_3)$ denote the Euler parameters [7] which describe the attitude of the cylinder. The Euler parameters satisfy

$$\sum_{i=0}^{3} \beta_i = 1 \tag{1}$$

and the general rotational motion can be viewed as motions on the surface of a unit four dimensional hypersphere. Denote the direction cosine matrix by $C_{ij}, i, j = [1, 2, 3]$ where $\hat{b} = C\hat{n}$. The direction cosines are related to the Euler parameters by

$$C = \begin{bmatrix} \beta_0^2 + \beta_1^2 - \beta_2^2 - \beta_3^2 & 2(\beta_1\beta_2 + \beta_0\beta_3) & 2(\beta_1\beta_3 - \beta_0\beta_2) \\ 2(\beta_1\beta_2 - \beta_0\beta_3) & \beta_0^2 - \beta_1^2 + \beta_2^2 - \beta_3^2 & 2(\beta_2\beta_3 + \beta_0\beta_1) \\ 2(\beta_1\beta_3 + \beta_0\beta_2) & 2(\beta_2\beta_3 - \beta_0\beta_1) & \beta_0^2 - \beta_1^2 - \beta_2^2 + \beta_3^2 \end{bmatrix} \tag{2}$$

Due to symmetry about the 1-axis, the mass moment of inertia about the body axis is denoted by I_1 and $I_2 = I_3 = I_c$. Let the physical parameters, ν, M_x, and m_c, denote the core volume, core magnetization, and mass of the suspended body, respectively. The nonlinear equation of motion for the cylindrical magnet in a magnetic field is given as follows:

$$\begin{Bmatrix} \dot{\omega}_1 \\ \dot{\omega}_2 \\ \dot{\omega}_3 \end{Bmatrix} = - \begin{Bmatrix} 0 \\ \frac{I_1 - I_c}{I_c} \omega_1 \omega_3 \\ \frac{I_c - I_1}{I_c} \omega_1 \omega_2 \end{Bmatrix} + \frac{\nu M_x}{I_c} \begin{Bmatrix} 0 \\ -C_{31}B_1 - C_{32}B_2 - C_{33}B_3 \\ C_{21}B_1 + C_{22}B_2 + C_{23}B_3 \end{Bmatrix} + \begin{Bmatrix} \Gamma_1/I_1 \\ \Gamma_2/I_c \\ \Gamma_3/I_c \end{Bmatrix} \tag{3}$$

$$\left\{\begin{array}{c} \dot{\beta}_0 \\ \dot{\beta}_1 \\ \dot{\beta}_2 \\ \dot{\beta}_3 \end{array}\right\} = \frac{1}{2} \left[\begin{array}{cccc} 0 & -\omega_1 & -\omega_2 & -\omega_3 \\ \omega_1 & 0 & \omega_3 & -\omega_2 \\ \omega_2 & -\omega_3 & 0 & \omega_1 \\ \omega_3 & \omega_2 & -\omega_1 & 0 \end{array}\right] \left\{\begin{array}{c} \beta_0 \\ \beta_1 \\ \beta_2 \\ \beta_3 \end{array}\right\} \tag{4}$$

$$\left\{\begin{array}{c} \dot{v}_1 \\ \dot{v}_2 \\ \dot{v}_3 \end{array}\right\} = \frac{\nu M_x}{m_c} \left[\begin{array}{ccc} B_{11} & B_{12} & B_{13} \\ B_{21} & B_{22} & B_{23} \\ B_{31} & B_{32} & B_{33} \end{array}\right] \left\{\begin{array}{c} C_{11} \\ C_{12} \\ C_{13} \end{array}\right\} - \left\{\begin{array}{c} 0 \\ 0 \\ g \end{array}\right\} + \frac{1}{m_c} \left\{\begin{array}{c} F_1 \\ F_2 \\ F_3 \end{array}\right\} \tag{5}$$

$$\left\{\begin{array}{c} \dot{x}_1 \\ \dot{x}_2 \\ \dot{x}_3 \end{array}\right\} = \left\{\begin{array}{c} v_1 \\ v_2 \\ v_3 \end{array}\right\} \tag{6}$$

The variables, B_i and B_{ij}, denote the i-th inertial component of the magnetic field and its gradient in the j-th inertial direction at the instantaneous centroid location of the suspended magnet, respectively. Hence, in general, $B_i = B_i(x, \rho)$, and $B_{ij} = B_{ij}(x, \rho)$ are dependent on the instantaneous centroid location of the suspended mass, $x = (x_1, x_2, x_3)^T$, and the current applied to the five electromagnets, $\rho = (\rho_1, \ldots, \rho_5)^T$.

By defining the (13 by 1) state vector

$$\eta = (\omega_1, \omega_2, \omega_3, \ \beta_0, \beta_1, \beta_2, \beta_3, \ v_1, v_2, v_3, \ x_1, x_2, x_3)^T \tag{7}$$

and external disturbances

$$q = \left(\begin{array}{cccccccc} \Gamma_1/I_1 & \Gamma_2/I_c & \Gamma_3/I_c & O_{1\times 4} & F_1/m_c & F_2/m_c & F_3/m_c & O_{1\times 3} \end{array}\right)^T \tag{8}$$

the equation of motion can be written as

$$\dot{\eta} = f(\eta, \rho) + q \tag{9}$$

The five currents are the only control variables.

Currently, the general analytical expressions for $B_i(x, \rho)$ and $B_{ij}(x, \rho)$ are not available. However, the magnetic field is approximated quadratically in a small neighborhood around a nominal position and current, (x_o, ρ_o). Indeed, based on empirical measurements from the laboratory and with the aid of computer modeling, numerical values for the field distribution, its gradient, and curvature have been obtained about a point which is conveniently chosen to be the origin of the inertial coordinates. Let $x = x_o + \delta x$ and $\rho = \rho_o + \delta \rho$ denote the instantaneous centroid positions and the coil currents respectively. Then the measured second-order description of the i-th field component about the nominal values are given by

$$\begin{aligned} B_i(x, \rho) &= B_i(x_o, \rho_o) + \left[\frac{\partial B_i}{\partial(x_o, \rho_o)}\right] \left\{\begin{array}{c} \delta x \\ \delta \rho \end{array}\right\} \\ &+ \frac{1}{2} \left\{\begin{array}{c} \delta x \\ \delta \rho \end{array}\right\}^T \left[\frac{\partial^2 B_i}{\partial(x_o, \rho_o)^2}\right] \left\{\begin{array}{c} \delta x \\ \delta \rho \end{array}\right\} + \text{Higher Order Terms} \end{aligned} \tag{10}$$

The field gradients are also approximated by the quadratic fields, i.e., linearly approximated.

2.2 Equilibrium State

For convenience, the nominal position and currents are chosen at an equilibrium state. Consider the candidate equilibrium state

$$\eta_o = (0, 0, 0, \ 1, 0, 0, 0, \ 0, 0, 0, \ 0, 0, 0)^T \tag{11}$$

This equilibrium state corresponds to the body frame being colinear with inertial frame with zero angular and translational velocities. Imposing the requirement, $\dot{\eta} = 0$ at state η_o for zero external disturbances, leads to the equilibrating field and gradients which satisfy

$$\left[\begin{array}{ccc} C_{21} & C_{22} & C_{23} \\ C_{31} & C_{32} & C_{33} \end{array}\right]_{\eta_o} \left\{\begin{array}{c} B_1 \\ B_2 \\ B_3 \end{array}\right\}_{\eta_o} = \left\{\begin{array}{c} 0 \\ 0 \end{array}\right\} \tag{12}$$

$$\frac{\nu M_x}{m_c} \left[\begin{array}{ccc} B_{11} & B_{12} & B_{13} \\ B_{21} & B_{22} & B_{23} \\ B_{31} & B_{32} & B_{33} \end{array}\right]_{\eta_o} \left\{\begin{array}{c} C_{11} \\ C_{12} \\ C_{13} \end{array}\right\}_{\eta_o} - \left\{\begin{array}{c} 0 \\ 0 \\ g \end{array}\right\} = \left\{\begin{array}{c} 0 \\ 0 \\ 0 \end{array}\right\} \tag{13}$$

The above equations reduce to the following constraints:

$$B_2 = B_3 = B_{11} = B_{21} = 0; \quad B_{31} = \frac{m_c}{\nu M_x} g \tag{14}$$

To compute the corresponding equilibrating currents, we note that the field and gradient at η_o is a linear function of currents in the five electromagnets [1] and are given by

$$B_i(x_o, \rho) = K_i \rho; \quad i = (1,2,3) \tag{15}$$

$$B_{ij}(x_o, \rho) = K_{ij} \rho; \quad i, j = (1,2,3) \tag{16}$$

where K_i and K_{ij} are 5 by 1 row vectors which denote the fields at x_o produced by each coil per unit of current. Thus the equilibrating currents, ρ_o, must satisfy the five linear equations

$$\begin{bmatrix} K_2 \\ K_3 \\ K_{11} \\ K_{21} \\ K_{31} \end{bmatrix} \rho_o = \begin{Bmatrix} 0 \\ 0 \\ 0 \\ 0 \\ \frac{m_c}{\nu M_x} g \end{Bmatrix} \tag{17}$$

which is identical to equation (54) in [1]. The 5 by 5 coefficient matrix turns out to be a well-conditioned full rank matrix and hence the equilibrating currents are unique and can be computed accurately. In summary, the current, ρ_o, which satisfies the latter equations, will generate a magnetic field that results in the equilibrium state, η_o.

2.3 Perturbed Motion About Equilibrium

Consider perturbed motion,

$$\rho = \rho_o + \delta\rho; \qquad \eta = \eta_o + \delta\eta \tag{18}$$

From the nonlinear equations, note that the roll rate of the cylinder, ω_1, is uncontrollable from the magnetic forces and the perturbed Euler parameter, $\delta\dot{\beta}_0$, equals zero at equilibrium, i.e., $\delta\beta_o$ is a constant. In addition, the variation in the Euler parameters is not independent since $\delta\dot{\beta}_1 = -\delta\dot{\beta}_2 - \delta\dot{\beta}_3$ from Eq.(1) and $\delta\beta_0 = 0$. This means that three of the thirteen states can be eliminated in describing the perturbed motion as outlined below.

By defining the reduced (10 by 1) state vector

$$\xi = (\omega_2, \omega_3, \ \beta_2, \beta_3, \ v_1, v_2, v_3, \ x_1, x_2, x_3)^T \tag{19}$$

and using the second-order field approximation in Eq. (10) about the equilibrium, the linearized equation about η_o is given by

$$\delta\dot{\xi} = \hat{A}\delta\xi + \hat{B}\delta\rho + q_r \tag{20}$$

where $\delta\omega_1$ and $\delta\beta_0$ are constants, $\delta\beta_1 = -\delta\beta_2 - \delta\beta_3 - \delta\beta_0$,

$$q_r = \begin{pmatrix} \Gamma_2/I_c & \Gamma_3/I_c & O_{1\times 2} & F_1/m_c & F_2/m_c & (F_3 + 2\nu M_x B_{31}\delta\beta_o)/m_c & O_{1\times 3} \end{pmatrix}^T \tag{21}$$

and

$$\hat{A} = \begin{bmatrix} O_{2\times 2} & -\frac{2\nu M_x}{I_c} B_1 I_{2\times 2} & O_{2\times 3} & \frac{\nu M_x}{I_c} \begin{bmatrix} -B_{31} & -B_{32} & -B_{33} \\ 0 & B_{22} & B_{23} \end{bmatrix} \\ \frac{1}{2}I_{2\times 2} & O_{2\times 2} & O_{2\times 3} & O_{2\times 3} \\ O_{3\times 2} & \frac{2\nu M_x}{m_c} \begin{bmatrix} -B_{13} & 0 \\ -B_{23} & B_{22} \\ -B_{33} & B_{32} \end{bmatrix} & O_{3\times 3} & \frac{\nu M_x}{m_c} \begin{bmatrix} B_{111} & B_{112} & B_{113} \\ B_{211} & B_{212} & B_{213} \\ B_{311} & B_{312} & B_{313} \end{bmatrix} \\ O_{3\times 2} & O_{3\times 2} & I_{3\times 3} & O_{3\times 3} \end{bmatrix} \tag{22}$$

586

$$\hat{B} = \nu M_x \begin{bmatrix} \frac{1}{I_c} \begin{bmatrix} -K_3 \\ K_2 \end{bmatrix} \\ O_{2\times5} \\ \frac{1}{m_c} \begin{bmatrix} K_{11} \\ K_{21} \\ K_{31} \end{bmatrix} \\ O_{3\times5} \end{bmatrix} \qquad (23)$$

It can be shown that all ten states are completely controllable from the five coil currents. The open-loop system at the equilibrium state is also very unstable. For a detailed discussion of the physical significance of all modes, the interested reader is referred to [1].

2.4   Sensing and Actuation

Five physical variables are sensed indirectly and they are the pitch and yaw angles, and three displacements of the centroid. For large angles, the pitch and yaw angles (hence direction cosines) are related nonlinearly to the Euler parameters as given by Eq.(2).

For small angles, the rotation and displacements are actually perturbed rotations and displacements about the equilibrium state. The five physical variables sensed, denoted as y', are related approximately linearly to the Euler parameters as

$$y' = \left\{ \begin{array}{c} \delta(\text{pitch}) \\ \delta(\text{yaw}) \\ \delta(\text{x-transl}) \\ \delta(\text{y-transl}) \\ \delta(\text{z-transl}) \end{array} \right\} \approx \left\{ \begin{array}{c} 2\delta\beta_2 \\ 2\delta\beta_3 \\ \delta x_1 \\ \delta x_2 \\ \delta x_3 \end{array} \right\} = \hat{C}\delta\xi \qquad (24)$$

where

$$\hat{C} = \begin{bmatrix} O_{2\times2} & 2I_{2\times2} & O_{2\times3} & O_{2\times3} \\ O_{3\times2} & O_{3\times2} & O_{3\times3} & I_{3\times3} \end{bmatrix} \qquad (25)$$

In the laboratory, the actual measured outputs denoted by y are voltages and are related to the angular and translation variables and perturbed states by

$$y = [\text{p2s}]\, y' = [\text{p2s}]\hat{C}\delta\xi \qquad (26)$$

Figure 2 shows the input and output block diagram of the LAMSTF plant. The input consists of five currents into five electromagnets and the measured outputs are five voltage signals. Very briefly, the current into the electromagnets generates a magnetic field which produces a net force and torque on the suspended cylinder, which is a permanent magnet. The resulting motion of the cylinder produces the pitch, yaw, and centroidal displacements that are sensed by a set of five optical shadow sensors that produce the output voltage signals. The sensor system has a high bandwidth and is modeled as an all-pass filter, i.e., the transfer function matrix is a constant, non-diagonal, non-singular matrix, denoted [p2s].
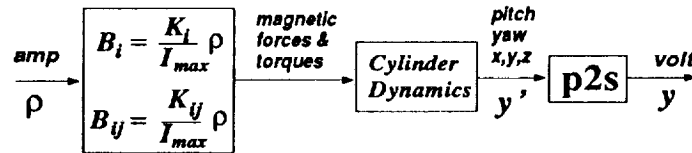
Figure 2: Block Diagram of LAMSTF Plant

3 Controller Design

3.1 Design Objectives

The main objective of the controller is to stabilize the cylinder and track a command signal about the equilibrium state. Of course the problem is complicated by the omni-presence of model errors and noise. Hence, robust tracking is sought. This requires the specification of a tracking performance index and the uncertainty set for which the tracking performance is supposedly guaranteed. While there are several ways to design multivariable stabilizing controllers, (for example, dissipative control, optimal linear regulator, eigensystem assignment, loop-at-a-time PID controller, or Youla parameterization), the challenging aspect is to guarantee a specific tracking performance in spite of imperfect knowledge of the actual physical system. Of course this guarantee is with respect to modeled uncertainty which itself may be uncertain. This in turn suggests that the designer's confidence level should be reflected in the degree of conservatism in the modeling of uncertainty, i.e., uncertainty in the uncertainty model itself is a real dilemma.

Controllers are sought for a set of plants that meet a certain tracking·performance in contrast to optimizing the closed loop system for a particular plant. The set of plants is defined by the nominal and uncertainty models. The linearized analytical model derived from first principles is used as the nominal model while the perturbations are obtained from engineering judgement without the benefit of any system identification test data. Figure 3 illustrates the interconnection of the nominal plant, modeled uncertainties, and the controller structure. Besides the tracking command and performance loops, uncertainties at the
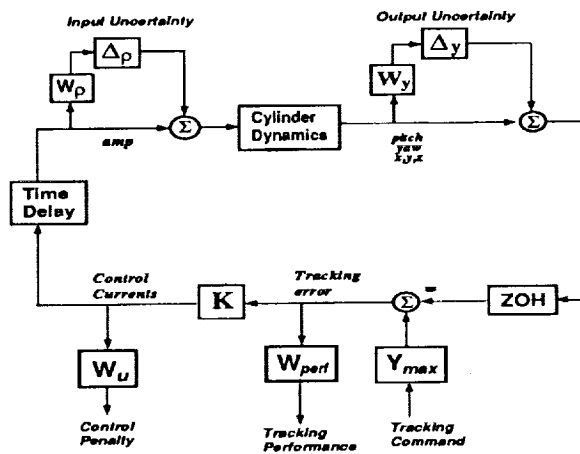
Figure 3: Interconnections of the LAMSTF system

plant input and output are included. The controller is also limited by a control penalty weight to prevent possible singular control solutions and to satisfy realistic actuator saturation constraints. Due to real time digital implementation, a computational time delay block and a zero-order-hold block are included. The following section provides details of the performance and uncertainty descriptions used in the control problem formulation.

3.2 Tracking Performance

The tracking performance of interest depends on the transfer functions from the tracking command, z_c, to the tracking error, e, where $e = z_c - y'$. This transfer function matrix is the sensitivity function matrix at the output and is written as

$$e/z_c = (I + GK)^{-1} \tag{27}$$

where GK denotes the loop gain matrix. In the sense of classical control, the inverse return difference (or sensitivity matrix) should be made small or alternately, the loop gain should be large over a bandwidth,

BW_{track}, of interest where tracking performance is desired. In terms of multivariable control, this requirement for smallness of the inverse return difference matrix can be defined by principal gains (i.e., singular values of transfer matrices) such that

$$\bar{\sigma}\left[(I + GK)^{-1}\right] \leq p(j\omega); \quad \forall \omega \in [0, \infty) \tag{28}$$

where the performance weighting function, $p(j\omega)$, which is chosen as a rational polynomial, should be relatively small over the bandwidth, BW_{track}.

So far, the above requirements assign equal importance to each component of the vector of error signals. However, two factors should further influence the tracking performance metric, namely, differing units and range of signals, and relative physical importance of signals. For this control design for LAMSTF, it is assumed that the maximum amplitudes of the desired tracking command are given by

$$Y_{max} = \text{diag}\left(\pm \tfrac{\pi}{180} rad \quad \pm \tfrac{\pi}{180} rad \quad \pm.0005 meters \quad \pm.0005 meters \quad \pm.0005 meters \right) \tag{29}$$

By normalizing the tracking command input by the absolute values of the above matrix, the command input will be normalized to unity. Note that the maximum singular value corresponding to this scaled transfer function from command input to tracking error can be interpreted as the maximum 2-norm error with respect to all unit 2-norm bounded tracking command vectors, scaled by Y_{max}. The tracking errors are then normalized by Y_{max}^{-1} to account for differing units and range of signals. Furthermore, the relative physical importance of the error signals are defined by a constant diagonal matrix, Φ, where $\Phi = \text{diag}(.9, .5, .5, .3, .3)$. The above requirements can be summarized as

$$\bar{\sigma}\left[\Phi Y_{max}^{-1}(I + GK)^{-1} Y_{max}\right] \leq p(j\omega); \quad \forall \omega \in [0, \infty) \tag{30}$$

In terms of H_∞ norm the above weighted constraint on the inverse return difference transfer function matrix becomes

$$\|W_{perf}(I + GK)^{-1} Y_{max}\|_\infty \leq 1 \tag{31}$$

where $W_{perf} = p(s)^{-1} \Phi Y_{max}^{-1}$.

Figure 4 shows the performance weight, $p(j\omega)$, used in the design. The first-order polynomial
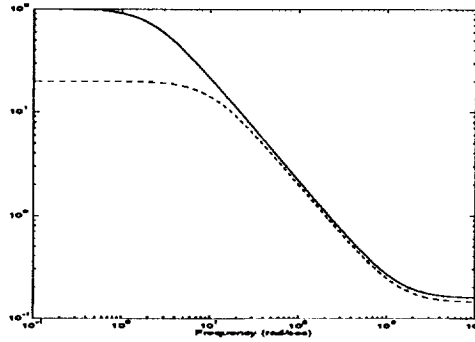
Figure 4: Frequency Weights $p(s)^{-1}$ for Tracking Performance. Performance case (solid), Robust case (dashed)

$$p(s) = f_{DC}\left[\frac{(s + \omega_n)}{(s + \omega_d)}\left(\frac{\omega_d}{\omega_n}\right)\right] \tag{32}$$

was chosen with $\omega_n = 2.2$ r/s, $\omega_d = 1400$ r/s, and $f_{DC} = .01$ for the performance case and $\omega_n = 10$ r/s, $\omega_d = 1400$ r/s, and $f_{DC} = .05$ for the robust case. This weight specifies the steady state tracking error to be within 1 % for the performance case, and within 5 % for the robust case. The weight decreases by 20 db per decade until 1400 rad/s. This frequency weighting results in the tracking error reaching 100% at a frequency of about 200 rad/s for both controllers. The slightly higher bandwidth for the performance case will yield a controller with a slightly faster rise time. Note that this weighting is suited for step commands which have similar slope. In the sequel, the performance parameters are varied to tradeoff with robustness.

3.3 Model Uncertainty and Noise

3.3.1 Uncertainties at Input

There are several causes for model uncertainties in the LAMSTF system. An important source of error, which is difficult to model, is the implicit error in the linearized model about the assumed equilibrium state. Because of unquantified uncertainties in the constants assumed for the second-order (first order for field gradients) magnetic field model, the true magnetic field produced by the five electromagnets may deviate from the predicted values. Since the true values for the equilibrium currents (and hence the correct linearized model) would require the precise knowledge of the magnetic field and its gradients as given by Equation (17), these errors affect both the equilibrating and stabilizing magnetic fields.

This error affects the values for the nominal plant $\delta \hat{A}$ and $\delta \hat{B}$. It can be shown through a perturbation analysis about equilibrium that inexact magnetic field values (parameter errors) and corresponding equilibrium current errors will appear as constant forcing terms in the linear state equations. These linearization errors are approximately modeled as uncertainties in the equilibrating currents, i.e., at the input of the plant.

Other sources of uncertainties include calibration errors, temperature effects, electrical noise and bias error in the current signal that produces the magnetic field. All of the above factors are lumped together and modeled as bounded multiplicative uncertainties at the input.

The uncertainties at the inputs are taken as $\Delta_\rho W_\rho$ where Δ_ρ are arbitrary unstructured matrices that satisfy

$$\|\Delta(s)_{curr}\|_\infty \leq 1; \tag{33}$$

and $W_\rho = f_\rho I_{5\times5}$.

Figure 5 shows the maximum multiplicative uncertainty assumed at the plant input. While the
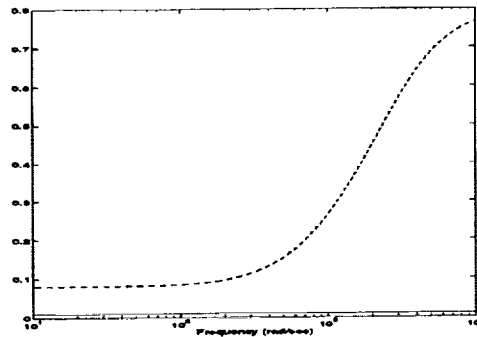
Figure 5: Frequency Weighting for Input Uncertainty. Performance case (solid), Robust case (dashed).

uncertainty for the performance case assumes only 1% error, the uncertainties in all five actuating current signals into the coils for the robust case is assumed to have 8% error at low frequencies and rolls up linearly at 300 rad/sec to attain values of more than 30% error at 1250 rad/sec (200 Hz). The uncertainties are assumed fully coupled, i.e., unstructured.

3.3.2 Uncertainties at Output

The sensing system provides measurements of the pitch and yaw angles and the location of the centroid. It consists of five shadow sensors which detect the amount of unblocked light passing the suspended element. The light is detected by photodetectors, converted to voltage signals, and transformed to provide the five position and orientation parameters. There are various limitations to performance of this system, including noise, calibration errors, and dynamic range.

The noise is expected to be larger at higher frequencies and control activity should be limited accordingly. The calibration errors cause inaccurate gains and may lead to spurious coupling between the different degrees of freedom. Also of importance is the linear range of the sensors which are limited to $\pm1^\circ$ for pitch and yaw

590

and .5 millimeters for x,y, and z axes. Any motion beyond the above ranges results in high non-linearity and/or sensor saturation.

To approximately model the above uncertainties, an unstructured frequency dependent multiplicative uncertainty at the plant output of the following form is proposed:

$$p_y(s) = f_y \left[\frac{(s + \omega_n)}{(s + \omega_d)} \left(\frac{\omega_d}{\omega_n} \right) \right] \tag{34}$$

with parameters, $\omega_n = 180$ r/s, $\omega_d = 1800$ r/s, and $f_y = .06$. While the output uncertainty for the performance case was chosen at 1% constant over all frequencies, the weight parameters for the robust case specify the maximum uncertainty in the sensor signal at low frequencies to be 6 % and increase, as shown in Figure (6), to 60 % at 1800 rad/sec to provide noise immunity (see Fig. 6).
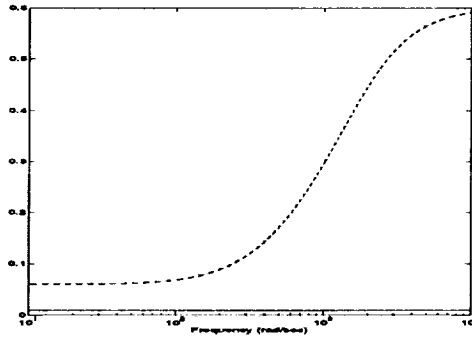
Figure 6: Frequency Weighting for Output Uncertainty. Performance case (solid), Robust case (dashed).

The above uncertainties were chosen for the pitch, yaw, and x,y,z outputs which have different units. Hence, as was done with the inputs, the outputs are initially normalized and then finally de-normalized to account for different units in the unstructured uncertainties. Figure 7 shows the output weighting procedure in block diagram form.
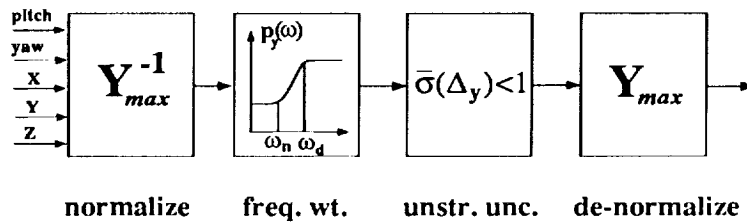
Figure 7: Output Uncertainty Weighting.

3.4 Controller Weights, Time Delay, and Zero-Order-Hold

In the implementation of controllers, the importance of various practical constraints besides signal noise becomes evident. First, the outputs of the actuators are limited by the saturation amplitude of the input currents. Figure 8 shows the frequency weighting of the control effort in all five channels. The DC gains are used for penalizing excessive control power while the increase in the penalty at higher frequency is used to encourage controller roll-off. The actuator electromagnets have sufficient bandwidth to behave as all-pass filters and hence are approximated by constants with saturation limits.

All controllers were designed assuming a continuous system but were implemented digitally. The use of real-time digital computers means that the analog signals must be discretized by sampling followed by zero-order-hold, with the further complication of a computational delay. The above discretization effects are
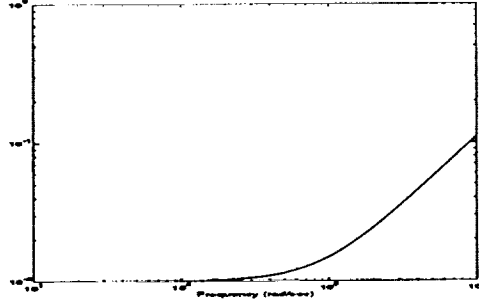
Figure 8: Controller Penalty Weighting

approximately accounted for in the continuous control design by introducing continuous approximations of a pure time delay and a zero-order-hold as shown below:

$$\Delta T = e^{-sT} \approx \frac{1 - \frac{sT}{2}}{1 + \frac{sT}{2}} \qquad\qquad ZOH = \frac{1 - e^{-sT}}{sT} \approx \frac{1 - \frac{sT}{6}}{1 + \frac{sT}{3}} \qquad (35)$$

A pure time delay of $\frac{1}{5}$ sampling period was assumed. It was discovered that compensators designed without the inclusion of these effects had poor performance when implemented digitally, due to significant phase errors occurring at high frequencies.

A small amount of pure time delay is implicitly accommodated for by the input and output multiplicative uncertainty used because the uncertainty is modeled as complex quantities bounded only by their norms. However, the phase delay accommodated is only about 5.7 degrees for an assumed uncertainty of 10 percent and is equal for all frequencies.

3.5 μ Analysis/Synthesis

The benefit of the μ-analysis and synthesis framework is that performance robustness for a fairly general class of robust control problems can be precisely defined by the scalar, μ. The underlying theory which forms the basis of this method is discussed in detail in [8]-[11]. Currently, μ cannot be computed directly for a general structure. Instead, an upper bound is computed for both analysis and synthesis purposes. Lower bounds are computed mainly to evaluate the degree of conservatism of the upper bound. Designing controllers by μ synthesis involves an iterative minimization of the upper bound using H_∞ methods. The μ-design problem is summarized as follows:

$$\begin{array}{cc} \text{minimize} & \|DF_l(P, K)D^{-1}\|_\infty \\ F_l(P, K) \in H_\infty, \ D \in \underline{D} \end{array} \qquad (36)$$

where the set of scaling matrices, $\underline{D}$, has a similar structure as $\underline{\Delta}$ (the structured uncertainty matrix) with an appended identity matrix. The terms, F_l, P, and K, denote the lower linear fractional transformation, augmented plant, and the controller, respectively.

For the LAMSTF problem, Figure 9 shows the augmented plant, P which includes the performance and uncertainty weights.

Figure 10(a) shows the actual uncertainty and the controller connections so that robust performance can be evaluated via μ-analysis. This involves the numerical evaluation of μ which is approximated by the lower and upper bounds. The analysis could include the evaluation of the degree to which robust stability and nominal performance are satisfied independently hence providing valuable hints on a possible tradeoff. The level and shape of μ achieved usually indicates a need for improvement in the controller.

Having decided that the controller needs refinement, an approach to improving μ is called the "D-K iteration". In this approach, K or D is optimized independently and sequentially; by fixing D, K is obtained from a scaled H_∞ optimization problem and, by fixing K, a convex optimization is performed at

592
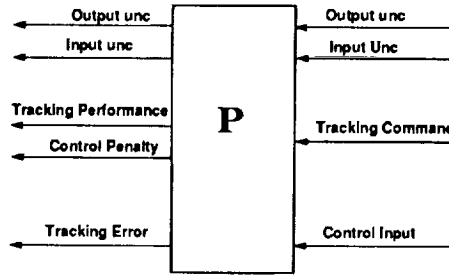
Figure 9: Augmented Plant of LAMSTF

each frequency with respect to $ln(D)$. Note that optimizing for D while keeping K fixed involves the search for the minimal upper bound on μ while optimizing for K while fixing D involves the minimization of an approximation of μ itself. Figure 10(b) shows the closed loop transfer function of interest, $F_l(P, K)$, and the scaling matrix, D which form the scaled H_∞ problem. Although this approach is iterative in nature and
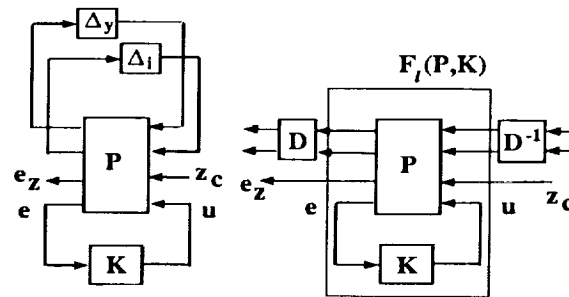
Figure 10: (a) Robust Performance; (b) μ-synthesis

convergence to a global minimum is not guaranteed, past numerical studies show excellent convergence. For example, in the recent robust line-of-sight control problem [6], typically 2 or 3 iterations were sufficient. In this study, 2 iterations are made. To solve the H_∞ problem the Glover-Doyle algorithm [9] is used. The MATLAB toolbox, μ-Tools [12] is used in this study for the analysis and synthesis of the controllers.

3.6 Control Designs

Four controllers are designed and analyzed in the following: performance H_∞, performance μ, robust H_∞, and robust μ. In computing the structured singular values, all controllers were reduced to 30 states by internal balancing. The controllers were reduced to ease computational burden, since many of the states were very weakly controllable and observable.

For the performance case, the H_∞ and μ controllers gave H_∞ norms of 1.75 and 1.18 and from Figure 11, μ values of 1.27 and 1.18 respectively (although the upper bound for perf MU case from the figure is larger, μ must be less than the corresponding H_∞ norm). Therefore, although the H_∞ norms are significantly different, robust performance is similar from the μ plots. This is expected for the performance case where the uncertainty levels specified are small. Note also that the upper and lower bounds of μ for both cases are close which is consistent with past experience.

For the robust case, the H_∞ and μ controllers gave H_∞ norms of 3.81 and 1.70 and from Figure 12, μ values of 2.75 and 1.70 respectively. The significant decrease in μ for the robust μ case over the robust H_∞ case means that a significant robust performance improvement is expected. This is expected for the robust case where the uncertainty levels specified are not small. Basically, due to the larger uncertainties specified, the H_∞ design produces very conservative results because performance and robustness constraints cannot be satisfactorily incorporated without using structured singular values. The peak of the μ plots for the robust HINF case also shows that it is difficult to satisfy robust performance due to the highly unstable
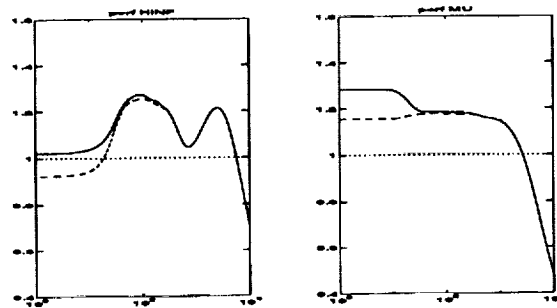
Figure 11: μ upper and lower bounds for Perf HINF (left) and Perf MU (right).

pitch and yaw modes at approximately 60 rad/sec [1]. The μ plots also indicate that tracking performance under significant uncertainty at low frequencies drives the design problem for both H_∞ and μ controllers. Again note that the upper and lower bounds of μ for both cases are close which is consistent with past experience. Note that the initial peaks are flattened for the μ controller indicating near optimal conditions.
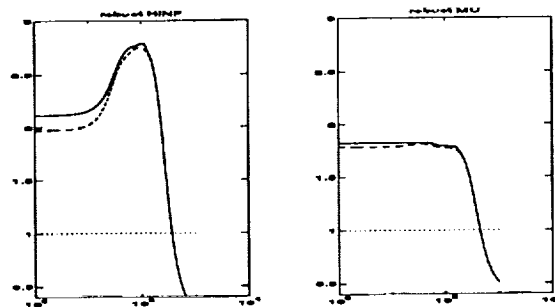
Figure 12: μ upper and lower bounds for Robust HINF (left) and Robust MU (right).

The previous plots show μ values for differing sets of constraints. For comparison purposes (perf case vs. robust case), the constraint weightings for the robust controllers were used for computing μ for all controllers. Figure 13 shows the near converged μ plots for H_∞ and μ controllers for performance and robust cases. Each plot shows robust performance (top line), nominal performance (middle) and robust stability (bottom). Note that at low frequencies, the performance controller is better while the robust controller is better at higher frequencies. It is also clear that the performance MU controller is not much better than performance HINF controller. However, robust MU controller is expected to perform better at lower frequency (i.e. tracking) while slightly worse at higher frequencies than robust HINF controller. Interestingly, in all cases, robust stability is easily satisfied even for the performance controllers. We note that the μ (peak) of performance μ controller is slightly smaller than the robust μ controller. This is probably due to factors such as suboptimality in the H_∞ and D-K iterations and model reduction errors.

In summary, the μ design did not improve over the H_∞ design for the performance case but is significantly better for the robust case. The performance controller is expected to perform better at lower frequencies where tracking occurs while the robust controller is expected to perform better at higher frequencies. These analytical predictions were tested in laboratory and are discussed in the next section.
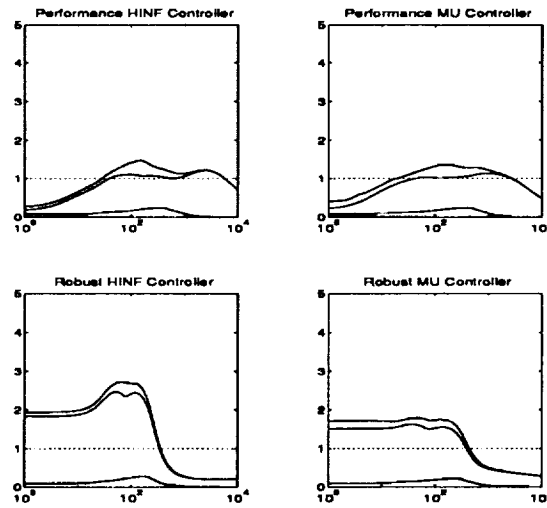
Figure 13: μ: upper bounds for robust perf, nominal perf, and robust stab

4   Results

4.1   Controllers Tested and Model Reduction

Speed limitations of the real time control computer required that the 30 state controllers be implemented at a sample rate of about 600 Hz. The four controllers had loop-gain bandwidth of about 110 Hz, and it was discovered that discretizing at this speed was inadequate. Therefore, further model reduction, through balanced realization, was performed and the controllers were implemented with fewer states at higher sampling rates. For the performance controllers 20 states were implemented at 800 Hz, while for the robust controller, which had a slightly larger bandwidth, 17 states were implemented at 850 Hz. The
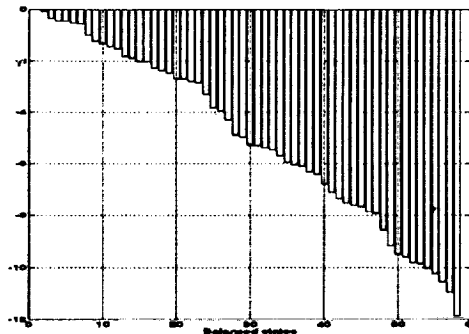
Figure 14: Normalized Hankel SV for Robust MU controller

normalized truncation error is shown in Fig. 14 for the robust MU controller case. For 30 states, the singular value error is less than 10^{-5} while for 17 states, the error is nearly 10^{-2}, i.e., the least significant normalized singular value increased by 3 orders of magnitude for the reduced models. A reasonably reduced controller is expected to be approximately the size of the augmented plant, which was 30. Therefore, for the highly reduced compensators which were implemented the robustness properties of the controllers must be reevaluated and these properties considered when interpreting the experimental results.

The μ values were recomputed for the 17 states and 20 states controllers which were actually imple-

mented. Figure 15 shows a significant decrease in robust performance predicted by reducing from 30 to 20 states for performance case and by reducing 30 states to 17 states for the robust case. Note that for the H_∞ cases, even robust stability (bottom lines) is not satisfied (cf. Figure 13). Therefore, the actual controllers implemented are not expected to perform as well for a reasonable sampling rate.
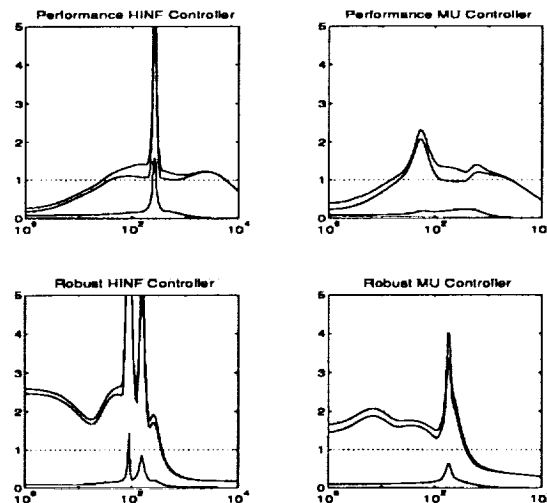
Figure 15: μ upper and lower bounds for reduced order Perf HINF (left) and Perf MU (right).

4.2 Comparison of Simulation and Experiment

Figure 16 shows the differences between simulation and experiments for the robust H_∞ and μ controllers. Each pair of plots shows a step tracking response in a particular axis and the total control power required to produce the response. The simulation involved an analog plant controlled by a discrete controller of the same order which was implemented. The simulation included a pure time computational delay of 4.3×10^{-4} seconds.

The figures show that the simulation is close to experimental results for the translational motions. The rise time and steady state values are fairly close in all cases. The damping however is quite different, especially in pitch and yaw. The power used in the test is quite similar to the predicted values except at later times where residual motions exist only in the experiments. Note that the experimental responses for the robust H_∞ design (Fig. 16) show large oscillations which are at approximately 20 Hz which are not apparent in the simulation. This discrepancy is consistent with the μ plots in Figure 15 where the μ peaks occur at approximately the same frequencies.

Figure 17 shows the simulation versus experimental comparison for the performance controllers. The responses are closer to simulation for these cases than for the robust design; however, they exhibit the same type of damping errors in the pitch and yaw tracking response.

4.3 H_∞ versus μ

Figure 18 shows the experimental comparisons between H_∞ and μ controllers for both performance and robust cases. The μ controller is only slightly better than H_∞ controller for the performance case. This is consistent with the fact that the μ values for both the robust and performance cases, as shown in Figure 13, are similar. However, the μ controller is significantly better than H_∞ controller for the robust case. Again, this is consistent with the significantly different μ values for the robust and performance cases, as shown in Figure 13. Notice that the μ controller generally requires less control power but gives better performance than H_∞ controller. Note also that the power levels are larger for tracking rotational degrees of
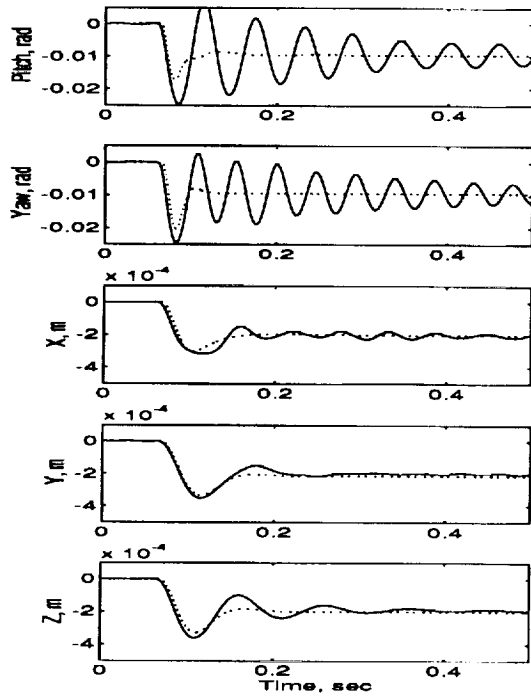
(a) Position, H_∞ (b) Control Power, H_∞
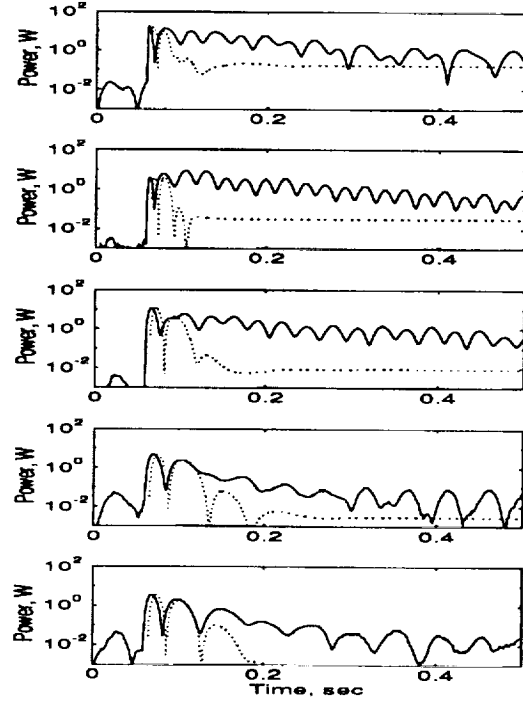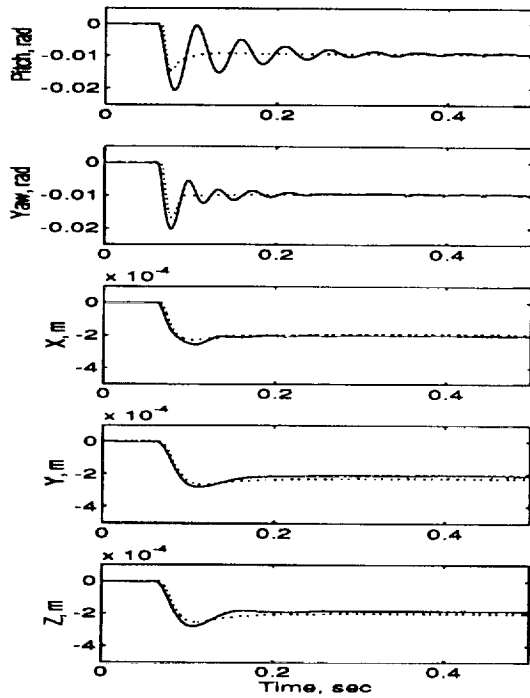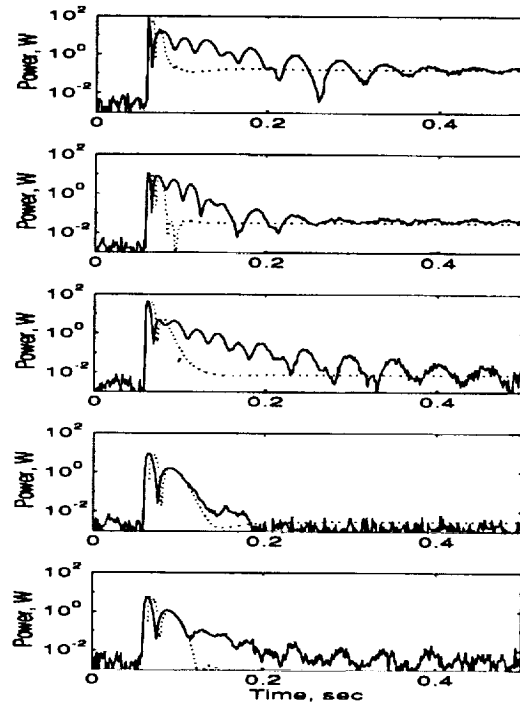
(a) Position, μ (b) Control Power, μ

Figure 16: Experiment (solid) vs Simulation (dotted), Robust designs
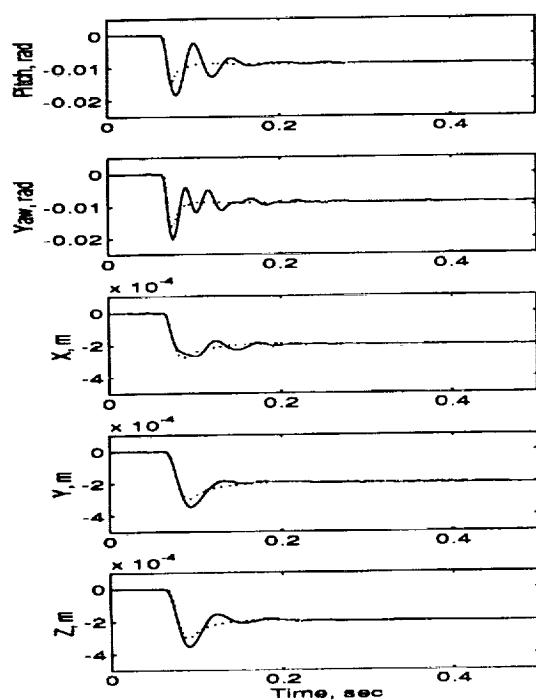
(a) Position, H_∞
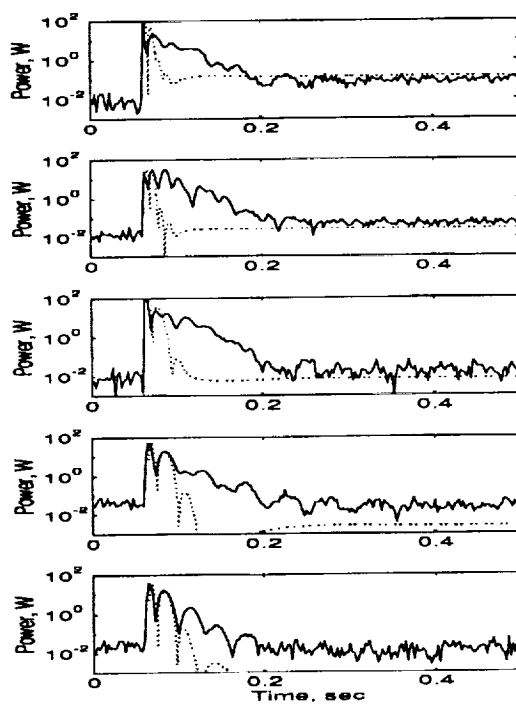
(b) Control Power, H_∞
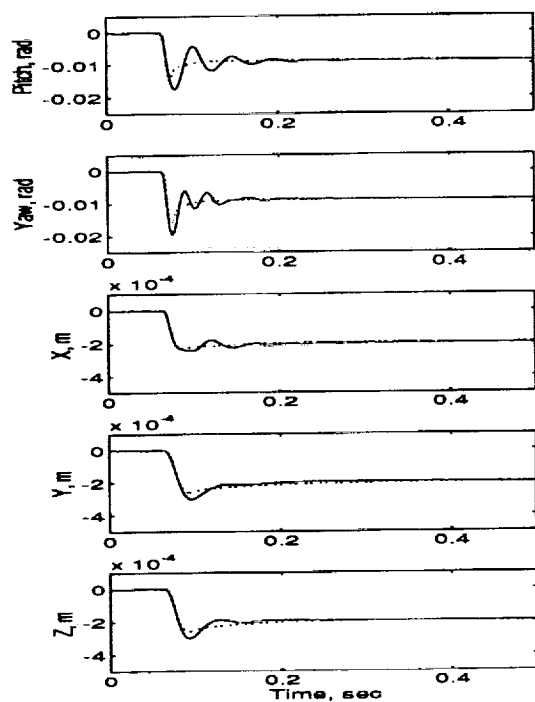
(a) Position, μ
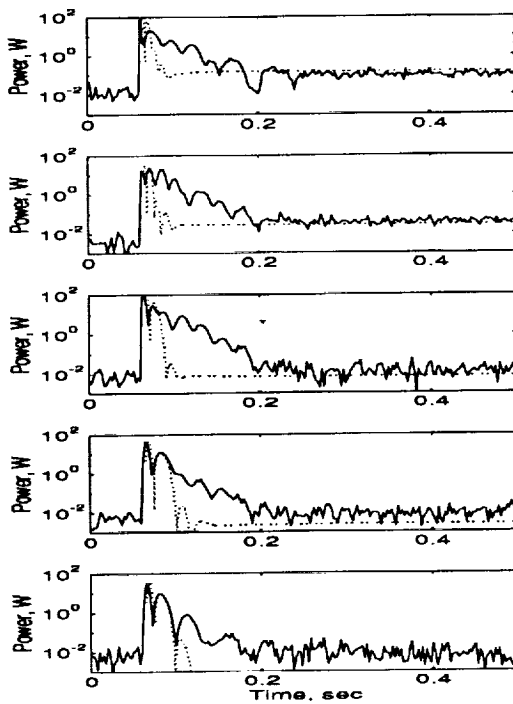
(b) Control Power, μ

Figure 17: Experiment (solid) vs Simulation (dotted), Performance designs

598

freedom. This is expected because the rotational modes, which have real poles near +60 rad/s, are violently unstable and at a higher frequency than the translational modes.

4.4 Performance and Robustness Tradeoffs

Figure 19 shows the experimental comparison between controllers designed for performance with small uncertainties versus controllers designed for performance with significant levels of modeled uncertainties. Figure 19 shows that the performance H_∞ controller has significantly better tracking response than the robust H_∞ controller. While it is clear that the performance controller gives significantly better tracking response than the robust controller for the H_∞ designs, for the μ designs the performance and robust controllers were more nearly matched. Unfortunately, the H_∞ is not able to handle the inclusion of significant levels of uncertainties along with the tracking performance constraints, and a low overall robust tracking performance is obtained in the laboratory.

4.5 Robust Tracking under Measurement Noise

To investigate the effect of external high frequency noise on the closed loop stability and tracking performance, colored Gaussian noise was introduced at the input to the controller. A large noise level was chosen to highlight its effects on the closed loop response. Figure 20 shows the frequency spectra of experimental response of the performance and robust cases for H_∞ controllers. The figures show improved noise rejection of up to a frequency of 300 and 200 Hz for rotational and translation axes respectively. At the lower frequencies, the robust case reduces the noise response by approximately 20 decibels. Note that the improved noise rejection properties of the robust case are anticipated from output uncertainty weighting shown in Figure 6 and the μ plots of Figure 15. Figure 21 shows experimental tracking response of y-axis under severe noise for performance and robust H_∞ controllers. Notice that the step in the tracking command input is almost lost in the noise. The other degrees of freedom also had similar noise added to their signals. The tracking response for the robust case is significantly better than the performance controller and it is very similar to the noiseless responses obtained previously.

5 Concluding Remarks

The purpose of the experiments was to address what-if questions on common models of uncertainties and was not explictly taylored for the LAMSTF testbed. The structure and the level of uncertainties assumed are only roughly known, without the benefit of any system identification results and are modeled as simple multiplicative uncertainties at the plant inputs and outputs. No attempt has been made to refine the nominal and uncertainty models through testing. Not surprisingly, comparisons between experiments and simulation indicate that the uncertainty model assumed is itself significantly inaccurate, especially in the rotational modes. Further robust system identification experiments aimed at improving the nominal and uncertainty models are needed for further improvement in robust performance. It is noted that the LAMSTF is highly open loop unstable. This means that some form of closed loop system identification can only be applied, which significantly complicates the problem of improving uncertainty models through experimental data.

In spite of the uncertainty in the uncertainties assumed, the experimental results confirmed the following simulation/design predictions: (i) μ design did not improve over the H_∞ design for the performance case but was significantly better for the robust case, (ii) performance controllers gave better tracking performance than robust controllers at lower frequencies, and (iii) robust controllers gave better tracking performance under high measurement noise levels. Analytical and experimental results indicate that a satisfactory level of robust tracking can be achieved for the highly unstable LAMSTF system. The speed of the real time controller significantly limited the implementation of modern multivariable robust controllers and further improvement is suggested. From a testbed standpoint, this study demonstrates analytically and experimentally that when significant uncertainties must be included in a control system, optimizing μ can be quite useful over direct H_∞ design.

Although nothing concrete has been proven, the results of this study provide a better understanding and appreciation of the physical significance of the numerous weighting parameters often encountered by the
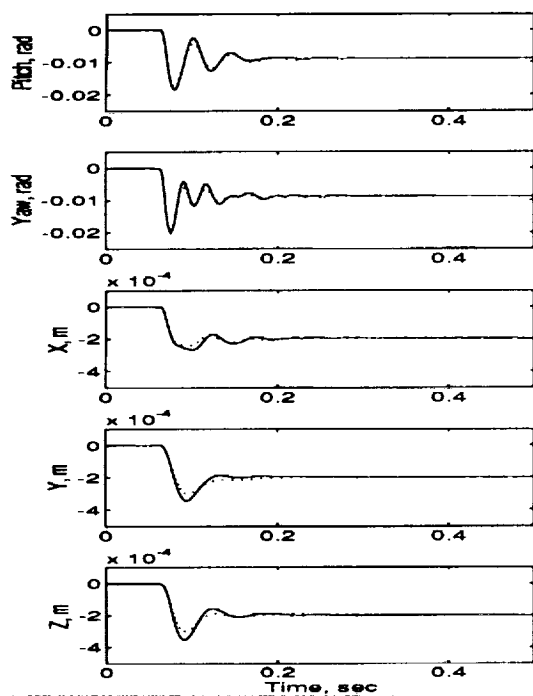
(a) Position, Perf Controller
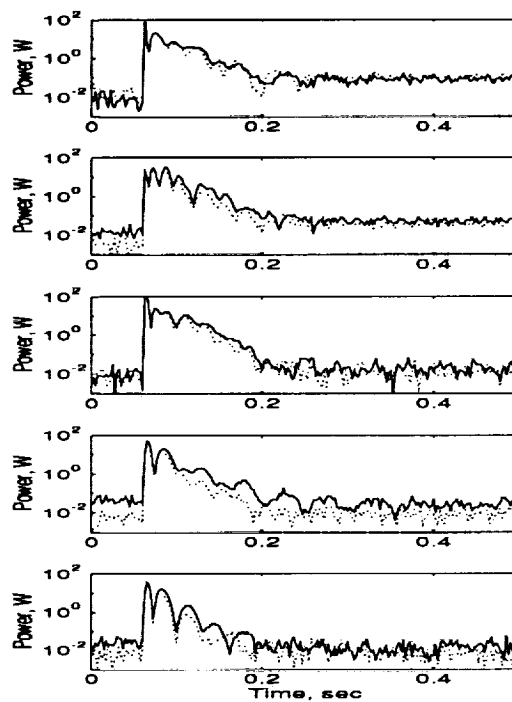
(b) Control Power, Perf Controller
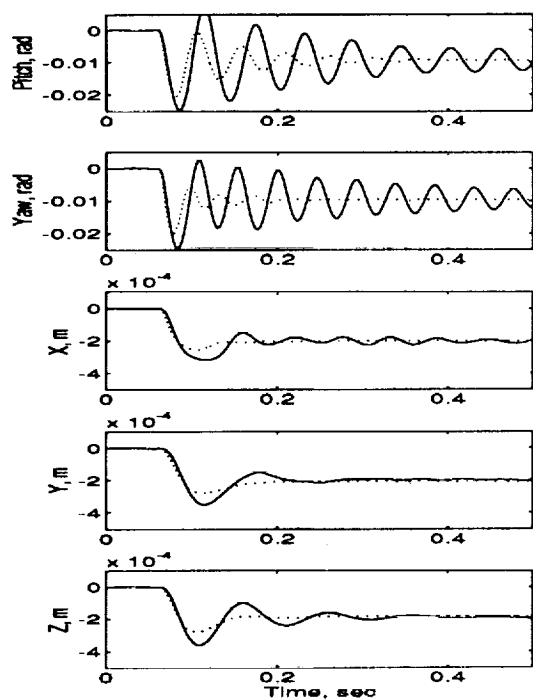
(c) Position, Robust Controller
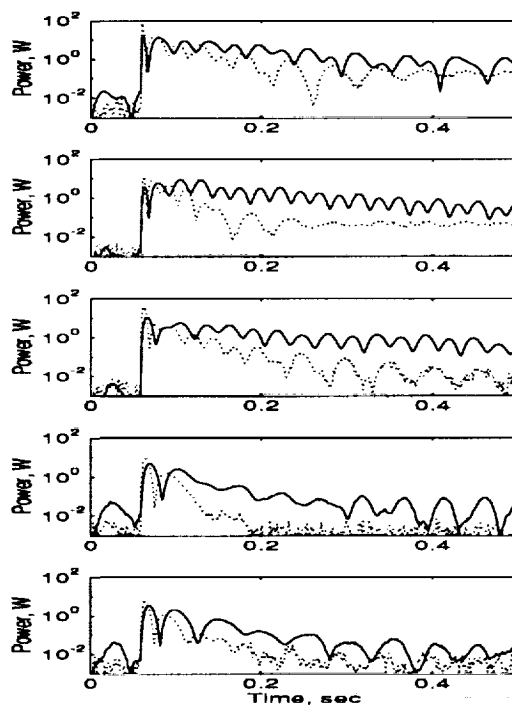
(d) Control Power, Robust Controller

Figure 18: Experimental comparison, H_∞ (solid) vs μ (dotted).
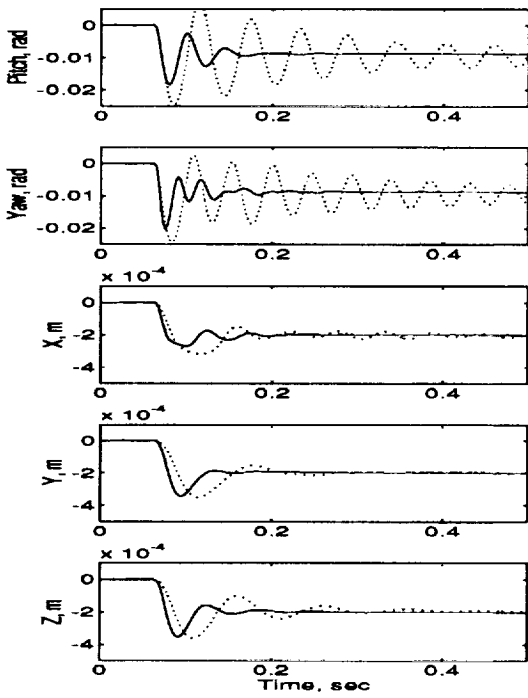
(a) Position, H_∞
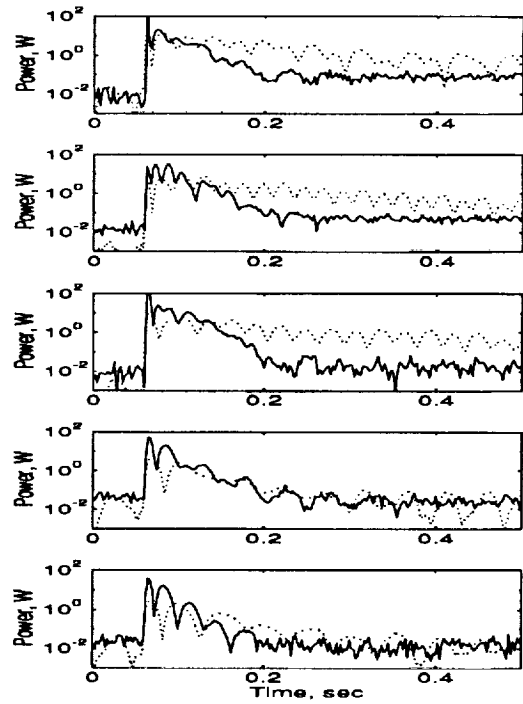
(b) Control Power, H_∞
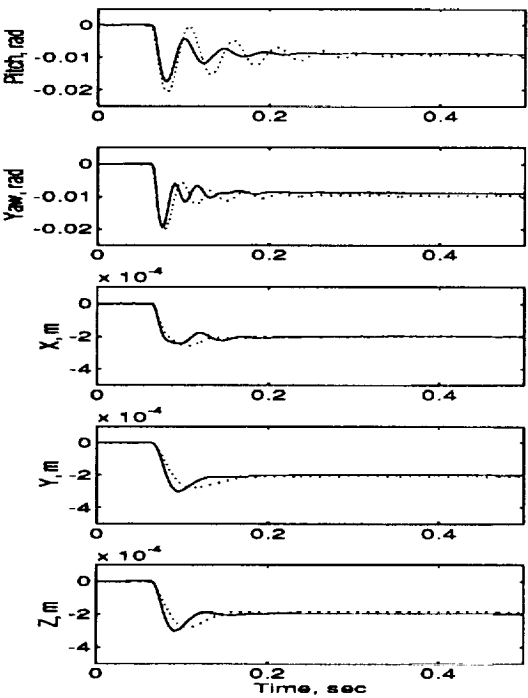
(a) Position, μ
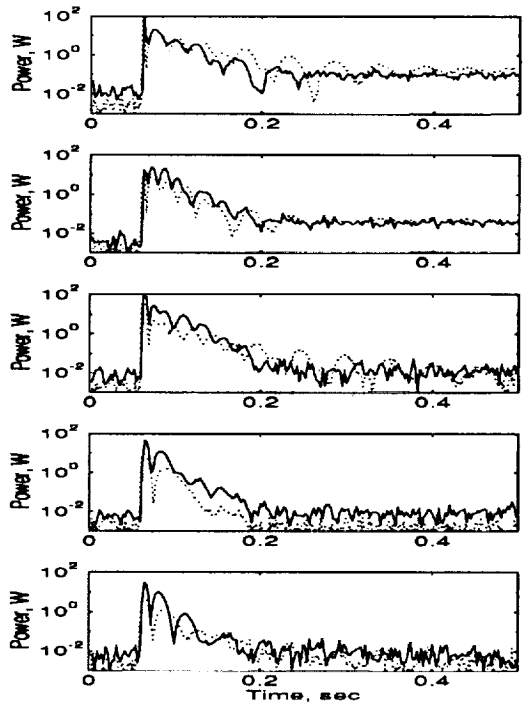
(b) Control Power, μ

Figure 19: Performance (solid) vs Robustness (dotted).
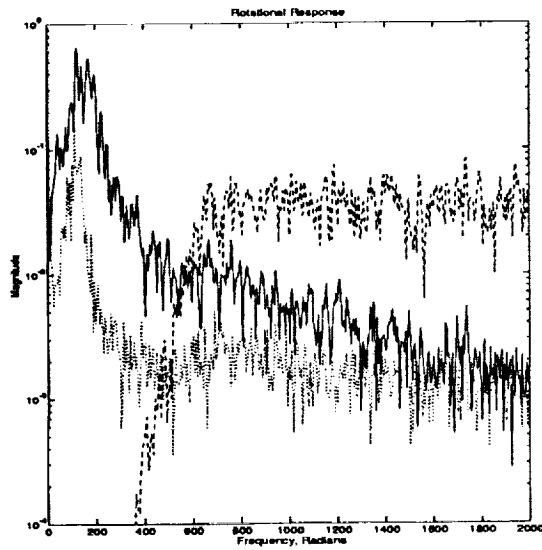
(a) Rotation
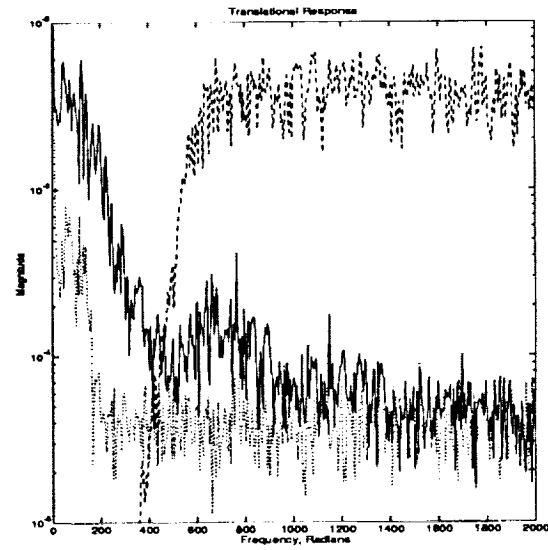
(b) Translation

Figure 20: Frequency spectra of experimental response with high frequency noise input. Performance (Solid), Robust (Dotted), Input (Dashed).
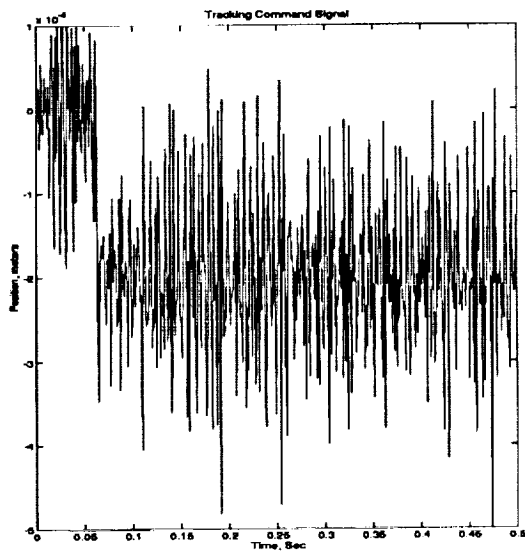
(a) Command input
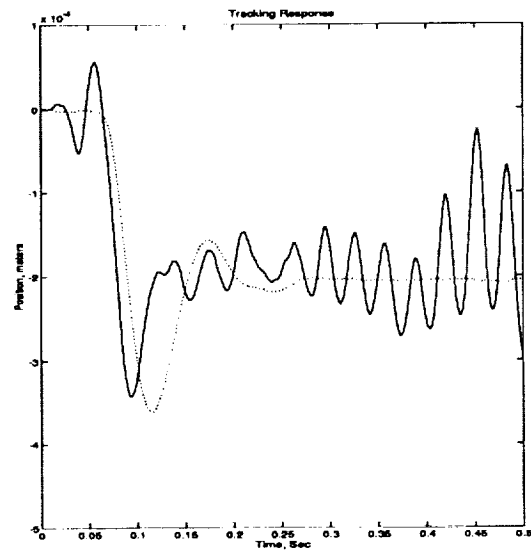
(b) Tracking response

Figure 21: H_∞ Controller tracking with noisy input. Performance (Solid), Robust (Dotted).

602

control designer in the application of H_∞ based control design techniques. In this regard, this study has been quite useful.

6 Acknowledgements

References

[1] Groom, N.J., and Britcher, C.P., "Open-Loop Characteristics of Magnetic Suspension Systems Using Electromagnets Mounted in a Planar Array," NASA-TP 3229, November 1992.

[2] Balas, G.J., and Doyle, J.C., "Robust Control of Flexible Modes in the Controller Crossover Region," *American Control Conference*, Pittsburg, PA, June 1989.

[3] Balas, G.J., and Doyle, J.C., "Robustness and Performance Tradeoffs in Control Design for Flexible Structures," *29-th IEEE CDC*, Hawaii, December 1990.

[4] Balas, G.J., and Lim, K.B., "Control of a Flexible Structure in the Presence of Natural Frequency Uncertainty with H_2 Performance Specifications," *American Control Conference*, San Francisco, CA, June 1993.

[5] Lim, K.B., Maghami, P.G., and Joshi, S.M., "A Comparison of Controller Designs for an Experimental Flexible Structure," *IEEE Control System Magazine*, Vol.12, No.3, June 1992.

[6] Lim, K.B., and Balas, G.J., "Line-of-Sight Control of the CSI Evolutionary Model: μ Control," *American Control Conference*, Boston, MA, June 1992.

[7] Junkins, J.L., and Turner, J.D., *Optimal Spacecraft Rotational Maneuvers*, Elsevier Science Publishers, New York, 1986.

[8] Doyle, J.C., "Analysis of Feedback Systems with Structured Uncertainties," Proc. IEE-D 129, 1982, pp. 242-250.

[9] Glover, K. and Doyle, J.C., "State-Space Formulae for all Stabilizing Controllers that Satisfy an H_∞ Norm Bound and Relations to Risk Sensitivity," *Systems and Control Letters*, vol. 11, pp. 167-172, 1988.

[10] Doyle, J.C., Glover, K., Khargonekar, P., and Francis, B., "State-Space Solutions to Standard H_2 and H_∞ Control Problems," *IEEE Transactions on Automatic Control*, Vol.34, No.8, August 1989.

[11] *MUSYN Robust Control Short Course Lecture Notes*, Arcadia, CA, September, 1989.

[12] Balas, G.J., Doyle, J. D., Glover, K., Packard, A. K., and Smith, R., *μ-Analysis and Synthesis Toolbox*, MUSYN Inc., Minneapolis, 1991.

Session 10b – Superconducting Suspensions

Chairman: Willard W. Anderson
NASA Langley Research Center

FEASIBILITY STUDY OF SUPERCONDUCTING LSM ROCKET LAUNCHER SYSTEM

Kinjiro Yoshida, Takaaki Ohashi, Katsuto Shiraishi, Hiroshi Takami
Depart. of Electrical Eng., Faculty of Eng., Kyushu University
6 - 10 - 1 Hakozaki Higashi - ku, Fukuoka 812 JAPAN

S/2 -33

//920

P. /5

SUMMARY

A feasibility study is presented on an application of superconducting linear synchronous motor (LSM) to a large - scale rocket launcher, whose acceleration guide tube of LSM armature windings is constructed as far as the depth of 1,500 meters under the ground. The rocket is released from the linear launcher just after it gets to a peak speed of about 900 kilometers per hour, and flies out the guide tube to obtain the speed of 700 kilometers per hour at the height of 100 meters above the ground. The linear launcher is brought to a stop at the ground surface for a very short time of 5 seconds by a quick control of deceleration. Very large current variations in the single - layer windings of LSM armature which is produced at the higher speed region of 600 to 900 kilometers per hour are controlled successfully by adopting the double - layer windings. The proposed control method makes the rocket launcher ascend stably in the superconducting LSM system, controlling the Coriolis force.

INTRODUCTION

As matters stand today, to build space infrastructures, the crew and the materials can be transported only by means of a rocket. Available rockets are loaded with liquid fuel which occupies 80% - 90% of the total weight for only a few percents of the payload. The cost of space transportation is extremely high [1]. By substituting superconducting LSM for the first acceleration step, the weight of liquid fuel can be greatly reduced and the payload transported at a time can be increased to a great extent. It is also expected to repeat ascending operations at much lower cost.

A feasibility study is presented on an application of a superconducting linear synchronous motor (LSM) to a large - scale rocket launcher facility with the acceleration guide tube of about 1,500 meters deep under the ground. The LSM armature windings are installed all along the acceleration guide tube and can drive in the vertical direction and guide in the horizontal direction the linear launcher vehicle, in which the superconducting magnets are mounted in the front and rear portions. A basic configuration of the linear launcher is a cylinder, in which the rocket is contained and connected through a passive suspension.

The computer program for simulating the basic operations of a superconducting LSM rocket launcher which is subjected to the Coriolis force has been developed in our Laboratory. Dynamics simulations ascending the 4 ton - vehicle with a 1 ton - rocket are obtained to meet a given acceleration pattern of quick acceleration and deceleration rate [2,3] by using the novel control method of the mechanical load angle and the armature currents, which have been

proposed by the authors [4]. The rocket is released at a peak speed of about 900 kilometers per hour, flies out the guide tube and achieves the speed of 700 kilometers per hour at the height of 100 meters above the ground. On the other hand, the linear launcher is stopped for a very short time of 5 seconds by a quick control of deceleration. In the single - layer windings of the LSM armature, very current variations are produced at the speed regions of 600 to 900 kilometers per hour [2]. This is caused by higher harmonic variations of the thrust forces due to the space harmonics of the armature windings. This problem is solved successfully by adopting the double - layer winding arrangement.

SUPERCONDUCTING LSM ROCKET LAUNCHER SYSTEM

Figure 1 shows a concept of a large - scale superconducting LSM - controlled rocket launcher system, which has the acceleration guide tube about 1,500 meters deep under the ground. The concept is based on our theoretical works on a superconducting LSM - controlled ground - based zero - gravity facility with the drop shaft of about 800 meters [5,6]. In figure 1, the LSM armature windings installed all along the acceleration guide tube are used to drive and guide the linear launcher.
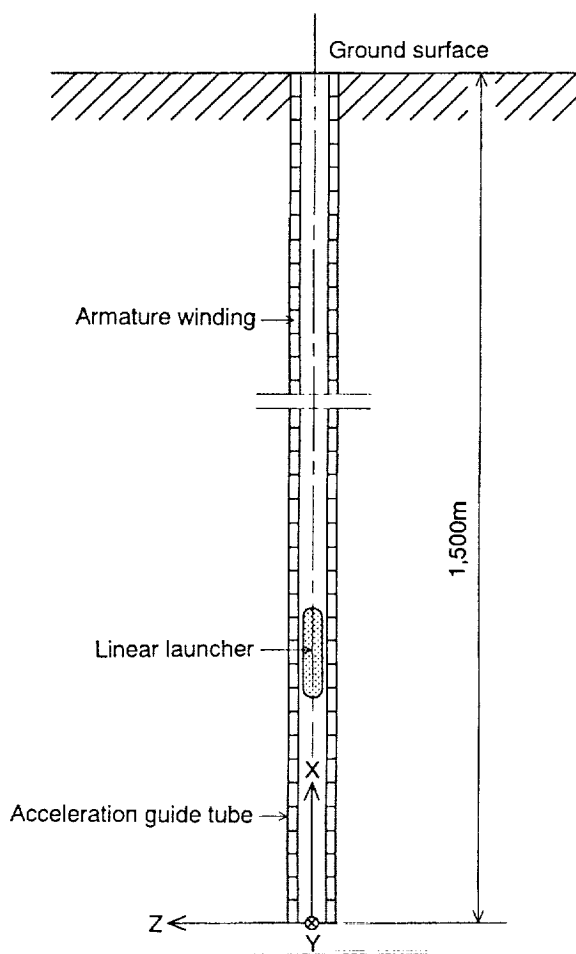
Figure 1. Vertical type superconducting - LSM controlled rocket launcher system.
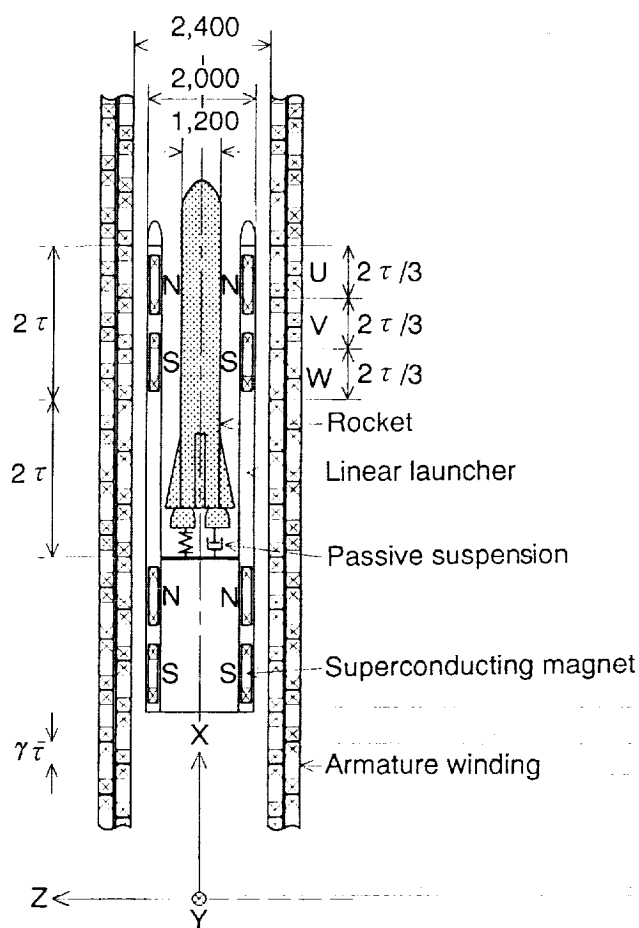
Figure 2. Acceleration guide tube of LSM armature and rocket launcher with superconducting magnets.

Figure 2 shows double - layer windings of the LSM armature which are composed of inside and outside coils, and the linear launcher on which the rocket is mounted through the use of passive suspension. The superconducting magnets are arranged with two poles facing the armature windings in the front and rear portions of a linear launcher vehicle.

Figure 3 shows a cylindrical configuration of the LSM launcher system which has four LSM's in symmetrical positions to produce guidance forces in the Y and Z directions. In the figure, the linear launcher is deflected by ΔY in the Y direction and by ΔZ in the Z direction. Inside and outside coils of each LSM armature are connected in series and each LSM is controlled independently using each current of their coils.

Z
Armature winding
LSM ④
Inside coil
Superconducting magnet
Outside coil
δ_{14}
z
ΔY 0'
y
LSM ③
0
ΔZ
LSM ①
Y
δ_{13}
δ_{11}
δ_{12}
LSM ②
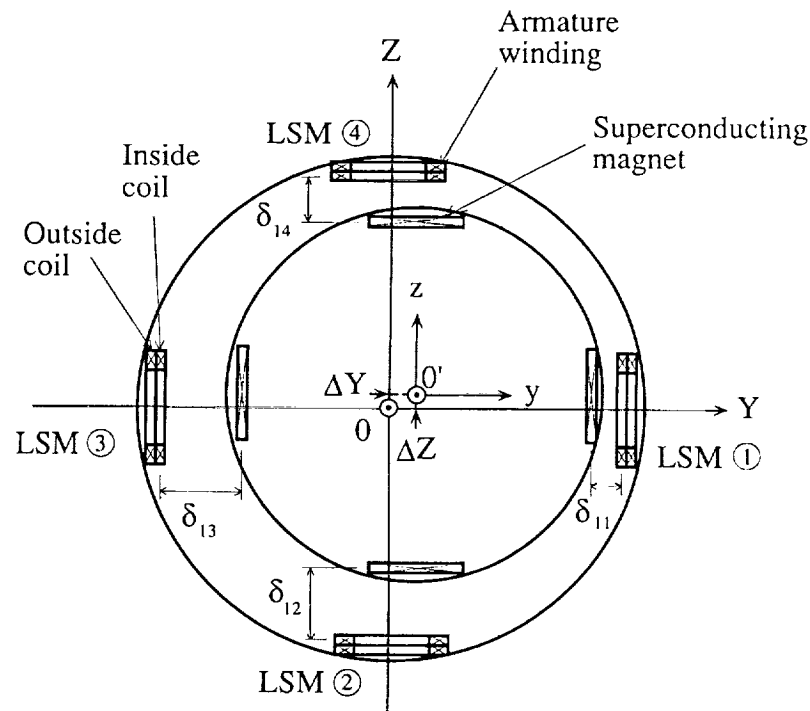
Figure 3. Model for analysis of rocket launcher.
(Cross - section of acceleration guide tube and four LSM's.)

THREE - DIMENSIONAL FORCE CALCULATION

For an arangement of the four superconducting LSM's shown in figure 3, each LSM can be also treated independently from the viewpoint of force calculation. According to figure 2, the superconducting magnets in a front part of the linear launcher almost do not couple with those in the rear part. The force calculation is thus essentially reduced to an analysis of the LSM with 2 - pole - superconducting magnets. Field solution for the air - core system, which includes the superconducting magnets, can be obtained analytically by using the law of Biot - Savart. The three - dimensional forces of thrust force F_X, lateral force F_Y and vertical force F_Z are expressed in an analytical form, which move the linear launcher in the X, Y and Z directions, respectively, in figure 3. By making each summation of X, Y and Z components of all forces in the four LSM's, resultant force F_X is applied as driving and braking forces, and resultant

forces F_Y and F_Z are used effectively as guiding forces.

EQUATIONS OF MOTION

Ascending Motion of Linear Launcher and Rocket

The linear launcher is accelerated to a peak speed, with loading the rocket, and after releasing the rocket, it is decelerated with no - load to be brought to rest at the end of the guide tube near the earth's surface. On the other hand, during the acceleration phase, the rocket is fixed to the launcher through a passive suspension, but after separating from the launcher, it ascends freely in the guide tube. The ascending motions in the X direction of the launcher and the rocket are described as follows :

$$
\begin{aligned}
M_L \frac{d}{dt} V_L = \quad & F_{X,11}(I_{11}, X_0, \delta_{11}, \Delta Z) + F_{X,12}(I_{12}, X_0, \delta_{12}, \Delta Y) \\
& + F_{X,13}(I_{13}, X_0, \delta_{13}, -\Delta Z) + F_{X,14}(I_{14}, X_0, \delta_{14}, -\Delta Y) \\
& + F_{X,21}(I_{21}, X_0, \delta_{21}, \Delta Z) + F_{X,22}(I_{22}, X_0, \delta_{22}, \Delta Y) \\
& + F_{X,23}(I_{23}, X_0, \delta_{23}, -\Delta Z) + F_{X,24}(I_{24}, X_0, \delta_{24}, -\Delta Y) \\
& - M_L G - F_{dL} + k_s \Delta H + k_d \Delta v
\end{aligned}
\tag{1}
$$

$$
M_R \frac{d}{dt} V_R = - M_R G - F_{dR} - k_s \Delta H - k_d \Delta v
\tag{2}
$$

where
M_L = linear launcher mass
M_R = rocket mass
V_L = speed of launcher
V_R = speed of rocket
$F_{x,ij}$ = thrust forces in the X direction
I_{ij} = winding currents of armature
X_0 = mechanical load angle defined by leading position of travelling magnetic field with moving superconducting - magnet
δ_{ij} = electrical airgap between coil centers of superconducting - magnet and armature
F_{dL}, F_{dR} = aerodynamic drag forces acting on launcher and rocket[7]
k_s, k_d = spring and damping coefficients of passive suspension
ΔH, Δv = relative height and speed of rocket with launcher
G = acceleration of gravity

Note that i denotes the ith LSM (see figure 3) and j the jth layer coil of double - layer windings, with the 1st and the 2nd coils corresponding to inside and outside layer coils, respectively.

After the linear launcher launches the rocket, the motion of the linear launcher is described by equation (1) from which the last two terms of $k_s \Delta H$ and $k_d \Delta v$, *i.e.* the coupling terms between motions of the launcher and the rocket, are excluded. The rocket flies away freely in the LSM guide tube according to the equation of motion, which is mentioned in the following section.

Guidance Motion of Linear Launcher and Rocket

The linear launcher and rocket are guided in the Y - Z plane, shown in figure 3, by the resultant lateral force F_Y and the resultant vertical force F_Z which are produced and controlled in the four LSM's. The Coriolis force is an external disturbance force for the launcher system which depends on the launcher and rocket speeds. When the Z axis is assumed to be in an eastward direction, the Coriolis force can be taken into account in equations of the Z - directed motions of the linear launcher and the rocket. The guided motions are described in the following.

Guidance Motions of the Launcher

During the acceleration phase, the Y - directed motion is

$$
\begin{aligned}
(M_L + M_R) \frac{d}{dt} \Delta \dot{Y} = \ & - \ F_{Z,11} (I_{11} , X_0 , \delta_{11} , \Delta Z) \ + \ F_{Y,12} (I_{12} , X_0 , \delta_{12} , \Delta Y) \\
& + \ F_{Z,13} (I_{13} , X_0 , \delta_{13} , - \Delta Z) \ - \ F_{Y,14} (I_{14} , X_0 , \delta_{14} , - \Delta Y) \\
& - \ F_{Z,21} (I_{21} , X_0 , \delta_{21} , \Delta Z) \ + \ F_{Y,22} (I_{22} , X_0 , \delta_{22} , \Delta Y) \\
& + \ F_{Z,23} (I_{23} , X_0 , \delta_{23} , - \Delta Z) \ - \ F_{Y,24} (I_{24} , X_0 , \delta_{24} , - \Delta Y)
\end{aligned}
\tag{3}
$$

The Z - directed motion is

$$
\begin{aligned}
(M_L + M_R) \frac{d}{dt} \Delta \dot{Z} = \ & F_{Y,11} (I_{11} , X_0 , \delta_{11} , \Delta Z) \ + \ F_{Z,12} (I_{12} , X_0 , \delta_{12} , \Delta Y) \\
& - \ F_{Y,13} (I_{13} , X_0 , \delta_{13} , - \Delta Z) \ - \ F_{Z,14} (I_{14} , X_0 , \delta_{14} , - \Delta Y) \\
& + \ F_{Y,21} (I_{21} , X_0 , \delta_{21} , \Delta Z) \ + \ F_{Z,22} (I_{22} , X_0 , \delta_{22} , \Delta Y) \\
& - \ F_{Y,23} (I_{23} , X_0 , \delta_{23} , - \Delta Z) \ - \ F_{Z,24} (I_{24} , X_0 , \delta_{24} , - \Delta Y) \\
& - \ (M_L + M_R) \ G - (M_L + M_R) \Omega V_L \ \cos \Phi
\end{aligned}
\tag{4}
$$

where $\quad \Omega \ = \ $ Angular speed of revolution of the earth
$\quad\quad\quad \Phi \ = \ $ Angle of terrestrial lattitude

After the linear launcher launches the rocket, during the deceleration phase, the Y - and Z - directed motions are described by using the equations (3) and (4) in which the mass M_L of the launcher itself is changed for the mass $(M_L + M_R)$.

Free Motion of the Rocket

After the rocket is released from the launcher and takes off with a high initial speed, the rocket continues to ascend with no control subject to the Coriolis force in the Z direction under the force of gravity in the X direction.

The free motion of the rocket is thus described as follows:

For the X - directed motion,

$$M_R \frac{dV_R}{dt} = -M_R G - F_{dR} \tag{5}$$

For the Y - directed motion,

$$M_R \frac{d}{dt} \Delta \dot{Y}_R = 0 \tag{6}$$

For the Z - directed motion,

$$M_R \frac{d}{dt} \Delta \dot{Z}_R = -M_R \Omega \Delta \dot{Z}_R \cos \Phi \tag{7}$$

Armature Current Control Method

The effective value of armature currents I_{ij} $(i = 1,2, \quad j = 1,..,4)$, which are included in equations (1), (3) and (4), are controlled to meet the given acceleration pattern.

Below the launch speed, I_{ij} is given by

$$
\begin{matrix} I_{11} \\ I_{21} \end{matrix} \Big\} = G_1(\alpha_{L0} - \dot{V}_L) + G_2(V_{L0} - V_L) + G_3(X_0 - X_\tau) - G_4 |\Delta Z|
$$
$$
- G_5 |\Delta \dot{Z}| + G_6 \Delta Y + G_7 \Delta \dot{Y} + I_{10} \tag{8}
$$

$$
\begin{matrix} I_{12} \\ I_{22} \end{matrix} \Big\} = G_1(\alpha_{L0} - \dot{V}_L) + G_2(V_{L0} - V_L) + G_3(X_0 - X_\tau) - G_4 |\Delta Y|
$$
$$
- G_5 |\Delta \dot{Y}| - G_6 \Delta Z - G_7 \Delta Z + I_{10} \tag{9}
$$

$$
\begin{matrix} I_{13} \\ I_{23} \end{matrix} \Big\} = G_1(\alpha_{L0} - \dot{V}_L) + G_2(V_{L0} - V_L) + G_3(X_0 - X_\tau) - G_4 |\Delta Z|
$$
$$
- G_5 |\Delta \dot{Z}| - G_6 \Delta Y - G_7 \Delta \dot{Y} + I_{10} \tag{10}
$$

$$
\begin{matrix} I_{14} \\ I_{24} \end{matrix} \Big\} = G_1(\alpha_{L0} - V_L) + G_2(V_{L0} - V_L) + G_3(X_0 - X_\tau) - G_4 |\Delta Y|
$$
$$
- G_5 |\Delta \dot{Y}| + G_6 \Delta Z + G_7 \Delta \dot{Z} + I_{10} \tag{11}
$$

where I_{10} = Demand stationary current

α_{L0} = Demand acceleration of launcher

612

$$V_{L0} = \text{Demand synchronous speed of launcher}$$
$$X_\tau = \text{Demand mechanical load angle}$$
$$\Delta\dot{Y}, \Delta\dot{Z} = \text{Launcher speeds in the Y and Z directions}$$
$$G_1 \sim G_7 = \text{feedback gains}$$

At the same time, the linear launcher should be controlled to ascend at the synchronous speed V_{X0} of the travelling magnetic field by producing the LSM thrust F_X. The mechanical load angle is controlled for all four LSM's to produce the sufficiently strong repulsive force in the resultant guidance forces F_Y and F_Z. When the launcher receives any disturbance forces in the Y and Z directions, the LSM guidance forces can compensate automatically and keep it at the center of the four LSM's.

Above the launch speed, I_{ij} is given by the equations which are obtained only by changing the negative sign for the positive sign in the first three terms of equations (8) - (11).

NUMERICAL EXPERIMENTS

The superconducting LSM rocket launcher system (see Table 1) is designed for the 1 - ton rocket to attain a speed of 700 kilometers per hour at the height of 100 meters above the ground. In the limited length of the LSM armature guide tube, the linear launcher is controlled to meet the designed acceleration pattern, which has the 6.6 - second acceleration phase with a quick variation from zero to 4 G's for 0.5 seconds and 4 G's kept for 6.1 seconds, and the 4.67 - second deceleration phase with a very quick variation from 4 G's to - 7.5 G's for 1.3 seconds, - 7.5 G's kept for 2.87 seconds and a very quick variation from - 7.5 G's to zero for 0.5 seconds.

Table 1. Superconducting LSM Rocket Launcher

Guide Tube :		Total weight	4 ton
Total length	1,500 m	No. of Superconducting Magnets	16
Diameter	4 m	Superconducting Magnets per one LSM :	
LSM Armature Guide Tube :		No. of poles	4
Total length	1,500 m	Coil length	1.3 m
Inside diameter	2.4 m	Coil width	0.5 m
Outside diameter	2.6 m	MMF	700 kAT
No. of LSM Armature	4	Pole pitch	1.5 m
Coil length	0.8 m	Rocket :	
Coil width	0.6 m	Total weight	1 ton
Linear Launcher :		Clearance Gap :	
Total length	9 m	Electrical gap between coil centers	20 cm
Diameter	2 m	Mechanical gap	10 cm

Figure 4 shows armature current response for the controlled dynamics of the launcher, with a parameter of shifted length $\gamma\tau$ between inside and outside coils of the double - layer distributed winding. In figure 4 (a), with a case of $\gamma\tau = 0$ m which corresponds to a single - layer of concentrated winding, very large current variations are caused in a higher speed range near the peak speed, and this means unstable and dangerous operation of the system. But it is found from figure 4 (a) - (d) that as the shifted length is increased, unstable current variations are damped and decreased, and in the case of $\gamma\tau = 0.3$ m the small current variations with higher harmonics as well as the large current variations are almost eliminated. When the shifted length $\gamma\tau$ is increased above 0.3 m, the current variations are induced again, as shown in figure 4 (e).

Figure 5 shows thrust forces accelerating and decelerating the linear launcher. As apparently in figures 5 (a) and (b), the thrust forces due to inside and outside armature windings include small higher - harmonic forces and other unstable harmonic forces produced discontinuously. The resultant thrust force in figure 5 (c) almost eliminates their harmonic forces and shows a very smooth curve in all operating regions. Figure 6 shows a harmonics - eliminated curve and the corresponding resultant guidance - force component F_Z due to inside and outside coils. In the following simulations , 0.3 m is thus used as $\gamma\tau$.

Simulated Motions of LSM Launcher and Rocket

Figures 7 (a) and (b) show that the rocket is released from the launcher just after the peak speed at the location of 1,000 m, launches with an initial speed of about 900 kilometers per hour, flies out the LSM guide tube with a speed of about 720 kilometers per hour and then attains the demand speed of 700 kilometers per hour at the height of 100 m above the ground. An instance when the rocket is released is known from an instance for $\Delta H = 0$ in figure 7 (h). As shown in figure 7 (c), the launcher follows very well the designed acceleration pattern according to the demand mechanical load angle in figure 7 (e).

Figure 7 (j) shows that the Coriolis force in the Z direction is compensated completely before a released point and after that the launcher itself is controlled quickly and stably in the center of the LSM guide tube while the rocket is deflected in the reverse direction of the Z axis, *i. e.* in the westward direction, by 3.8 cm at the flying - out point of the guide tube end. The deflection is sufficiently small compared with a mechanical clearance between the rocket and the inside coil of LSM armature, so that the rocket does not come into collision with the wall of the inside coils. Figure 7 (l) shows that the launcher oscillating motion in the Z direction is damped and the rocket is moved quite slowly in the westward direction, due to the Coriolis force.

CONCLUSIONS

The concept of a vertical type superconducting LSM rocket launcher system under the ground, in which the novel armature control method is successfully applied for the double - layer armature windings of the acceleration guide tube, is proposed and designed for a feasibility

614

study. The computer program for simulating controlled dynamics of the system is developed, which can take into account interesting and important effects of the Coriolis force.

If the rocket attains the speed of 700 kilometers per hour at the height of 100 m above the ground, the weight reduction of the liquid fuel enables the rocket payload to increase more than 15%. The superconducting LSM rocket launcher system which launches the 1 - ton rocket is designed for that purpose. Simulated results show that, on the condition of the Coriolis force, the linear launcher and rocket ascend together, accelerated and guided stably in the center of the guide tube, as high as the released point of 1,000 meters. After their separation, the launcher is decelerated and controlled to be brought to a stop with compensation for the Coriolis force while, due to the Coriolis force, the decreasing rocket is moved slowly in the westward direction, but because of the nearly zero initial - speed of the well - guided launcher at the released point, even the maximum deflection at the flying - out position is so small that there are no collisions with the guide tube.

ACKNOWLEDGEMENTS

REFERENCES

1. O'Neill, Gerard K. : The Low (Profile) Road to Space Manufacturing, Special Section of Astronautics & Aeronautics, March 1978.

2. Yoshida, K. ; Ohhashi, T. ; Noritomi, K. : Ascending - Control Simulation of Superconducting LSM Rocket Launcher, Proc. the 4th Sym. on Electromagnetic Force Applications, Kanazawa, June 1992, pp. 153 - 158.

3. Yoshida, K. ; Ohhashi, T. ; Shiraishi, M. ;Takami, H. : Effects of Double Layer Armature Windings on Controlled Dynamics of Superconducting LSM Rocket Launcher, Proc. the 5th Sym. on Electromagnetic Force Applications, Hitachi, June 1993, pp. 51 - 55.

4. Yoshida, K. ; Nagao, S. : Levitation and Propulsion Control Simulation of Regardless - of - Speed Superconducting LSM Repulsive Maglev Vehicle, Proc. the 3rd Sym. on Electromagnetic Forces, June 1991, pp. 201 - 206.

5. Yoshida, K. ; Kunihiro, A. : Drop Motion Control of Capsule in Superconducting LSM Controlled Ground - Based Zero - Gravity Facility , Proc. the Second Sym. on Electromagnetic Force Applications, Nagoya, June 1990, pp. 5 - 10.

6. Yoshida, K. ; Kunihiro, A. ; Ohhashi, T. : Superconducting LSM Dynamics in Ground - Based Zero - Gravity Facility, Proc. Inter. Conf. on the Evolution and Modern Aspects of Synchronous Machines, Zurich, Aug. 1991, Part 3, pp. 797 - 802.

7. Yamamoto, A. : Pressure Variations, Aerodynamic Drag and Tunnel Ventilation in Shinkansen Type Tunnel, Rail. Tech. Res. Rep., RTRI JNR, . No. 871, pp. 62 - 64 (1973).
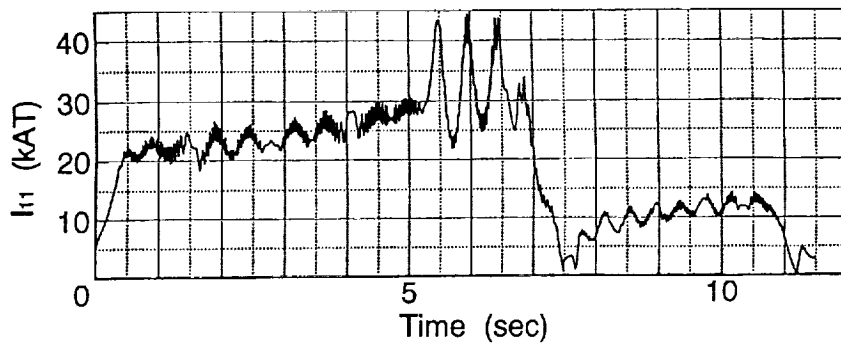
(a) $\gamma\tau = 0$ m
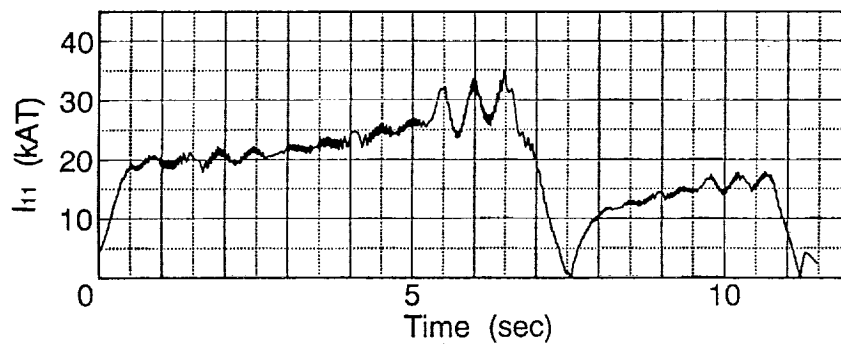
(b) $\gamma\tau = 0.15$ m
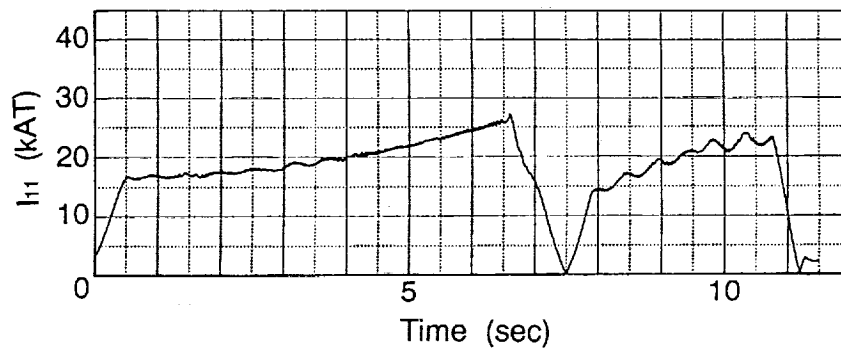
(c) $\gamma\tau = 0.30$ m
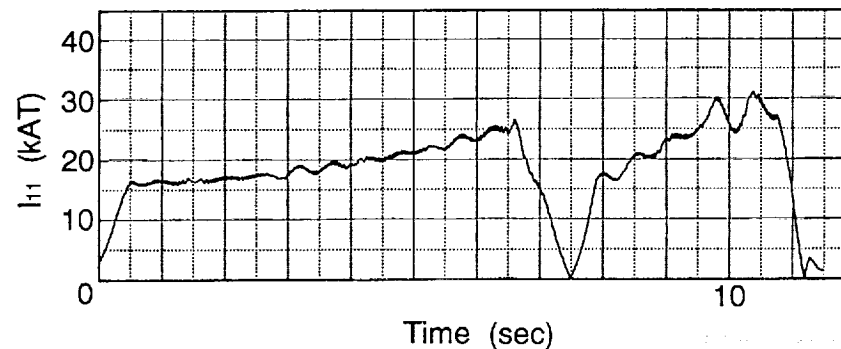
(d) $\gamma\tau = 0.35$ m

Figure 4. Currents of double - layer armature winding.

C - 3.
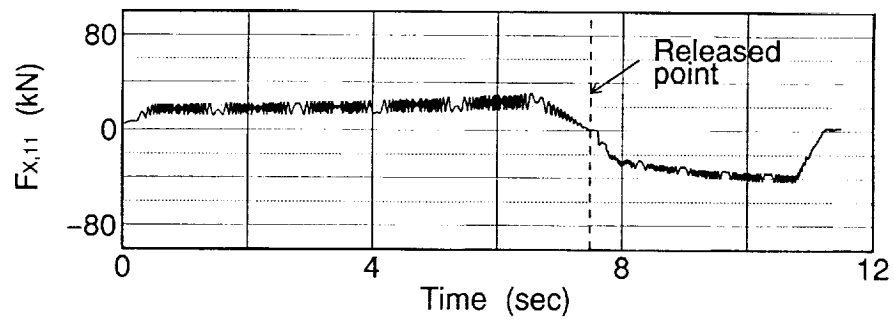
(a)Thrust force due to inside armature winding
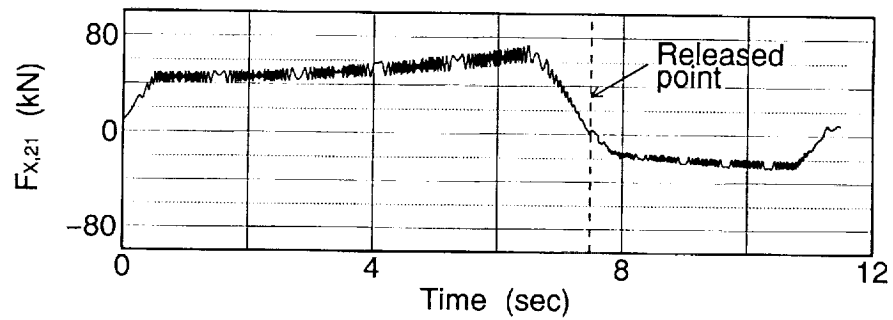
(b) Thrust force due to outside armature winding
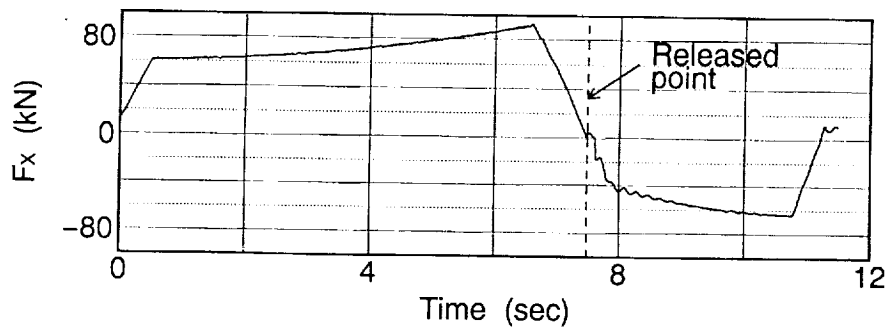
(c) Resultant thrust force

Figure 5. Thrust force due to inside and outside coils of armature windings and resultant thrust force.
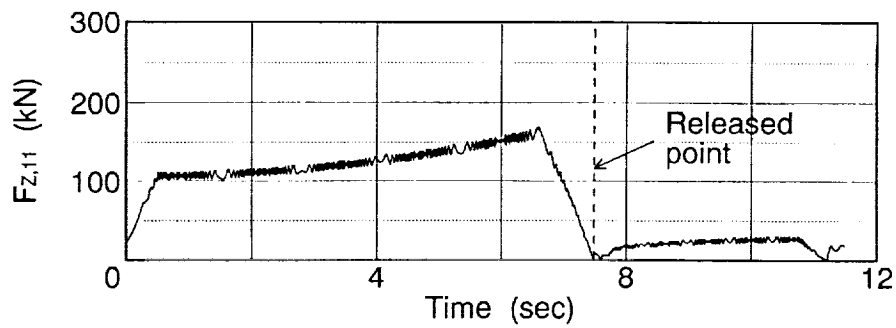
(a) Guidance force due to inside armature winding
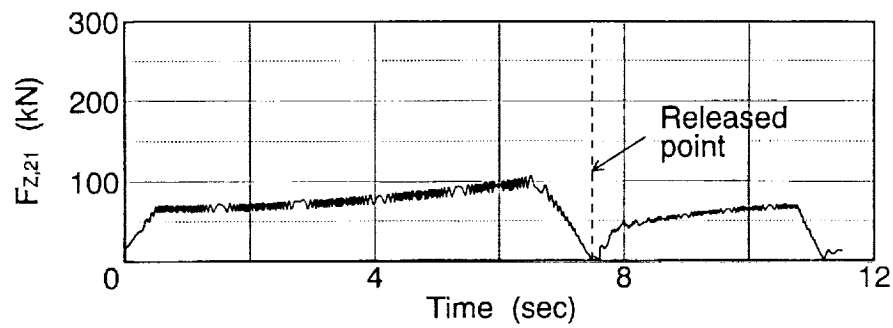
(b) Guidance force due to outside armature winding
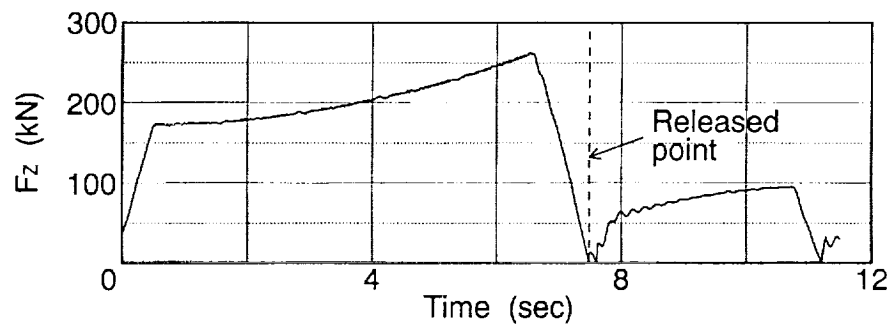
(c) Resultant force

Figure 6. Guidance forces due to inside and outside coils of armature windings and resultant Guidance force.
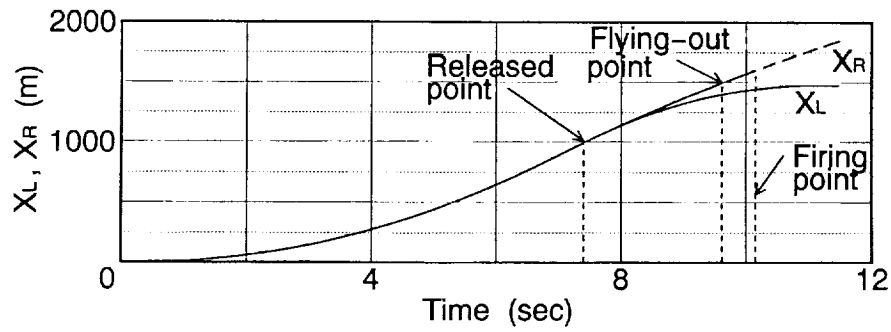
(a) Position of ascending launcher and rocket
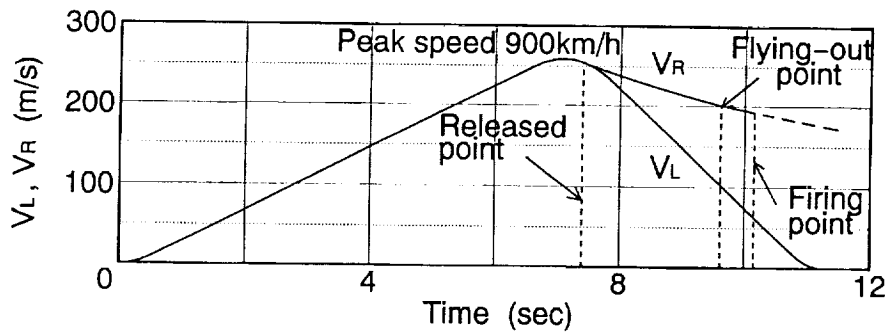
(b) Speed of ascending launcher and rocket
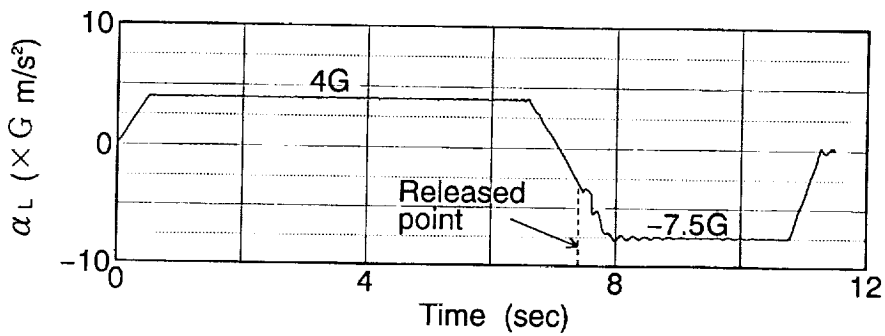
(c) Acceleration of ascending launcher
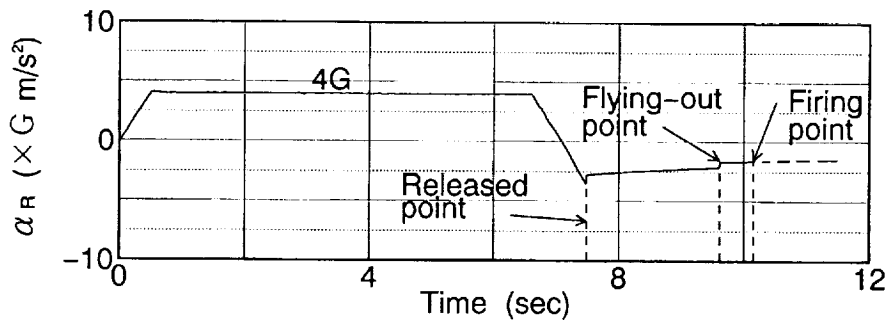
(d) Acceleration of ascending rocket

Figure 7. Ascending motion of LSM rocket launcher ($\gamma\tau = 0.3$m)
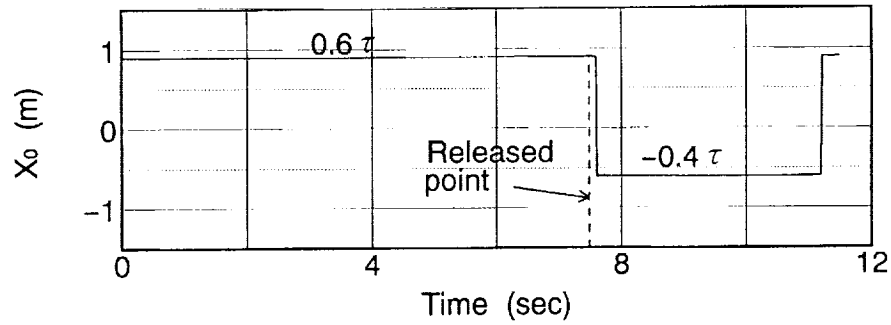
(e) Mechanical load angle
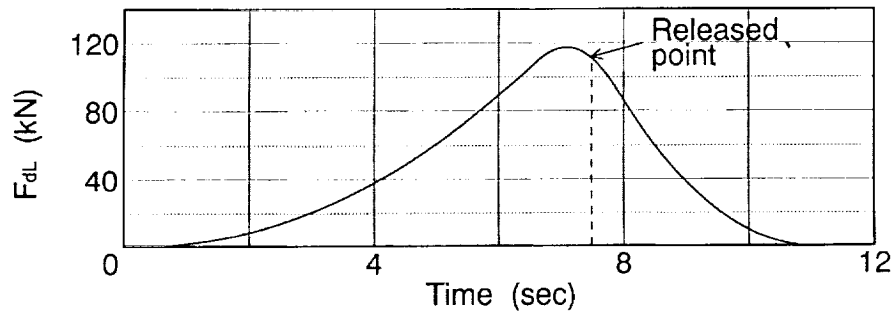
(f) Aerodynamic drag acting on launcher
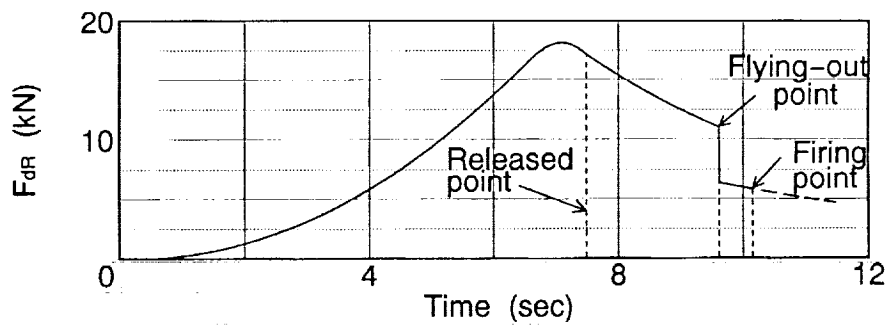
(g) Aerodynamic drag acting on rocket
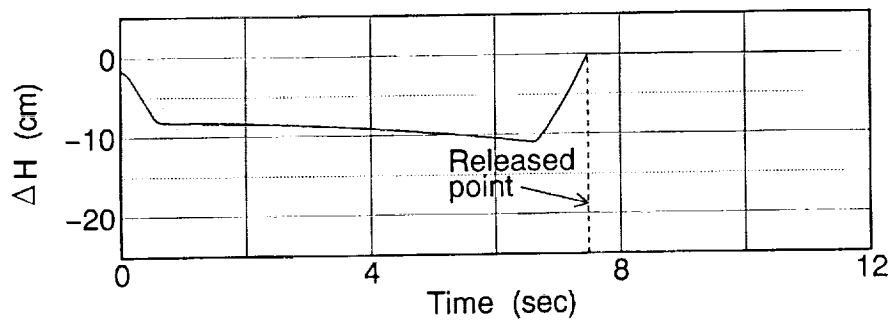
(h) Relative height between launcher and rocket

Figure 7. Ascending motion of LSM rocket launcher ($\gamma\tau = 0.3$m)
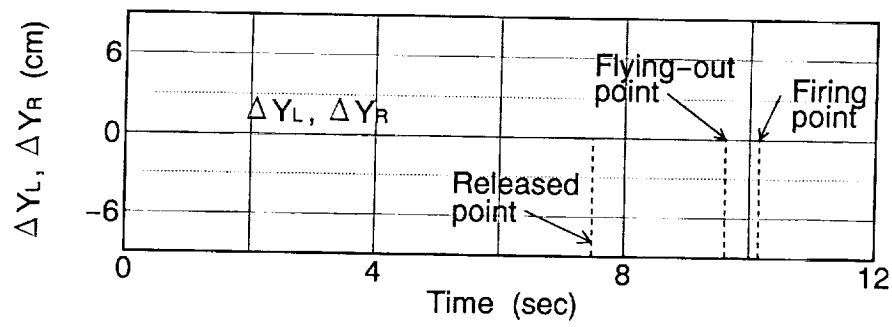
(i) Launcher and rocket deflections in the Y direction.
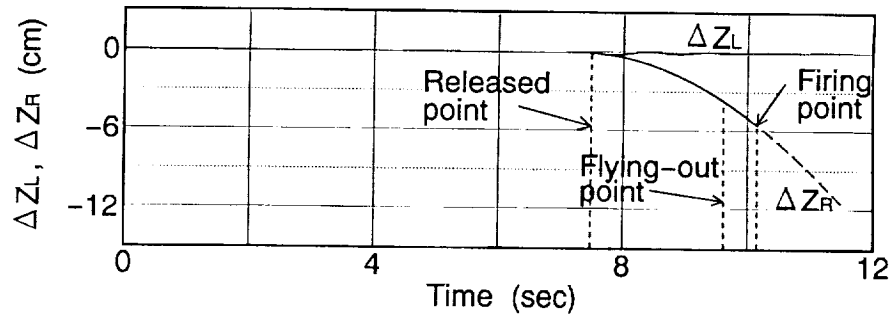
(j) Launcher and rocket deflections in the Z direction.
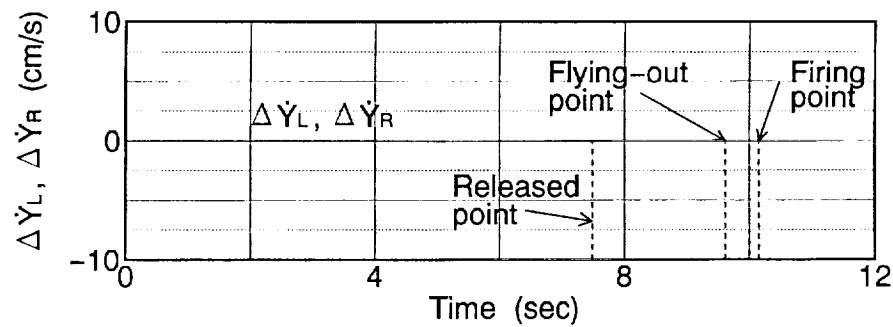
(k) Launcher and rocket speeds in the Y direction.
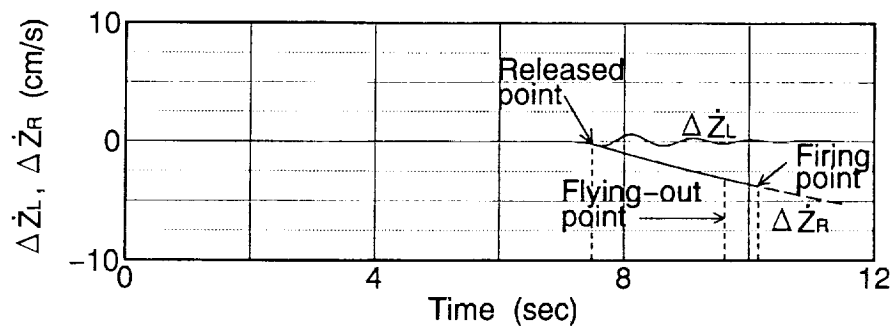
(l) Launcher and rocket speeds in the Z direction.

Figure 7. Ascending motion of LSM rocket launcher ($\gamma\tau = 0.3$m)

Session 11 – Precision Applications

Chairman: Nelson J. Groom
NASA Langley Research Center

MAGNETICALLY SUSPENDED STEPPING MOTORS FOR CLEAN ROOM AND VACUUM ENVIRONMENTS

Toshiro Higuchi
Kanagawa Academy of Science and Technology
Kawasaki, Japan
The University of Tokyo
Tokyo, Japan

SUMMARY

To answer the growing needs for super-clean or contactfree actuators for uses in clean room, vacuum chamber and space, innovated actuators which have the functions of stepping motors and magnetic bearings in one body have been developed. The rotor of the magnetically suspended stepping motor is suspended exactly like a magnetic bearing and rotated and positioned exactly like a stepping motor. The important trait of the developed motor is that it is not a simple mixture or combination of a stepping motor and a conventional magnetic bearing, but an amalgam of a stepping motor and a magnetic bearing. Owing to optimal design and feed-back control, a toothed stator and rotor are all that are needed structurewise for stable suspension. More than ten types of motors such as linear type, high accurate rotary type, two-dimensional type and high vacuum type have been built and tested. This paper describes the structure and design of these motors and their performance for such applications as precise positioning rotary table, linear conveyor system and θ-Z positioner for clean room and high vacuum use.

INTRODUCTION

The need for a super-clean environment is increasing in such areas as semiconductor processing, biotechnology experiments, in vacuo processing etc. Also, there is a need for an actuator that can operate without maintenance in these environments. However, conventional actuators are not always ideal from the view point of cleanliness. They are known to generate dust and oil vapor, and thus lower the yield rate and reliability of manufacturing processes and experiments. Types of contaminants and their sources are as follows. 1)oil vapor from lubricated parts (e.g. ball-bearings, linear guides, gears), 2)metal and oxide "flakes" from rubbing surface of metal-metal contact (e.g. ball-bearings), 3)carbon dust from brushes of DC motor, 4)evaporation of paint and insulation coating (e.g. coils), 5)gas evaporation from surfaces in vacuum. From the above examples, it can be concluded that an ideal actuator from the view point of cleanliness is the type where positioning, actuation, support of a moving object are carried out without mechanical contact.

Various contactless positioning tables, vehicles etc intended for use in clean-room have already been developed at research institutes, universities and companies. Such examples are: 1) linear

induction motor and air bearing, 2) linear induction motor and magnetic levitation, 3) linear DC motor and air bearing, 4) rotary induction motor and magnetic bearing.

The above machines are a combination of a contactless (brushless) propelling/positioning motor and a contactless guiding/supporting mechanism. For use in vacuum and space, of course, an air bearing can not operate. And, the co-existence of magnetic bearing and motor tends to complicate and enlarge the whole structure. Thus, development of a totally new motor having the function of contactless motor and magnetic bearing/levitation at once was expected to enable the design of more compact and light machines which are especially demanded in vacuum and space use.

The research group led by the author has succeeded in developing such a motor by magnetically suspending a stepping motor rotor. The magnetically suspended stepping motor has the propelling and positioning abilities of an ordinary stepping motor and the contactless supporting function of a magnetic bearing at the same time in one construction. Owing to the characteristic toothed pole structure of the motor, its design and driving conditions were optimized to minimize the possible fluctuation of the attractive force acting between the stator and rotor. From experiments, gap fluctuation amplitude has been confirmed to be no greater than 1% of preset gap length.

Since the first prototype appeared in 1985, more than ten kinds of magnetically suspended stepping motors have been built. In this paper, the structure and design of the magnetically suspended stepping motor are described. And some actual examples of the developed motors are introduced about their construction, control method, and performance.

IDEA AND STRUCTURE OF THE MAGNETICALLY SUSPENDED STEPPING MOTOR[1,2]

The basic idea of the magnetically suspended stepping motor (MS-type stepping motor) will be explained by comparing its structure and operating principles with conventional linear stepping motors and magnetic bearings. Figure 1 is a diagram of conventional Permanent Magnet (PM)-type linear stepping motor. The mover in the figure consists of a laminated silicon steel core, permanent magnets and coils. Propulsive force is gained by superposition of magnetic flux generated by the coils onto the magnetic flux of the permanent magnet. A strong attractive force, approximately ten times the propulsive force acts between the mover and the stator. Ball-bearings, which are the main source of dust and oil vapor are used to maintain a constant gap.

Figure 2 illustrates the idea of the MS-type stepping motor element. Its structure is quite similar to that of the PM-type stepping motor, but the permanent-magnets are replaced by electromagnets (Main Coils). It was expected that by controlling the magnetomotive force of the Main Coil according to the gap sensor signal, the gap between the mover and the stator will be controlled constant like an active magnetic bearing in spite of the toothed pole structure essential to a stepping motor. Thus, it can be said that the MS type stepping motor is an amalgam of a stepping motor and a magnetic bearing.

Figure 3 shows the structure of the MS-type stepping motor element. The mover is made of laminated silicon steel. Six coils are wound around it. Two larger coils (Main Coils) are connected in series and produce magnetic flux Φm. Coils a1 and a2 are connected in series and when one

coil produces a magnetic flux in the same direction as Φm the other produces a magnetic flux counter-direction to Φm. The same applies for coils b1 and b2. The rotor has four toothed poles T1, T2, T3, T4. Let one pitch of stator be expressed as 2pi rad., then the phase relation of the toothed poles may be expressed as T1 0 rad. (i.e. teeth of toothed pole T1 in phase with that of stator); T2 pi rad. ; T3 -pi/2 rad. ; T4 pi/2 rad. As indicated in the figure, the X axis is defined as the direction of propulsion, and H as gap length. Figure 4 shows the equivalent circuit of the MS-type stepping motor element. 'U' stands for the magnetomotive force of the coils; 'R' stands for the reluctance values of the toothed poles. Magnetic reluctance and magnetic hysteresis of the iron core were assumed to be negligible.

ANALYTICAL PROOF OF STABLE SUSPENSION BY A STEPPING MOTOR

From the equivalent circuit of the SM-type stepping motor element (Figure 4), the magnetic co-energy may be expressed as a function with the following parameters as the following equation.

W =function (Um, Ua, Ub, p1, p2, p3, p4, X, tooth width, valley width, H)
Where   W: magnetic co-energy of the system.
        Um, Ua, Ub: magnetomotive force of coils.
    p1, p2, p3, p4,: permeance of toothed poles T1, T2, T3, T4.
        X: longitudinal displacement of rotor.
        H: gap length.

Attractive force and propulsive force of the stepping motor element are given as the derivative of the magnetic co-energy by H and X as follows.
Attractive force = dW/dH,   Propulsive force = dW/dX

By using the assumed flux pattern method, permeance   p1, p2, p3, p4 of toothed poles T1, T2, T3, T4 are given as functions of X, tooth width, valley width, H. Figure 5 is the calculated value of the attractive force using the above equations. The horizontal axis is X/pitch, and the vertical axis normalized attractive force. F1, F2, F3, F4 are attractive force acting on toothed poles T1, T2, T3, T4 respectively. Due to the toothed pole structure of the motor, attractive force acting on each toothed pole fluctuates as the rotor moves in the X direction. Figure 5 shows the fluctuation of F1. However, summation of forces F1 to F4 is more or less constant and insensitive to change of X. This is due to the phase relations of the toothed poles mentioned before. It should be noted that the above calculation proves that an active magnetic suspension control can be achieved by only controlling the magnetomotive force (that is current) of main coil independent of displacement X and the currents of the coils A and B.

The optimal structure and driving conditions of the motor were estimated. In designing the motor, the "optimal" design was set as such a design that the fluctuation of the attractive force acting between the stator and mover becomes minimum when the mover is driven in the X direction.   In other words, parameters that define the shape and size of the toothed poles were chosen so that the attractive force becomes most insensitive to change of X. It was found from calculation that (attractive force fluctuation / average force) becomes minimum when the value of (tooth width / pitch) lies between 0.45 and 0.5.

Driving of the motor can be done in exactly the same manner as 2 phase PM stepping motor by using coil A (A1+A2) and coil B (B1+B2). The driving method commonly called mini–step drive or micro–step drive, where the currents are provided like sinusoidal forms, is preferable to MS stepping motor. Rapid change of the currents of coils A and B may disturb the calm suspension. And micro–drive method is also desirable for precise positioning and smooth movement.

SUPER CLEAN ROTARY SERVO ACTUATOR[4]

Since the one MS stepping motor unit shown in Figure 3 does not have the function of attitude control in itself, totally contactless suspension of a rigid body requires several MS stepping motor units and electromagnets. Now our research group has made and tested more than 10 types of MS stepping motors applying the MS units. Three typical examples will be described in the following chapters.

In this chapter outer rotor type actuator shown in Figure 6 is explained. Its structure is illustrated in Figure 7. Inner surface of the rotor is toothed like an inner gear. Four MS stepping motor units installed as a stator rotate the rotor exactly like a stepping motor. For the magnetic levitation, in addition to the four MS stepping units, five eddy current type gap sensors and four electromagnets are placed as shown in Figure 7. Four MS stepping motor units and the gap sensors S1 and S2 compose a radial magnetic bearing by controlling the attractive forces of the MS units according to the sensor signals.

In order to keep the axial displacement and attitude of the rotor, the attractive forces of four electromagnets which pull up the rotor against the gravity are controlled by PD control circuit from the signals of sensors S3,S4, and S5.

Since a stepping motor has the ability of self positioning or open–loop drive, a developed actuator does not need any sensor for rotation and keeping an ordered position. However, when more accurate positioning is required, closed loop control with sensor feed back is effective in stepping motors. Moreover, to realize fine velocity control and torque control, sensor feed back is inevitable.

As shown in Figure 7, a resolver is installed in the actuator for precise position control. The resolver has a resolution of 1,536,600 pulses per revolution. Position control is done by using positional digital data and velocity digital data processed from resolver signal as shown in Figure 8 . Very precise positioning with 8.44 arc–sec step motion can be obtained as shown in Figure 9. For the measurement of the rotor position, a capacitor type gap sensor is used to detect the displacement between it and metal plate winged on the rotor. Even though the position controller does not imply integration in feed back loop, no difference is found between corresponding forward and backward steps. Because of no mechanical friction by means of magnetic suspension, steady state error and lost motion can not be observed. The specification of the actuator is listed in Table 1. By the aid of a precise positioning sensor, an MS type stepping motor can display the ability of a very precise positioning actuator.

ACTUATOR FOR HIGH VACUUM[4]

One of the most promising applications of magnetic bearings and magnetic levitation is application in vacuum. Since the developed motors do not need any lubricants like magnetic bearings, they are useful in vacuum environments. For the ultra high vacuum, however, careful attention should be paid to gases from the coils and resin of laminated cores of magnetic circuits which contaminate the vacuum environment. In order to prevent the gases in the vacuum environment, a thin non-magnetic metal sheet is used to seal the coils and laminated core in the actuator designed for ultra high vacuum shown in Figure 10.

Its construction is explained in Figure 11. It can rotate and move up and down by installing the linear MS units and rotary MS units to the inner stator shown in Figure 12. As presented in Figure 10 and Figure 11 the stator is completely capsulated and sealed by thin stainless steel. So the gas from coils is completely kept inside the actuator. The rotor, on the other hand, is made of iron and aluminum. On the central part of the inner surface of the rotor cylinder teeth are made so as to control the rotary motion. And on the upper and lower parts of it cylinder circular grooves are machined for up and down motion. To prevent the emission of the gas from iron, the surface of the iron part is masked by nickel.

While by means of the shelter, the gas from the actuator can be eliminated, several problems had to be solved for building up a magnetically suspended actuator. The major hurdle is to get good gap sensors to detect the position and attitude of the rotor for levitation control. Since there is a thin metal shield between the rotor and stator, it is impossible to use optical sensors and an eddy current type gap sensor. An inductance type gap sensor where position of a target is detected by sensing the change of permeance of a magnetic circuit shown in Figure 13 is newly developed. The frequency response of the sensor is up to 10 kHz and good enough for levitation control as a magnetic bearing. One gap sensor magnetic circuit can detect displacements of X and Y. Two sensor magnetic circuits are installed in upper and lower parts of the stator to detect four degrees of freedom of the rotor position and attitude for active magnetic levitation like a magnetic bearing.

As mentioned in the prior chapter, four MS stepping units make up a radial magnetic bearing. It is possible to compose a θ-Z MS actuator by using a radial magnetic bearing with 4 rotary MS units and that with 4 linear MS units. Due to the gravity, moving the rotor upward is much harder than rotating it. So, another radial bearing with 4 linear MS units is added as shown in Figure 11 to produce enough propelling force to move up and hold the rotor.

Both the rotary and up and down motion are controlled independently and synchronously like a 2 degree of freedom robot by open loop and micro step driving method of a stepping motor. The specification of the developed actuator for the use in vacuum is shown in Table 2. It is expected that the developed actuator will be applied as a wafer handling robot in vacuum and clean room.

LINEAR CONVEYER SYSTEM

VR type MS Stepping Motor Element

As there are two types in stepping motors: Permanent Magnet type and Variable Reluctance type, an MS stepping motor element originated from VR type can also be created. In Figure 14 structure and equivalent circuit of magnetic circuit of the VR type MS unit are shown. Comparing the MS unit based on PM type shown in Figure 3, a VR type MS unit does not need main coils but only four independent coils and amplifiers. However their operating principle is the same. As shown in Figure 15, by controlling the current of each coil so as to produce the same magnetomotive force to each pole gap as in a PM type MS unit, a VR type MS unit also obtains both the functions of attractive force control and positioning control.

Prototype of Magnetically Suspended Linear Conveyer[3]

The linear unit shown in Figure 14 requires power supply wiring to the moving part. In actual applications, however, there seem to be many cases where the elimination of the wiring to the slider by locating the coils to the stator is preferred. Figure 16 is a schematic diagram showing the basic magnetic circuit of the Stator-Coil-VR type motor. The length of the laminated slider core is chosen so that the operating principles of the Stator-Coil-VR type and the formerly described VR type shown in Figure 14 are the same. How to choose the length is explained as listed below.

(1) In the equivalent circuit of the VR type shown in Figure 14, the resistors and batteries are connected in parallel. This means that the position of the toothed poles (T2 and T3 e.g.) are interchangeable.

(2) Toothed poles of the Stator-Coil type are situated in a cyclic array (i.e. T1-T3-T2-T4-T1-T3-....), therefore, if the slider core forms a closed magnetic circuit equivalently with four toothed poles, the equivalent circuit will be the same as the VR type shown in Figure 14.

(3) The length of the slider core is chosen to satisfy the equation: Length = 4 × (pitch between toothed poles). When this equation is satisfied, as is the case of Figure 16, the equivalent circuits of the Stator-Coil type and the Slider-Coil type are the same even if the slider core exists over five toothed poles.

In order to confirm the idea of the Stator-Coil VR type linear MS stepping motor, a magnetically suspended conveyer is constructed. In Figure 17 a simplified cross sectional diagram is shown. And Figure 18 is a photograph showing the lower stator cores and the slider (upper stators are removed to show the internal structure). The slider has 4 laminated slider cores on each side. A pair of lower stator cores and a pair of upper stator cores are used to move and keep the longitudinal position and to control the horizontal position, rolling and pitching of the slider. Yawing and lateral motion of the slider are passively held by facing longitudinally grooved plates and permanent magnets.

32 eddy current type gap sensors are situated on the lower touch down surface. Control circuits are designed so that the gap sensor signals and energized magnet coils are switched according to the position of the slider. The slider could be magnetically suspended and propelled smoothly.

630

CONCLUSIONS

Magnetic suspension of a rotor or slider of stepping motors is realized by developing an MS stepping motor element which can control the attractive force and the propelling force independently. By using a number of the elements, various kinds of contactless positioning mechanisms have been built and tested to confirm the effectiveness of the theoretical estimation about their design. The developed actuators, having the function of stepping motor and magnetic bearing at once, are expected to be applied as positioning mechanism, conveying system, and direct-drive actuators for robots, in clean room, vacuum chamber,space and hostile environments.

ACKNOWLEDGMENTS

REFERENCES

1. Higuchi,Toshiro: Applications of Magnetic Bearings in Robotics. Magnetic Bearings, Proceedings of the First International Symposium on Magnetic Bearings 1988, Springer-Verlag, pp. 83-99.
2. Higuchi, Toshiro;and Kawakatsu, Hideki:Development of Super-clean Actuator for Machines and Robots, Proceedings of MOTOR-CON,June 1988.
3. Higuchi,Toshiro;and Kawakatsu, Hideki:Development of a Magnetically Stepping Motor for Clean-room Transportation and Sample Handling, Proceedings of International Conference of Maglev'89, July 1989, pp.363-368.
4. Higuchi,T.;Horikoshi,A.;and Komori,T.:Development of an Actuator for Clean Rooms and Ultra High Vacua, Proceedings of the Second International Symposium on Magnetic Bearings,July 1990, pp.115-122.

Table 1. Specification of the clean servo actuator.

Levitation Control	Rotor Mass	8 kg
	Axial Stiffness	4 N/μm
	Gap Fluctuation	10μm
Position Control	Max. Speed	3 r.p.s.
	Max. Torque	1 kgf m
	Repeatability	±1.8 sec

Table 2. Specification of θ–Z actuator for ultra high vacuum.

	Up & Down	Rotation
Repeatability	±5 μm	±10 sec
Max Propulsive Force	4.5 kgf	5 kgf cm
Positioning Resolution	2.9 μm/pulse	10.5 sec/pulse
Stroke (up & down)	10 mm	
Radial Stiffness	2.0 N/μm	
Rotor Mass	2.7 kg	
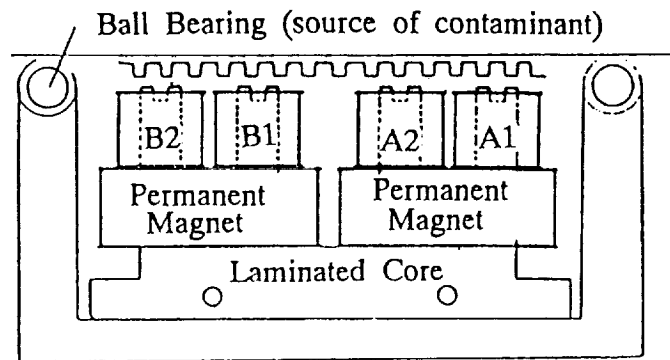
Figure 1. Conventional Permanent Magnet
(PM)-type linear stepping motor.
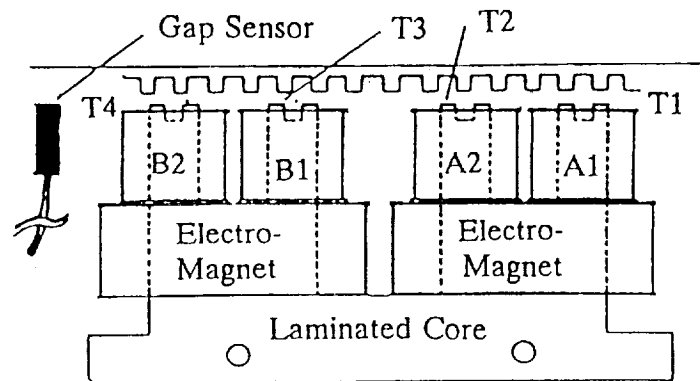
Figure 2. Idea of the MS-type linear stepping motor.
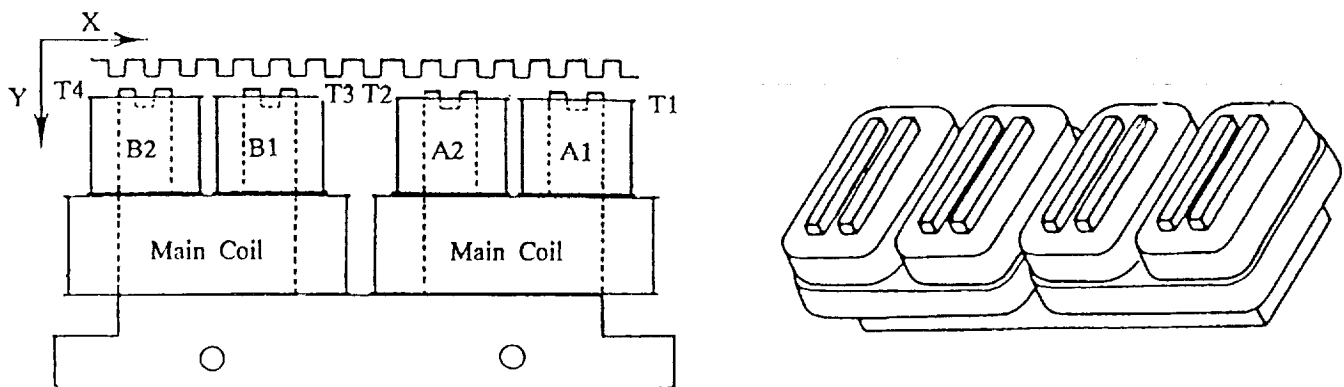
Figure 3. Structure of the MS-type stepping motor element.
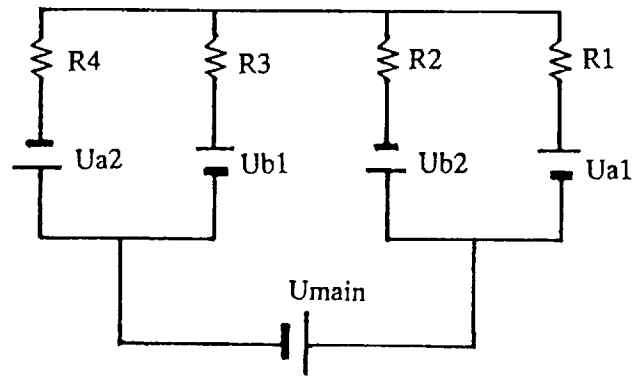
Figure 4. Equivalent circuit of the MS–type
stepping motor element.
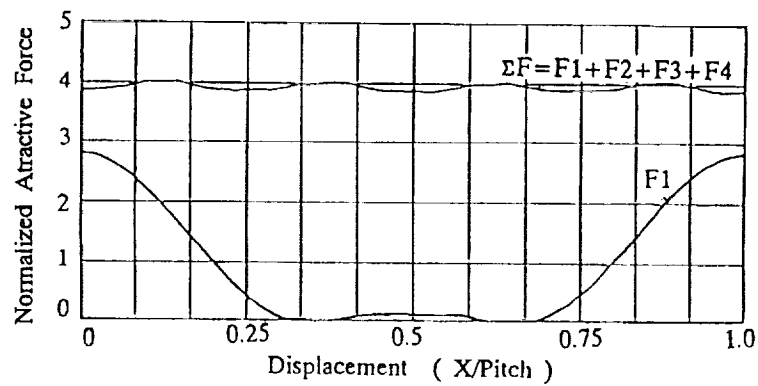
Figure 5. Calculated value of attractive force
of a pole and poles.
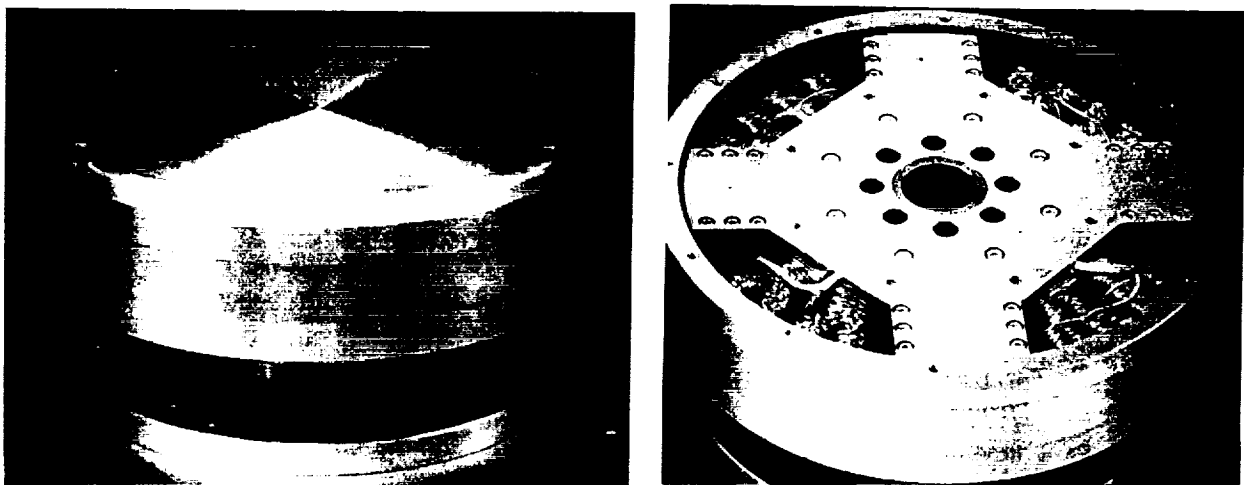
Figure 6. Photos of outer rotor rotary servo actuator.
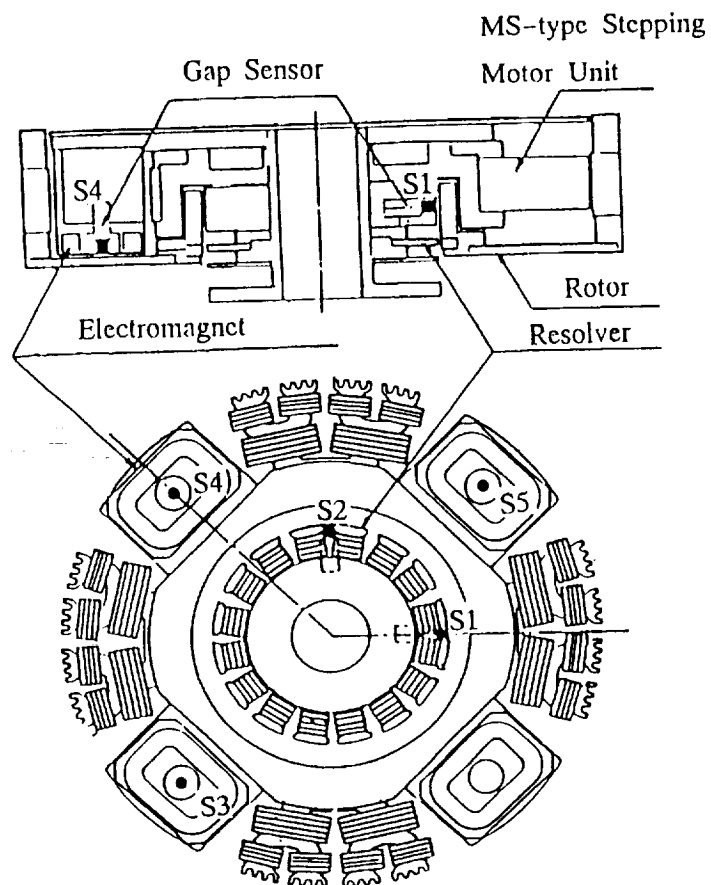
Figure 7. Structure of clean rotary servo actuator.
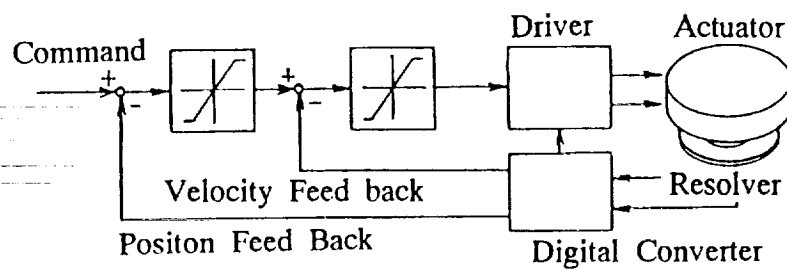
Figure 8. Diagram of position controller for the servo actuator.
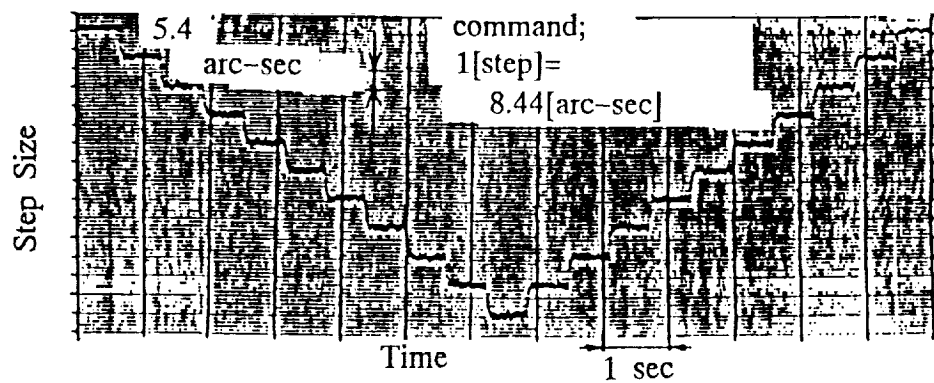
Figure 9. Minimum stepwise movement of forward and backward rotation.

Figure 10. Photos of θ–Z actuator for ultra high vacuum.

Rotor

Gap Sensor

Linear Unit

Rotary Unit

Gap Sensor

Metal Seal Flange
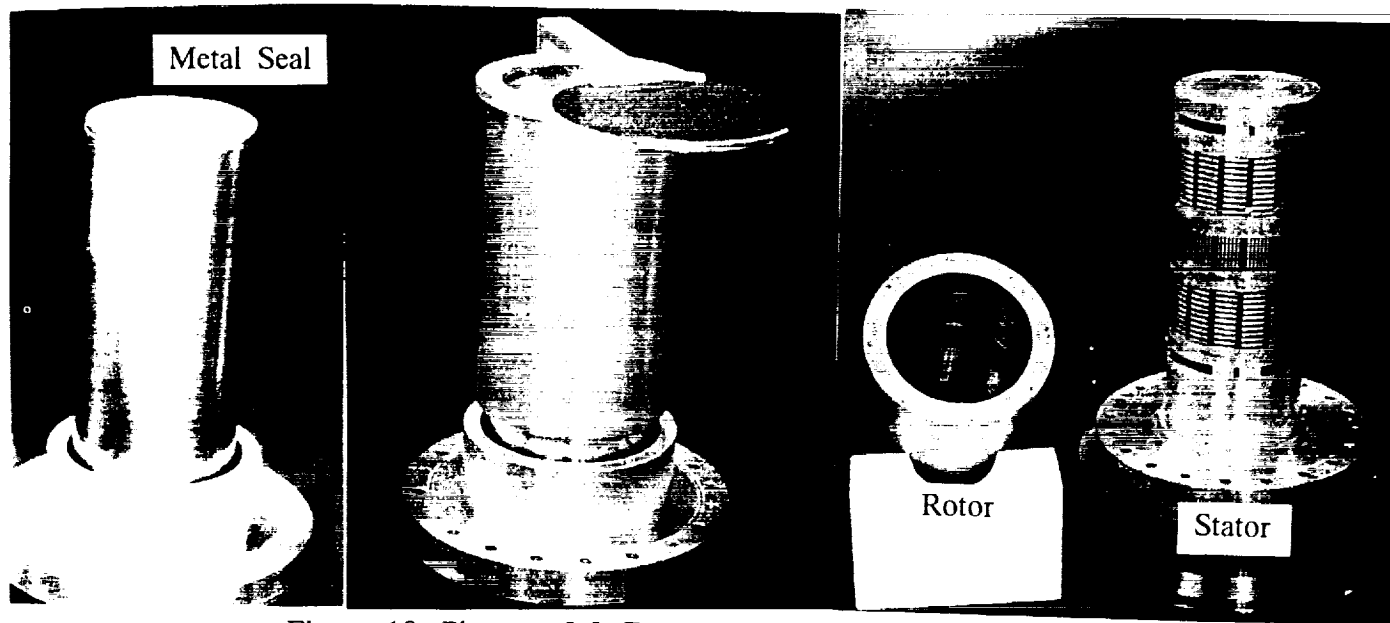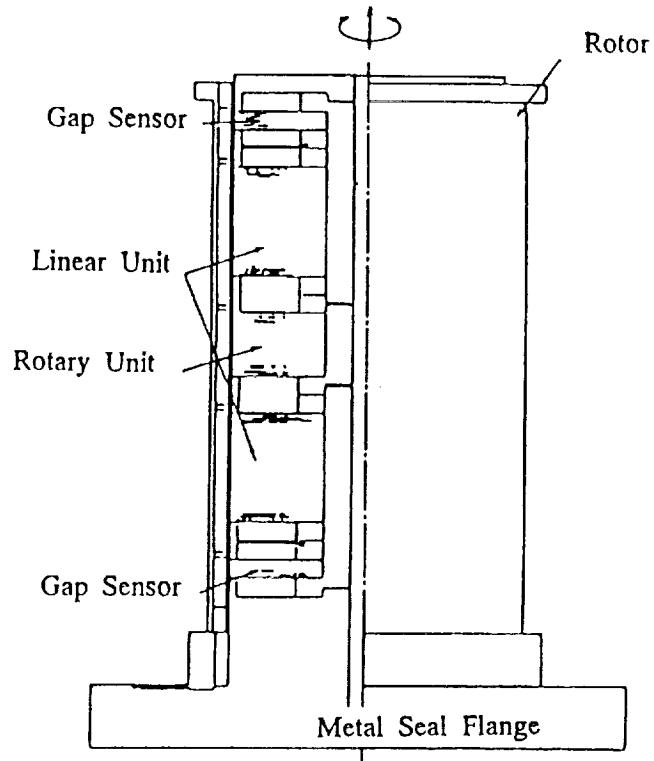
Figure 11. Section view of the actuator
for high vacuum.

Main Coil

B1   B2

A2

A1

T4

T3

T1   T2

Linear Unit

B1

A2   B2

A1

T4

T3

T1   T2

Rotary Unit
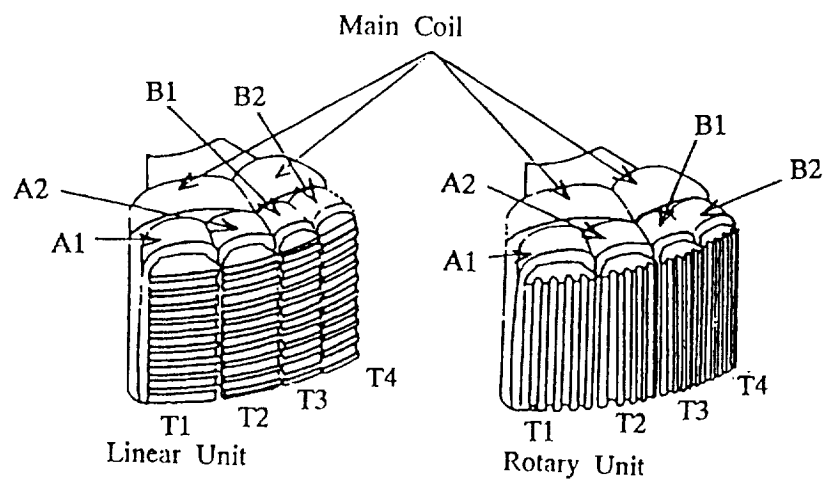
Figure 12. MS-type linear and rotary stepping motor units.
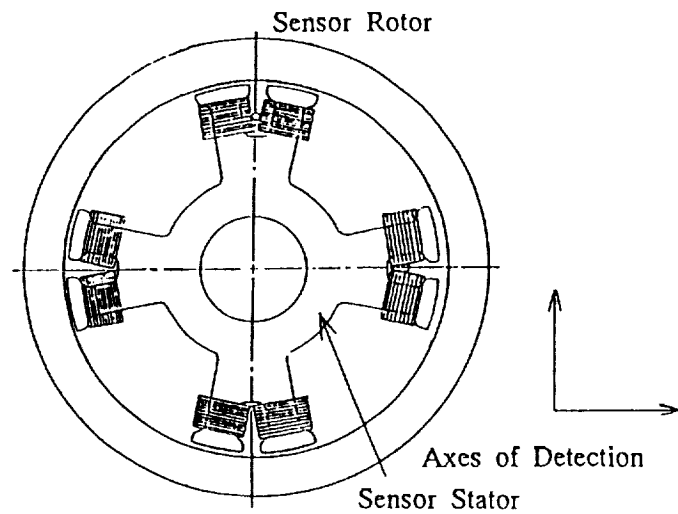
Figure 13. Inductance type gap sensor.
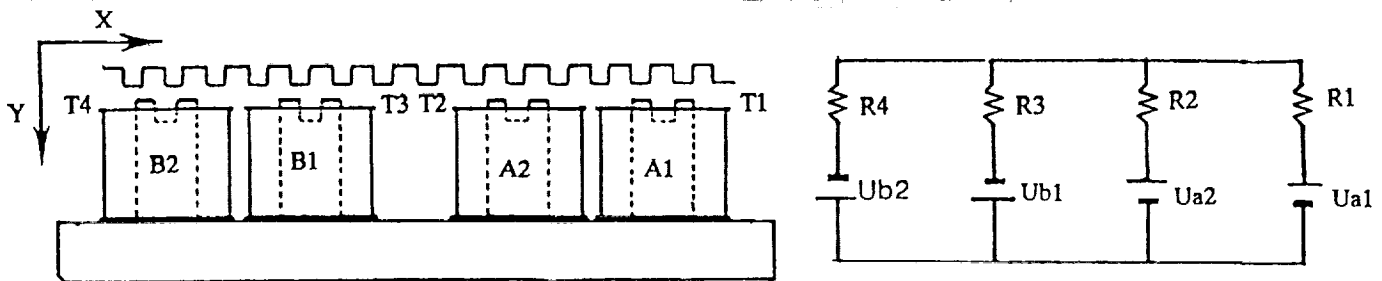
Figure 14. Structure and equivalent circuit of magnetic circuit of the VR type MS unit.

d:gap value
do:preset gap
b:bias
A:amplifier

(a) PM type
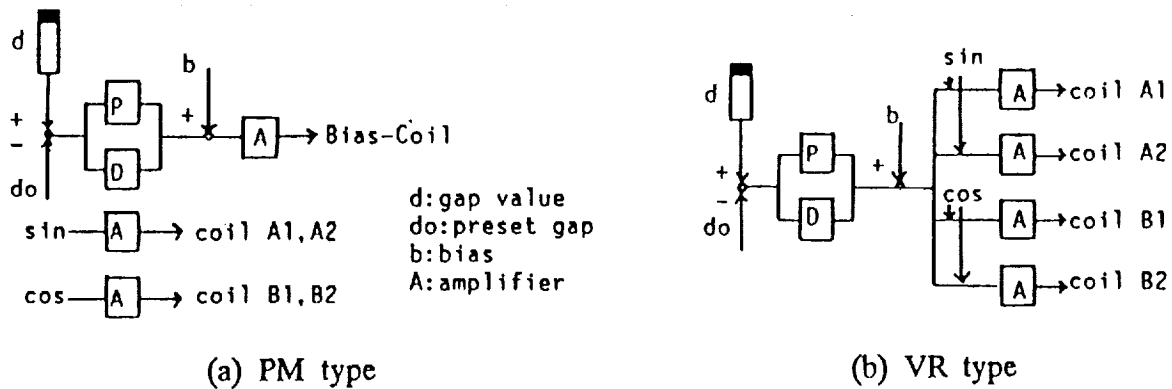
(b) VR type

Figure 15. Control circuits for PM and VR MS stepping motor elements.
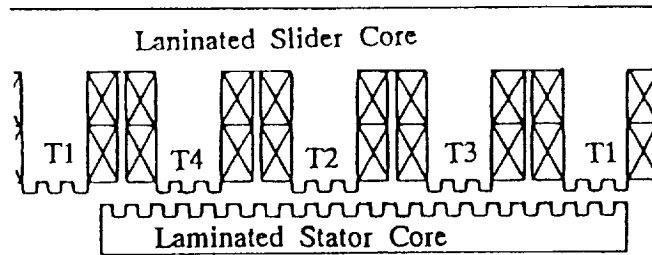
Figure 16. Schematic diagram of
Stator-Coil-VR type motor.
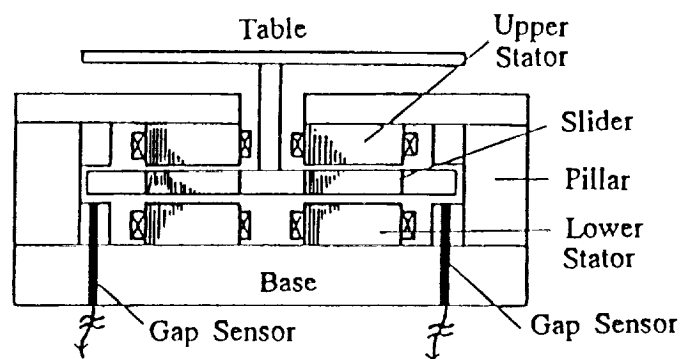
Figure 17. Cross sectional diagram of
MS stepping conveyer.
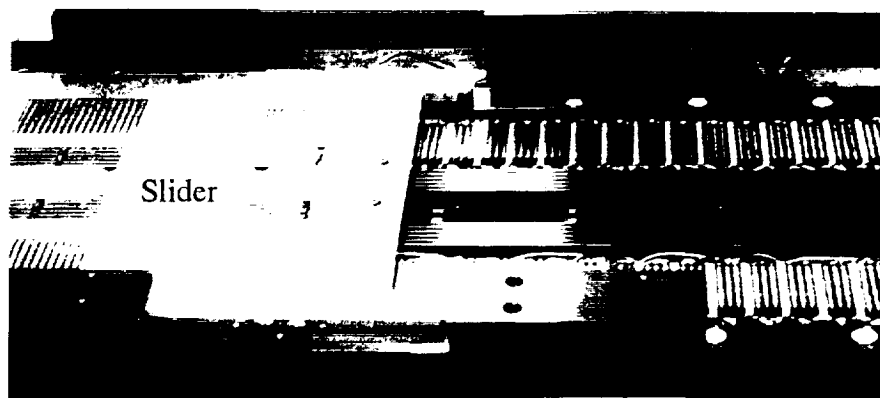
Figure 18. Photograph showing the lower stator cores and the slider.

SIX DEGREE OF FREEDOM FINE MOTION POSITIONING STAGE BASED ON MAGNETIC LEVITATION*

R. W. Arling
Independent Consultant
Windham, NH

S. M. Kohler
Sandia National Laboratories
Albuquerque, NM

S/4-37

//922

P. /2

SUMMARY

The design of a magnetically suspended six degree of freedom positioning system capable of nanometer positioning is presented. The sample holder is controlled in six degrees of freedom (DOF) over 300 micrometers of travel in X, Y and Z directions. A design and control summary, and test results indicating stability and power dissipation are included. The system is vacuum compatible, uses commercially available materials, and requires minimal assembly and setup.

INTRODUCTION

Positioning systems are employed in a variety of end products. High precision fine range positioning stages are often coupled to larger motion X-Y stages for increased travel. This combination allows utilization of available dynamic range for extension to the nanometer regime. Conventional fine positioning systems employ piezoelectric, linear, or DC motors. Motors are coupled directly, or through lead screws and friction drives for actuation. Flexures and/or bearings are employed to constrain the motion to the desired degrees of freedom. Performance of these conventional systems is compromised by the requirement of providing six independent degrees of positioning with stacked, reduced degree of freedom systems. The positioning problem becomes difficult due to undesirable couplings between "independent" axes. In addition, the systems suffer performance degradation from friction, backlash, etc. Vacuum compatibility further reduces available options or, at the very least, greatly increases complexity.

Magnetic levitation is an attractive alternative to the conventional positioning systems outlined above. Recent success of multiple degree of freedom efforts provided the impetus for development of a commercially available design based on techniques proposed in [1-2]. The intent of the design is to provide positioning for silicon wafers used in integrated circuit production. Friction and particle generation are eliminated, and vacuum operation is possible. The nonlinear nature and computational

---

PAGE 640 INTENTIONALLY BLANK

PRECEDING PAGE BLANK NOT FILMED

requirements of magnetic positioning have, however, impeded the development of the technology. The advent of high speed processing now allows real time linearization at speeds commensurate with the controller bandwidth requirements. The limitations of stacked stage design are overcome by use of a single body acted on magnetically to provide motion in X, Y, and Z linear axes, as well as rotations about these axes. This system has been constructed, controlled, and tested and represents the subject of this paper.

FUNCTIONAL OVERVIEW

Electromagnetic actuators housed in a fixed frame are employed to provide stabilizing and actuating forces to a 10 kg. sample holder. The unipolar force capability of the actuators requires their arrangement in pairs to provide a quasi push-pull effect. The sample holder is counterbalanced against gravity with permanent magnets to reduce the power expenditure in the electromagnetic actuators. Local position feedback of the suspended sample holder is provided by commercial capacitive based sensors. Absolute position feedback is established with a laser interferometer system. Actuation signals are generated in a DSP based CPU and are based on six modal controllers whose position information is derived from either transformed capacitive sensors or laser interferometer measurements. Real time linearization is provided though application of analytical relationships and empirically determined lookup tables.

Magnetic gaps are adjusted with movable actuators to provide a nominal spacing of 300 microns, with total travel of +/- 150 microns from nominal. Permanent (counterbalancing) magnet gaps are adjustable to provide correct force balance of the sample holder.

SYSTEM DESCRIPTION

Mechanical Assembly

The primary mechanical components are illustrated in Figure 1.

Stage Frame. The stage frame is fixed in position relative to the motion of the sample. It supports 16 electromagnetic actuators arranged in 8 pairs located symmetrically about its periphery. Due to the unipolar force characteristics of the electromagnetic actuators, the pairings provide a quasi push-pull effect. Four pairs provide vertical force, and four pairs provide lateral force. The frame also supports the active portion of capacitive based position sensors for measuring magnetic gaps.

Stage Platen (Mirror Support Structure). The Stage Platen, in conjunction with the Interferometer Mirror and Sample Holding Apparatus, is acted upon as a single body by the actuators located in the frame. The stage platen contains iron targets for completion of the actuator magnetic circuit, as well as one half a kinematically designed mount for interferometer mirror attachment. The stage platen also houses targets for the capacitive based position sensors.
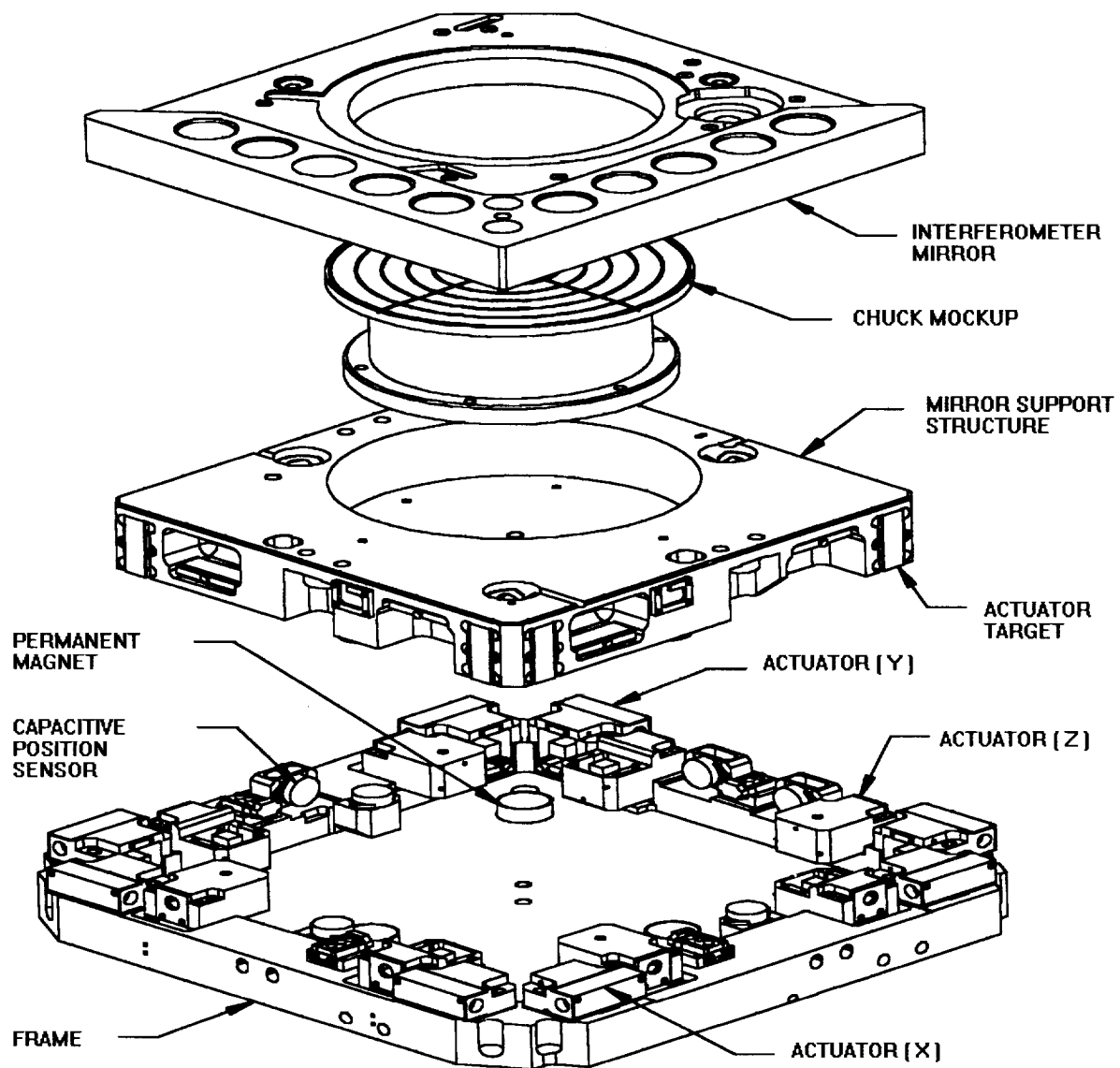
Figure 1. Stage mechanical components.

Interferometer Mirror. The interferometer mirror provides reflective surfaces for a laser interferometer system. In addition, it provides capability for secure attachment of a sample holder to minimize motion to the interferometer measurement points.

Magnetic Actuators. Actuators are individual modules of three types: lateral, vertical (upward), and vertical (downward). All actuators are nominally identical in electrical and force characteristics. The actuator mounts are adjustable to allow gap setting.

Chuck Assembly. A solid pedestal and chucking mechanism provides attachment of a sample (silicon wafer).

Permanent Magnets. Three pairs of permanent magnets provide a gravity counterbalance for the suspended stage Platen/Mirror assembly. The magnets in the platen and frame are oriented with poles appropriate to provide force to offset the Platen/Mirror weight. This counterbalancing force is necessary to minimize the power expended in the electromagnetic actuators. The mounting system allows adjustment of permanent magnet gaps to balance the Platen/Mirror. Proper adjustment provides a slight downward bias of the suspended assembly to guarantee a stable resting position.

Electrical Components

The electrical system is composed of the following subsystems: digital chassis, power amplifier chassis, power supplies, and user interface.

Digital Chassis. The digital chassis contains the following VME based circuit cards: a 32 bit floating point Digital Signal Processing (DSP) microprocessor card, a 32 channel 16 bit analog to digital conversion card, 14 bit digital to analog conversion cards, laser interferometer interface cards, and VME to user interface card.

Power Amplifier Chassis / Power Supplies. The power amplifier chassis contains 16 amplifier cards to provide current to each of the actuators. Linear transconductance amplifiers with scale factors of 100 mA / V are employed. Amplifier bandwidth ranges between 15 kHz and 20 kHz depending on actuator inductance, which varies with magnetic gap. The worst case bandwidth contributes less than two degrees of phase loss at 100 Hz. Linear power supplies provide current at +/- 40 volts to the actuator amplifiers.

User Interface. The user interface is a PC that serves as a development system for the software and provides control inputs, data collection, and display of relevant system information.

Position Sensing

Capacitive Position Sensors. Commercially available capacitive based position sensors measure the position of the stage platen relative to the stage frame (i.e., magnetic gaps). Six sensors are located in the frame, with corresponding targets located in the stage platen. Three sensors measure laterally (X, Y, Θ_z), and three measure vertically (Z, Θ_x, Θ_y).

Laser Interferometer. A laser interferometer measures absolute position of the laser interferometer mirror with respect to the machine frame. Recall that the fine stage is, for practical uses, coupled to a coarse positioning stage for larger travel capabilities. The actual coordination of the various position measuring systems is discussed later in the paper. The laser interferometer system provides measurement of X, Y, Θ_z, Θ_x, and Θ_z. The stated resolution of the system is $\lambda/128$ ($\lambda = 633$ nm for HeNe laser), or approximately 5 nm linear.

644

The actuators employed in this system are represented schematically in Figure 2. Material, geometry, and electrical coils are designed to maximize frequency response and force, and minimize packaging volume and power dissipation.

The actuator core and target are constructed of commercially available 0.15 mm laminations of Superperm 49. The laminations are stacked to a thickness of approximately 12 mm and clamped in the actuator housings. A free standing coil of 550 turns of #26 copper wire is fitted over the center section of the lamination "E" and the entire assembly is potted in epoxy. The face of the actuator is ground to provide a uniform surface. A similar construction process is used in the construction of the targets. The target assemblies are potted into the Stage Platen, and the sides are ground flat. When current is passed through the electrical coil in the "E" structure, a force that seeks to reduce the distance between "E" and "I" is developed. The force produced is a highly nonlinear function of gap and applied current. Linearization of the force - gap - current relationship is required for implementation of effective control technique. A specialized test fixture is employed for the actuator characterization [3]. Information is obtained by incrementing and recording the gap throughout the expected range of travel. At each gap setting, the current is discretely increased and, for each point, a force value is recorded. The data obtained is represented as a curve of force versus current, parametric on gap. This information is translated into a three dimensional look-up table for use by the controller. Figure 3 is a representative curve of the uncompensated actuator characteristics.
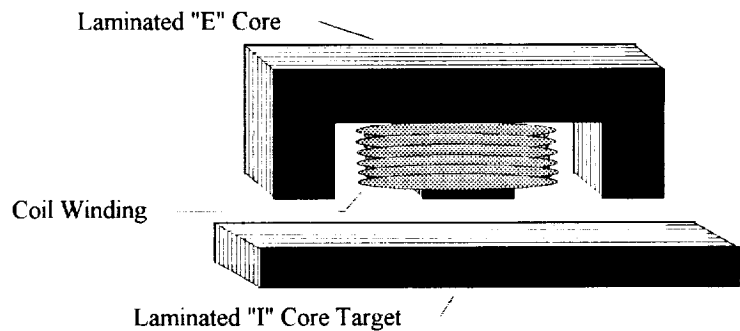
Figure 2. Schematic actuator / target representation.
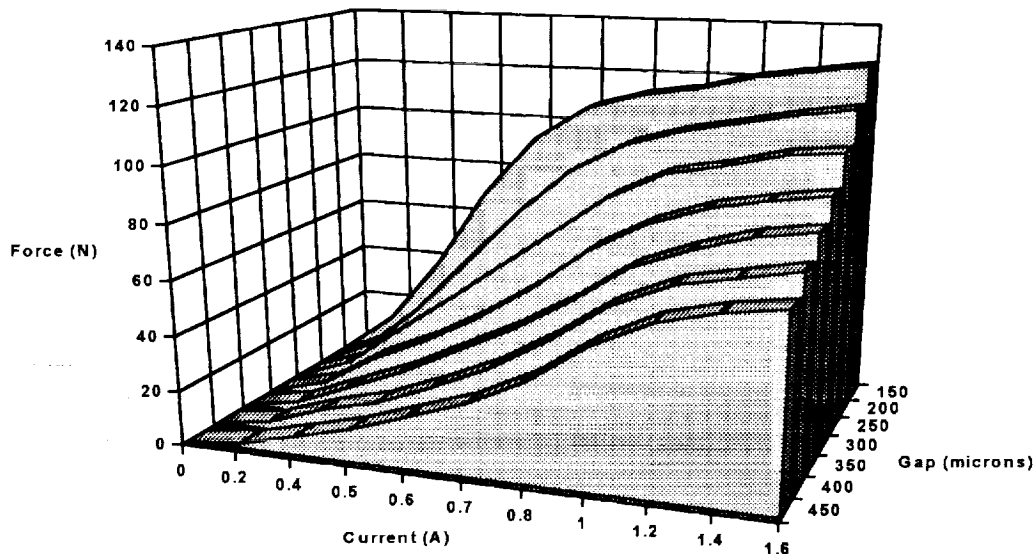
Figure 3. Uncompensated actuator force curve.

The lookup table is employed for large force commands. For small force commands, as for stabilization about an operating point, the force relationship is approximated [2] as

$$F \propto (i / g)^2 ,\qquad\qquad (1)$$

where f is desired force, g is measured gap, and i is required current.

STRUCTURAL CONSIDERATIONS

High controller bandwidth is a requirement of the positioning system described in this paper. To achieve high bandwidths, effort is made to design for high stiffness in the mechanical parts and couplings. The goal of this initial design is to utilize common, machinable materials in the construction. Given this constraint, geometric optimization of the parts is undertaken as a means of providing stiffness. Finite element analysis is employed prior to design of the parts, and verification of the predictions is provided by modal testing. Knowledge of the modal frequencies proves invaluable in controller efforts as well as system troubleshooting. Most of the optimization involves the interferometer mirror, as the effects of distortions in this component are readily apparent as positioning error. Material for the mirror is Zerodur®, selected for its suitability for extreme temperature stability in mirror surface fabrication. Stage Platen, Frame, and actuator housings are nickel plated aluminum.

The Stage Platen to Interferometer Mirror mounting receives attention due to the dissimilar coefficients of thermal expansion between the two materials. A kinematic mount of three hemispherical steel balls and V-grooves is employed in the coupling. A magnetic preload increases the loading between the ball and groove. A vertical adjustment scheme is incorporated into the mount to provide for Interferometer Mirror leveling with respect to measurement laser beams.

CONTROL SYSTEM

Digital control of the system is desirable due to the geometrical transforms required between sensors and actuators and the real time linearization of 16 independent actuators. The overall control strategy is outlined in Figure 4.

The electromagnetic actuators, as previously mentioned, are located in the fixed Stage Frame and act upon iron targets imbedded in the (suspended) Mirror / Platen assembly. The sensors, both capacitive and interferometer based, measure points of the suspended body different from the actuation points. It is therefore required to transform the measurement and actuation points to modal coordinates for controller operation. These operations require a priori knowledge of geometry and center of gravity of the suspended mass, which are readily available from the CAD models. Command positions and controller design are based on six modal controllers operating simultaneously in the DSP. The interferometer provides position feedback for all modal controllers with the exception of Z. Capacitive sensors provide magnetic gap information for lookup table reference, as well as position feedback for Z motion.
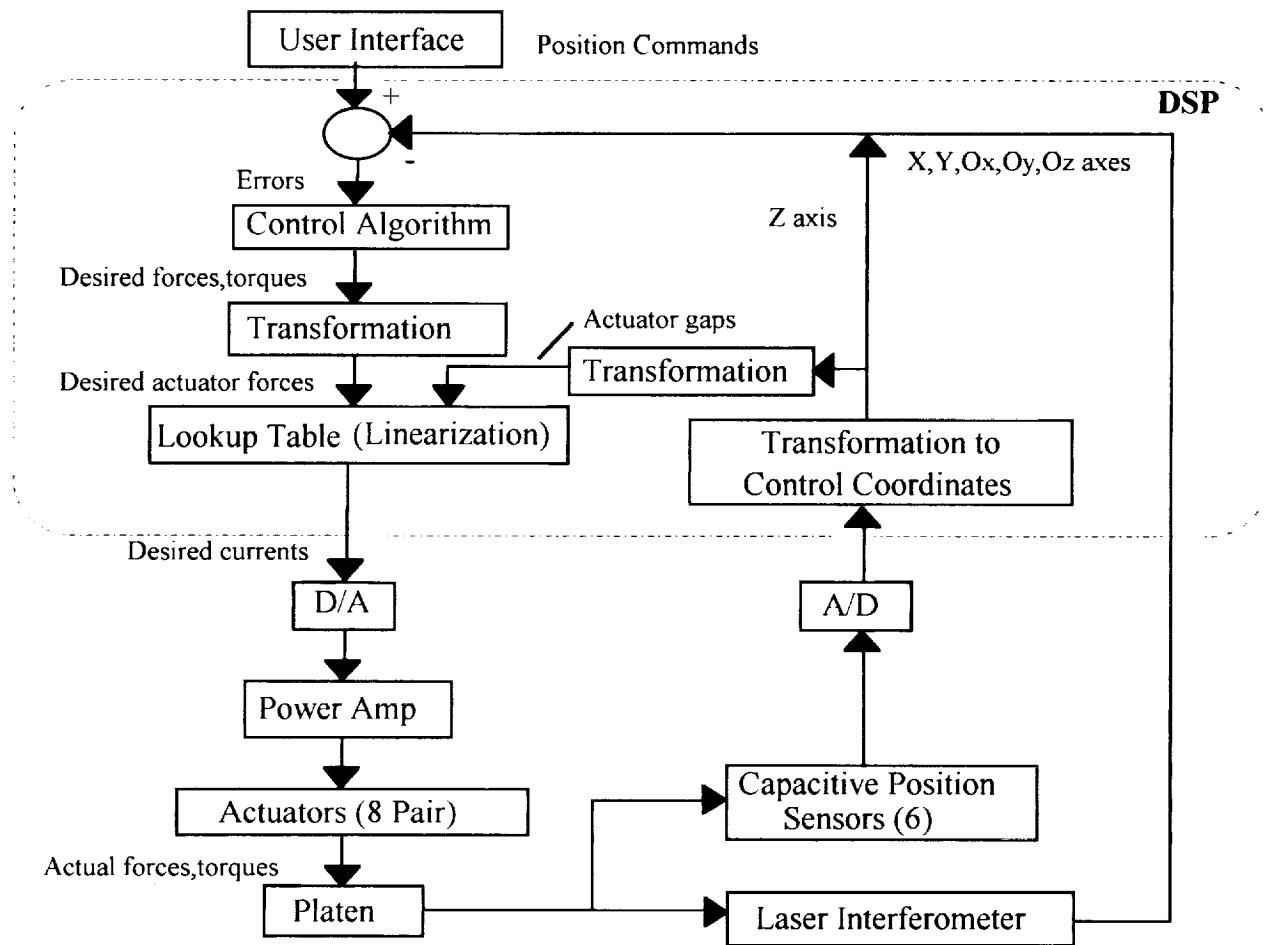
Figure 4. Control approach.

A PID (Proportional - Integral - Derivative) control algorithm is employed for each of the six modal controllers. Gains are selected to provide a critically damped, 30 Hz. gain crossover system in each axis at the 2500 Hz sampling rate. The 30 Hz. gain crossover is selected to avoid excitation of known structural resonances. A higher order controller will address structural issues, but processor limitations preclude implementation. A digital notch filter is employed to filter a predicted structural resonance set up by the kinematic mount between Stage Platen and Interferometer Mirror, but extension of this technique to all structural resonances is limited. Effort is in progress to address the bandwidth limitations imposed by structural resonance through mechanical and electrical filtering means, and additional computational capability. Part of the difficulty encountered in designing a controller for a fully suspended system is the inability to observe system behavior until levitation is achieved. Numerical simulation is relied on heavily to carry out controller development.

Positioning Stability

Stability Detractors

Positioning stability of the system is dependent on a number of factors. Floor vibration, varying laser interferometer environment, and sensor noise all contribute negatively to the system's intrinsic stability potential. With this in mind, brief descriptions of the Test Setup and stability detractors external to the stage system are included below.

Test Setup. The entire fine stage system is mounted to a coarse X-Y stage system which, in turn, is mounted to a 1m x 1m x 0.5m (l,w,h) cast iron base. Also attached to the base is a bridge of similar dimensions mounted above the stage structure to support the laser interferometer optics. The entire structure is encased in a Plexiglas shell (not shown). The structure is mounted on 4 vertical posts resting on a concrete floor. Elastomer isolation pads approximately one inch thick are located between the structure and top of the posts. The Test Setup is shown in Figure 5.

Floor Vibration. The concrete floor supporting the Test Setup also supports various pumps and other rotating machinery used in building HVAC. Measurement of environmental vibration levels in the cast iron base indicates substantial 28 to 31 Hz. energy in the Z direction [Table 1]. The large Z motions can be attributed to a rigid body resonant frequency of 30 Hz. determined by supported mass and isolation stiffness. The discrepancy in X and Y versus Z is due to non-uniform isolator stiffness in these directions. This frequency range is of particular concern due to the 30 Hz. gain crossover. Vibration below this frequency is tracked out by the control system, while those significantly above this frequency are attenuated by the isolation, structure, and controller.

Laser Interferometer Environmental Stability. The stability of a laser interferometer is, in part, affected by changes in the beam wavelength due to variations in the density of the medium through which the beam passes. Density (of air in this case) is a function of temperature, relative humidity, and barometric pressure. The laser wavelength in air will change 1 part per million (PPM) for a 1° C change in temperature, a 2.5 mm of Hg change in pressure, or a 30% change in relative humidity. Of these three, the air temperature is the least controlled. The Plexiglas shield encasing the test setup provides some stability, and the short term variations are expected to be minimal. Since the system stability test data relies on the interferometer, no stability information is extrapolated beyond the Test Setup's reference frame.

Capacitive Sensor Noise. Capacitive based sensors measure magnetic gaps for look up table reference and provide the sole source of position feedback for Z axis motion. The ability to accurately measure magnetic gaps is far less critical to the ultimate positioning than is actual position feedback. Noise has been reduced to 50 nm p-p on the capacitive sensors and cables, but still represents an obvious limitation to performance.
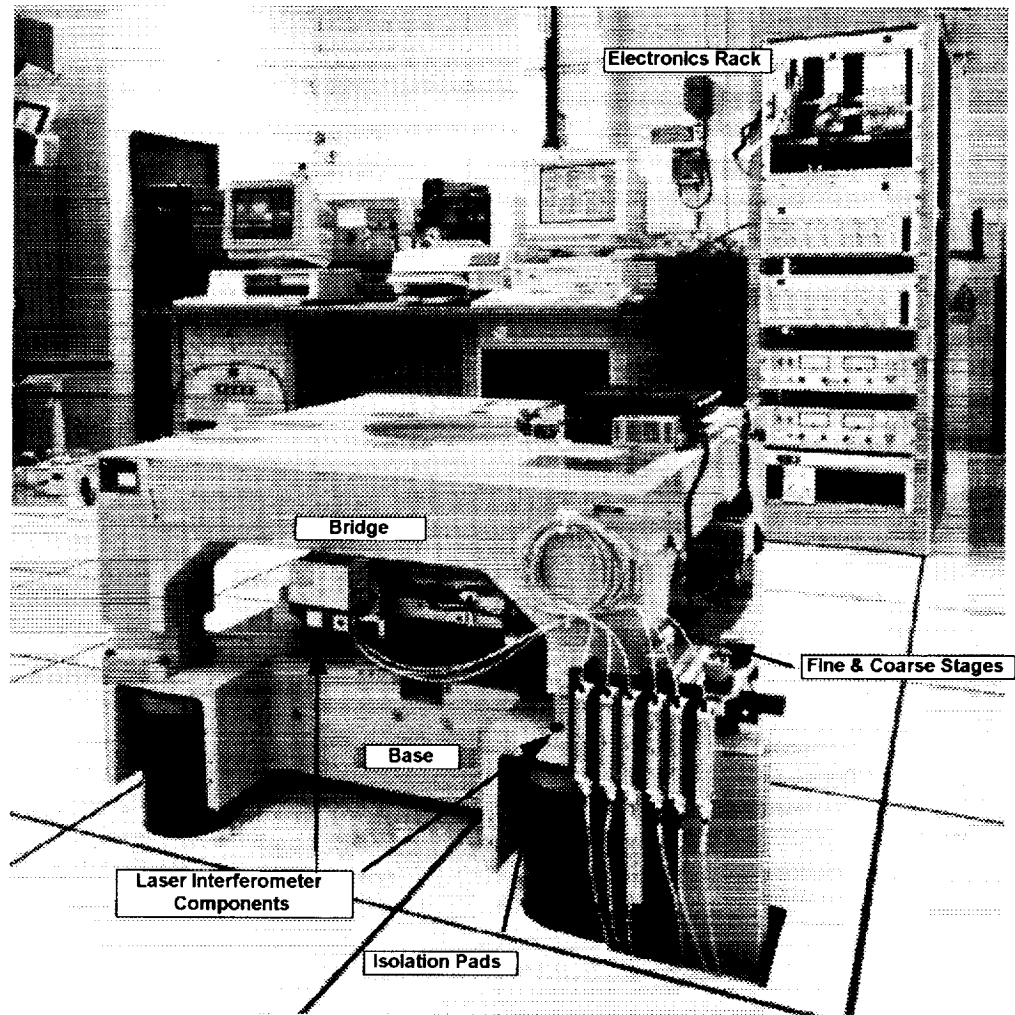
Figure 5. System Test Setup.

Stability Results

Measured stability of the system is indicated in Table 1. The large discrepancy in stability between axes is attributable to both lack of vibration isolation and sensor/cable noise in the Z axis.

Table 1. Floor Induced Motion and Positioning Stability

Axis	Input Motion @ Base (nm p-p)		Stability (nm p-p)
	Wide Band	28-31 Hz.	Stability (nm p-p)
X	308	22	20
Y	482	44	25
Z	390	348	100

The system responds to inputs as expected for a 30 Hz. system. Figures 6 and 7 indicate the results from a test to command position changes in (X, Y, Z), and (Θ_x, Θ_y, and Θ_z) simultaneously. Discrepancies in the responses for a given group are predicted by simulation and result from differences in the degree of saturation among the various actuators. A large, multi-axis move produces large variations in actuator force demands. Actuators that are heavily saturated exhibit inductive lags in output relative to lightly loaded actuators. The momentary force imbalances appear as crosstalk of linear responses and angular responses.

microns

Time (seconds)
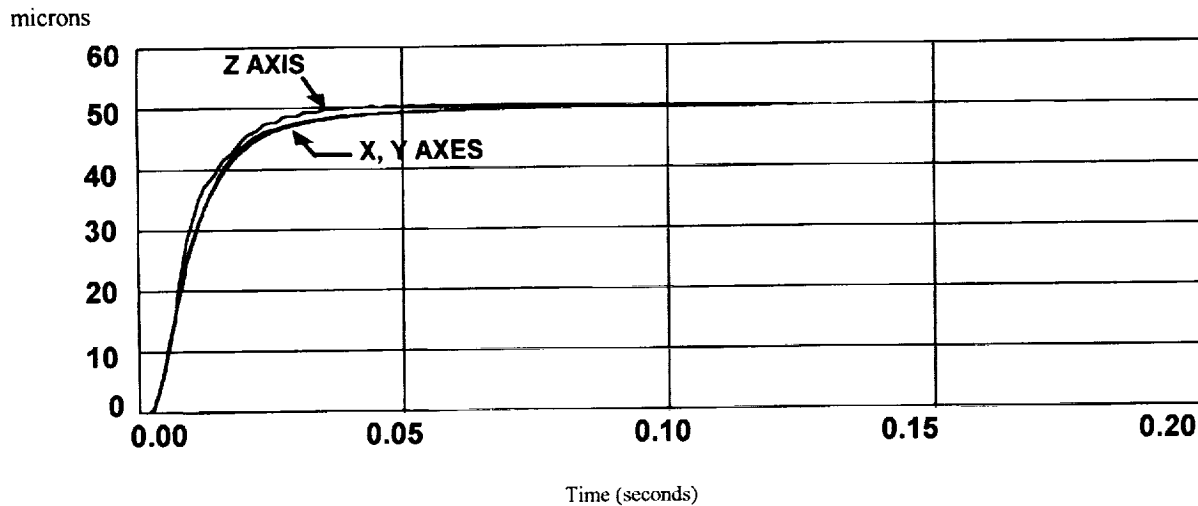
Figure 6. Linear step response.

micro radians

Time (seconds)
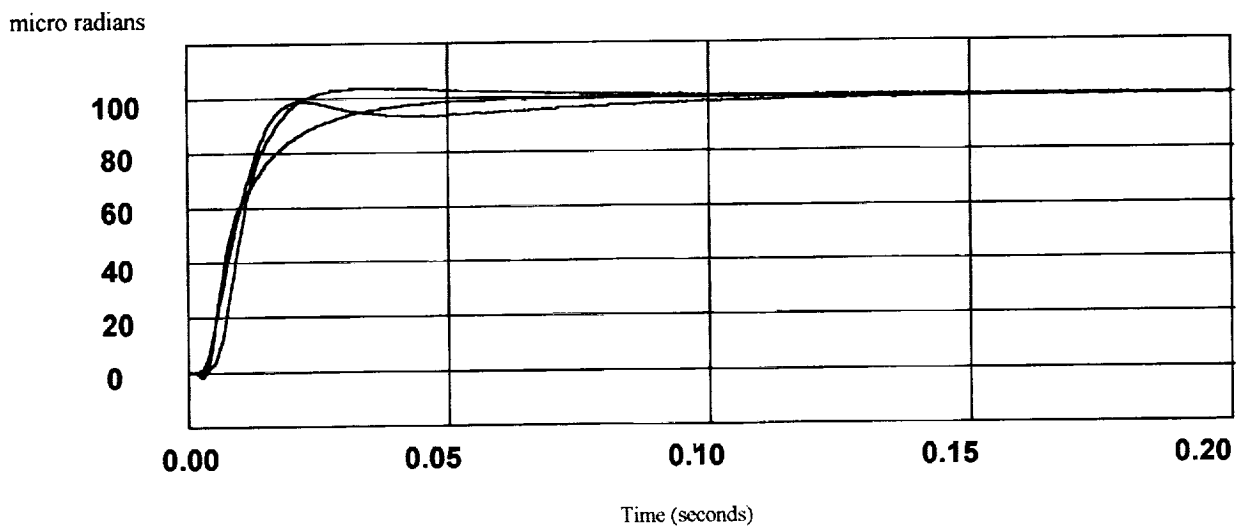
Figure 7. Angular step response.

Power Dissipation

Power dissipation for the positioning system is broken down into two categories: quiescent and peak. Quiescent dissipation refers to the rms power dissipated in the actuators while maintaining position. This value is dependent on such parameters as the effectiveness of the permanent magnet counterbalance, external disturbances, etc. The peak value indicates the peak power dissipated in the actuators during the simultaneous 50μm linear, 100μrad angular move demonstrated above.

Table 2. Power Dissipation

	Vertical (W)	Lateral (W)	Total (W)
Quiescent	0.017	0.102	0.119
Peak	0.674	1.376	2.050

In relation to power dissipation, it should be noted that the actuators are mounted in the Stage Frame to provide a conductive path for heat transfer. In addition, the suspended Platen/Mirror assembly is effectively isolated thermally due to the air gaps. These features are particularly useful in vacuum applications where cooling is problematic.

CONCLUSIONS

This paper has outlined the successful development of a fully suspended and controlled positioning system based on magnetic levitation. Results have confirmed the acceptability of this technology to a wide variety of positioning applications requiring extreme repeatability and accuracy. The test data, though some of the earliest taken with the system, shows performance to be within the capabilities of associated hardware. Extension of the system's stability to the resolution of the laser interferometer system is achievable with modest design modifications. Development is continuing specifically to improve the vibration isolation of the test setup and address the bandwidth and structural resonance issues.

Improvement in the vibration isolation of the Test Setup is possible with the addition of a commercially available system designed for this purpose. Such systems will have the effect of lowering the Test System rigid body modes to the vicinity of two to three Hertz, providing greater attenuation at frequencies critical to the controller.

The addition of processing capability will allow increased controller bandwidth, thus increasing the speed of response and disturbance rejection. The saturation effects associated with actuator inductance

can be addressed by an increase in the amplifier voltage rails beyond the +/- 40 volts employed in the initial effort. Commercial hardware is available to satisfy both of these requirements.

ACKNOWLEDGMENTS

REFERENCES

1. Trumper, D.L.: *Magnetic Suspension Techniques for Precision Motion Control*. Ph.D. Thesis, Dept. of Electrical Engineering and Computer Science, Massachusetts Institute of Technology, Cambridge, Mass., September 1990.

2. Trumper, David L.; Sanders, James C.; Nguyen, Tiep H.; Queen, Michael A.; *Experimental Results in Nonlinear Compensation of a One-Degree-of-Freedom Magnetic Suspension*, International Symposium on Magnetic Suspension Technology, NASA Langley Research Center, Hampton, VA., August 1991.

3. Poovey, Tony; Holmes, Mike; Trumper, David: *A Kinematically Coupled Magnetic Bearing Test Fixture*. Proceedings of ASPE 1992 Annual Meeting, Grenelefe, FL, October 1992.

ANALYSIS OF ACHIEVABLE DISTURBANCE ATTENUATION IN A PRECISION MAGNETICALLY-SUSPENDED MOTION CONTROL SYSTEM

Alexander V. Kuzin, Michael L. Holmes, Roxana Behrouzjou, David L. Trumper

Department of Electrical Engineering, University of N. Carolina at Charlotte, Charlotte, NC 28223 USA

S/5-37

11923

P. 13

SUMMARY

The results of the analysis of the achievable disturbance attenuation to get an Angstrom motion control resolution and macroscopic travel in a precision magnetically-suspended motion control system are presented in this paper. Noise sources in the transducers, electronics, and mechanical vibrations are used to develop the control design.

INTRODUCTION

Precision motion control at the nanometer level is required in many potential applications, e.g., for semiconductor manufacturing, large-travel probe microscopy, probing and analysis of integrated-circuit structures, and the testing of micromachines. Magnetic suspension makes possible performance of precision motion control systems which can not be achieved by other means [1]. An important requirement in precision motion control systems with magnetic suspension is that the disturbance influence on control coordinates of motion should be below a given value. There are fundamental trade-offs between the conflicting objectives of reducing sensitivity to disturbances (mechanical vibrations) and parameter uncertainty on the one hand, and filtering out any internally generated noise (sensor noise) on the other. It is the existence of these trade-offs which makes control system design for fine-motion control systems difficult. This paper deals with analysis of achievable disturbance attenuation in precision magnetically-suspended motion control systems. The objective is to get an Angstrom resolution in a 100 μm cube of accessible travel of the suspended platen.

DESCRIPTION OF THE SYSTEM

The magnetically-suspended six-degree-of-freedom motion control stage will be floated in oil to support its weight, provide mechanical damping, and high-frequency coupling [2]. In one possible design, the platen is suspended by a symmetric arrangement of twelve electromagnets $M1 - M12$ (Fig.1). The electromagnets are mounted in the machine frame and act on ferromagnetic targets

mounted in the platen. These electromagnets are arranged symmetrically at the corners of the platen. Since the electromagnets can exert only attractive forces, the actuators are arranged in pairs on opposite faces of the platen. The capacitance probes $C1 - C6$ provide measurement of the coordinates of the platen.

Magnet Force Measurements

In order to design a control system for the purpose of achieving levitation of the platen, accurate measurements of the magnet force characteristics were made. To carry out these measurements, the magnetic bearing calibration fixture has been used with the following characteristics [3]: measurement of the electromagnet actuator force from minimum to maximum core flux density at separation gaps ranging from 10 to 1000 microns; peak force capability on the order of hundreds of newtons; adjustment of the target separation gap as well as the rotation of the target relative to the actuator.

To study the magnetic force dependence of angle position of the platen, the measurements of magnetic force for maximum possible platen rotation about the short and long axis of the electromagnet were made. According to the magnet force measurements, it was accepted that in the first approach we can neglect the influence of rotation on the force characteristics of the electromagnets. The force of each electromagnet is the function of current of the electromagnet i_i and the gap between the surface of the electromagnet and platen target q_i

$$F_{m_i} = k_{i_i} i_i - k_{q_i} q_i, \tag{1}$$

$$i = 1, ..., 6.$$

The negative sign in the formula shows that the magnetic force decreases when gap increases.

Fluid damping

The platen will be floated in low-vapor-pressure viscous oil in order to support its weight and thus minimize power dissipation. The oil flotation provides several advantages. First, oil increases the high-frequency coupling between the platen and the frame. At frequencies above those which are well controlled by the active suspension, the platen motions are controlled through viscous coupling to the frame. Second, the oil supplies viscous damping to platen and frame vibrations and resonances. Such resonances can be troubling for ultra-precision control systems, and it is far better to solve them in the mechanical domain rather than attempting to compensate for them in the feedback controller domain. There are two kinds of damping influence from the fluid to the floated moving platen. The first one is the force of inertial friction of the fluid or its resistance to shear. This force is propotional to the contact area of the two separate surfaces, the speed of relative motion, and inversely proportional to the distance separating the two surfaces having the relative motion.

$$F_{d1} = \mu A \frac{v}{q}, \tag{2}$$

where μ - viscosity of fluid; A - area; q - separating distance; v - speed of movement. The second one is the squeeze film damping force. The load-carrying phenomenon arises from the fact that a viscous lubricant cannot be instantaneously squeezed out from between two surfaces that are approaching each other. It takes time for these surfaces to meet and during that interval, because of the lubricant's resistance to extrusion, a pressure is built up and the load is actually supported by the oil film. If the load is applied for a short enough period, it may happen that the two surfaces will not meet at all. According to the design (Fig.1), the nearest distance between the platen and the frame is the distance between the surfaces of the capacitive sensors and their targets on the platen. For one capacitive probe we have the case of a single circular plate of radius R approaching a flat plate. For this case the damping force F_d is [4]

$$F_{d2} = \frac{3\pi \mu R^4 v}{2q^3}. \tag{3}$$

The comparison of the equations (2) and (3) shows that the squeeze film damping force is much greater than the shearing damping force and therefore, we can neglect the latter in the calculations. Formula (3) allows us to estimate the desirable forces of electromagnets which they have to provide for movement of the platen along the corresponding coordinate.

The results of the damping force calculations allow us to make the conclusion that due to the large mechanical damping, which we can control through the choice of the fluid viscosity, area of the contacting surfaces and the distance between the contacting surfaces, we do not need additional electrical damping implemented in the controller design. So, to control the platen motion we can use the simple proportional controller.

Development of model for system dynamics

According to the equations for magnetic forces and moments we have the following model for system dynamics

$$m\ddot{x} + b_x \dot{x} - 3k_q x = F_{x_{dist}} + k_i(i_1 + i_2 + i_3); \tag{4}$$

$$m\ddot{y} + b_y \dot{y} - 2k_q y = F_{y_{dist}} + k_i(i_4 + i_5); \tag{5}$$

$$m\ddot{z} + b_z \dot{z} - k_q z = F_{z_{dist}} + k_i i_6; \tag{6}$$

$$J_x \ddot{\gamma} + b_\gamma \dot{\gamma} - 2L^2 k_q \gamma = M_{x_{dist}} + Lk_i(i_5 - i_4); \tag{7}$$

$$J_y \ddot{\psi} + b_\psi \dot{\psi} - \frac{3L^2}{2} k_q \psi = M_{y_{dist}} + Lk_i[i_1 - \frac{1}{2}(i_2 + i_3)]; \tag{8}$$

$$J_z \ddot{\theta} + b_\theta \dot{\theta} - \sqrt{3}L^2 k_q \theta = M_{z_{dist}} + Lk_i(i_3 - i_2); \tag{9}$$

where m - mass of platen; J_x, J_y, J_z - inertia moments of platen about axes x, y, z; $\ddot{x}$, $\ddot{y}$, $\ddot{z}$, $\ddot{\gamma}$, $\ddot{\psi}$, $\ddot{\theta}$ - accelerations of the platen along corresponding coordinate; $F_{i_{dist}}$ - disturbance force ; $M_{i_{dist}}$ -

disturbance moment; b_i, $(i = x, y, z, \gamma, \psi, \theta)$ - damping coefficients along corresponding coordinate i; $\dot{x}$, $\dot{y}$, $\dot{z}$, $\dot{\gamma}$, $\dot{\psi}$, $\dot{\theta}$ - velocities of the platen along of corresponding coordinate. The previous equations show that in the first approach we can use the equation for each coordinate independently of the other coordinates and design the controller only for this coordinate.

CONTROL SYSTEM DESIGN

An important requirement in precision motion control systems with magnetic suspension is that the disturbance influence on control coordinates of motion should be below a given value. To provide low-noise control system design, the analysis of disturbances and their mathematical models are necessary. The system under consideration is shown in Fig.2, where P and C are the plant and controller transfer functions. The signals in the system are as follows: r - reference or command signal; e - tracking error; u - control signal, controller output; f - plant disturbance; x - plant output; s - sensor noise.

Analysis and mathematical model of disturbances

The main disturbances in the system are mechanical vibrations of the frame and sensor noise. To analyze the mechanical vibration disturbance, the measurements of the floor vibrations using a Wilcoxon research seismic accelerometer, model 731, and a DT-2823 data acquisition board for a PC-computer were used. The measured signal of vibration acceleration is presented in the Fig.3. The histogram of the measured vibration acceleration signal shows that signal amplitudes follow a Gaussian probability distribution with a mean of zero (Fig.4). For a Gaussian distribution there is correlation between standard deviation or root-mean-square (RMS) value and peak-to-peak value which is shown in Table 1. This correlation allows an estimate of the peak-to-peak value of random process if the RMS value is known. To analyze the spectral range, the spectrum of vibrations was measured using HP-35665A dynamic signal analyzer. This spectrum showed that the spectral range of vibrations is inside the 0 - 35 Hz region. Therefore, we can accept that vibration disturbance is the white noise with some spectral density which goes through the low-pass filter with the noise bandwidth equal to 35 Hz. According to this mathematical model the vibration signal looks as white noise with spectral density $S_f(\omega) = 1.41 \cdot 10^{-9} \frac{N^2}{sec}$ which goes through a first-order low-pass filter with a transfer function

$$W_1(s) = \frac{1}{T_1 s + 1}, \tag{10}$$

where $T_1 = .0071 sec.$

The graph of the imitation signal of vibration and the histogram of the imitation signal are shown in Fig.3 and Fig.4 respectively and show good coincidence between real and imitation signals. The analogous method was used for the design of the mathematical model of the sensor noise. Similarly, the sensor noise looks as the white noise with spectral density $S_s(\omega) = 3.33 \cdot 10^{-13} \frac{V^2}{sec}$ which goes through a first-order low-pass filter with a transfer function

$$W_2(s) = \frac{1}{T_2 s + 1},\qquad(11)$$

where $T_2 = .00025 sec.$

For noise and error amplitudes which follow a Gaussian (normal) probability distribution with a mean of zero, the mean square value equals the variance σ^2 of the output error signal and RMS equals the standard deviation σ. Mean square error σ^2 for our system looks as follows:

$$\sigma^2 = \frac{1}{2\pi} \int_{-\infty}^{\infty} |\frac{P(j\omega)}{1 + P(j\omega)C(j\omega)}|^2 S_f(\omega) d\omega + \frac{1}{2\pi} \int_{-\infty}^{\infty} |\frac{P(j\omega)C(j\omega)}{1 + P(j\omega)C(j\omega)}|^2 S_s(\omega) d\omega. \qquad(12)$$

Our control problem may be formulated as follows. Assuming that the noise and the disturbance are the stationary random functions having known correlation functions or spectral densities, it is required for known structure of the controller to find the parameters which would provide the stability of a closed-loop system and minimize noise level of the output signal.

Analysis of One-Degree-of-Freedom System

According to the previous conclusions we can analyze the dynamics of our system for each coordinate independently. So, let us analyze the one-degree-of-freedom system corresponding to vertical linear motion of the platen. The system under consideration is shown in Fig.5. In this case the equation of the movement of the platen looks as follows:

$$m\ddot{x} + b_x \dot{x} - k_x x = F_{dist} - k_i i, \qquad(13)$$

where $F_{dist} = -m\ddot{x}_f$ - disturbance force, caused by the vibrations of the frame relative to inertial space; $F_d = -b_x \dot{x}$ - damping force; $F_m = k_i i - k_x x$ - force of electromagnet; $x_m = x_f + x$, $\ddot{x}_m = \ddot{x}_f + \ddot{x}$; x_m is the coordinate of the platen relative to the inertial space, x_f is the coordinate of the frame relative to the inertial space, and x is the gap between the electromagnet and platen which it is necessary to stabilize during the functioning of the control system. To make the system closed-loop we need to add to the equation of motion (13) the equation of the x position sensor of the platen

$$u_s = k_s x, \qquad(14)$$

where u_s - output voltage of sensor; k_s - proportional coefficient which represents transformation of displacement into sensor output voltage; and the equation of controller which transforms output voltage of sensor into control current of electromagnet with some proportional coefficient k_c:

$$i = k_c x. \qquad(15)$$

Equation for variance σ_x^2 of the output signal looks as follows

$$\sigma_x^2 = \sigma_{xf}^2 + \sigma_{xs}^2 \qquad(16)$$

$$= \frac{1}{2\pi} \int_{-\infty}^{\infty} |\frac{1}{m(j\omega)^2 + b_x(j\omega) + (k_i k_c k_s - k_x)} W_1(j\omega)|^2 S_f(\omega) d\omega$$

$$+\frac{1}{2\pi}\int_{-\infty}^{\infty}|\frac{k_i k_c}{m(j\omega)^2 + b_x(j\omega) + (k_i k_c k_s - k_x)}W_2(j\omega)|^2 S_s(\omega)d\omega$$

$$=\frac{T_1(b_x T_1 + 1)}{2(k_i k_c k_s - k_x)T_1((b_x T_1 + 1)(k_i k_c k_s T_1 + b_x - k_x T_1) - (k_i k_c k_s - k_x)T_1))}S_f(\omega)$$

$$+\frac{T_2(k_i k_c)^2(b_x T_2 + 1)}{2(k_i k_c k_s - k_x)T_2((b_x T_2 + 1)(k_i k_c k_s T_2 + b_x - k_x T_2) - (k_i k_c k_s - k_x)T_2))}S_s(\omega).$$

Equation (16) is of great importance, because it allows us to solve the problem of trade-offs between the conflicting objectives of reducing sensitivity to mechanical vibrations and filtering out the sensor noise. We can evaluate the value of the variance and, therefore, the peak-to-peak deviation of the output signal in relation with the parameters of the system and choose these parameters in accordance with the required peak-to-peak deviation of output signal and system's bandwidth. The first integral in equation (16) is decreasing with increasing coefficient k_c of the controller and the second one is increasing in this case. This is clear if the time constants T_1 and T_2 in equation (16) are equal to zero. Fig.6 represents the graph of dependence of the first and second integrals in (16) and their sum of controller coefficient. Therefore, the equation for mean square of output signal deviation has the extreme value (in particular, a minimum) and we can find this coefficient of the controller which produces this minimum. The predicted, according to correlation,

$$PP_x = 8 \cdot \sigma_x \tag{17}$$

peak-to-peak deviation of x coordinate and peak-to-peak deviation from simulation results for different controller and damping coefficients are shown in Fig.7. The results of Fig.7 show that for controller coefficients above 20 $[\frac{A}{V}]$ (system bandwidth above 20 $[\frac{rad}{sec}]$), the sensor noise dominates and we can neglect the influence of the vibration acceleration noise. The typical sensor noise and simulated error motions of the oil floated stage under closed loop control are shown in Fig. 8. The pure proportional controller reduces the system sensitivity to noise and we can get Angstrom-scale stability of the closed-loop system.

Correlation of the parameters of the system and bandwidth

To analyze the correlation of the system parameters and bandwidth we can roughly define the bandwidth ω_b of our control system as cross-over frequency and find it as frequency ω_c for which $|P(j\omega)C(j\omega)| \cong |(\frac{k_c k_m k_s}{k_d m})/(j\omega - \frac{k_x}{k_d})| = 1$

$$\omega_c = \sqrt{\frac{k_c^2 k_m^2 k_s^2 - k_x^2 m^2}{k_d^2 m^2}} \cong \frac{k_c k_m k_s}{k_d m} \cong \omega_b. \tag{18}$$

For parameters of the system: $k_m = 3.33 N/A$; $k_s = 2 \cdot 10^5 v/m$; $m = 1 kg$

$$\omega_b = 6.66 \cdot 10^5 \frac{k_c}{k_d}.$$

The points of different bandwidth are shown in Fig.7.

Simulation of asymptotic tracking

To evaluate the correspondance of the designed control system to the required objective of a 100 μm accessible travel, the simulation of asymptotic tracking of the platen in vertical direction was made. The nonlinear dependence of the damping force from the separation gap according to equation (3) was used in the simulation. The results of simulation are shown in Fig. 9, where the force equals the sum of forces of three pairs of vertical electromagnets (Fig.1) and current equals the sum of currents in those electromagnets. The results of the simulation show that the control system provides required asymptotic tracking of a reference signal and an acceptable level of the currents in electromagnets.

CONCLUSIONS

Experimental measurements of the accelerations in laboratory and the noise of real capacitive probes combined with the statistical approach to the design of the control system and simulation of the system under closed-loop control indicate that the required peak-to-peak deviations of the platen coordinates and system's bandwidth can be achieved through the appropriate choosing of the proportional controller coefficients, fluid film damping coefficients, and appropriate sensor noise filtering. Thus the stage should be capable of operating to its specified resolution in common laboratory environments without the need for any special vibration isolation devices.

A hardware prototype of a precision magnetically-suspended six-degree-of-freedom motion control stage with Angstrom resolution is now under construction, allowing experimental verification of the performance which has been analytically predicted.

REFERENCES

1. Trumper, D.L.: Magnetic Suspension Techniques for Precision Motion Control, Ph.D. Thesis, Dept. of Elec. Eng. and Comp. Sci., M.I.T., Camb., Massachusetts, 1990.
2. Trumper, D.L.: Analysis and Design of a Viscously-Damped Magnetic Suspension System. Proceedings of the 1993 NSF Design and Manufacturing Systems Conference, vol.2, January 6-8, 1993.
3. Poovey, T., M. Holmes, D. Trumper: A Kinematically Coupled Magnetic Bearing Calibration Fixture, Accepted for publication in *Precision Engineering Journal*, 1993.
4. Fuller, D. D.: *Theory and Practice of Lubrication for Engineers*, A Wiley-Interscience Publication, JOHN WILEY&SONS, 1984.
5. Solodovnikov, V.V.: *Statistical Dynamics of Linear Automatic Control Systems*, London: D. Van Nostrand Company, LTD, 1965.
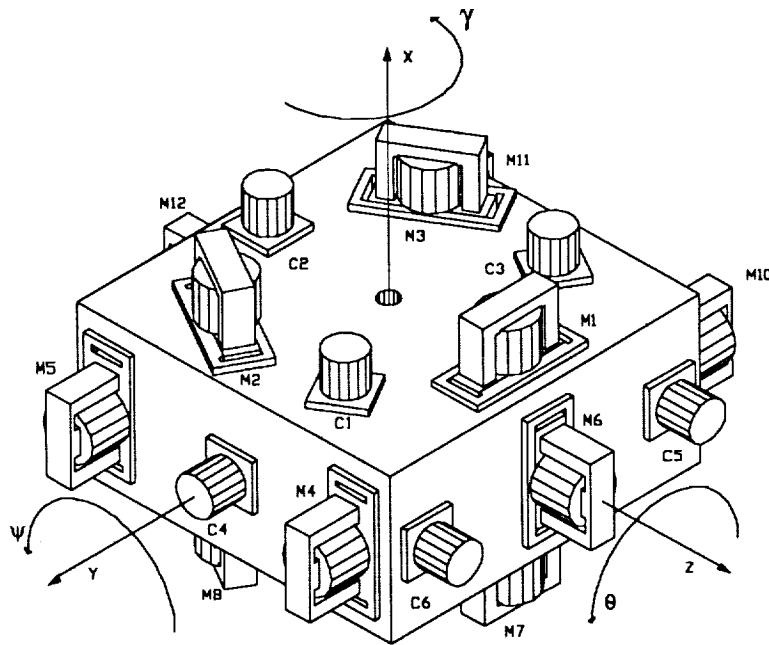
Figure 1: Schematical system design
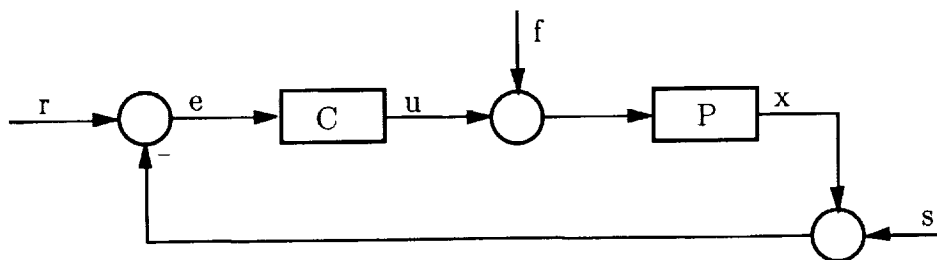
Figure 2: Scheme of general system
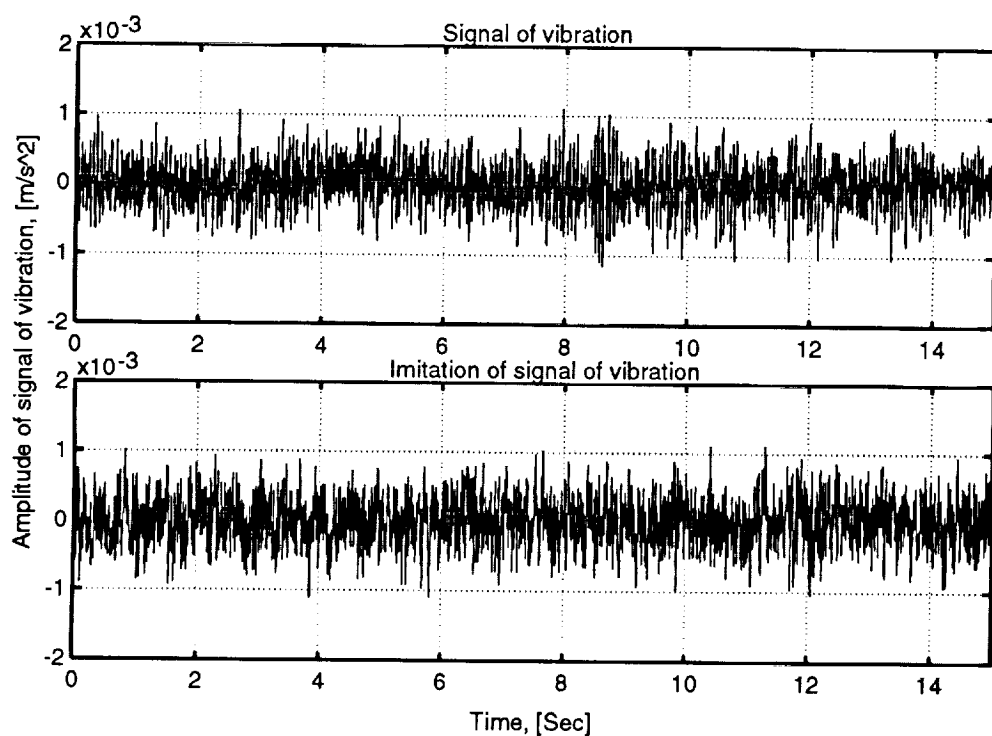
Figure 3: Signal of vibration and its imitation
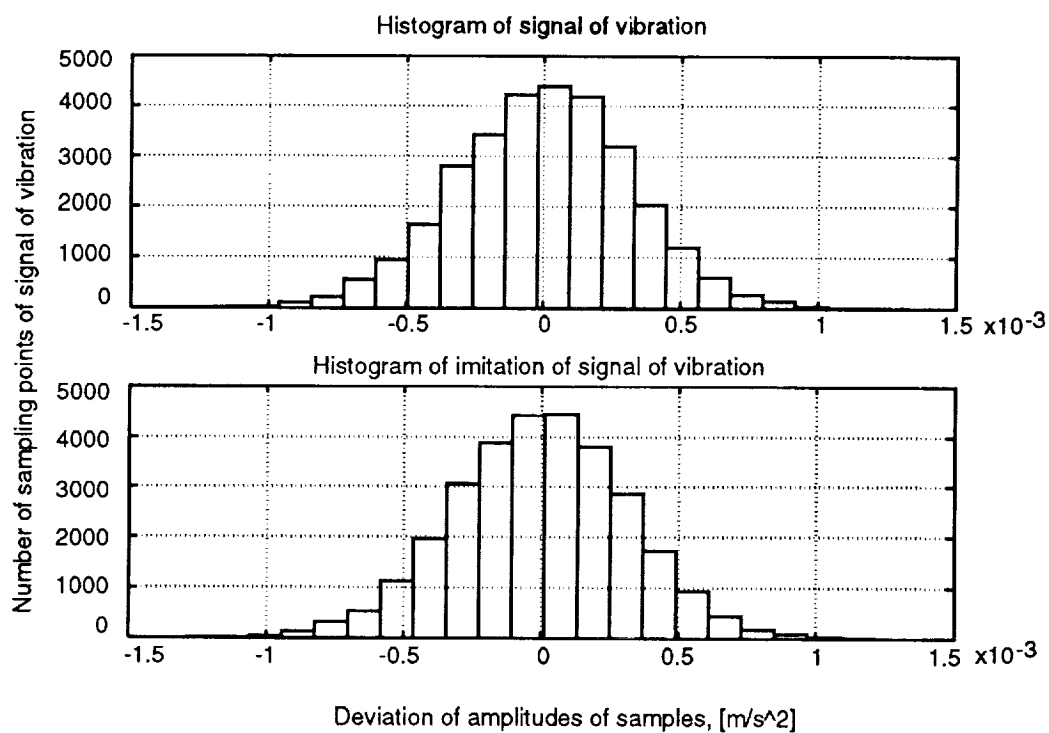
Figure 4: Histograms of signal of vibration and their imitation

Table 1: Correlation between peak-to-peak and RMS values
for Gaussian random processes

Peak-to-peak value, N σ N=1..8; σ- standard deviation(RMS)	Probability of appearance of amplitudes, greater then N σ
1 σ	32%
3 σ	13%
4 σ	4.6%
5 σ	1.2%
6 σ	.27%
7 σ	.047%
8 σ	.0063%

662

Figure 5: Scheme of the system
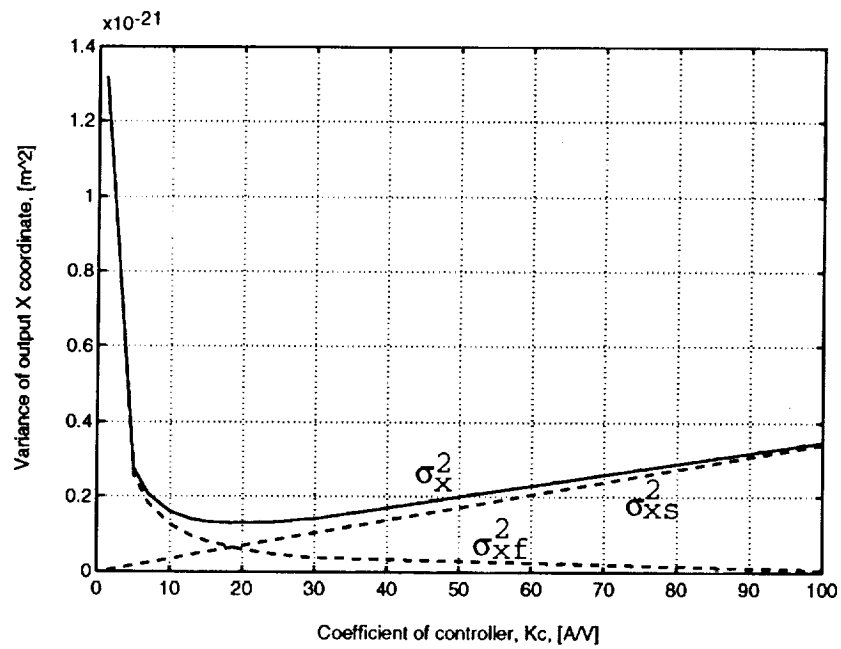
Figure 6: Dependence of the output signal variance of the controller coefficient
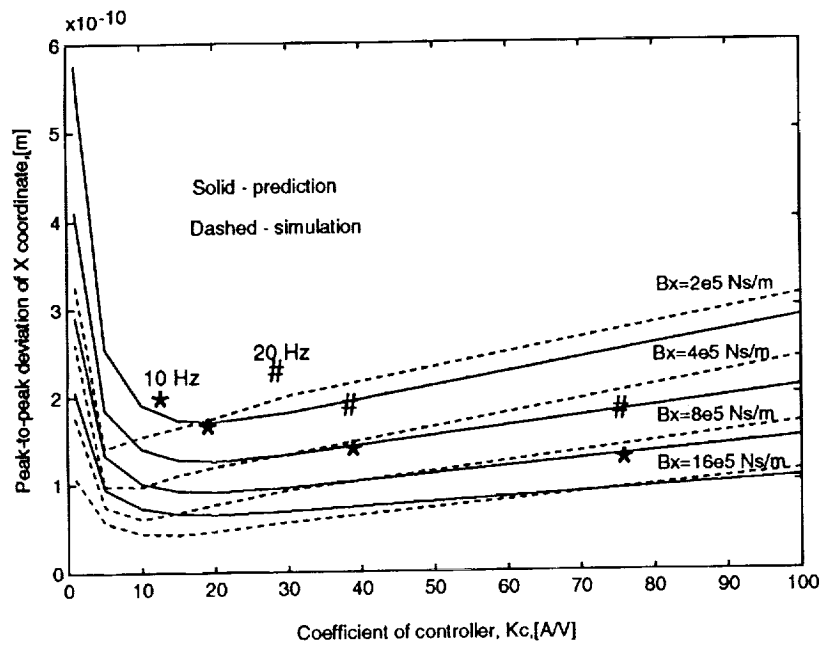
Figure 7: Peak-to-peak deviation
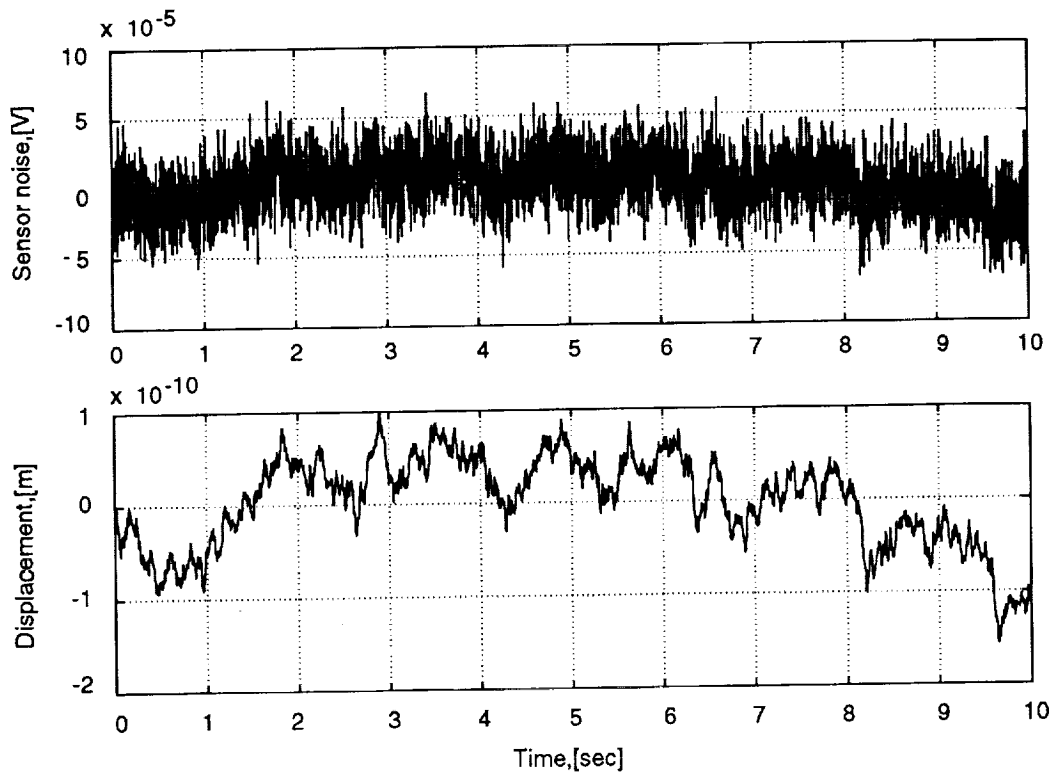
Figure 8: Typical sensor noise and simulated error motions
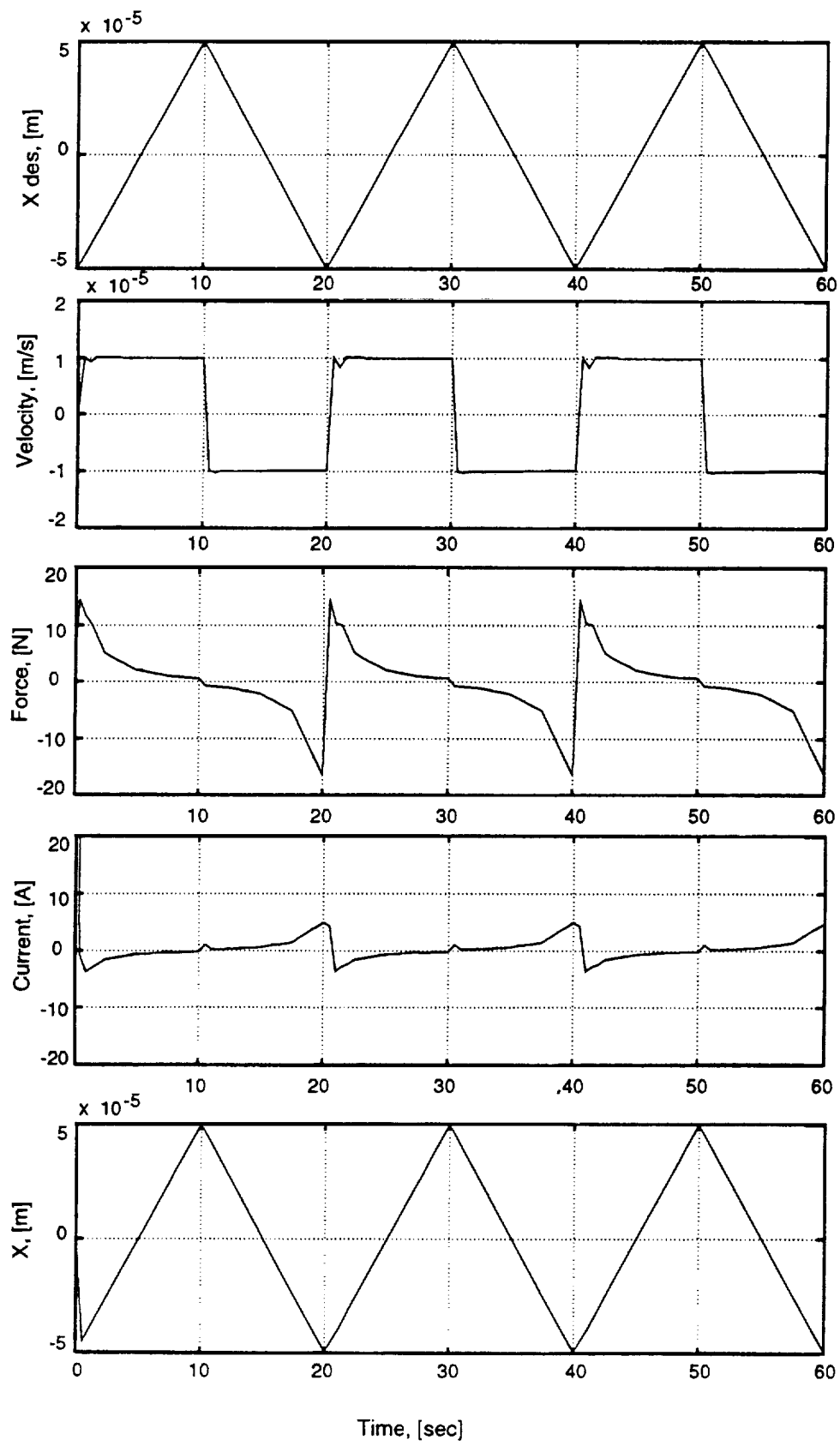
Figure 9: Simulation of asymptotic tracking

Session 12 – Maglev, Advanced Concepts

Chairman: Nelson J. Groom
NASA Langley Research Center

FUTURE ULTRA-SPEED TUBE-FLIGHT

S16-37
ABS. ONLY

11924
P-2

Robert M. Salter
XERAD, Inc.
Santa Monica, California

ABSTRACT

Future long-link ultra-speed surface transport systems will require electromagnetically (EM) driven and restrained vehicles operating under reduced-atmosphere in very straight tubes. Such tube-flight trains will be safe, energy conservative, pollution-free, and in a protected environment. Hypersonic (and even hyperballistic) speeds are theoretically achievable.

Ultimate system choices will represent tradeoffs between amortized capital costs (ACC) and operating costs. For example, long coasting links might employ aerodynamic lift coupled with EM restraint and drag make-up. Optimized, combined EM lift and thrust vectors could reduce energy costs but at increased ACC. (Repulsive levitation can produce lift-over-drag 1/d ratios a decade greater than aerodynamic). Alternatively, vehicle-emanated, induced-mirror fields in a conducting (aluminum sheet) road bed (a la Magneplane) could reduce ACC but at substantial energy costs.

Ultra-speed tube flight will demand fast-acting, high-precision sensors and computerized magnetic shimming. This same control system can maintain a magnetic "guide way" invariant in inertial space with inertial detectors imbedded in tube structures to sense and correct for earth tremors.

Ultra-speed tube flight can compete with aircraft for transit time and can provide even greater passenger convenience by single-model connections with local subways and feeder lines.

Although cargo transport generally will not need to be performed at ultra speeds, such speeds may well be desirable for high throughput to optimize channel costs. Thus, a large and expensive pipeline might be replaced with small EM-driven pallets at high speeds.

Various suspension approaches will be reviewed including servo-stabilized permanent magnet levitation.

Ultimate long-link tube trains may utilize more than one levitation scheme as it transcends stationary, acceleration, and coasting phases.

MAGLEV CRUDE OIL PIPELINE

Ernst G. Knolle
Knolle Magnetrans
South San Francisco, CA

SUMMARY

This maglev crude oil pipeline consists of two conduits guiding an endless stream of long containers. One conduit carries loaded containers and the other empty returns. The containers are levitated by permanent magnets in repulsion and propelled by stationary linear induction motors. The containers are linked to each other in a manner that allows them, while in continuous motion, to be folded into side by side position at loading and unloading points. This folding causes a speed reduction in proportion to the ratio of container diameter to container length. While in side by side position, containers are opened at their ends to be filled or emptied. Container size and speed are elected to produce a desired carrying capacity.

INTRODUCTION

The Difficulty of Conventional Crude Oil Pumping

Long distance land transportation of crude oil, especially heavy crude, is very expensive with present technology. Oil from the north slope of Alaska is a classic example. It needs to be transported many thousands of miles to the market. However, in the first 800 miles, from Prudhoe Bay to Valdiz by a conventional pumping method, the Alaska pipeline consumes, including interest and capital recovery, roughly one-third of the oil's value (ref. 1). The major reasons for this excessive cost are:

a. The pipeline was designed with special concerns for the environment. For instance, remote control valves were installed at 5 mile intervals to limit spills to 64,000 barrels for each single line break.

b. The line also had to withstand temperature extremes of minus 70 degrees Fahrenheit when empty of oil in midwinter, and plus 145 degrees Fahrenheit when filled with oil at the maximum pumping rate of 2 million barrels a day, without adversely affecting the surroundings.

c. Pumping capacity of about 500 horsepower per mile at pressures of up to 1200 pounds per square-inch was needed to push the oil along at barely 7 miles per hour.

d. To pump a large volume of 2 million barrels per day at this slow speed of 7 miles per hour required a 48 inch diameter pipeline.

e. A 48 inch diameter pipeline under 1200 pounds per square-inch pressure needs 2 inch thick walls.

As a result of (a) to (e) above and more, environmental concerns, temperature extremes and large diameter pipelines with thick walls under high pressure, all added up to high cost major construction.

How a Maglev Pipeline Would Improve Crude Oil Transportation

In assembly line fashion, the crude oil is put into containers at atmospheric pressure and sealed. The containers are then magnetically suspended over a track and propelled to their destination with linear induction motors. Freed of the drag caused by adhesion to the inside of a pipe and no matter if the oil is hot or cold, the oil can now be moved at much higher speed, for example, thirty times as fast as when conventionally pumped. Since capacity equals speed times cross sectional area, a thirty fold speed increase allows a thirty fold decrease in cross sectional area, which in turn means much less weight. Hence, the containers can be small and light, and they can easily be magnetically suspended with permanent magnets in repulsion. A conduit provides guidance and containment. The containers fold up at the ends of the line and slow to a crawl, at which time they are filled or emptied.

BASIC COMPONENTS OF MAGLEV PIPELINE

Permanent Magnets in Repulsion as the Means of Suspension

The crude oil is put into containers which are suspended by permanent magnets in repulsion as shown in Figure 1. Not shown are lateral guidance controls, which can be either mechanical or magnetic. Figure 7 p.682 (refs. 2, 3 & 4) shows details of lateral guidance. A particular advantage of using permanent magnets in repulsion is that they require no power to levitate and the containers always remain levitated even when the system is turned off and has stopped. New magnetic compounds now virtually last forever in this type of application.

Magnets attached to containers and magnets inside conduit repel each other vertically.

Empty return line
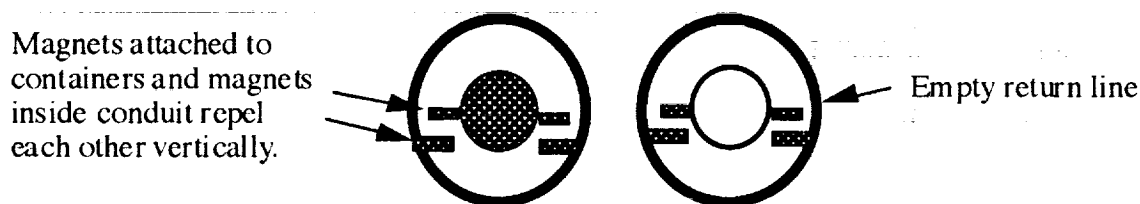
Figure 1. Typical cross section of maglev pipeline.

Electric Linear Induction Motors (LIM) for Propulsion

The primary portion of a typical electric linear induction motors (LIM) is shown in Figure 2. The secondary to this LIM consists of a metal sandwich attached to the bottoms of the containers (ref. 5). The speed of the shown LIM can be varied by varying the frequency of the supplied power. For instance, the speed can be reduced from 200 to 100 miles per hour (mph) by reducing the frequency from 150 to 75 cycles per second (cps). The LIM can also be reversed for braking. A power supply with appropriate controls would be required to meet the full range of possible operating needs.

672

30 feet long, 26 poles three phase, 1000 V, 325 Amps
150 cps, 900 lbs thrust at 200 mph
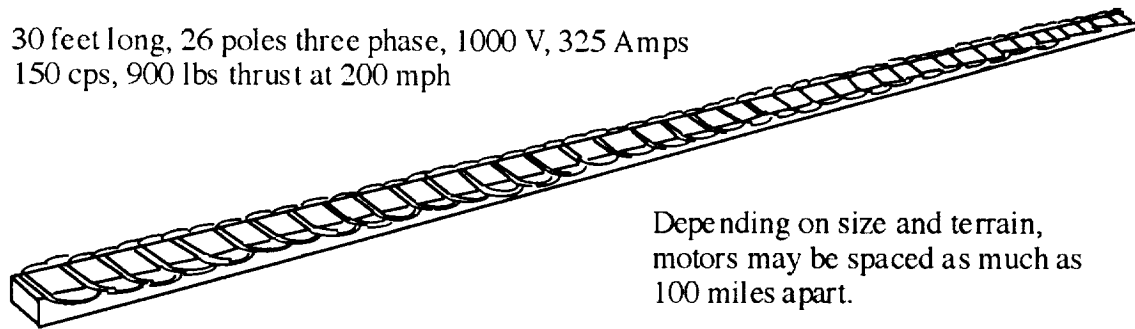
Depending on size and terrain,
motors may be spaced as much as
100 miles apart.

Figure 2. Typical high speed high performance linear induction motor (LIM).

Dynamic Mechanical Loading and Unloading

The containers are flexibly attached to each other end to end and move in unison. A short distance before the end of the line is a cam that forces alternate container joints to diverge onto upper and lower tracks. This causes the containers to fold up against each other and slow down, the last stages of which are shown in Figure 3 (ref. 6). After they have completely folded, they pass through either a filling or a dumping station followed by a U-turn.

Nozzles enter containers
and move with them

Fil box

Filling
station

3 G deceleration   Upper track

Containers

Containers moving at steady 4 fps   Lower track
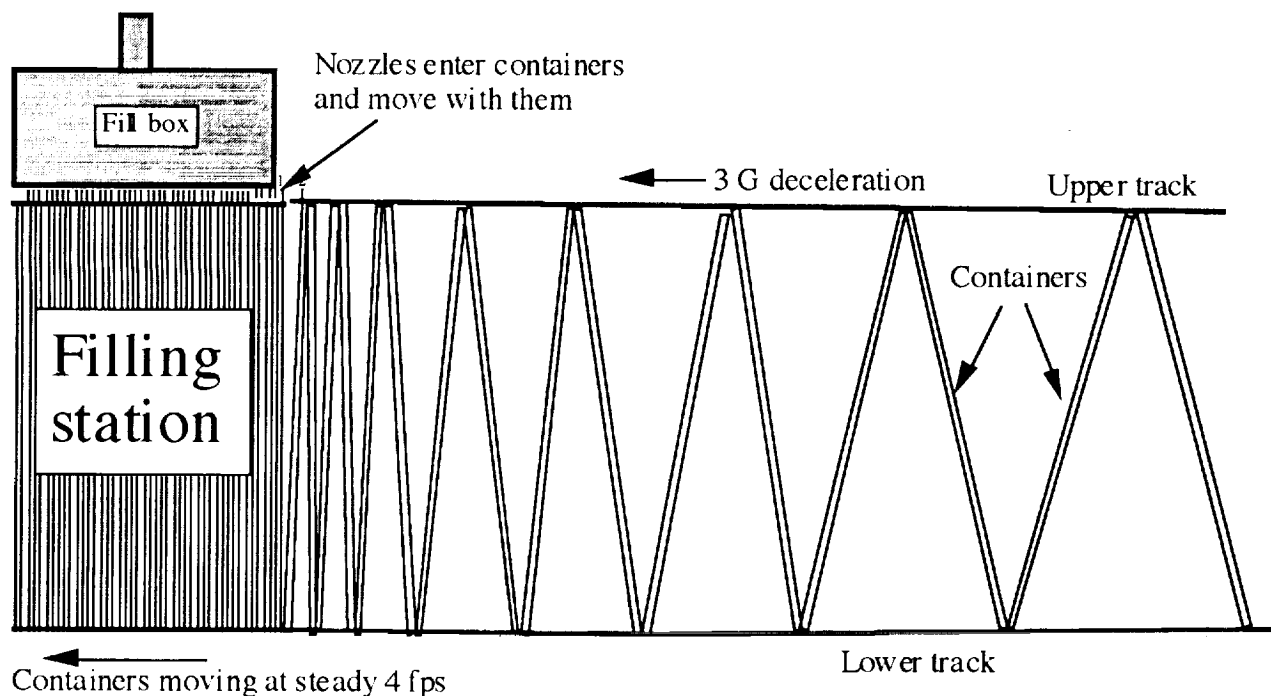
Figure 3. Typical folding and filling of containers.

Comments on Figure 3. Figure 3 is a cutout from a drawing that shows a 200 mph system. While this might be a look into the future in bulk materials transportation, initial speeds of between 50 and 100 mph would be advocated with provisions to step the speed up to a higher level later.

673
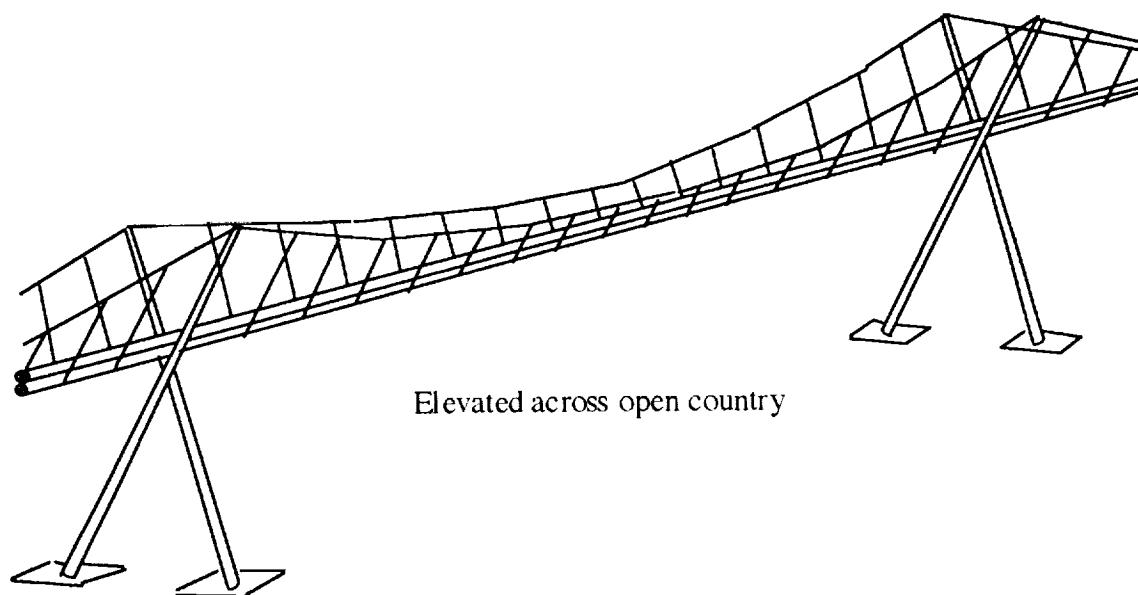
Figure 4. Typical design of maglev crude oil pipeline.

MAGLEV PIPELINE COST AND CAPACITY

Construction Cost. A detailed cost estimate shows that, if a medium size maglev crude oil pipeline were to be built in 1993 as an elevated system as shown in Figure 4, it would cost about $500,000 per mile. Not included in this estimate are the costs of (1) right-of-ways, (2) power generators if needed, (3) service roads and (4) end facilities. The elevated design is preferred because of the continued need for very straight alignment similar to overhead wires or catenaries of high speed railroads.

Table 1. Assorted Carrying Capacities, Barrels per Day

Nominal container diameter (inches)	Speed 25 mph	Speed 50 mph	Speed 75 mph	Speed 100 mph
3	34,000	68,000	102,000	136,000
4	60,000	120,000	180,000	240,000
6	138,000	276,000	414,000	552,000
8	240,000	480,000	720,000	960,000
12	550,000	1,100,000	1,650,000	2,200,000

Size, Speed and Capacity. The carrying capacity of the pipeline is determined by multiplying the container cross-sectional area with the system velocity. The cross-sectional area is determined by the elected container diameter. However, the speed can be changed at any time later which in turn changes system capacity. Table 1 shows the pipeline capacities for various sizes and speeds when running continuously for 24 hours. Conversion factors are (a) one barrel = 42 gallons, (b) 7.48 gallons = 1 cubic foot, (c) oil weight is 55 pounds per cubic foot and (d) 550 foot-pounds/sec = one horsepower. These factors were used to

compute the data in Table 1 and also the energy use of the system, which is reflected in operating and maintenance expenses of later chapters.

COMPARING MAGLEV COST WITH THE ALASKA (PUMPED) PIPELINE

About 25 years ago, oil was discovered in Prudhoe Bay, Alaska. As shipping lanes were blocked most of the year by ice, a 48-inch diameter, 800 miles long, 2,000,000 barrels per day pipeline was constructed to Valdiz. Completed in 1976, it cost in excess of $9 billion, or over $11 million per mile. Taking inflation from 1976 to 1993 as roughly 100%, it follows that if the Alaska pipeline were to be built today it would cost about $22 million per mile. This would compare with the above 1993 estimated maglev pipeline cost of $500,000 plus costs of environmental stuff, right-of-ways, end facilities, service roadways, power lines and power generating plants. Without going into too much detail, let's be generous and say we could build the maglev pipeline with everything included for $4 million per mile in 1993 dollars, or we could have built it for $2 million per mile in 1976. Table 2 shows reported Alaska pipeline statistics (ref. 1), and Table 3 compares the Alaska pumped pipeline cost of $11 million per mile with our maglev pipeline cost of $2 million per mile (both 1976 dollars).

Table 2. Alaska Oil Pipeline Operating Results, 17 Years Recorded, 3 Years Estimated

	Year	Million Barrels per Day	Tariff Rate $/Barl.	Oper. Expense $/Barl.	Tax Loading Rate
		(a)	(b)	(c)	(d)
1	1976	0	6.00	0.4	0.33
2	1977	0.3	6.00	0.6	0.33
3	1978	1.1	6.00	0.8	0.33
4	1979	1.2	6.00	1	0.33
5	1980	1.5	6.00	1.2	0.33
6	1981	1.5	6.00	1.2	0.33
7	1982	1.6	6.00	1	0.33
8	1983	1.7	6.00	0.9	0.33
9	1984	1.7	6.00	0.8	0.33
10	1985	1.8	5.00	0.7	0.33
11	1986	1.8	4.75	0.65	0.33
12	1987	2	3.90	0.58	0.2
13	1988	2.1	3.40	0.57	0.2
14	1989	1.9	3.50	0.83	0.2
15	1990	1.8	4.00	1.1	0.2
16	1991	1.8	3.50	1	0.2
17	1992	1.8	3.70	1.2	0.2
18	1993	1.7	3.50	1.25	0.2
19	1994	1.7	3.60	1.32	0.2
20	1995	1.6	3.50	1.35	0.2

Comments on Table 2. This data was extracted from evidence presented in 1992 to the Federal Energy Regulatory Commission (ref. 1). Table 3 uses this data as follows: Annual revenues, columns (a) x (b) x 365, annual expenses, columns (a) x (c) x 365, annual income taxes, columns (a) x (b) x (d) x 365. An

'After Tax Margin' of 6.4% as return on investment or profit was arbitrarily elected by the owners of the pipeline, the annual total of which is calculated by multiplying 0.064 with the amounts of investment balance, columns (g) and (k) in Table 3.

Table 3. Investment Comparison of Pumped vs. Maglev Pipeline Using Recorded Alaska Pipeline Data ($1,000,000)

	Common Data		Pumped Pipeline				Maglev Pipeline			
Year	Rev-enue	Tax Margin	O & M Expense	After Tax Margin	Earned Surplus	Invest-ment Balance	O & M Expense	After Tax Margin	Earned Surplus	Invest-ment balance
(a)	(b)	(c)	(d)	(e)	(f)	(g)	(h)	(i)	(j)	(k)
1	0	0	0	577	-577	9600	65	114	-179	1966
2	657	217	66	614	-240	9840	67	126	247	1719
3	2409	795	321	630	663	9177	70	110	1434	285
4	2628	867	438	587	735	8442	73	18	1669	-1384
5	3285	1084	657	540	1004	7438	76	-89	2214	-3598
6	3285	1084	657	476	1068	6370	79	-230	2352	-5950
7	3504	1156	584	408	1356	5014	82	-381	2646	-8596
8	3723	1229	558	321	1615	3399	85	-550	2959	-11555
9	3723	1229	496	218	1780	1619	89	-740	3145	-14701
10	3285	1084	460	104	1637	-19	92	-941	3049	-17750
11	3121	1030	427	-1	1665	-1684	96	-1136	3131	-20881
12	2847	569	423	-108	1962	-3646	100	-1336	3514	-24395
13	2606	521	437	-233	1881	-5527	104	-1561	3542	-27937
14	2427	485	576	-354	1720	-7247	108	-1788	3622	-31559
15	2628	526	723	-464	1844	-9091	112	-2020	4010	-35569
16	2300	460	657	-582	1764	-10855	117	-2276	3999	-39568
17	2431	486	788	-695	1851	-12706	122	-2532	4356	-43923
18	2172	434	776	-813	1775	-14481	126	-2811	4422	-48345
19	2234	447	819	-927	1895	-16376	131	-3094	4750	-53095
20	2044	409	788	-1048	1895	-18271	137	-3398	4897	-57992

Comments on Table 3. 1976 was the start up year without saleable production. Earned surplus column (f) = (b) - (c) - (d) - (e) and column (j) = (a) - (c) - (h) - (i). Investment balance is reduced annually by earned surplus, except at the beginning when it was increased due to negative earned surplus. Note how the pumped pipeline reached payoff in eight years and maglev in two years after the start of production.

Table 4. Computation $10 Million per Day Financial Advantage of Maglev over Pumping, Based on Actual Alaska Crude Oil Pipeline Experience ($1,000,000)

Year	Pumped		Maglev		Annual Maglev Savings	Annual Million Barrels	Daily Maglev Savings	Present Value of (g)
	(a)	(b)	(c)	(d)	(e)	(f)	(g)	(e)
1	-577	577	-179	114	861	0	0.00	0.00
2	-240	614	247	126	975	110	2.67	5.83
3	663	630	1434	110	1290	402	3.54	7.35
4	735	587	1669	18	1503	438	4.12	8.15
5	1004	540	2214	-89	1839	548	5.04	9.50
6	1068	476	2352	-230	1991	548	5.45	9.79
7	1356	408	2646	-381	2079	584	5.70	9.74
8	1615	321	2959	-550	2215	621	6.07	9.89
9	1780	218	3145	-740	2322	621	6.36	9.87
10	1637	104	3049	-941	2456	657	6.73	9.94
11	1665	-1	3131	-1136	2601	657	7.12	10.03
12	1962	-108	3514	-1336	2781	730	7.62	10.21
13	1881	-233	3542	-1561	2989	767	8.19	10.45
14	1720	-354	3622	-1788	3336	694	9.14	11.11
15	1844	-464	4010	-2020	3722	657	10.20	11.81
16	1764	-582	3999	-2276	3929	657	10.77	11.87
17	1851	-695	4356	-2532	4342	657	11.90	12.49
18	1775	-813	4422	-2811	4645	621	12.73	12.73
19	1895	-927	4750	-3094	5022	621	13.76	13.10
20	1895	-1048	4897	-3398	5352	584	14.66	13.30
					20-year average:		7.59	9.86

Comments on Table 4 and Figure 5. The Alaska pipeline construction was financed on extremely favorable terms (6.4% interest) by oil companies who expected to later benefit greatly from its use. (See also "*Comments on Table 2*"). In the first five columns of Table 4 a more realistic investment value of 12.8% is imputed (by subtracting the 'After Tax Margin' of 6.4% a second time) and thereon computing the maglev over pumped pipeline savings: (e) = ((a) - (b)) - ((c) - (d)). Table 4 columns (a), (b), (c) and (d) are copies of columns (f), (e), (j) and (i) of Table 3. The last column (e) of Table 4 then shows that a maglev crude oil pipeline in Alaska could have saved an average of about $10,000,000 per day over a 20 year period for a total of 20 x 365 x $10 million = $73 billion. Column (e) is annually compounded present value of column (g) at 5% interest.
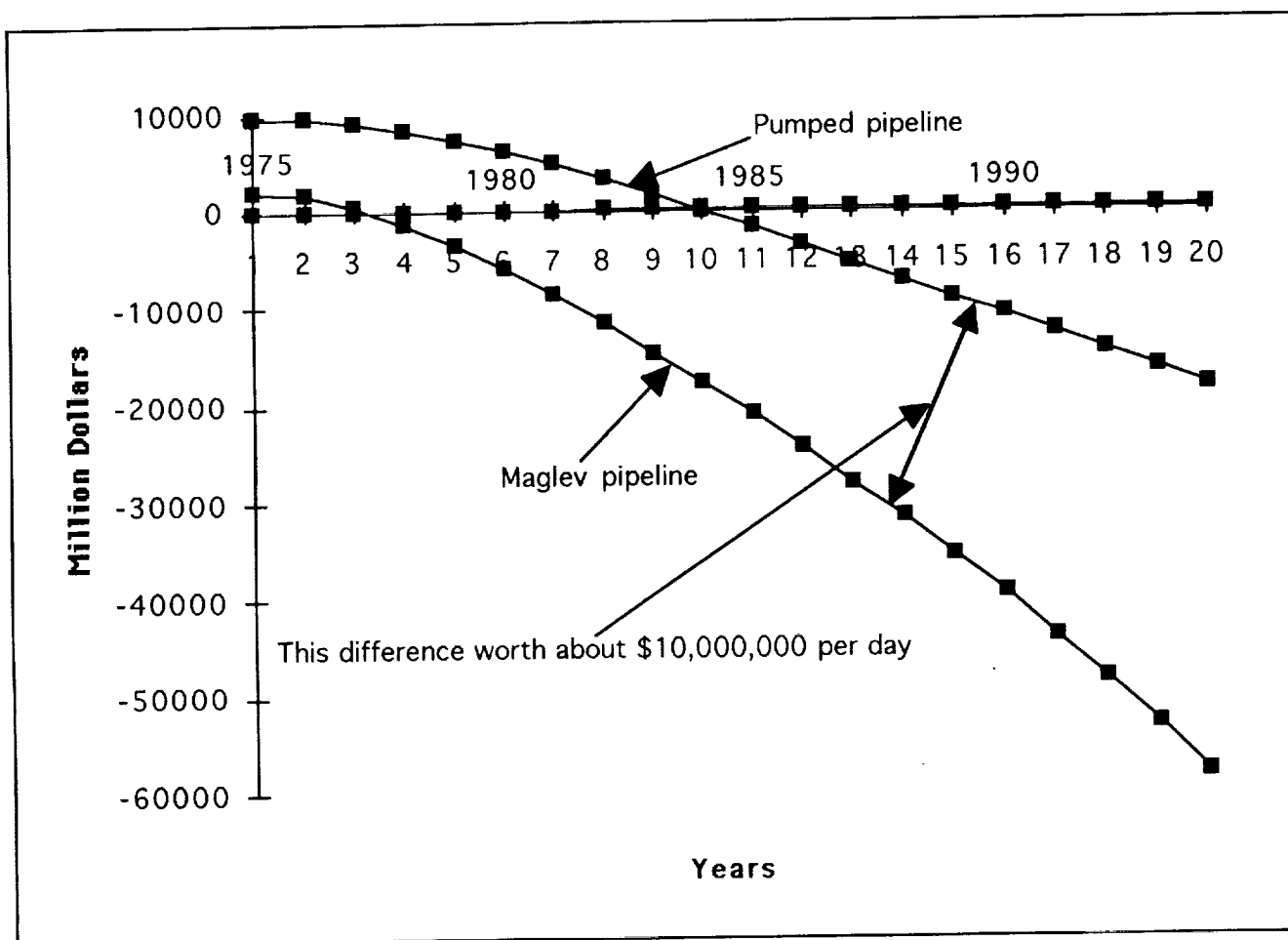
Figure 5. Amortization curve comparison of existing Alaska pumped pipeline with maglev pipeline based on reported 'After Tax Margin' of 6.4% as shown in columns (g) and (k) of Table 3. It shows that 20-year average savings worth $10 million per day could have been achieved with a maglev crude oil pipeline instead of the existing pumped oil pipeline.

General consensus in the oil industry is that the Alaska oil pipeline was a financial disappointment. It was built with a view of oil prices rising and remaining around $40 per barrel, which would have justified a $6 per barrel pipeline transportation charge. Instead the oil prices dropped back down to less than $20 per barrel. The above tables and Figure 5 bear this out. If the investors in the Alaska pipeline had demanded a more normal 'After Tax Margin' of around 13% instead of 6.4%, the pipeline company would have quickly gone bankrupt.

MAGLEV CRUDE OIL PIPELINE FUTURE - HOW ABOUT KASAKHSTAN?

There are several regions in the world where large oil fields are indicated which have limited economic access to markets. One of them lies in Tengiz, Kasakhstan, where a 1500 mile long maglev crude oil pipeline could economically carry the oil to a Black Sea shipping port. However, the maglev picture there is not quite as rosy as shown above for Alaska. In addition to this line being about twice as long as the Alaska pipeline, the required capacity is only 1,000,000 barrels per day instead of Alaska's 2,000,000 barrels per day. Furthermore, investors are not likely to be found who would advance capital at 6.4% as they did in Alaska.

Table 5 and Figure 6 show 15-year projected financial results of a 1500 mile long maglev crude oil pipeline in Kasakhstan, starting with 250,000 barrels per day in the first year and increasing in 5 years to 1,000,000 barrels per day, financed and taxed under conditions generally found in the U.S.A., i.e., 70% debt, 30% equity, interest on debt 13%, return on equity 20%, (combined cost of money 15.1%), cost escalation 5%, income taxes 40%, tax depreciation 10%, property taxes 1%. Table 5 shows the result assuming that original construction cost was $4 million per mile and revenues at $4.00 per barrel (plus annual escalation). Figure 6 shows three curves, $4, $3 and $2 million per mile original construction cost levels with respective $4.00, $3.00 and $2.00 per barrel revenue levels (also plus annual escalation).

Table 5. 15 Year Projected Financial Results of 1500 Mile, 1,000,000 Barrels per Day Maglev Crude Oil Pipeline in Kasakhstan at Original Cost Estimate of $4 Million per Mile and Revenues at $4.00 per Barrel ($1,000,000)

Line	Year	Revenue	Opr. Exp	Prop. Taxes	Tax Deprec.	Interest on Debt	Income Tax	Return on Equity	Debt Repay-ments	Remain. Debt Balance
		(a)	(b)	(c)	(d)	(e)	(f)	(g)	(h)	(i)
1	1996	423	131	90	845	769	0	507	-872	9327
2	1997	665	137	92	845	849	0	560	-748	10075
3	1998	932	144	94	845	917	0	604	-586	10661
4	1999	1223	151	96	845	970	0	640	-378	11039
5	2000	1798	159	98	845	1005	0	662	139	10900
6	2001	2157	167	100	845	992	21	654	485	10415
7	2002	2265	175	102	845	948	78	625	587	9828
8	2003	2378	184	104	845	894	140	590	702	9126
9	2004	2497	193	106	845	830	209	548	830	8295
10	2005	2622	203	108	845	755	284	498	973	7322
11	2006	2753	213	110	845	666	367	439	1133	6189
12	2007	2891	224	112	845	563	458	371	1310	4879
13	2008	3035	235	114	0	444	897	293	1170	3710
14	2009	3187	247	117	0	338	994	223	1358	2351
15	2010	3346	259	119	0	214	1102	141	1568	783

Table 6 shows how the initially estimated capital requirement of $4 million/mile times 1500 miles = $6 billion increases by inflation and capitalized interest during three years' of construction to $8.454 billion. This amount plus first year loss of $0.872 billion (Table 5, line (1), column (h)) equals the $9.327 billion in Table 5, line (1), column (i).
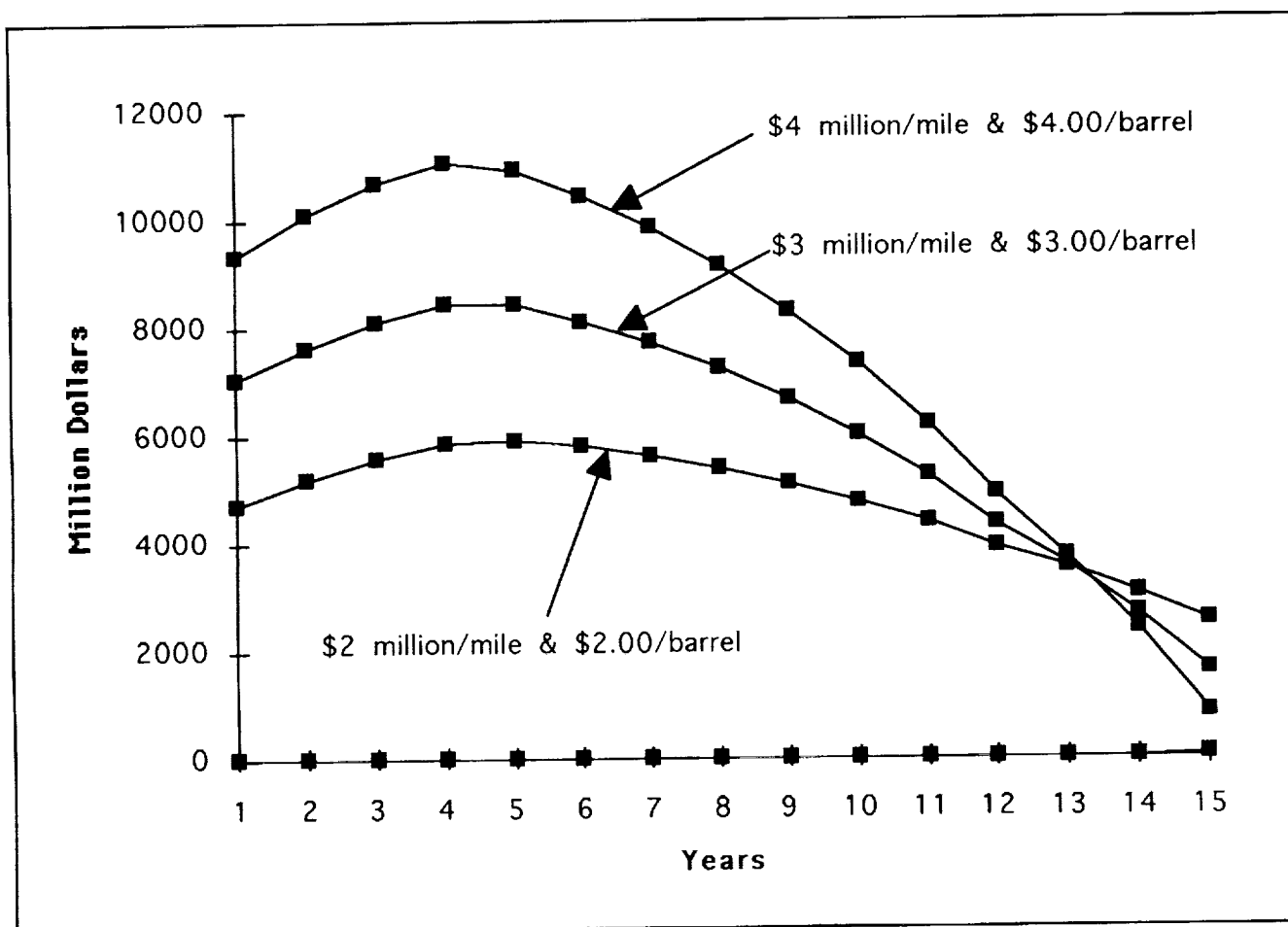
Figure 6. Amortization of capital investment for a 1500 mile maglev crude oil pipeline in Kasakhstan assuming initial capital investments of $4 million/mile, $3 million/mile and $2 million/mile with respective revenues of $4.00/barrel, $3.00/barrel and $2.00/barrel.

Table 6. Computation of Capital Requirement for $4 Million per Mile, 1500 Mile Kasakhstan Maglev Crude Oil Pipeline, 3 Years Construction, Inflation 7% and Capitalized Interest (Cost of Money) 15.1% ($1,000,000)

Line	Year	7% p/a Inflated Plant	Construction Completed		Capita-lized Interest	Total Invest-ment
		$	%	$	$	$
1	1993	6000	20	1200	181	1381
2	1994	6420	50	3210	693	5284
3	1995	6869	30	2061	1109	8454
4			100	6471	1984	8454

Comments on Kasakhstan and Other Prospects. Above comparison tables and examples are just a small sample of variations, which have been run by computer to gain insight on how they affect the end result. For example, in Table 5, in the first few years, the cost of money (interest on debt, column (e), plus

680

return on equity, column (g)) is more than 10 times as large as operating expense, column (b). Hence, keeping capital costs down is much more important than keeping operating expenses down. Figure 6 shows the amortization curves rising in the first few years due to the losses as calculated in Table 5, column (h), lines (1) to (4). If oil field production could be started at full capacity in the first year of pipeline operations, billions of dollars could be saved. However, in Alaska, it took five years before they had enough oil for the pipeline to run at full capacity. As to the cost of money, if one could finance a project with just one percent less in interest, for example cut interest on debt from 13% to 12% for the $4 million/mile curve in Figure 6, it would mean construction cost savings of $100 million and 15 year operations savings of $1.5 billion.

GREAT OPPORTUNITY FOR HIGH TECH AND MONEY MAKING

The above described basic components of the maglev crude oil pipeline, the permanent magnets, the linear induction motors and the container string with its folding function, are all pretty well straight forward and relatively simple and reliable technologies. There are opportunities for improvements in magnets, materials and container design, but the most challenging tasks lie in the field of maintenance (especially leakage prevention), lateral guidance, controls and failure prevention.

Linear Induction Motors (LIMs) and Controls. As stated in Figure 2 above, LIMs may be spaced as much as 100 miles apart at unmanned stations. However, the LIM shown in Figure 2 is only suitable for driving the system at high speed. For start up, intermediate speeds and reverse braking, several other specially designed LIMs are to be located next to the high speed LIMs. Additionally, for every type of LIM needed in operations throughout the speed range and reverse braking there will need to be one or more LIMs of equal size on standby. Motors may need to either be cooled heavily during start up or switched on and off in rotation. As an example, there might be five heavy thrust start up LIMs at each station that get the containers up to a speed of 5 mph. Each would take a turn and run for 20% of the time, and be off 80% of the time for cooling. There would also be a danger of overheating the containers. They must not stay too long over an active LIM.

To get a comparison of the magnitude, the largest movements of weight on land are unit trains for coal, ore or grain. They often have 100 cars, each carrying 100 tons for a total of 10,000 tons per train. A 100 mile long section of a maglev pipeline, having a capacity of 1,000,000 barrels per day, would weigh also about 10,000 tons (not counting the empty return line). So, the starting LIMs for each 100 mile section of maglev pipeline would have to exert a propulsion effort comparable to that of the (usually) eight locomotives of a unit train. However, for a 1500 mile Kasakhstan line it would require an effort equivalent to 120 locomotives. While this looks like an enormous physical task, the cost savings with maglev as calculated above would also be enormous.

Power Supply to LIM Stations. The Alaska pipeline has a mix of energy sources for pumping. Near Prudhoe Bay several pump stations receive natural gas from the oil field. Further along, oil from the line is dropped off, refined and then used for jet engine powered pumping. Also some power is obtained from private utilities. A maglev pipeline would probably also look at the best available but reliable source. If no other sources are available, one or more small power generating stations would be built and power lines strung along the same posts that carry the pipeline, see Figure 4.

Surge Suppressors. Common at hydroelectric power stations are surge towers for the purpose of preventing structural damage from sudden shut downs of the turbines following a power failure. The tremendous kinetic energy of the approaching water is dissipated by rising up in these surge towers and overflowing. The long stream of maglev pipeline containers has a similar problem and a similar solution. Along the line at intervals are longitudinal surge suppressor stations. These are locations where the containers are, for a short distance, forced by an upper and lower track to partially fold, similar to what is shown in Figure 3, above. However, unlike the rigidly fixed lower track in Figure 3, the lower track in a surge suppressor station is vertically movable so that it can absorb longitudinal surges that may run through

the containers. These stations also serve to compensate for longitudinal temperature expansions and contractions of the containers.

Lateral Guidance of Containers. Some 150 years ago, a transportation scientist by the name of Earnshaw, after experimenting with permanent magnets in repulsion, declared that 'it is impossible to suspend vehicles with permanent magnets in repulsion without secondary help', which is today known as Earnshaw's Theorem (ref. 4). While Einstein was able to refute Newton, nobody has yet been able to refute Earnshaw. Hence, we are stuck with the need for lateral guidance to ensure that the containers stay above their magnetic track and not fall off to the sides. Several methods of lateral guidance controls have been satisfactorily tested. They are items (1) to (3) below. However, items (4) and (5) below are being looked at as possible future alternatives.

(1) Self-adjusting, self-lubricating commercially available plastic sliders attached in pairs to each side of each container. The sliders follow polished stainless steel lined channels which are attached to the inside of the conduits, see left half of Figure 7. The sliders are periodically renewed. Unlike electro magnetic systems described below, this lateral guide method is fully operational throughout the speed range and needs no backup support system in case of power failure or at slow speed.

(2) Shown in the right half of Figure 7 are electro magnets attached in pairs to each side of each container, which are controlled by a gap sensor. A gap separates the electro magnets from dual channels with steel inserts. Power for the electro magnets may be generated off the permanent track magnets that suspend the containers (Figure 1). This system requires backup support in case of power failure and possibly also at low speed.

(3) Electro magnets with steel rails as in (2) above, except they are switched around. The electro magnets are stationary and the steel rails are attached to the moving containers. Power for the electro magnets can be either generated off the permanent magnet track or supplied by power lines that run along the pipeline. This system also requires backup support in case of power failure.
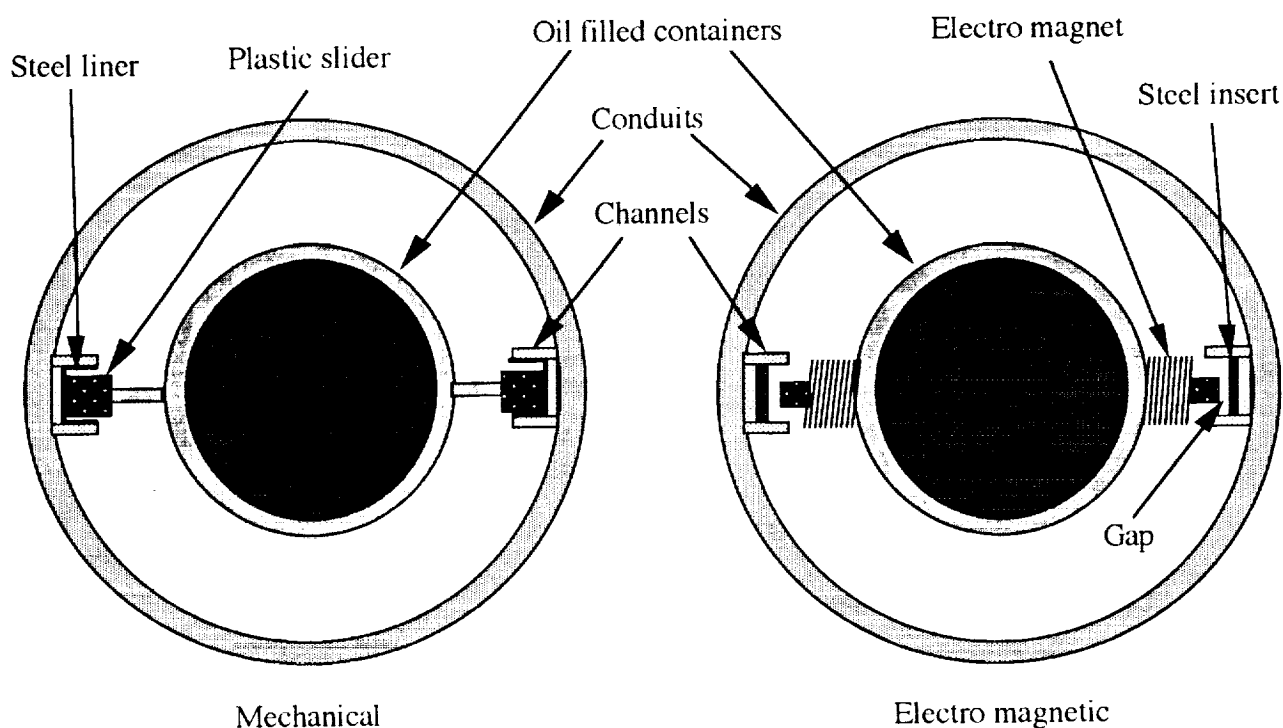

Figure 7. Typical choices of lateral guidance systems, mechanical or electro magnetic. For clarity, levitation magnets and LIMs are not shown.

(4) New magnetic suspension technology achievements as reported in NASA's 1991 first International Symposium on Magnetic Suspension Technology (ref. 7). These include practical applications of replacing friction bearings of rotary machinery with non-contact electro magnetic bearings. It seems feasible to have the container string of the maglev pipeline take the place of a rotating shaft of similar diameter and likewise have it controlled to remain contactless in the center while moving along at great speed. This system would also need backup support in case of power failure.

(5) A possible break-through in technology. Magnetic suspension by means of permanent magnets in repulsion is somewhat similar to riding a bicycle. At no speed and at low speed both have a strong tendency to fall over. However, at high speed it is nearly impossible to tip over with a bicycle. Remember, the kid shouting: 'Look Ma, no hands'? A bike becomes more and more self-steering as speed increases. By the same token, it should be possible to develop a kind of magnetic rudder that automatically steers the maglev containers through the center of the conduits when at high speed. Backup guidance support would be need at low speed, but power failures might not affect it.

Quality Controls and Failure Protection. If a light bulb goes out in a life buoy that marks a shipping channel, an automatic mechanism rotates another bulb in its place. If the second one goes, a third one comes up. New aircraft engines are tested numerous times. After each test, they are taken apart, checked and X-rayed until the probability of future failure has become extremely low. These are two examples of how to prevent disasters of major proportions. Both aircraft and shipping disasters, in addition to loss of life, can run into millions, even billions of dollars.

The above Kasakhstan pipeline proposal would carry 1,000,000 barrels of oil per day; that means about a million dollars' worth of oil every hour. Figure 6 shows how running at less than full capacity in the first five years has increased the indebtedness instead of decreasing it. It is obvious that any delay, breakdown or shut down would run into big financial losses. Hence, life buoy style, aircraft style and even better quality controls must be incorporated in design, operations and maintenance of a maglev crude oil pipeline, which might be the subject of a future paper.

CONCLUSION

It is obvious that, as easily accessible sources of fossil fuel become depleted, a more economic land transportation mode needs to be developed. The 800 mile long Alaska (pumped) pipeline is an example of unsatisfactory and uneconomical present day pumping technology. Other remotely located oil fields lie untapped as they wait for advancements in transportation technology. Magnetic levitation is that new advancement in technology. A maglev crude oil pipeline could go very long distances and still be highly profitable in the hands of private enterprise. In the Alaska case, $10 million per day ($73 billion over 20 years) might have been saved, had the maglev technology been available and had it been used. Twice as long as the Alaska pipeline, a maglev crude oil pipeline from Tengiz in Kasakhstan to the Black Sea was calculated above to be also financially feasible.

The major components of the maglev crude oil pipeline are either mechanical or basic electrical in nature, which may need little further refinement. However, there are several areas of design and operations which need to be addressed and refined. To name a few, operational safety, quality control, failure prevention, start up procedure, shutdown procedure, lightning strikes, leakage, spills, earthquakes, ground shifting, temperature extremes, vandalism, guerilla attacks, etc. It is not going to be a simple project. However, the future looks bright for maglev pipelines. There is an immediate need to also transport coal, grain and ore more economically. Further into the future, it may some day be economically feasible to transport water by maglev pipeline from the north to arid lands in Arizona, New Mexico and Texas and turn them into lush green agricultural lands to supplement the world food supply.

REFERENCES

1. Official Stenographers Report, Federal Energy Regulatory Commission, Docked No: IS92-3-000, Technical Conference, Amerada Hess Pipeline Company, June 3, 1992.

2. Knolle, E. G.; *Knolle Magnetrans, A Magnetically Levitated Train System,* , NASA CP 3152, August 19-23, 1991, pp. 907-918.

3. Strnat, K. J., *Rare-Earth Permanent Magnets: Two Decades of New Magnetic Materials*, ASM, Paper No. 8617-005, 1986.

4. Laithwaite, E. R.; *Transport Without Wheels*, Westview Press, Boulder, Colorado, pp. 304-317, 1977.

5. Nonaka, S. and Higuchi, T.; *Design Strategy of Single-Sided Linear Induction Motors for Propulsion of Vehicles*, IEEE Trans., Cat, No. 87CH2443-0, pp. 1-11, 1987.

6. Knolle, E. G.; *Articulated Train System,* U.S. Patent No.3,320,903, Re. 26673, 1969.

7. *International Symposium on Magnetic Suspension Technology*, NASA Conference Publication 3152, Langley Research Center, 1991.

684

Appendix

Attendees

Byong Ahn
Charles Stark Draper Laboratory
555 Technology Square
M.S. 03
Cambridge, MA 02139
617-258-2832

Paul Allaire
University of Virginia
Dept. Mech, Aerosp, Nuclear
Thornton Hall, McCormick Road
Charlottesville, VA 22901
804-924-3292

Willard W. Anderson
NASA Langley Research Center
Mail Stop 479
Hampton, VA 23681-0001
804-864-1718

Tyler M. Anderson
Boeing Defense & Space Group
P.O. Box 3999
MS 182-24
Seattle, WA 98124
206-773-2291

Bill G. Asbury
Lockheed Engineering and Sciences
144 Research Drive
Hampton, VA 23666
804-766-9600

Clayton C. Bear
Revolve Technologies, Inc.
1240 - 700 - 9 Avenue, S.W.
Calgary, Alberta T2P 3V4 CANADA
403-261-5338

Brij B. Bhargava
Ashman Consulting Services
P.O. Box 3189
Santa Barbara, CA 93130-3189
805-964-2104

Barry Blair
Waukesha Bearings
P.O. Box 1616
Waukesha, WI 53187
414-547-3381

Karl Boden
KFA-IGV
PF-1913
W-5170
Julich D-52425 GERMANY
49-2461-614604

Dr. Hans J. Bornemann
Kernforschugszentrum Karlsruhe
INFP, P. O. Box 3640
76021 Karlsruhe GERMANY
49-7247-82-6389

Lyle A. Branagan
Pacific Gas & Electric
3400 Crow Canyon Road
San Ramon, CA 94583
510-866-5735

Colin P. Britcher
Old Dominion University
Dept. of Aerospace Engineering
Norfolk, VA 23529-0247
804-683-4916

Thomas C. Britton
Lockheed Engr. and Science Co.
24 West Taylor Road
Mail Stop 161
Hampton, VA 23681-0001
804-864-6619

Stephen Chapman
Magnetic Bearings, Inc.
5241 Valleypark Drive
Roanoke, VA 24019
703-563-4936

David E. Cox
NASA Langley Research Center
Mail Stop 161
Hampton, VA 23681-0001
804-864-8149

Harold R. Davis
The University of British Columbia
Department of Physics
6224 Agricultural Road
Vancouver, B.C. V6T 1Z1 CANADA
604-822-2961

686

Dr. Horst Ecker
Technical University Vienna
Inst. fr. Machine Dyn. & Measuremt
Wiedner Hauptstr. 8-10/303
Vienna A-1040 AUSTRIA
43-222-58801-5567

James H. Eggleston
46th TEST Group/TKE
1E21 EST Track Road
Holloman AFB, NM 88330-7847
505-679-2941

James B. Fischer
Electron Energy Corporation
3307 E. Romelle Avenue
Orange, CA 92669
714-538-7328

Martha L. Fisher-Votava
Sundstrand Aerospace
4747 Harrison Avenue
Rockford, IL 61125-7002
815-394-2729

Karl Flueckiger
Charles Stark Draper Laboratory
Mail Stop 3H
555 Technology Square
Cambridge, MA 02139
617-258-3850

Lucas E. Foster
Old Dominion University
Dept. of Aerospace Engineering
Norfolk, VA 23529-0247
804-683-3720

Giancarlo Genta
Politecnico di Torino
Mechanics Department
C. Duca degli Abruzzi
24-10120 Torino, ITALY
39-11-5646901

Michael J. Goodyer
The University of Southampton
Dept. of Aero. and Astro.
Southampton SO9 5NH ENGLAND
44-703-592374

Henry Guckel
WI Cntr for Applied Microelectronics
Electrical & Computer Engineering
1415 Johnson Drive
Madison, WI 53706-1691
608-263-4723

Ram Gurumoorthy
GECRD
1 River Road
Bldg. K-1, Rm. 4C20
Schenectady, NY 12065
518-387-6657

Roy D. Hampton
University of Virginia
ROMAC Labs, Mech & Aero Engrg
Thornton Hall, McCormick Road
Charlottesville, VA 22901
804-924-3767

Lee M. Hartwell
RKR Associates
1607 Southwood Blvd.
Arlington, TX 76013
817-795-7124

Robin Harvey
Hughes Research Labs
3011 Malibu Cyn Road
Malibu, CA 90265
310-317-5236

Toshiro Higuchi
University of Tokyo
KSP East 405, 3-2-1 Sakado
Takatsu-ku
Kawasaki-shi 213 JAPAN
81-44-819-2048

Kwok W. Hui
Dresser Rand Company
P. O. Box 560
Olean, NY 14760
716-375-3328

John Y. Hung
Auburn University
Dept of Electrical Engineering
200 Broun Hall
Auburn University, AL 36849-5201
205-844-1813

James D. Hurley
Mechanical Technology Inc.
968 Albany Shaker Rd.
Latham, NY 12110
518-785-2177

A. Dean Jacot
Boeing Aerospace Company
P. O. Box 3999
MS 82-24
Seattle, WA 98124
206-773-8629

Graham Jones
Technology Insights
10240 Sorrento Valley Road
Suite 320
San Diego, CA 92121
619-455-9080

Brian R. Jones
Lawrence Livermore Nat. Laboratory
P. O. Box 808
L630
Livermore, CA 94550
415-423-3058

Swarn Kalsi
Grumman Corporation
M/S B29-25
Bethpage, NY 11714
516-356-9624

Yoichi Kanemitsu
EBARA Research Company, LTD.
MSR Dept., Electro-physics Lab.
2-1, fujisawa 4-chome
Fujisawa-shi 251   JAPAN
81-466-83-7640

Claude R. Keckler
NASA Langley Research Center
Mail Stop 479
Hampton, VA 23681-0001
804-864-1718

Allan J. Kelley
The University of Tokyo
Kanagawa Academy of Sci. & Tech.
KSP E. 405, 3-2-1 Sakado
Takatsu-ku Kawasaki 213 JAPAN
81-44-819-2093

Yoshida Kinjiro
Kyushu University
Dept. of Electrical Engineering
6-chome 10-1, Hakozaki Higashi-ku
Fukuoka 812 JAPAN
092-641-1101, X5307

Ronald L. Klein
West Virginia University
Dept of Electrical/Computer Eng.
P.O. Box 6101
Morgantown, WV 26506-6101
304-293-3998

Josiah D. Knight
Duke University
Dept. of Mechanical Engineering
Box 90300
Durham, NC 27708-0300
919-660-5337

Ernst G. Knolle
Knolle Magnetrans
2691 Sean Court
S. San Francisco, CA 94080
415-871-9816

S. Kohler
Sandia National Laboratories
Albuquerque, NM 87185

John C. Kroeger
Honeywell Satellite Sys.
Box 52199
Phoenix, AZ 2199
602-561-3175

Dr. Alexander V. Kuzin
UNC-Charlotte
Precision Engineering Lab
Charlotte, NC 28223
704-547-4324

Jaynarayan H. Lala
Charles Stark Draper Lab., Inc.
555 Technology Square
MS 73
Cambridge, MA 02139
617-258-2235

Kyong B. Lim
NASA Langley Research Center
Mail Stop 161
Hampton, VA 23681-0001
804-864-4342

Chin E. Lin
National Cheng Kung Univ.
Inst. of Aeronautics and Astronautics
Tainan 70101 TAIWAN
886-6-274-1820

Reinhard F. Luerken
Thyssen Henschel America, Inc.
2730 Wilshire Boulevard
Suite 500
Santa Monica, CA 90403
310-828-9768

James P. Lyons
GE Corporate R&D
P.O. Box 8, EP-116
Schenectady, NY 12309
518-387-5015

Sam Mallicoat
Microfield Graphics, Inc.
9825 SW Sunshine Court
Beaverton, OR 97005
503-626-9393

Oliver Marroux
Aerospatiale
66 Route de Verneuil
Les Mureaux, 78133 FRANCE
33-1-34922822

David B. Martin
Northrop ATDC
N214/XA
8900 E. Washington Boulevard
Pico Rivera, CA 90660
310-942-3362

Osami Matsushita
The National Defense Academy
Dept. of Mechanical Engineering
603 Kandatsu-machi
Kanegawa JAPAN 239
81-468-41-3810, X2326

Wally McLellan
Magnetic Bearings, Inc.
5241 Valleypark Drive
Roanoke, VA 24019
703-563-5936

Chase K. McMichael
Texas Center for Superconductivity
University of Houston
4800 Calhoun
Houston, TX 77204-5506
713-743-8254

James L. Milner
National Maglev Initiative, USDOT
400 7th Street, S.W.
Room 5106, RDV-1
Washington, DC 20590
202-366-0515

R. Mark Nelms
Auburn University
Dept. of Electrical Engineering
200 Broun Hall
Auburn, AL 36849
205-844-1830

Steven A. Nolan
Rockwell International
Rocketdyne Division, Mail Stop IA32
6633 Canoga Avenue, P.O. Box 7922
Canoga Park, CA 92309-7922
818-718-4430

Alan B. Palazzolo
Texas A&M University
Mechanical Engineering
College Station, TX 77843-3123
409-845-5280

Da-Chen Pang
University of Maryland
Department of Mech. Engg.
College Park, MD 20742
301-405-787

Richard F. Post
Lawrence Livermore National Lab
P. O. Box 808, L-644
Livermore, CA 94551
510-422-9853

A. K. Pradeep
General Electric CR&D
P. O. Box 8
Schenectady, NY 12301
518-387-6588

Mark A. Preston
General Electric Corporate R&D
P. O. Box 8, Building EP
Room 116
Schenectady, NY 12301
518-387-5588

Douglas B. Price
NASA Langley Research Center
Mail Stop 161
Hampton, VA 23681-0001
804-864-6605

Michael Proise
Grumman Corporation
Mail Stop B29-25
Bethpage, NY 11714
516-346-2100

James C. Riple
Allied Signal
28626 Vista Madera
Rancho Palos Verdes, CA 90732
310-512-4586

James D. Roberge
SatCon Technology Corporation
12 Emily Street
Cambridge, MA 02139
617-661-0540, X272

Robert Salter
Xerad
1526 14th Street
Santa Monica, CA 90404

Philippe Save De Beaurecueil
Southern California Edison Company
GO3 Third Floor
2131 Walnut Grove Avenue
Rosemead, CA 91770
818-302-8272

Dr. Hideo Sawada
National Aerospace Laboratory
7-44-1 Jindaijihigashi-machi
Chofu-shi
Tokyo 182 JAPAN
81-422-47-5911

J. Schmeid
Sulzer Escher Wyss Ltd.
Abteilung T733
Postfach
CH-8023 Zurich SWITZERLAND
41-1-278-3118

Richard Schoeller, Jr.
Naval Surface Warfare Center
3A Leggett Circle
Annapolis, MD 21402-5067
410-267-2651

Dr. Roland Y. Siegwart
Mecos Traxler AG
Gutstrasse 38
Winterthur S CH-8400 SWITZERLAND
41-52-2329288

Devendra K. Sood
GE Aircraft Engines
1000 Western Avenue
M.D.-170MW
Lynn, MA 01910
617-594-3061

Albert F. Storace
General Electric Aircraft Engines
1 Neumann Way
Mail Drop A334
Cincinnati, OH 45215
513-774-5047

Claus C. Thiesen
Technical Services Company
10510 N.E. 45th Street
Kirkland, WA 98033
206-822-2609

R. Torti
SatCon Technology Corp.
12 Emily Street
Cambridge, MA 02139-4507
617-661-0540

694

Michael Urednicek
REVOLVE Technologies Inc.
1240 Western Canadian Place
700 Ninth Avenue S.W.
Calgary, Alberta T2P 3V4 CANADA
403-261-5329

Jim Walker
Walker Technology
17561 Hada Drive
San Diego, CA 92127
619-487-4788

Michael H. Walmer
Electron Energy Corporation
924 Links Avenue
Landisville, PA 17538
717-898-2294

Mark E. Williams
University of NC at Charlotte
Precision Engineering Department
Charlotte, NC 28223
704-547-3145

REPORT DOCUMENTATION PAGE

Public reporting burden for this collection of information is estimated to average 1 hour per response, including the time for reviewing instructions, searching existing data sources, gathering and maintaining the data needed, and completing and reviewing the collection of information. Send comments regarding this burden estimate or any other aspect of this collection of information, including suggestions for reducing this burden, to Washington Headquarters Services, Directorate for Information Operations and Reports, 1215 Jefferson Davis Highway, Suite 1204, Arlington, VA 22202-4302, and to the Office of Management and Budget, Paperwork Reduction Project (0704-0188), Washington, DC 20503.

1. AGENCY USE ONLY(Leave blank)	2. REPORT DATE May 1994	3. REPORT TYPE AND DATES COVERED Conference Publication

4. TITLE AND SUBTITLE
Second International Symposium on Magnetic Suspension Technology

5. FUNDING NUMBERS
WU 233-03-01-01

6. AUTHOR(S)
Nelson J. Groom and Colin P. Britcher, Editors

7. PERFORMING ORGANIZATION NAME(S) AND ADDRESS(ES)
NASA Langley Research Center
Hampton, VA 23681-0001

8. PERFORMING ORGANIZATION REPORT NUMBER
L-17369

9. SPONSORING/MONITORING AGENCY NAME(S) AND ADDRESS(ES)
National Aeronautics and Space Administration
Washington, DC 20546-0001

10. SPONSORING/MONITORING AGENCY REPORT NUMBER
NASA CP-3247
Part 2

11. SUPPLEMENTARY NOTES
Nelson J. Groom: Langley Research Center, Hampton, VA; Colin P. Britcher: Old Dominion University, Norfolk, VA

12a. DISTRIBUTION/AVAILABILITY STATEMENT

Unclassified–Unlimited

Subject Category 18

12b. DISTRIBUTION CODE

13. ABSTRACT (Maximum 200 words)
In order to examine the state of technology of all areas of magnetic suspension and to review related recent developments in sensors and controls approaches, superconducting magnet technology, and design/implementation practices, the 2nd International Symposium on Magnetic Suspension Technology was held at the Westin Hotel in Seattle, Washington on August 11–13, 1993.

The symposium included 18 technical sessions in which 44 papers were presented. The technical sessions covered the areas of bearings, bearing modelling, controls, vibration isolation, micromachines, superconductivity, wind tunnel magnetic suspension systems, magnetically levitated trains (MAGLEV), rotating machinery and energy storage, and applications. A list of attendees appears at the end of the document.

14. SUBJECT TERMS
Magnetic bearings; Magnetic suspension; Large gap magnetic suspension; Small gap magnetic suspension; Sensors; Superconducting magnetic suspension systems; Control systems

15. NUMBER OF PAGES
278

16. PRICE CODE
A13

17. SECURITY CLASSIFICATION OF REPORT Unclassified	18. SECURITY CLASSIFICATION OF THIS PAGE Unclassified	19. SECURITY CLASSIFICATION OF ABSTRACT Unclassified	20. LIMITATION OF ABSTRACT

NSN 7540-01-280-5500